



**HAL**  
open science

# Initiation and propagation of fractures in anisotropic media, taking into account Hydro-Mechanical couplings

Sourena Moosavi

► **To cite this version:**

Sourena Moosavi. Initiation and propagation of fractures in anisotropic media, taking into account Hydro-Mechanical couplings. Applied geology. Université de Lorraine, 2018. English. NNT : 2018LORR0254 . tel-02104028

**HAL Id: tel-02104028**

**<https://hal.univ-lorraine.fr/tel-02104028v1>**

Submitted on 19 Apr 2019

**HAL** is a multi-disciplinary open access archive for the deposit and dissemination of scientific research documents, whether they are published or not. The documents may come from teaching and research institutions in France or abroad, or from public or private research centers.

L'archive ouverte pluridisciplinaire **HAL**, est destinée au dépôt et à la diffusion de documents scientifiques de niveau recherche, publiés ou non, émanant des établissements d'enseignement et de recherche français ou étrangers, des laboratoires publics ou privés.



## AVERTISSEMENT

Ce document est le fruit d'un long travail approuvé par le jury de soutenance et mis à disposition de l'ensemble de la communauté universitaire élargie.

Il est soumis à la propriété intellectuelle de l'auteur. Ceci implique une obligation de citation et de référencement lors de l'utilisation de ce document.

D'autre part, toute contrefaçon, plagiat, reproduction illicite encourt une poursuite pénale.

Contact : [ddoc-theses-contact@univ-lorraine.fr](mailto:ddoc-theses-contact@univ-lorraine.fr)

## LIENS

Code de la Propriété Intellectuelle. articles L 122. 4

Code de la Propriété Intellectuelle. articles L 335.2- L 335.10

[http://www.cfcopies.com/V2/leg/leg\\_droi.php](http://www.cfcopies.com/V2/leg/leg_droi.php)

<http://www.culture.gouv.fr/culture/infos-pratiques/droits/protection.htm>



Université de Lorraine  
Ecole doctorale SIRENa

Thèse

Présentée et soutenue publiquement pour l'obtention du titre de  
DOCTEUR DE L'UNIVERSITE DE LORRAINE

Mention: Mécanique, Génie Civil

par Sourena MOOSAVI

**Initiation et propagation de la fracturation en milieu  
anisotrope avec prise en compte des couplages hydro  
mécaniques**

Présentée le 07/12/2018

Membres du jury Rapporteurs	Monsieur Philippe Cosenza, Professeur, Université de Poitiers Monsieur Dashnor Hoxha, Professeur, Université d'Orléans
Examineurs	Monsieur Albert Giraud, Professeur, Université de Lorraine Madame Sylvie Granet, EDF R&D, EDF Lab, Saclay
Directeur de thèse	Monsieur Richard Giot, Professeur, Université de Poitiers
Co-Directeur de thèse	Monsieur Luc Scholtès, Maître de Conférences, Université de Lorraine

# Contents

<b>Acknowledgement</b>	<b>7</b>
<b>Abstract in english</b>	<b>8</b>
<b>Résumé en français</b>	<b>9</b>
<b>Résumé elargi français</b>	<b>10</b>
<b>Introduction</b>	<b>14</b>
<b>1 Fracture propagation in TI media</b>	<b>18</b>
1.1 Phenomenology and observation	18
1.1.1 The influence of transverse isotropy	18
1.1.2 Hydromechanical couplings	22
1.2 Theoretical aspects	24
1.2.1 Generalized Griffith-Irwin theory	26
1.2.2 Calculating SIF using J-integral	27
1.2.3 Bifurcation angle	30
1.2.4 Cohesive Zone Model–CZM	32
1.3 Numerical modeling	33
1.3.1 Continuum–based methods	34
1.3.2 Discontinuum–based methods	42
1.4 Conclusion	44
<b>2 A fully coupled 3D HM-XFEM model for transverse isotropic media</b>	<b>46</b>
2.1 Introduction	46
2.2 HM-XFEM model representation	47
2.2.1 Domain definition and hypotheses	47
2.2.2 Governing equations	48
2.2.3 Variational formulations of conservation equations	51
2.2.4 Discretization with XFEM	52
2.2.5 Crack propagation along non-predefined paths in TI medium	57
2.2.6 Numerical implementation	59
2.3 Validation of the HM-XFEM model	60
2.3.1 Properties and geometry of the medium and boundary conditions	60
2.3.2 Numerical results	62
2.4 Conclusion	64
<b>3 Modeling fracture propagation in TI media using the BPM</b>	<b>67</b>
3.1 A BPM for TI materials	68
3.1.1 Formulation	68
3.1.2 Introduction of TI	70
3.2 Calibration of the model	71
3.2.1 Reference behaviors	73
3.3 Fracture propagation	77
3.3.1 Homogeneous/isotropic material	79
3.3.2 TI medium	81
3.4 Conclusion	87

CONTENTS

---

4 Conclusion	88
References	90
A Influence of stress induced microcracks on the tensile fracture behavior of rocks	102

# List of Figures

4	Shale gas site	15
5	CO2 storage site	16
6	Nuclear waste disposal site	16
1.1	Transverse isotropic elastic constants	19
1.2	Influence of TI on elastic properties	20
1.3	Fracture in TI samples, experimental	21
1.4	Hydromechanical couplings	23
1.5	Hydraulic fracture network	23
1.6	Principle fracture modes	24
1.7	Crack-tip stress field	28
1.8	J-integral scheme	28
1.9	Crack in anisotropic elastic solid	31
1.10	Linear softening law for Cohesive Zone Model	33
1.11	Cohesive Zone Model representation	33
1.12	FEM crack model representation	35
1.13	Element erosion model representation	35
1.14	XFEM model representation	37
1.15	FDM model grid representation	38
1.16	BEM discontinuity model representation	39
1.17	BEM technics	39
1.18	Meshless model representation	40
1.19	Peridynamic crack model representation	41
1.20	Phase field crack model	41
1.21	Discrete Element Method constitutive laws	43
1.22	Particle Bonded Method fracture model	44
2.1	HM-XFEM problem presentation	47
2.2	Interface orientation convention	47
2.3	Lorentz law diagrams	50
2.4	Level-set model presentation	53
2.5	Level-set model crack front	54
2.6	Heaviside function representation	54
2.7	HM-XFEM element model	55
2.8	Approximation space for CZM	55
2.9	Crack boundary parameters	57
2.10	Crack propagation detection on non predefined path	58
2.11	Virtual crack extension in CZM	59
2.12	HM-XFEM sample configuration	60
2.13	crack opening for $\theta = 0^\circ$	62
2.14	crack opening for $\theta = 15^\circ$	62
2.15	crack opening for $\theta = 30^\circ$	63
2.16	crack opening for $\theta = 45^\circ$	63
2.17	crack opening for $\theta = 60^\circ$	63
2.18	crack opening for $\theta = 75^\circ$	64
2.19	crack opening for $\theta = 90^\circ$	64
2.20	Test case configuration for a TI model	65
2.21	Simulated crack surface in 3D	65

3.1	DEM model features . . . . .	67
3.2	Interaction range representation . . . . .	69
3.3	BPM interaction law . . . . .	70
3.4	BPM rupture criterion . . . . .	70
3.5	Introduction of TI characteristic into the medium . . . . .	71
3.6	Polar representation of contact orientation in DEM . . . . .	72
3.7	The influence of weakness planes on macro-properties of DEM . . . . .	73
3.8	Triaxial compressive DEM model . . . . .	74
3.9	Effect of anisotropy on elastic properties Tournemire shale . . . . .	75
3.10	Effect of anisotropy on elastic properties COx claystone . . . . .	76
3.11	Failure pattern for Tournemire shale experimental observation vs BPM . . . . .	77
3.12	Shear bending BPM results . . . . .	78
3.13	Anisotropy in Tournemire shale and COx claystone . . . . .	78
3.14	Open and closed flaw representation BPM . . . . .	79
3.15	BPM simulated rock failure mechanism . . . . .	79
3.16	Comparison of the BPM predictions with respect to LEFM . . . . .	80
3.17	Divider, Short Transverse, and Arrester configurations . . . . .	81
3.18	Stress-strain responses of 3 edge cracked samples, Divider, short transverse and arrester . . . . .	82
3.19	COx claystone fracture propagation for Divider, Short Transverse, and Arrester configuration . . . . .	82
3.20	Tournemire shale fracture propagation for Divider, Short Transverse, and Arrester configuration . . . . .	83
3.21	COx claystone fracture patterns $\theta = 15, 30, 45, 60, 75$ . . . . .	84
3.22	Anisotropy impact on stress-strain response and toughness evolution for COx claystone . . . . .	85
3.23	Anisotropy impact on stress-strain response and toughness evolution for Tournemire shale . . . . .	85
3.24	Tournemire shale fracture patterns $\theta = 15, 30, 45, 60, 75$ . . . . .	86
4.1	crack opening for $\theta = 0^\circ$ . . . . .	88
4.2	Introduction of TI characteristic into the medium . . . . .	89

# List of Tables

2.1	HM-XFEM medium characteristic . . . . .	61
2.2	Cohesive interface characteristic . . . . .	61
3.1	Tournemire shale calibrated BPM . . . . .	74
3.2	COx claystone calibrated BPM . . . . .	75



# Acknowledgement

First of all I would like to thank région Grand Est for offering the financial support and making this research project possible. I also should thank the laboratory GeoRessources for providing me with a pleasant working atmosphere.

I would like to thank my supervisors for giving me the opportunity to work on this interesting topic where I developed several practical and theoretical skills. I am grateful to my supervisor Professor Richard Giot for giving me the opportunity to develop my own individuality and self-sufficiency by allowing me to work with such independence. I also need to thank my co-supervisor Doctor Luc Scholtès for his engagement through the learning process of this research project, his continuous support and motivation.

# Abstract in English

Current emphasis in petroleum industry toward increasing the reservoirs efficiency, along with the interest in exploitation of other sources of energy buried deep underground created a renewed interest in rock fracture mechanics in general and hydraulic fracturing specifically. Hydraulic fracturing, informally referred to as “fracking,” is an oil and gas well development process that typically involves injecting water, under high pressure into a bedrock formation via the well. This process is intended to create new fractures in the rock as well as increase the size, extent, and connectivity of existing fractures. However some of the very important features of this process have been overlooked. Among these neglected features one can name of inability of the vast majority of existing models to tackle at once the propagation of hydraulic fractures in fractured rocks-masses where a competing dipole mechanism exists between fracturing of the intact rock and re-activation of exiting fracture networks. Another feature that has been ignored is its intrinsically three-dimensionality which is neglected by most models. Among all different types of numerical methods that have been developed in order to assess the mechanism of fracturing phenomenon very few, if any, can handle the entire complexity of such process. In the present thesis, fluid-driven crack initiation and propagation in transverse isotropic rocks is simulated using a coupled model comprising of eXtended Finite Element Method (XFEM) and cohesive zone models. The HM-XFEM developed in this thesis is an extension to previous models developed introduced in multiscale hydrogeomechanics team of GeoRessources. An emphasis is put on considering the anisotropic nature of the medium and on studying its influence on the propagation path. This latter is investigated by the concept of bifurcation angle previously introduced in literature. In complementary efforts was made to have a better understanding of crack initiation in transversely isotropic media, we also used the discrete element method (DEM) in order to gain insights into the mechanisms at stake. Both methods exhibit their advantages and disadvantages in modeling fracturing phenomenon. The different nature of two methods, DEM being a discontinuous and XFEM being a continuous method, reveals potentials of both methods and renders a good comparison of which method suits the problem in hand the best, considering the the objectives of the design.

# Résumé en Français

L'accent mis actuellement par l'industrie pétrolière sur l'augmentation de l'efficacité des réservoirs, ainsi que sur l'intérêt grandissant pour l'exploitation d'autres sources d'énergie enfouies profondément sous terre a suscité un regain d'intérêt pour la mécanique de la fracturation des roches en général et la fracturation hydraulique en particulier. La fracturation hydraulique, appelée de manière informelle "fracturation", est un processus qui consiste généralement à injecter de l'eau, sous haute pression dans une formation rocheuse via le puits. Ce processus vise à créer de nouvelles fractures dans la roche et à augmenter la taille, l'étendue et la connectivité des fractures existantes. Des avancées récentes dans la modélisation et la simulation de fractures hydrauliques ont eu lieu, au confluent de facteurs qui incluent une activité accrue, une tendance vers une complexité accrue et une compréhension approfondie du modèle mathématique sous-jacent et de ses défis intrinsèques. Cependant, certaines des caractéristiques très importantes de ce processus ont été négligées. Parmi les caractéristiques négligées, on peut citer l'incapacité de la grande majorité des modèles existants de s'attaquer à la fois à la propagation de fractures hydrauliques dans la roche intacte, à l'initiation de nouvelles fractures ainsi qu'à la réactivation des fractures existantes. Une autre caractéristique qui a été ignorée est sa dimension intrinsèque en trois dimensions, négligée par la plupart des modèles actuellement proposés. Parmi tous les différents types de méthodes numériques développées pour évaluer le mécanisme du phénomène de fracturation, très peu sont capables de représenter la totalité des mécanismes mis en jeu. Dans la présente thèse, l'initiation et la propagation de fissures induites par les fluides dans des roches isotropes transversales sont simulées à l'aide d'un modèle hydromécanique (HM) couplé basé la méthode XFEM (eXtended Finite Element Method) et un modèle de zones cohésives. Le HM-XFEM développé dans cette thèse est une extension des modèles précédemment développés dans l'équipe hydro-géomécanique multi-échelle de GeoRessources. L'accent a été porté plus particulièrement sur la prise en compte de l'anisotropie du milieu et sur son influence sur le chemin de propagation. Ce dernier est défini à partir du concept d'angle de bifurcation introduit auparavant dans la littérature. En complément des développements réalisés dans le modèle HM-XFEM, effort a été fait pour mieux comprendre l'initiation de la fissure en utilisant la méthode des éléments discrets (DEM) à l'aide du logiciel open source YADE Open DEM. La nature différente des deux méthodes, DEM étant une méthode discontinue et XFEM, une méthode continue, révèle les potentiels des deux méthodes et permet de comparer correctement la méthode qui convient le mieux au problème à résoudre, compte tenu des objectifs de la conception.

# Résumé élargi en Français

## Introduction

La fracturation hydraulique est un processus qui consiste à injecter de l'eau sous haute pression dans une formation rocheuse via un puit. Ce processus a pour objectif de créer de nouvelles fractures dans la roche et d'augmenter la taille, l'étendue et la connectivité des fractures existantes. Plusieurs modèles ont été proposés pour simuler ce processus mais ceux-ci ont été construits sur la base de nombreuses hypothèses simplificatrices du fait de la complexité des phénomènes en jeu. Parmi les caractéristiques négligées, on peut citer l'incapacité de la grande majorité des modèles existants de s'attaquer à la fois à la propagation des fractures dans la roche intacte, à l'initiation de nouvelles fractures ainsi qu'à la réactivation des fractures existantes. Il convient également de mentionner que l'une des caractéristiques très importantes ignorées par la plupart des modèles est la propriété anisotrope des roches. Parmi les différents types de méthodes numériques développées pour simuler la fracturation hydraulique, très peu sont capables de représenter la totalité des mécanismes mis en jeu. Le modèle HM-XFEM développé dans cette thèse est une extension des modèles précédemment développés dans l'équipe hydro-géomécanique multi-échelle de GeoRessources. L'accent a été porté plus particulièrement sur la prise en compte de l'anisotropie du milieu et sur son influence sur le chemin de propagation. Ce dernier est défini à partir du concept d'angle de bifurcation introduit auparavant dans la littérature. En complément des développements réalisés dans le modèle HM-XFEM, un effort a été fait pour mieux comprendre l'initiation des fissures dans les milieux fragiles hétérogènes en utilisant la méthode des éléments discrets (DEM). La nature différente des deux méthodes, la DEM étant une méthode discontinue et la XFEM, une méthode continue, révèle les potentiels des deux méthodes et permet d'identifier la méthode qui convient le mieux au problème à résoudre, compte tenu des objectifs de l'étude.

## Méthodes

Pour tenter d'examiner l'initiation et la propagation des fissures dans des roches isotropes transverses (TI), nous avons eu recours à la modélisation numérique. En effet, Les analyses théoriques et analytiques sont limitées compte tenu de la complexité inhérente au problème, de l'anisotropie, aux couplages hydromécaniques, à l'hétérogénéité des matériaux, etc. Le domaine de la mécanique de la rupture numérique est relativement mature et de nombreux progrès ont été réalisés. Néanmoins, la modélisation de la propagation de fracture reste un problème délicat et de nouvelles méthodes continuent à apparaître. Depuis le début des années 1980, on assiste à une croissance exponentielle de la sophistication et de la puissance des méthodes numériques appliquées à l'étude de l'initiation et de la propagation des fractures dans les roches et les bétons. Une de ces méthodes est la méthode des éléments finis étendus (XFEM) qui a été développée pour faciliter la résolution des problèmes liés aux entités localisées qui ne sont pas résolues efficacement par le raffinement du maillage (utilisé dans la méthode des éléments finis conventionnelle-FEM). L'un des principaux avantages de la méthode XFEM réside dans le fait qu'elle supprime la nécessité de mailler les surfaces de discontinuité, réduisant ainsi les coûts de calcul associés à la MEF classique. XFEM, comme la plupart des méthodes continues, utilise un critère basé sur les facteurs d'intensité des contraintes pour simuler le déclenchement et la propagation d'une fracture. En complément, nous avons également utilisé une méthode discontinue, la méthode aux éléments discrets (DEM), pour simuler les processus de propagation de fissures. Dans la DEM, la fissure se propage à la suite de la rupture des liaisons interparticulaires en fonction de leur résistance (par exemple, leur résistance à la traction). Dans de tels modèles, la propagation de la fracture résulte

de la nucléation, de l'interaction et de la coalescence des fissures et ne nécessite pas de traitement numérique spécifique contrairement à la plupart des approches continues telles que XFEM.

### Le HM-XFEM

L'isotropie transverse affectant essentiellement la propagation de la fissure le long de chemins non prédéfinis, le développement et la mise en œuvre numériques ont été réalisés dans les fichiers FORTRAN et Python relatifs au modèle HM-XFEM implémenté dans Code Aster. Plus spécifiquement, les opérateurs impactés par l'isotropie transverse sont CALC-G et PROPA FISS, ainsi que POST CHAM XFEM pour la phase de post-traitement des simulations. L'opérateur CALC-G permet le calcul des facteurs d'intensité de contrainte. Ce dernier est implémenté dans le fichier FORTRAN op0100.F90, qui a donc dû être modifié pour intégrer l'isotropie transverse. Nous avons dû créer de nouveaux fichiers FORTRAN correspondant à la version isotrope transverse des fichiers de base du code. Tous ces fichiers permettent le calcul des facteurs d'intensité de contrainte. En particulier, nous avons dû implémenter les fonctions d'enrichissement pour la partie asymptotique liée au fond de fissure.

### Le BPM

Le comportement de la matrice de roche TI est simulé à l'aide d'un modèle de particules collées (BPM) proposé par [157] et implémenté dans le code libre YADE Open DEM [166]. Le coeur du modèle est dans une certaine mesure similaire aux autres BPM [144, 188]. Le matériau rocheux est représenté par un assemblage polydisperse dense de particules rigides et sphériques interagissant selon des lois de contact prédéfinies. Le BPM proposé a été utilisé avec succès pour simuler l'initiation et la propagation de fractures dans des roches isotropes à différentes échelles et dans différentes conditions de chargement [58, 75, 157]. [51] a proposé une version améliorée pour modéliser des roches isotropes transverses en introduisant une composante texturale dédiée dans le support numérique. Suivant l'approche développée par [55], une modification de la microstructure du milieu est effectuée en insérant des plans de faiblesse à l'échelle interparticulaire.

## Résultats

### Le HM-XFEM

Le modèle hydromécanique présenté ici est un bloc 3D avec une hauteur  $LZ = 10 m$ , une longueur  $LX = 10 m$  et une largeur  $LY = 2 m$ . Ce bloc contient une discontinuité de type interface cohésive. Cette interface est localisée par l'équation de level-set normal  $l_{sn} = Z - 5$  et traverse tout le bloc dans le sens horizontal en le divisant en deux sous-blocs identiques. Ce test a déjà été utilisé pour la validation des éléments hydromécaniques mis en œuvre dans Code Aster en considérant un milieu isotrope. Nous avons décidé de l'étendre à l'isotropie transverse afin de vérifier notre propre étude. Les résultats obtenus sont basés sur le cas-test standard modifié de Code Aster (WTNV148) avec les caractéristiques isotropes transverses intégrées dans le modèle. Les champs de déplacement et les champs de pression interstitielle sont étudiés pour différentes orientations du matériau par rapport au plan d'interface. Les angles de stratification de  $0^\circ$  (parallèle à la fissure) à  $90^\circ$  (perpendiculaire à la fissure) par pas de  $15^\circ$  sont pris en compte (Figure 1).

### Le BPM

Nous nous intéresserons ici à la propagation de la fracture de mode I afin d'étudier l'influence de TI sur un tel processus. La discontinuité représentant une fracture préexistante dans l'échantillon est introduite dans le milieu sous la forme d'une interface fermée, purement frictionnelle. Nous avons étudié l'influence de l'orientation du matériau par rapport à cette fracture sur les mécanismes d'initiation et de propagation. Comme prévu, la résistance (la ténacité) du matériau augmente lorsque les stratifications tendent vers une direction perpendiculaire aux plans de stratification

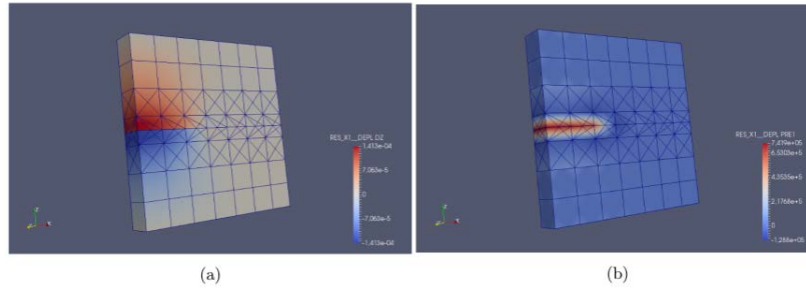


Figure 1: Modèle HM-XFEM développé dans Code\_Aster représentant le matériel IT, a) Le champ de déplacement résultant pour l'angle de stratification de  $\theta = 0^\circ$ . et b) Le champ de pression interstitielle résultant pour l'angle de stratification de  $\theta = 0^\circ$ .

(Figure 2). On peut observer que des angles de stratification supérieurs à  $\theta = 15^\circ$  peuvent provoquer la déflexion de la fracture selon le degré d'anisotropie du matériau (Figure 3). Les simulations sont effectuées sur des échantillons de roche synthétiques calibrés sur les argilites du COx et les argilites de Tournemire, mais, par souci de brièveté, nous ne montrons ici que les résultats pour les argilites de Tournemire.

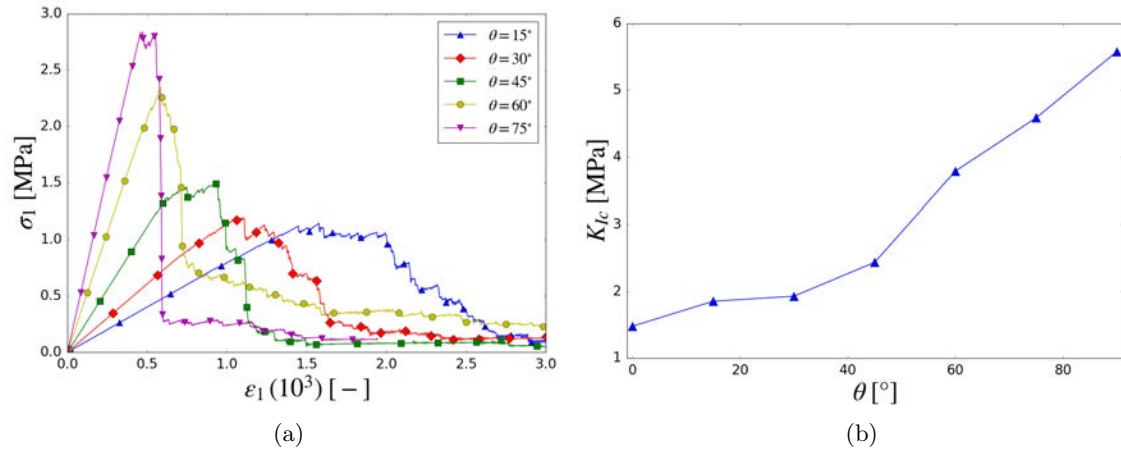


Figure 2: a) Réponse contrainte-déformation (tension uniaxiale) d'échantillons d'argilite de Tournemire Short-Transverse présentant (edge crack) différentes orientations des plans de stratification,  $\theta = 15^\circ, 30^\circ, 45^\circ, 60^\circ, 75^\circ$ , b) Evolution de  $K_{Ic}$  en fonction de l'angle de stratification  $\theta$ .

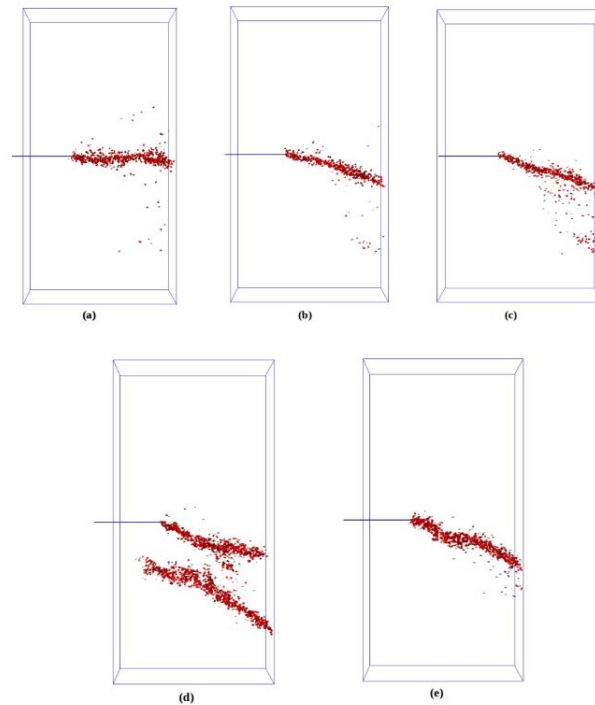


Figure 3: Chemins de fissurations pour les argilites de Tournemire, pour différentes orientations des plans de stratification a)  $\theta = 15^\circ$  , b)  $\theta = 30^\circ$  , c)  $\theta = 45^\circ$  , d)  $\theta = 60^\circ$  , e)  $\theta = 75^\circ$ .

## Conclusion

Nous avons développé deux approches différentes basées sur deux méthodes numériques, à savoir le BPM et le HM-XFEM, pour étudier la propagation des fractures dans les matériaux isotropes transverses. Le modèle HM-XFEM anisotrope est basé sur un outil numérique introduit précédemment par [65] et [139] pour la simulation de la propagation des fractures hydrauliques. Nous avons réussi à intégrer la propriété isotrope transverse dans le modèle HM-XFEM existant, et l'étude de l'impact de l'isotropie transverse sur la propagation de la fracture hydraulique a été étudiée. Une approche de modélisation discrète est également proposée pour étudier la propagation des fractures dans un milieu isotrope transverse sans couplage hydro-mécanique. L'anisotropie est directement introduite dans le milieu numérique par le biais de plans de faiblesse orientés préférentiellement selon le plan d'isotropie du matériau. Le modèle est utilisé pour simuler des essais de traction sur des échantillons de roche synthétique contenant une fissure préexistante. Cette approche reproduit toutes les caractéristiques typiques des matériaux fragiles, notamment le comportement élastique linéaire lors de petites déformations, la nucléation des fissures avant la rupture et le développement d'une fracture par la coalescence de ces fissures. De plus, en utilisant le BPM anisotrope proposé, une très bonne description du comportement de deux roches isotropes transverses est obtenue à la fois en termes de processus de déformation et de rupture. Le modèle est capable de décrire à la fois l'évolution de l'endommagement et la localisation des déformations lors de la rupture. L'influence de l'orientation de la stratification sur la ténacité ( $K_{Ic}$ ) est étudiée. D'autres mesures sont actuellement prises pour étendre et développer les modèles proposés pour des phénomènes plus complexes. Des efforts sont en cours pour développer le BPM pour la simulation de la fracturation hydraulique dans des milieux isotropes transverses. Le modèle HM-XFEM que nous avons développé actuellement ne permet que de simuler la propagation de fractures hydrauliques le long de chemins prédéfinis. Des efforts supplémentaires sont nécessaires pour étendre le modèle à la propagation de fracture sur des chemins non prédéfinis.

# Introduction

## Statement of the problem

An understanding of the mechanics and mechanisms of rock fracture is a key element in solving many engineering problems that involve geotechnical structures. A “geotechnical structure” may be simply a rock mass containing fossil fuels such as oil and gas or a mineral with valuable elements such as copper, iron, or aluminum. The rock mass becomes a structure when man enters the picture by drilling a well, boring a tunnel, or digging a longwall, room and pillar, or open pit mine. Therefore, an understanding of the fracture mechanisms taking place in rocks is an essential prerequisite for designing engineering structures [152].

Fractures are important in geotechnical, and hydrogeological practice partly because they provide pathways for fluid flow. Many economically significant petroleum, geothermal, and water supply reservoirs form in fractured rocks. Fracture systems control the dispersion of chemical contaminants into and through the subsurface. They also affect the stability of engineered structures and excavations. Dealing with and exploiting fracturing of rock has been part of mining engineering for hundreds of years, but the analysis of fracture of rock or other materials has only developed into an engineering discipline since the mid 1940s [4]. Rock failure is often controlled by fracture initiation, propagation and coalescence, especially in hard rocks where explicit fracturing rather than plasticity is the dominant mechanism of failure. Hence, prediction of the explicit fracturing process is necessary when the rock mass stability is investigated for engineering purposes [11].

Depending on the application of the engineering project, the presence and expansion of cracks and fractures can play a role in advantage or to disadvantage of engineers and designers. One field where the expansion of fractures plays a favorable role in fulfilling the objectives of the project is the oil and gas industry. Hydraulic fracturing is widely used in the oil and gas industry to stimulate production from wells (Figure 4). Hydraulic fracturing is a well-stimulation technique commonly used in low permeability rocks like tight sandstone, shale, and some coal beds to increase oil and/or gas flow to a well from petroleum-bearing rock formations. In this method a horizontal well is drilled in the rock. Then a huge quantity of water is injected with a very high pressure in the well, in order to create a fracture network as dense and as extended as possible. The fracture network expands from natural cracks found in the vicinity of the well. Finally, the fracturing fluid is drained off.

In the opposite, there is a range of applications for which the expansion and propagation of cracks must be prevented. When a reservoir is being exploited, or converted into a carbon dioxide storage site, it is essential to guarantee the impermeability of the cap rocks. Depending on the regional stress and on the reservoir characteristics, fluid driven fractures may propagate in the reservoir and eventually reach the cap rocks. The chances that these cracks penetrate in the cap rocks depend on the properties of both the reservoir rock and the cap rock. This phenomenon must be prevented by all means in order to efficiently exploit a reservoir or safely operate a  $CO_2$  storage (Figure 5).

For nuclear waste storage (Figure 6), the threat formed by the spreading of radioactive elements is significant, considering the damage the radioactive materials cause to the environment. The excavation of storage compartments modifies the in situ stresses and is accompanied by the appearance of cracks in the surroundings of the excavated volumes. This is enhanced by the thermal effects induced by the presence of nuclear waste [172]. The flow of fluids in these cracks favors the migration and the diffusion of the radionuclides [112]. The spreading of radioactive elements is then likely to happen in an extended area around the storage compartments. It is then essential to apprehend and model the behavior of porous rock masses that include cracks whether for extracting natural resources or for the development of storage compartments.



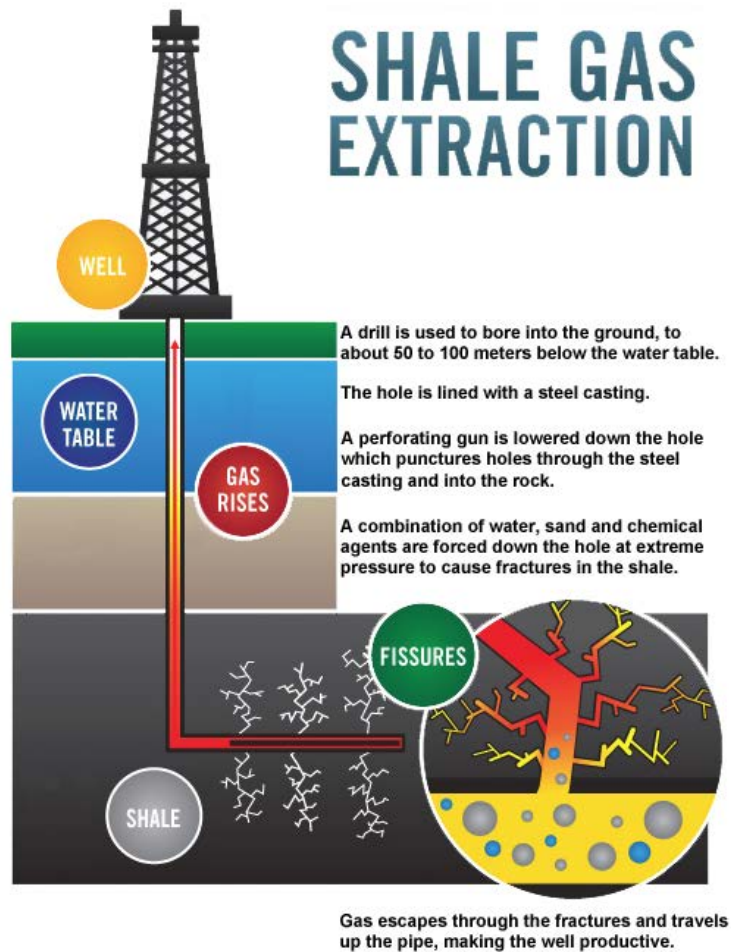


Figure 4: Hydraulic fracturing in rocks.

Among the potential types of rock formations with various engineering functionalities such as acting as the cap rock in  $CO_2$  storage and hosting radioactive wastes or containing oil and gas in petroleum engineering we can recall argillaceous rock formations. Such rocks are transversely isotropic in nature which makes it inevitable to understand its impact on the behavior of such rocks. Nowadays, much of the research is directed towards investigating the thermal, hydraulic, mechanical, and chemical (THMC) properties of low permeability sedimentary rocks such as argillaceous rocks [1]. Argillaceous rocks are characterized by the presence of closely spaced bedding planes, resulting in anisotropy of their behaviour (mechanical, hydraulic, thermal). Argillaceous rocks are often the constituent of cap rocks. The presence of such anisotropic rocks in mining industry is also a very often encountered. It is then of significant importance to understand the mechanical behavior of such anisotropic formations.

The aim of this study is to develop numerical models capable of modeling the initiation and propagation of fractures in rocks, taking into account their anisotropic behavior along with the hydro-mechanical couplings involved in the fracturing phenomenon.

## Methodology

In an attempt to investigate crack initiation and propagation in transverse isotropic (TI) rocks, we resort to numerical modeling to gain insights into the problem at stake. Because theoretical

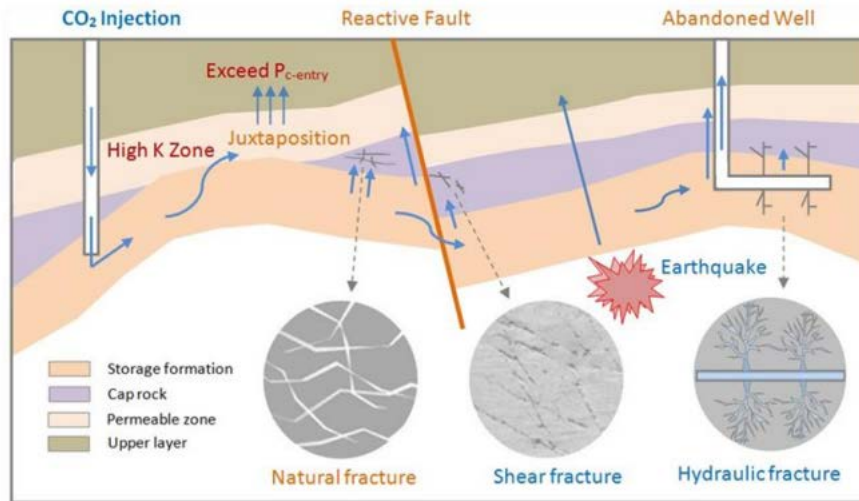


Figure 5: CO2 storage site. [19]

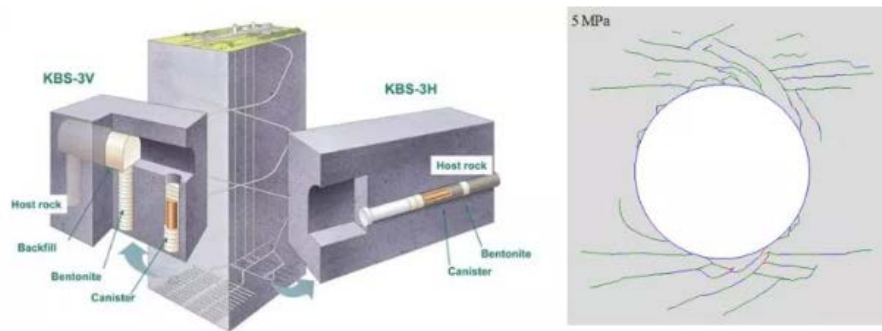


Figure 6: Conceptual configuration of a nuclear repository (left); and Predicted fracturing pattern around the deposition hole after 40 years heating (right). From csiro-mining geomechanics website

and analytical analyses are limited considering the inherent complexity of the problem such as anisotropy, hydromechanical couplings, material heterogeneity, etc.

The field of computational fracture mechanics is relatively mature, and many advances have been made. Nevertheless, modeling fracture propagation remains a challenging problem, and new methods continue to arise. Since the early 1980s, there has been an exponential growth in the sophistication and power of numerical methods which have been applied to the study of failure, initiation and propagation of fractures in rock and concrete. One of such methods is the extended finite element method (XFEM) that was developed to ease difficulties in solving problems with localized features that are not efficiently resolved by mesh refinement (used in conventional finite element method-FEM). One of the objectives of XFEM was the modeling of fractures. A key advantage of XFEM is that it suppresses the need to mesh and remesh the discontinuity surfaces, thus alleviating the computational costs and projection errors associated with conventional FEM, and the need for restricting discontinuities to mesh edges. XFEM like most of continuum methods use criterion generally based on SIF to simulate fracture initiation and propagation. On the other side of the spectrum, in discontinuum methods like bonded particle models (BPMs) crack propagates as a result of interparticle bonds or element breakages according to the definition of their strength (e.g., their tensile strength). In such models, the propagation of fracture results from the nucleation, interaction and coalescence of cracks and does not require specific numerical treatments contrary to most continuum approaches such as XFEM.

The two codes used in this research are *Code\_Aster* and *Yade*. *Code\_Aster* is an open source

finite element software developed by EDF *R&D*. The calculation of SIF to analyze propagation of discontinuities in crack containing structures is already possible in *Code\_Aster* for a range of engineering problems concerned with elastic isotropic materials or isotropic hydro-mechanical crack propagations. Originally, Ferté [64] proposed a method to study the propagation of 3D cohesive cracks on non predefined paths using XFEM. As a continuation of Ferté's work, Paul [139] developed a procedure in order to study the propagation of fluid-driven cracks on non predefined paths. In this study we take Paul's model one step further by introducing material anisotropy (i.e., transverse isotropy) in to the model. In addition, in order to investigate the influence of transverse isotropic characteristic of rocks on the fracturing process, we utilized the BPM implemented in the open source software YADE Open DEM. We first calibrated the model to simulate representative behaviors of TI rocks and then considered specific fracture mechanics test simulations so as to gain insights into the propagation of fractures in such materials.

## Outline of the thesis

The present research study intends to model the initiation and propagation of fractures in transversely isotropic media. To fulfill this purpose, we build our developments on the model previously carried out by Paul [139] which in turn was built on the foundation of a model laid by Ferté [64]. In addition, we used a bonded particle model to investigate the initiation and propagation of fracture in transverse isotropic rocks.

In Section 1.1 a comprehensive literature survey on the fracture propagation in TI media is also given. We have a look at the material and environmental aspects influencing the fracturing process, *i.e.* the anisotropy of the medium and the hydromechanical couplings involved. We also have a look at in situ and laboratory observations of fractures and its consequences. We emphasize the importance of fracturing mechanism in engineering design and give a brief introduction of fracture modes. In Section 1.2, an insight in to the theory of LEFM dealing with fluid driven fractures in TI media is given. The Cohesive Zone Model-CZM as a remedy to the shortcomings of LEFM is introduced and calculation of SIF using J-integral is presented. At the end of Section 1.2, different types of calculation method for computing bifurcation angle is given and the pertaining equations giving the bifurcation angle in TI media are developed. In Section 1.3, different numerical methods are presented. We analyze and compare their advantages and disadvantages with regard to modeling of fracture propagation. In Chapter 2, the HM-XFEM model as a robust method for modeling hydraulic fracture is presented. The implementation of the method in an open source code (*Code\_Aster*) is described and the perspective of the work is discussed. In Chapter 3, we introduce a bonded particle model (BPM) for modeling transverse isotropic brittle materials. We present the methodology and the calibrating process and we demonstrate the capabilities of BPM in modeling rock fracturing phenomenon. We then set up fracture mechanics test simulations to study the propagation of fractures in TI materials. In Chapter 4, we conclude our study by discussing the advantages and shortcomings of the methods we used.

# Chapter 1

## Fracture propagation in TI media

### 1.1 Phenomenology and observation

The whole process of rock failure is a complicated interaction of stress fields and crack propagation governed by material and environmental aspects [152]. Hence, an understanding of the mechanics and mechanisms of rock fracture is a key element in solving many engineering problems that involve geological structures.

The design procedure in rock engineering might be quite different from other applications concerned with fracture mechanics, although the theory and arithmetic might be similar. In some cases in rock mechanics, the objective is to promote fracturing, contrary to majority of other engineering applications of fracture mechanics where the fracture is preferred to be avoided and prevented from propagation. An example of rock fracture problem where controlled fracture propagation is the objective, is shale gas exploitation (Figure 4). It is one of the most common domains of application for fracture formation. Shale gas production has grown tremendously in the past decade and is now a major source of energy. Shale gas production relies on fracture formation by fluid injection i.e. “*hydraulic fracturing*”. Hydraulic fracturing is a commonly used technique to enhance reservoir permeability and well efficiency. Another example of hydrofracturing is the hot, dry rock geothermal energy extraction which demands the formation of surface area by hydrofracturing. Also in rock comminution problems, one must not only initiate fracture but also drive these to free surfaces, hopefully with a minimal amount of energy expended. Other applications concerned with the control of fluid driven cracks include underground storage of carbon dioxide, toxic or radioactive waste [112], geophysics, for example water-driven propagation of fracture along glacier beds [177], preconditioning of ore bodies for large-scale underground caving operations [93, 195], disposal of waste drill cuttings [129], remediation projects in contaminated soils [130, 131, 66], improvement of the performance of water wells.

As was pointed out at the very beginning of this section, fracturing is governed by material and environmental aspects. As far as the material aspect is concerned we can particularly mention material properties such as anisotropic characteristic of the medium, and for environmental aspect the presence of fluid. These aspects bring us back to the very objective of this thesis which is understanding the influence of transverse isotropy on the propagation of fractures. In the following we have a closer look at the impact of both transverse isotropy and hydro-mechanical couplings on the fracturing process.

#### 1.1.1 The influence of transverse isotropy

Anisotropy is the property of being directionally dependent, as opposed to isotropy, which implies identical properties in all directions. It can be defined as a difference, when measured along different axes, in a material’s physical or mechanical properties. Transverse isotropy (hexagonal symmetry) is one of the eight classes of anisotropic (crystalline) symmetry. The classes range from, at one extreme, isotropy specified by two elastic constants and having spherical symmetry, to the other extreme of triclinic symmetry specified by up to 21 elastic constants and having no symmetry apart from inverse symmetry (so that it takes as long for a wave to travel from A to B as from B to A). Transversely isotropic materials are characterized by five independent elastic constants and present an axis of rotational symmetry so that the properties are identical (isotropic)

for all directions at right angles to the axis, and while the axis is vertical there is vertical transverse isotropy.

Transverse isotropy can be expressed in the form of a compliance matrix (inverse of elastic stiffness) as below.

$$\begin{bmatrix} \epsilon_x \\ \epsilon_y \\ \epsilon_z \\ \gamma_{yz} \\ \gamma_{zx} \\ \gamma_{xy} \end{bmatrix} = \begin{bmatrix} \frac{1}{E} & \frac{-\nu}{E} & \frac{-\nu'}{E'} & 0 & 0 & 0 \\ \frac{-\nu}{E} & \frac{1}{E} & \frac{-\nu'}{E'} & 0 & 0 & 0 \\ \frac{-\nu'}{E'} & \frac{-\nu'}{E'} & \frac{1}{E'} & 0 & 0 & 0 \\ 0 & 0 & 0 & \frac{1}{2G'} & 0 & 0 \\ 0 & 0 & 0 & 0 & \frac{1}{2G'} & 0 \\ 0 & 0 & 0 & 0 & 0 & \frac{1}{2G} \end{bmatrix} \begin{bmatrix} \sigma_x \\ \sigma_y \\ \sigma_z \\ \tau_{yz} \\ \tau_{zx} \\ \tau_{xy} \end{bmatrix} \quad (1.1)$$

There are five independent elastic constants that needs to be determined to characterize a TI material.  $E$  and  $E'$  are the elastic moduli in the plane of transverse isotropy ( $Ox, Oy$ -axes in Figure 1.1) and in a direction normal to it ( $Ox, Oz$ -axes in Figure 1.1), respectively.  $\nu$  is the Poisson's ratio characterizing transverse contraction (or expansion) in the plane of isotropy when tension (or compression) is applied in this plane, and  $\nu'$  for the same when tension (or compression) is applied in a direction normal to the plane of isotropy.  $G$  is the shear modulus in the plane of transverse isotropy.  $G'$  is the shear modulus characterizing the change in angle between the directions in the plane of isotropy and any directions perpendicular to it.

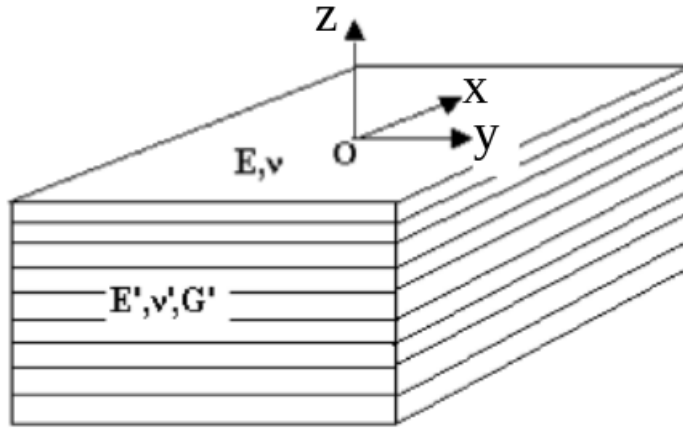


Figure 1.1: Cartesian coordinate system with  $Ox, Oy$ -axes lying on the isotropy plane and  $Oz$ -axis perpendicular to it in a transversely isotropic rock. After [61]

These relationships can be converted to an inverse form, in terms of the stiffness matrix.

$$\begin{bmatrix} \sigma_x \\ \sigma_y \\ \sigma_z \\ \tau_{yz} \\ \tau_{zx} \\ \tau_{xy} \end{bmatrix} = \begin{bmatrix} C_{11} & C_{12} & C_{13} & 0 & 0 & 0 \\ C_{12} & C_{11} & C_{13} & 0 & 0 & 0 \\ C_{13} & C_{13} & C_{33} & 0 & 0 & 0 \\ 0 & 0 & 0 & C_{44} & 0 & 0 \\ 0 & 0 & 0 & 0 & C_{44} & 0 \\ 0 & 0 & 0 & 0 & 0 & \frac{C_{11}-C_{12}}{2} \end{bmatrix} \begin{bmatrix} \epsilon_x \\ \epsilon_y \\ \epsilon_z \\ \gamma_{yz} \\ \gamma_{zx} \\ \gamma_{xy} \end{bmatrix} \quad (1.2)$$

where

$$\begin{aligned}
 C_{11} &= \frac{E(E' - E\nu'^2)}{(1 + \nu)\{(1 - \nu)E' - 2\nu'^2E\}} \\
 C_{33} &= \frac{E^2(1 - \nu^2)}{(1 + \nu)\{(1 - \nu)E' - 2\nu'^2E\}} \\
 C_{12} &= \frac{E(E' + E\nu'^2)}{(1 + \nu)\{(1 - \nu)E' - 2\nu'^2E\}} \\
 C_{13} &= \frac{EE'\nu'(1 + \nu^2)}{(1 + \nu)\{(1 - \nu)E' - 2\nu'^2E\}} \\
 C_{44} &= G' \\
 C_{44} &= G
 \end{aligned} \tag{1.3}$$

Using these relationships, the five elastic moduli, i.e.,  $E$ ,  $E'$ ,  $\nu$ ,  $G'$  and  $\nu'$ , can be calculated using the following equations:

$$E = C_{33} - \frac{2C_{13}^2}{C_{11} + C_{22}} \tag{1.4}$$

$$E' = C_{11} + \frac{C_{13}^2(C_{12} - C_{11}) + C_{12}(-C_{33}C_{12} + C_{13}^2)}{C_{11}C_{33} + C_{13}^2} \tag{1.5}$$

$$\nu = \nu_{32} = \frac{C_{13}}{C_{11} + C_{12}} \tag{1.6}$$

$$\nu' = \frac{C_{33}C_{12} - C_{11}^2}{C_{33}C_{11} + C_{13}^2} \tag{1.7}$$

The shear modulus  $G'$  can then be derived using the conventional relationship with other elastic parameters.

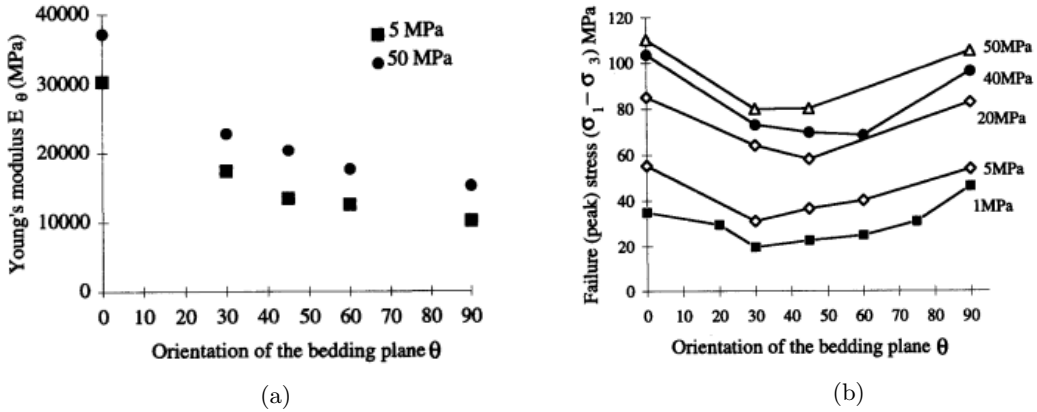


Figure 1.2: (a) Variation of axial Young modulus  $E_\theta$  vs loading orientation during triaxial test with different confining pressures, (b) Variation of failure stress vs loading orientation for various confining pressure [134].

Among anisotropic sedimentary rocks, one type of argillaceous rocks, termed shales, represents a particular interest for nuclear waste storage and oil industry. The existence of bedding planes as well as their micro-structure *i.e.* shape of minerals in natural shale formations, attribute a transverse isotropic characteristic to shale rocks. Niandou et al. [134] investigated the mechanical behavior of Tournemire shale (Figure 1.2). Using triaxial compression tests and hydrostatic compressibility tests. They concluded the elastic behavior of shale is non-linear and the shale exhibits large anisotropic plastic deformation. Besides, the existing shale fracture mechanics tests [156, 33, 110] show that the fracture toughness of shales are highly anisotropic. The measured

properties can be very scattered between different shales, even for the same type of shale owing to (1) the heterogeneity of shales, (2) the elastic anisotropy nature of shale matrix, (3) strong non-elastic deformation, and (4) the strong environmental effect, e.g., humidity, in influencing the testing results [119].

During the shale fracking process, bedding planes usually act as planes of weakness that diverts crack propagation, i.e., the fractures can either extend along or penetrate across the bedding plane when a fracture meets a bedding plane. For instance, [33] observed a general tendency of the fractures to be tortuous and kinked. According to them, fractures initiated perpendicular to the bedding might be expected to deflect along the bedding planes and remain in this propagation direction for some distance.




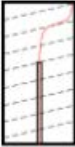

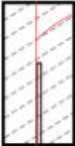

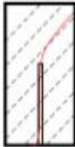

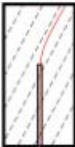



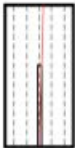
Bedding Orientation	Fractured Using Freshwater	
	Photograph	Sketch
0°		
15°		
30°		
45°		
60°		
75°		
90°		

Figure 1.3: Fractured shale cores with different bedding orientations. The red line shows the failure pattern caused by fluid injection into the samples. After [82]

Shales are strongly anisotropic, so that their fracture propagation trajectories depend on the interaction between their structural properties and the in situ stress. [82] through a series of

hydraulic fracturing experiments on shale cores using different bedding orientations showed the influence of the anisotropic characteristics on the propagation of hydraulic fractures. In their experiments, different types of fracture propagation modes were formed because of the different bedding orientations (Figure 1.3).

The types of fracture propagation observed after the shale cores' failure were:

- Curved fractures: these cracks are slightly curved and deviated from the loading direction,
- Layer-activated fractures: these are straight or slightly straight fractures that propagated along the bedding plane and the rock matrix,
- Central-linear fractures: fractures that propagated along the loading direction.

### 1.1.2 Hydromechanical couplings

Now looking into the hydraulic fracturing from a phenomenological point of view we will see that hydraulic fracturing involves several coupled phenomena [2, 31, 139]:

- the preferential fluid flow in the fracture depends on the fracture faces,
- mechanical deformation of the surrounding porous medium is induced by the fluid pressure on fracture lips,
- the deformations in the porous matrix induced by the tectonic shifts, the regional stress state or the residual stresses caused by the exploitation of the reservoir (subsidence),
- the fracture and the porous medium exchange fluid,
- the fracture propagates, and therefore, hydraulic fracture is a moving boundary problem.

Therefore, fully modelling the hydraulic fracturing process requires solving a coupled system of governing equations consisting of (1) elasticity equations that determine the relationship between the fracture opening and the fluid pressure, (2) non-linear partial differential equations for fluid flow (usually lubrication theory) that relate the fluid flow in the fracture to the fracture opening and the fluid pressure gradient, (3) a fracture propagation criterion (usually given by assuming LEFM is valid) that allows for quasi-static fracture growth when the stress intensity factor is equal to the fracture toughness, and (4) diffusion of fracturing fluid in the rock formation (see Figure 1.4).

Propagation of fluid-driven fractures has been the subject of numerous scientific papers [27, 2]. Most of these efforts have been driven by the oil and gas industry, and have been oriented towards the development of numerical models to predict the propagation of hydraulic fractures in the often complex geological settings under which extraction of hydrocarbons takes place.

In recent years, many researchers have recognized the existence of the complexity of hydraulic fracture extension. Warpinski [186, 187] discovered that the main fracture and the branch fractures extended simultaneously through the field tests and put forward the concept of fracture propagation zone. Afterwards, through physical simulation experiments [17, 18] and [36, 37] found that hydraulic fracture presented three kinds of extension path when it intersected with natural fractures: crossing natural fractures, extending along natural fractures, or the two cases occurring simultaneously. Although due to the insufficient and imperfect understanding of the fracture network forming mechanism in shale reservoirs, there is always blindness in the fracturing design of shale reservoirs (Figure 1.5a).

Based on fracture extension characteristic in shale reservoirs, [188] classified hydraulic fractures into four major categories: the single plane biwing fracture, complex multiple fracture, complex multiple fracture with open natural fractures, and complex fracture network, as shown in Figure 1.5b.

The early research efforts [69, 68, 50] concentrated on obtaining analytical solutions for the complex fluid-solid interaction problems by assuming a simple fracture geometry, such as the well-known 2-D plane strain PKN and KGD models, and the axisymmetric penny-shaped model. These



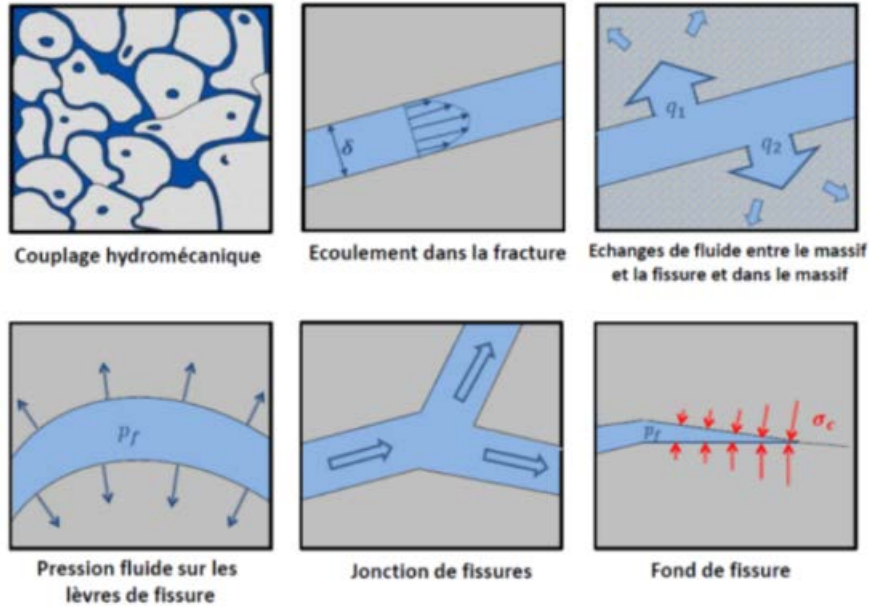


Figure 1.4: The different components of the model HM-XFEM

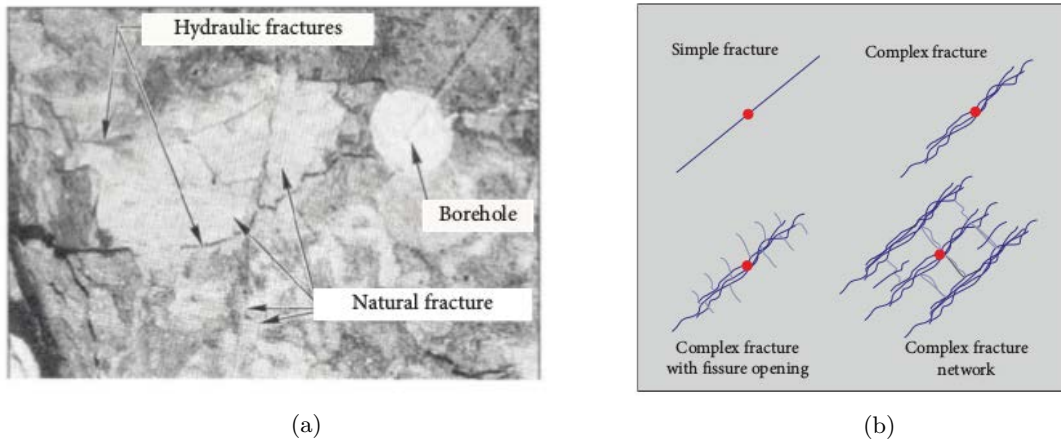


Figure 1.5: (a) Complex fracture extension in fractured shale reservoir [188], (b) Classification of fracture from simple to complex [188].

solutions usually suffer from the limitations of the analytical models such as simplification of the problem either with respect to the fracture opening profile or the fluid pressure distribution. Hence, a good deal of effort has been undertaken in the development of numerical models to simulate the propagation of hydraulic fractures for more complex and realistic geometries, with the first such so-called pseudo-3D model developed in the late 1970s [41]. In recent years, some newly developed numerical methods, such as the extended finite element method (XFEM) and particle simulation method, have been applied to investigate hydraulic fracture problems. However, because of the difficulty posed by modeling a fully 3-D hydraulic fracture, numerical simulation still remains a particularly challenging problem.

## 1.2 Theoretical aspects

The fundamental questions that arise in engineering fracture mechanics problems are “how can one predict the failure load of these flawed structures?”, “what combination of load and flaw geometry parameters leads to failure?”, and “what material parameters is the fracture process governed by?” [152]. Many failure criteria and theories such as the well known Mohr-Coulomb criterion can predict failure conditions for rock. However, these theories cannot be expected to deal with questions of crack propagation such as (1) the length and width of a hydraulic fracture created in an oil or gas well, (2) conditions resulting in crack advance of hydraulic fractures in geothermal application. The answers to the questions formulated above lie in a parameter known as the Stress Intensity Factor (SIF),  $K$ . This parameter appears from a straightforward analysis of stresses at the crack-tip. A similar parameter known as the strain energy release rate,  $G$ , is derived from a simple energy approach that treats crack growth as an instability phenomenon.

When attention is focussed on the local fields of elastic stress and displacement associated with the singularity near a crack tip, it is always possible to reduce the consideration of the most general situation to a sum of plane and antiplane problems [162]. In treating the crack tip fields by reductions to plane and antiplane problems and subsequently to three characteristic modes, a choice for convenience can be made in defining these modes and their corresponding SIFs. As Irwin pointed out in various papers [89, 90, 91], in fracture mechanics, mostly from a mathematical viewpoint, three basic modes of crack extension are distinguished: I, II, III (Figure 1.6). These are: (a) the opening mode encountered in symmetrical extension and bending of cracked materials where displacement discontinuity is perpendicular to the plane of the crack; (b) the sliding mode which is presumed to occur in skew-symmetric plane loading of cracked materials where, at the leading edge of the crack, the displacement discontinuity is in the plane and parallel to the direction of the crack; (c) the tearing mode which is assumed to occur in skew-symmetric bending (twisting) of cracked plates or skew-symmetric loading of cracked plates by forces perpendicular to their planes where the displacement discontinuity is perpendicular to the plane of material and in the plane of the crack. In all these cases, it is assumed that the crack is a straight through cut perpendicular to the plane of the material [60]. In reality, the fracturing phenomenon and the types of existing discontinuities are much more complex and often we encounter a combination of these three modes *i.e.* mixed modes.

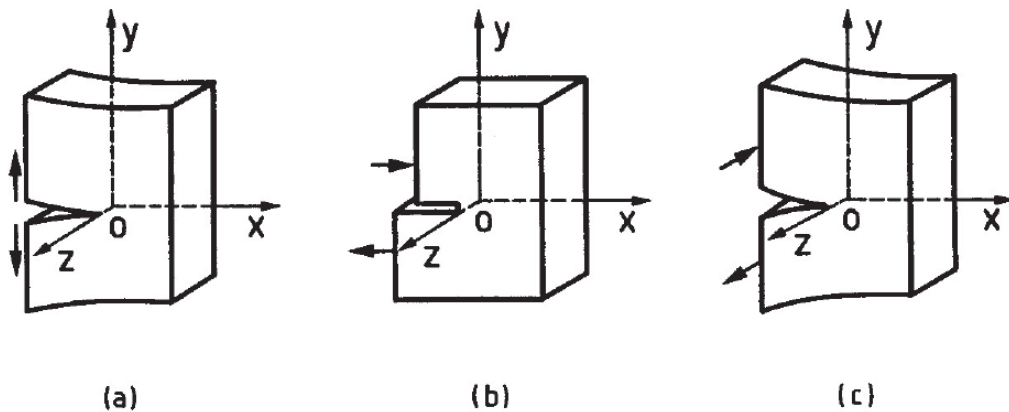


Figure 1.6: The three basic modes of crack extension. (a) Opening mode, I, (b) Sliding mode, II, (c) Tearing mode (antiplane mode), III (from [70]).

Traditional failure criteria are not capable of adequately explaining many structural failures that occur at stress levels considerably lower than the ultimate strength of the material. In 1921, Griffith, through his experiments on fiber glass noticed that the strength of real materials is much smaller (by two orders of magnitude) than their theoretical strength. The discipline of fracture mechanics emerged in order to explain such phenomena. A major objective of fracture mechanics is

to study the load-carrying capacity of structures in the presence of initial defects, where a dominant crack is assumed to exist [62].

Fracture mechanics research is considered to have officially begun in 1920 with Griffith's energy-based analysis of cracks. Two key factors gave impetus to the development of fracture mechanics: the size effect, and the inadequacy of traditional failure criteria. The strength of a material measured from a laboratory specimen is many times lower than that predicted from calculations. The traditional failure criteria were inadequate because they could not explain failures which occur at a nominal stress level considerably lower than the ultimate strength of the material. Griffith [74] suggested that the low fracture strength observed in experiments \*, as well as the size-dependence of strength, was due to the presence of microscopic flaws in the bulk material. Griffith's experiments showed that the product of the square root of the flaw length ( $a$ ) and the stress at fracture ( $\sigma_f$ ) was nearly constant ( $\sigma_f \sqrt{a} \approx C$ ). An explanation of this relation in terms of linear elasticity theory is problematic. Linear elasticity theory predicts that stress at the tip of a sharp flaw in a linear elastic material is infinite, meaning the structure containing a flaw should immediately fail under any load no matter how small. Hence, Griffith explained his observation in an energy based analysis by resorting to theory of thermodynamics. Decades later in 1957, G. R. Irwin [88] modified Griffith's theory and developed it to what would become Linear Elastic Fracture Mechanics (LEFM). It should be pointed out that both terms Fracture Mechanics and LEFM are used interchangeably in literature (hereforth we use the term LEFM).

LEFM is based on the principle that all the materials contain initial defects in the form of cracks, voids or inclusions which can affect the load carrying capacity of engineering structures. Near the defects high stresses prevail that are often responsible for lowering the strength of the material. One of the objectives of fracture mechanics, as applied to engineering design is the determination of the critical load of a structure by accounting for the size and location of initial defects. Thus, the problems of initiation, growth and arrest of cracks play a major role in the understanding of the mechanism of failure of structural components.

LEFM first assumes that the material is isotropic and linear elastic. In LEFM, most formulas are derived for either plane stresses or plane strains, associated with the three basic modes of loadings on a cracked body: opening, sliding, and tearing (Figure 1.6).

Each one of the crack extension modes mentioned in the forgoing is associated with a corresponding strain energy release rate,  $G_I$ ,  $G_{II}$ ,  $G_{III}$ , or crack tip stress intensity factor,  $K_I$ ,  $K_{II}$ ,  $K_{III}$ , (where the G's are proportional to the squares of the respective K's). The values of  $G$  may be evaluated by assuming the material to be ideally brittle and, hence, the phenomenon to be reversible and by calculating the elastic work for incremental closure of the crack. On the other hand, the SIFs, which are the strengths of stress singularities at the crack tips, are determined from the infinitesimal elasticity solution of the problem. Since  $G$ 's and  $K$ 's are directly related, it suffices to discuss crack stability, based on the concept of SIFs [60].

To sum up we can mention that the basic premise of LEFM analysis can be outlined as follows:

- Based on linear elasticity theories, the stress field near a crack tip is a function of the location, the loading conditions, and the geometry of the specimen or object, which reads as:

$$\begin{aligned}\sigma_{ij}^{Tip} &\equiv \sigma_{ij}^{Tip}(Location, Loading, Geometry) \\ &\equiv \sigma_{ij}^{Tip}(r, \theta, K)\end{aligned}$$

where location can be represented by  $r$  and  $\theta$  using the polar coordinate system whereas the loading and geometry terms can be grouped into a single parameter  $K$  (SIF).

$$K \equiv K(\sigma^{(Loading)}, Geometry)$$

- The critical stress intensity factor ( $K_c$ ) is called the fracture toughness of the material, and is material specific.

$$K_c \equiv K_c(Material)$$

---

\*Griffith used glass fiber for his experiments

- The stress intensity factor  $K$  should NOT exceed  $K_c$ .

$$K < K_c$$

More details on the nature of aforementioned parameters are given in the following.

### 1.2.1 Generalized Griffith-Irwin theory

In examining the stability of cracks, it is paramount to determine the relationships between the elastic stresses and the input energy rate or strain energy release rate in crack extension. The elastic energy release rate may be regarded as the force tending to open the crack [100]. Griffith's theory shows that fracture occurs when the energy stored in the structure overcomes the surface energy of the material. He states that as the crack grows by a small amount  $da$  ( $a$  being the crack half length) at each end, energy flows into the crack tips where it is consumed in the fracture process, i.e., in overcoming the forces binding the material. Simply put, crack propagation will occur if the energy released is sufficient to provide all the energy that is required for crack growth. If the crack grows stably, then

$$dW = -d\Gamma \quad (1.8)$$

where  $\Gamma = 4a\gamma$  is the surface energy consumed in the creation of the cracks per unit thickness, and  $\gamma$  is the surface energy density, i.e., the energy required to create a unit traction-free crack surface. The quantity  $W$  is the work that can be extracted from the loading system during the crack formation. If the boundaries of the system are fixed, then  $W$  equals the elastic strain energy released during the crack formation. If the boundaries are free to move as in the problem studied by Griffith [74],  $W$  equals to the change in the potential energy of the system.

For stable crack growth, the energy balance condition in Equation 1.8 may be rewritten as

$$\frac{\partial}{\partial a}(W + \Gamma) = 0 \quad \text{or} \quad -\frac{\partial W}{\partial a} = \frac{\partial \Gamma}{\partial a} \quad \text{or} \quad G = R \quad (1.9)$$

where

$$G = -\frac{\partial W}{\partial a} = \text{energy release rate}$$

$$R = \frac{\partial \Gamma}{\partial a} = \text{crack resistance}$$

As a first approximation, it can be assumed that the energy required to produce a crack is the same for each increment of crack growth, i.e.,  $R$  is a constant. Thus, the above crack propagation criterion can be rewritten as

$$G = G_c \quad (1.10)$$

or

$$\begin{cases} G < G_c & \rightarrow \text{no propagation} \\ G = G_c & \rightarrow \text{propagation} \end{cases} \quad (1.11)$$

where  $G_c$  is the critical energy release rate.

When the energy accumulated in the body is sufficient to break the bonds ahead of the tips, catastrophic brittle failure takes place.

Decades after Griffith, Irwin proposed a solution defining the stress field in the area immediately surrounding the crack tip. In his solution, he proposed the concept of SIFs. Considering the relationship between strain energy release rate and SIF (the value of  $G$  is proportional to the square of the respective  $K$ ), Irwin suggested the value of critical SIF (fracture toughnesses) to be the criterion for fracture propagation.

Simply put, the generalized Griffith-Irwin fracture theory states that, under the loading conditions as described previously, crack extension will start when the corresponding SIF reaches a critical value i.e., the critical SIF or fracture toughness ( $K_c$ ) [60].

### 1.2.2 Calculating SIF using J-integral

LEFM, can be based on either energy calculations or stress-intensity calculations. The calculation methods are related and provide identical results in predicting fracture loads of structures containing sharp flaws of known size and location. However the stress-intensity approach is more generally used because it deals directly with crack-tip stresses and strains, which are more commonly used in engineering.

The SIF calculation can be carried out experimentally, theoretically or numerically. Each methodology has its own advantages but the use of numerical methods has become very popular [73]. Normally, the analytical calculations are more complex to execute; however they have some advantages, because an analytical solution can be applied for a range of crack lengths. The numerical techniques require the calculation of stress or strain field for each crack length and therefore for each value of SIF [175].

Some of the numerous numerical methods to calculate SIFs, are as follows:

- Compounding method (semi-analytical technique), [30]
- Displacement extrapolation (Numerical technique), [138, 42]
- Force method (Numerical technique), [146, 167]
- Singularity subtraction technique (Numerical technique), [128]
- J-integral (Numerical technique), [150]
- Virtual crack closure technique (Numerical technique), [153]
- etc.

Using the conventional theory of elasticity, it is possible to calculate the stress field at the tip of a crack in an arbitrary body with an arbitrary crack under arbitrary loading. Using the coordinate system in Figure 1.7, the crack tip stresses for mode I loading are:

$$\sigma_{ij} = \frac{K_I}{\sqrt{2\pi r}} f_{ij}(\theta) + C_1 r^0 + C_2 r^{1/2} + \dots \quad (1.12)$$

If  $r$  is very small (as assumed by Irwin), the first term of the solution is very large (infinite for  $r=0$ ); therefore, the other terms can be neglected. Because all cracking and fracturing take place at or very near the crack tip (where  $r \geq 0$ ), it is justifiable to use only the first term of the solution to describe the stress field in the area of interest. For the stress in the  $y$ -direction along the plane  $\theta = 0$ ,  $f_{yy}(\theta) = 1$  [117], so that:

$$\sigma_{yy} = \frac{K_I}{\sqrt{2\pi r}} \quad \text{for } \theta = 0 \quad (1.13)$$

Equation 1.13 shows that the crack-tip stress in the  $\sigma_{yy}$  direction depends on the distance  $r$  from the crack tip. A similar relation applies to other directions, or if the entire stress field is taken into account. As a general solution, Equation 1.13 applies to the geometry under Mode I loading.

The stress near the crack tip (Equation 1.13) is also directly proportional to the applied stress ( $\sigma$ ), as long as stresses are in the elastic regime. Therefore, under elastic conditions:

$$\sigma(\text{applied}) \propto \sigma_{yy} = K_I/\sqrt{2\pi r} \quad (1.14)$$

which means that  $K_I$ , can be defined in terms of the applied stress and of a distance  $r$  near the crack tip.

In general, the relation between SIF and crack tip stresses are formally defined as:

$$K_I = \lim_{r \rightarrow 0} \sqrt{2\pi r} \sigma_{yy}(r, 0) \quad (1.15)$$

$$K_{II} = \lim_{r \rightarrow 0} \sqrt{2\pi r} \sigma_{yx}(r, 0) \quad (1.16)$$

$$K_{III} = \lim_{r \rightarrow 0} \sqrt{2\pi r} \sigma_{yz}(r, 0) \quad (1.17)$$

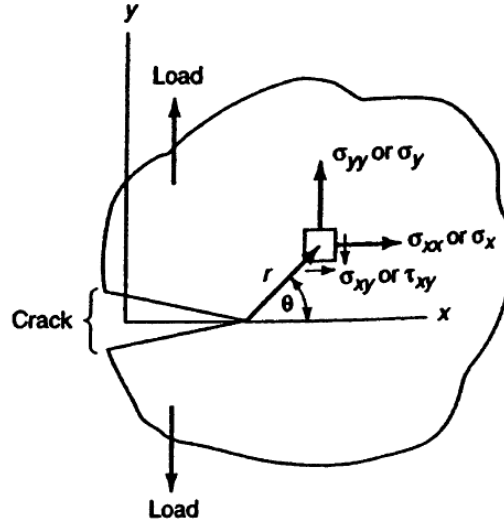


Figure 1.7: Coordinate system and stresses at crack-tip.

Now in calculating the SIF, domain forms of the contour J-integral and associated contour interaction integrals remain the most popular method for extracting SIFs from finite-element calculations.

The J-integral represents a way to calculate the strain energy release rate, or work (energy) per unit fracture surface area, in a material. The theoretical concept of J-integral was developed in 1967 by Cherepanov [35] and in 1968 by Rice [150] independently, who showed that an energetic contour path integral (called J) was independent of the path around a crack.

The J-integral is defined by:

$$J = \int_{\Gamma} \left( W dy - T \cdot \frac{\partial u}{\partial x} ds \right) \quad (1.18)$$

Here  $\Gamma$  is a curve surrounding the notch tip, the integral being evaluated in a counterclockwise sense starting from the lower flat notch surface and continuing along the path  $\Gamma$  to the upper flat surface (Figure 1.8).  $T$  is the traction vector defined according to the outward normal along  $\Gamma$ ,  $T_i = \sigma_{ij}n_j$ ,  $u$  is the displacement vector, and  $ds$  is an element of arc length along  $\Gamma$ .

By taking  $\Gamma$  close to the notch tip, the integral will depend only on the local field. In particular, the path may be shrunk to the tip  $\Gamma_t$  (Figure 1.8) of a smooth-ended notch and since  $T = 0$  there,

$$J = \int_{\Gamma_t} W dy \quad (1.19)$$

so that  $J$  is an averaged measure of the strain on the notch tip.

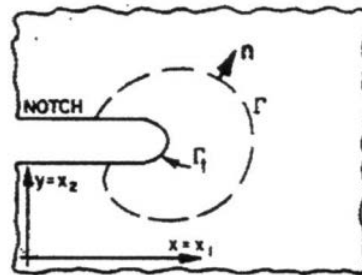


Figure 1.8: Flat surfaced notch in two-dimensional deformation field (all stresses depend only on  $x$  and  $y$ ).  $\Gamma$  is any curve surrounding the notch tip;  $\Gamma_t$  denotes the curved notch tip.

Rice [149] suggests the relation between J-integral and SIFs as follows:

$$J = \frac{1 - \nu^2}{E} (K_I^2 + K_{II}^2) + \frac{1 + \nu}{E} K_{III}^2 \quad (1.20)$$

Considering a cohesive zone model (see section 1.2.4), it can be shown that the J-integral can be calculated as follows:

$$J = \int_{\Gamma} t_c \cdot \nabla[u] \cdot \theta d\Gamma \quad (1.21)$$

where  $t_c$  is the traction on crack lips and  $\theta$  is the virtual crack extension field and  $u$  is the displacement of the crack lips. Considering the cohesive traction decomposed as  $t_c = t_{c,n}n + t_{c,t}t + t_{c,b}b$ , and making use of notation  $[\nabla u] \cdot \theta = \frac{\partial[u]_n}{\partial\theta}n + \frac{\partial[u]_t}{\partial\theta}t + \frac{\partial[u]_b}{\partial\theta}b$ , then, equating equations 1.20 and 1.21, as stated in [64] SIFs may alternatively be computed by:

$$\begin{aligned} K_I^2 &= -\frac{E}{1 - \nu^2} \int_{\Gamma} \frac{\partial[u_n]}{\partial\theta} t_{c,n} d\Gamma \\ K_{II}^2 &= -\frac{E}{1 - \nu^2} \int_{\Gamma} \frac{\partial[u_t]}{\partial\theta} t_{c,t} d\Gamma \\ K_{III}^2 &= -2\mu \int_{\Gamma} \frac{\partial[u_b]}{\partial\theta} t_{c,b} d\Gamma \end{aligned} \quad (1.22)$$

Equation 1.20 and accordingly equation 1.22 are valid for isotropic elastic medium. The equivalent of equation 1.20 for transverse isotropic medium can read as follows according to the work of Kassir and Sih [100]:

$$\begin{aligned} J &= \frac{\pi c_{11}(n_1^{1/2} + n_2^{1/2})}{2c_{44}(c_{13} + c_{44})(1 + m_1)(1 + m_2)} K_I^2 \\ &\quad + \frac{\pi c_{11}(n_1 n_2)^{1/2}(n_1^{1/2} + n_2^{1/2})}{2c_{44}(c_{13} + c_{44})(1 + m_1)(1 + m_2)} K_{II}^2 + \frac{\pi n_3^{1/2}}{2c_{44}} K_{III}^2 \end{aligned} \quad (1.23)$$

where  $n_1, n_2$  are the roots to the following characteristic equation:

$$c_{11}c_{44}n^2 + [c_{13}(c_{13} + 2c_{44}) - c_{11}c_{33}]n + c_{33}c_{44} = 0 \quad (1.24)$$

and where

$$m_j = \frac{c_{11}n_j - c_{44}}{c_{11} + c_{44}} = \frac{(c_{13} + c_{44})n_j}{c_{33} - c_{44}n_j}, \quad j = 1, 2 \quad (1.25)$$

Equating equation 1.23 to equation 1.21 would give the equivalent of equation 1.22 for TI medium, which could be written as:

$$\begin{aligned} K_I^2 &= \frac{2c_{44}(c_{13} + c_{44})(1 + m_1)(1 + m_2)}{\pi c_{11}(n_1^{1/2} + n_2^{1/2})} \int_{\Gamma} \frac{\partial[u]_z}{\partial\theta} t_{c,z} d\Gamma \\ K_{II}^2 &= \frac{2c_{44}(c_{13} + c_{44})(1 + m_1)(1 + m_2)}{\pi c_{11}(n_1 n_2)^{1/2}(n_1^{1/2} + n_2^{1/2})} \int_{\Gamma} \frac{\partial[u]_n}{\partial\theta} t_{c,n} d\Gamma \\ K_{III}^2 &= \frac{2c_{44}}{\pi n_3^{1/2}} \int_{\Gamma} \frac{\partial[u]_t}{\partial\theta} t_{c,t} d\Gamma \end{aligned} \quad (1.26)$$

### 1.2.3 Bifurcation angle

One cannot predict the crack propagation path without having the knowledge of the angle of crack initiation. The problem needs to be studied in mixed mode since the state of loading at the crack tip could be very complex and may result in mixed mode fracture. The problem involving mixed mode fracture has been extensively investigated during the past couple of decades, and several criteria have been proposed for predicting crack initiation angles.

The criteria presented so far can be gathered under three headings: stress-based criteria, energy-based criteria, and strain-based criteria. The critical condition refers to one of the extremum of the stated parameter, i.e., stress, energy, or strain [103]. The three theories prevalent in the literature to predict incipient crack turning angles for isotropic materials are:

- Maximum Tangential Stress (MTS), or interchangeably maximum hoop stress[60],
- Maximum energy release rate [87],
- Minimum strain energy density [163].

Among the above mentioned approaches, MTS has considerable appeal for isotropic materials because of its simplicity, and remains probably the most widely used approach. An extension of MTS to anisotropic materials was introduced in [155]. The bifurcation angle criterion given in [155] depends on the stress field existing just before the onset of crack propagation.

The stress analysis of an infinite anisotropic plate containing an elliptical opening has been addressed by [111] using a complex variable solution. By reducing the minor axis dimension to zero, [191] obtained the following stress distribution in the neighborhood of the crack:

$$\begin{aligned}\sigma_x &= \frac{\sigma^\infty \sqrt{a}}{2r} \Re \left\{ \frac{s_1 s_2}{(s_1 - s_2) \psi_2^{1/2}} - \frac{s_1}{\psi_1^{1/2}} \right\} + \frac{\tau^\infty \sqrt{a}}{2r} \Re \left\{ \frac{1}{(s_1 - s_2) \psi_2^{1/2}} - \frac{s_2^2}{\psi_1^{1/2}} \right\} \\ \sigma_y &= \frac{\sigma^\infty \sqrt{a}}{2r} \Re \left\{ \frac{1}{(s_1 - s_2) \psi_2^{1/2}} - \frac{s_2}{\psi_1^{1/2}} \right\} + \frac{\tau^\infty \sqrt{a}}{2r} \Re \left\{ \frac{1}{(s_1 - s_2) \psi_2^{1/2}} - \frac{1}{\psi_1^{1/2}} \right\} \\ \tau_{xy} &= \frac{\sigma^\infty \sqrt{a}}{2r} \Re \left\{ \frac{s_1 s_2}{(s_1 - s_2) \psi_1^{1/2}} - \frac{1}{\psi_2^{1/2}} \right\} + \frac{\tau^\infty \sqrt{a}}{2r} \Re \left\{ \frac{1}{(s_1 - s_2) \psi_2^{1/2}} - \frac{s_2}{\psi_1^{1/2}} \right\}\end{aligned}\quad (1.27)$$

where  $\psi_i = \cos \theta + s_i \sin \theta$  and  $r, \theta, \sigma^\infty, \tau^\infty$  are defined in Figure 1.9.  $s_1$  and  $s_2$  are roots of the characteristic equation:

$$a_{11}s^4 - 2a_{16}s^3 + (2a_{12} + a_{66})s^2 - 2a_{26}s + a_{22} = 0 \quad (1.28)$$

for the general case, or

$$a_{11}s^4 + (2a_{12} + a_{66})s^2 + a_{22} = 0 \quad (1.29)$$

for the orthotropic case.

The equations are written in terms of the compliances  $a_{ij}$  which are related to engineering constants  $E_{ij}$  through:

$$a_{11} = \frac{1}{E_{11}}; a_{22} = \frac{1}{E_{22}}; a_{12} = a_{21} = -\frac{\nu_{12}}{E_{11}}; a_{66} = \frac{1}{G_{12}} \quad (1.30)$$

The crack tip stress field can be re-written in terms of the SIF for each of two possible two dimensional loading:

- Plane symmetric loading:

$$\begin{aligned}\sigma_x &= \frac{K_I}{\sqrt{2\pi r}} \Re \left[ \frac{s_1 s_2}{s_1 - s_2} \left( \frac{s_2}{(\cos \theta + s_2 \sin \theta)^{1/2}} - \frac{s_1}{(\cos \theta + s_1 \sin \theta)^{1/2}} \right) \right] \\ \sigma_y &= \frac{K_I}{\sqrt{2\pi r}} \Re \left[ \frac{1}{s_1 - s_2} \left( \frac{s_1}{(\cos \theta + s_2 \sin \theta)^{1/2}} - \frac{s_2}{(\cos \theta + s_1 \sin \theta)^{1/2}} \right) \right] \\ \sigma_{xy} &= \frac{K_I}{\sqrt{2\pi r}} \Re \left[ \frac{s_1 s_2}{s_1 - s_2} \left( \frac{1}{(\cos \theta + s_1 \sin \theta)^{1/2}} - \frac{1}{(\cos \theta + s_2 \sin \theta)^{1/2}} \right) \right]\end{aligned}\quad (1.31)$$



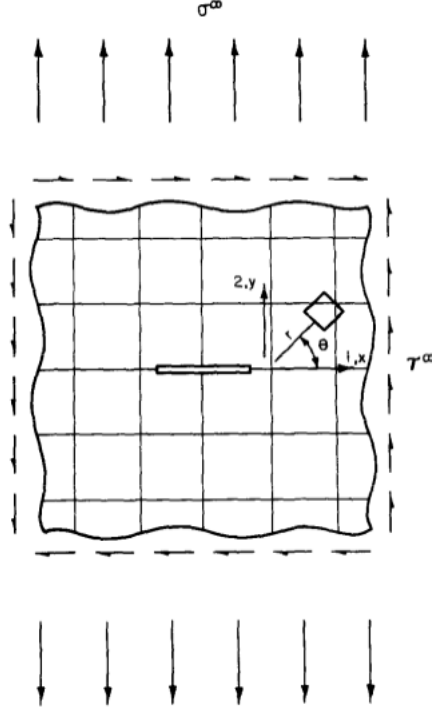


Figure 1.9: A crack in a homogeneous anisotropic elastic solid, from [155].

– and for plane skew-symmetric loading:

$$\begin{aligned}
 \sigma_x &= \frac{K_{II}}{\sqrt{2\pi r}} \Re \left[ \frac{1}{s_1 - s_2} \left( \frac{s_2^2}{(\cos \theta + s_2 \sin \theta)^{1/2}} - \frac{s_1^2}{(\cos \theta + s_1 \sin \theta)^{1/2}} \right) \right] \\
 \sigma_y &= \frac{K_{II}}{\sqrt{2\pi r}} \Re \left[ \frac{1}{s_1 - s_2} \left( \frac{1}{(\cos \theta + s_2 \sin \theta)^{1/2}} - \frac{1}{(\cos \theta + s_1 \sin \theta)^{1/2}} \right) \right] \\
 \sigma_{xy} &= \frac{K_{II}}{\sqrt{2\pi r}} \Re \left[ \frac{1}{s_1 - s_2} \left( \frac{s_1}{(\cos \theta + s_1 \sin \theta)^{1/2}} - \frac{s_2}{(\cos \theta + s_2 \sin \theta)^{1/2}} \right) \right]
 \end{aligned} \tag{1.32}$$

Having extended MTS, for anisotropic material, [155] discuss the bifurcation angle as follows. According to [60], the direction of crack extension is controlled by the ratio of tensile normal stress to strength on a given plane. The crack will grow along the plane on which this ratio ( $R$ ) is a maximum:

$$R = \frac{\sigma_\theta}{\sigma_\theta^{max}} \tag{1.33}$$

where  $\sigma_\theta$  is the circumferential (tangential) stress:

$$\sigma_\theta = \sigma_x \sin^2 \theta + \sigma_y \cos^2 \theta - 2\sigma_{xy} \sin \theta \cos \theta \tag{1.34}$$

and  $\sigma_x$ ,  $\sigma_y$ ,  $\sigma_{xy}$  are the Cartesian stresses at a point which polar coordinates are  $r$  and  $\theta$  with respect to the crack tip. By plugging the stress field for anisotropic medium given in equations 1.31 and 1.32 into equation 1.34, one obtains an equation function of  $K_I$ :

$$\sigma_\theta = \frac{K_I}{\sqrt{2\pi r}} \Re \left[ \frac{1}{s_1 - s_2} (s_1 (s_2 \sin \theta + \cos \theta)^{3/2} - s_2 (s_1 \sin \theta + \cos \theta)^{3/2}) \right] \tag{1.35}$$

and an equation function of  $K_{II}$

$$\sigma_\theta = \frac{K_{II}}{\sqrt{2\pi r}} \Re \left[ \frac{1}{s_1 - s_2} ((s_2 \sin \theta + \cos \theta)^{3/2} - (s_1 \sin \theta + \cos \theta)^{3/2}) \right] \tag{1.36}$$

For mixed mode, equations 1.35 and 1.36 can be combined:

$$\sigma_\theta = \frac{K_I}{\sqrt{2\pi r}} \Re[A(s_1 B - s_2 C)] + \frac{K_{II}}{\sqrt{2\pi r}} \Re[A(B - C)] \quad (1.37)$$

where

$$\begin{aligned} A &= \frac{1}{s_1 - s_2} \\ B &= (s_2 \sin \theta + \cos \theta)^{3/2} \\ C &= (s_1 \sin \theta + \cos \theta)^{3/2} \end{aligned} \quad (1.38)$$

Equation 1.33 can then be written as:

$$\frac{\sigma_\theta}{\sigma_\theta^{max}} = \frac{1}{K_{Ic}^1 \cos^2 \theta + K_{Ic}^2 \sin^2 \theta} \left[ K_I \Re[A(s_1 B - s_2 C)] + K_{II} \Re[A(B - C)] \right] = 1 \quad (1.39)$$

Finally the angle of propagation  $\theta_0$  is found by maximizing Equation 1.39 or its normalized equivalent:

$$Max \frac{\Re[A(s_1 B - s_2 C)] + \frac{K_{II}}{K_I} \Re[A(B - C)]}{\cos^2 \theta + \frac{K_{Ic}^1}{K_{Ic}^2} \sin^2 \theta} \quad (1.40)$$

#### 1.2.4 Cohesive Zone Model–CZM

LEFM has proven to be a useful tool for solving fracture problems, although it suffers from some limitations stemming from the strong assumptions that could be mainly listed as follows:

- If the size of the process zone approaches any relevant lengthscale of the medium (structure typical size, initial crack length, distance between crack tips), the response of the structure is subjected to a *size effect* that LEFM fails to predict,
- In 3D, Griffith's criterion stating that crack propagates when  $G = G_c$  is very hard to verify along a front,
- Crack may not initiate from a sound structure: a pre-crack has to be put in. Thus, the sensitivity of the response to the shape and orientation of the pre-crack has to be studied, and the failure load cannot always be accurately reproduced.

In order to adress some of these issues, cohesive zone model was introduced originally by Barenblatt [12] and Dugdale [57]. Later on, Hillerborg [83] used this model for concrete under the name of *fictitious crack model*. The cohesive process zone model is a general model which, in principle, is applicable to materials other than concrete or cementitious composites; e.g., crazing in polymers has been modelled using a cohesive surface methodology [176], and Schwalbe and collaborators modelled successfully the effect of strength mismatch in welded joints using a cohesive zone model [116]. The cohesive zone model has also been applied successfully by [141, 63] to rocks to investigate hydraulic fracture propagation.

The cohesive zone model consists in introducing cohesive traction forces on the fracture walls, that obey a softening traction-displacement relation [141]. The cohesive traction is generally derived from a potential and is directly related to the displacement jump  $\delta$  (see Figure 1.10). Once the critical stress  $\sigma_c$  is reached, the damage process starts, irreversibly.

In this work the cohesive zone model relies on the principle of minimization of the total potential energy of the system:

$$\min_{u, \delta, \delta = \llbracket u \rrbracket} (E_p(\mathbf{u}, \delta)) \quad (1.41)$$

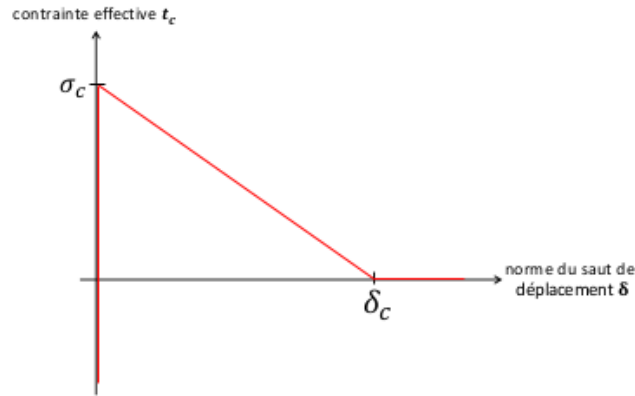


Figure 1.10: A linear softening law between the cohesive traction and the displacement jump. From [141]

The cohesive zone model, has been extensively used with great success to simulate fracture and fragmentation processes in concrete, rock, ceramics, metals, polymers, and their composites. Rather than an elastic crack tip region as presumed in classic LEFM with its associated infinite stress at the sharp crack tip, the cohesive zone model assumes the existence of a fracture process zone characterized by a traction-separation law. In this way, the cohesive zone model avoids the singularity in the crack tip stress field that is present in classic fracture mechanics.

Cohesive zone models are inserted along predefined crack paths. The potential crack surface is made up of

- an adherent zone ahead of the crack front,
- a cohesive process zone,
- a fully opened zone. The cohesive traction is null in this zone.

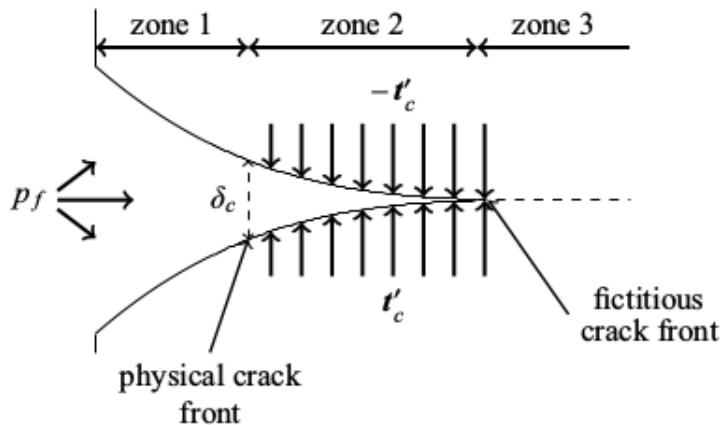


Figure 1.11: Cohesive Zone Model. From [63]

### 1.3 Numerical modeling

Computational fracture mechanics has long been used for determination of the stress intensity factors, and later has been expanded into the simulation of crack nucleation and propagation. Generally, numerical methods can be classified into continuum and discontinuum approaches [126].

Continuum and discontinuum methods can be interpreted as: *indirect* and *direct* respectively [144], depending on whether fracture is represented directly or indirectly. Most indirect approaches idealize the material as a continuum and utilize average measures of material degradation in constitutive relations to represent irreversible microstructural fracture [106], while most direct approaches idealize the material as a collection of structural units (springs, beams, etc.) or interacting particles and utilize the breakage of individual structural units or bonds to represent damage. Most computational models used to describe the mechanical behavior of rock for engineering purposes are based on the indirect approach, while most used to understand the behavior in terms of the progress of fracture development and rupture are based on the direct approach. In the following we give a literature survey of both continuum and discontinuum methods used specifically for studying fracture propagation processes.

### 1.3.1 Continuum-based methods

The conventional continuum methods can be categorized as follows:

- Finite element method,
  - Element erosion method,
  - Extended finite element method,
  - Other finite element-based methods.
- Finite difference method,
- Boundary element method,
- Meshfree methods,
- Peridynamics,
- Phase Field method

#### 1.3.1.1 Finite Element Method–FEM

The FEM is the most widely employed numerical method for studying fracture mechanics problems (Figure 1.12). The formulation of the FEM is based on a variational statement of the governing physics. The domain is discretized into subdomains (elements) which are interconnected through common discrete points (nodes). The primary unknown field variables are nodal values. The formulation reduces the problem to the solution of a system of algebraic equations in terms of the nodal variables (for dynamic problems, the result is a system of ordinary differential equations). Finite element systems tend to be relatively banded and symmetric for most problems [115]. FEM is capable of modelling complex geometries, loading conditions and heterogeneous material distributions [124]. [23] used FEM for modeling of fractures in orthotropic materials while [154] used FEM to model fractured induced anisotropy in poroelastic media. In particular, where they modeled fractures as very thin, highly permeable and compliant porous layers, allowing them to compute the wave velocities and quality factors at the macroscale as a function of frequency and propagation angle. Nevertheless, the classical displacement-based FEM is not able to describe the strain localisation properly since the differential motion equations change type and lead to an ill-posed boundary value problem. A number of techniques have been implemented into the standard FEM to facilitate the computational simulation of crack propagation problems, such as element erosion methods and XFEMs [124, 168].

#### Element Erosion Method–EEM

This method is considered as one of the simplest methods in dealing with fracturing process within the framework of the standard FEM [15, 168]. According to the element erosion (deletion) algorithms, there is no need to represent the topology of cracks, and the fracturing process can

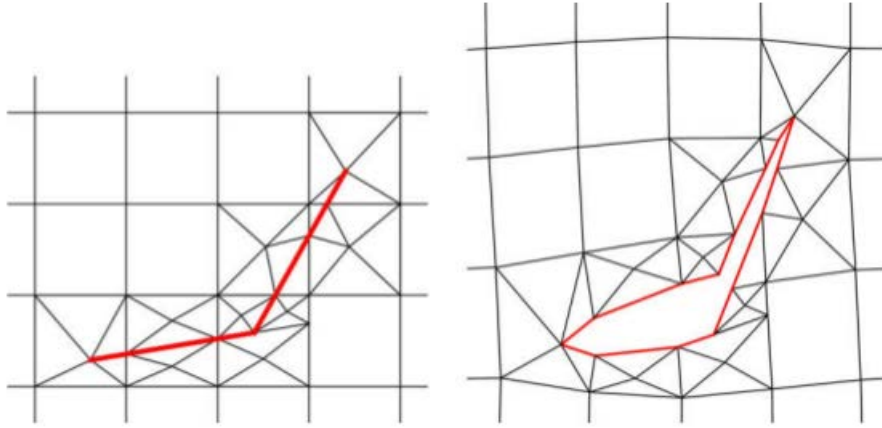


Figure 1.12: A finite element model of a crack. Left: undeformed. Right: deformed under vertical tension, from [193]. Mesh is conforming to the discontinuity which causes computational costs and must be updated for crack propagation.

be modelled by a set of deactivated elements [126]. As shown in Figure 1.13, the elements, which contain the crack, are deactivated and have no material resistance or stress for the rest of the simulation process. A removed element represents a meso/macrocrack. The deactivation of elements in this method can be achieved through two approaches: (1) complete element deletion technique, in which the deleted elements are replaced by rigid masses and (2) setting the stress of the deactivated elements to zero [147]. This method has been widely used to simulate the fracture process of rock, particularly due to impact and blasting loads. However the mesh dependency of this method makes it not well suited for fracture analysis. From the fracture mechanics point of view, element deletion is insensitive to the size effect of strength and the element meshes commonly used in engineering applications are commonly too coarse to capture gradients near the crack tip which leads to an overestimation of the fracture energy [142]. Hence, fracture models with element deletion should be used and interpreted with caution. Because of this shortcomings, there is no research study on fracture propagation in transverse isotropic materials using element erosion method, nor is there any extension of the method to hydrofracture studies.

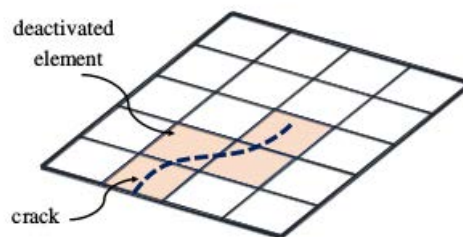


Figure 1.13: Schematic illustration of crack simulation using element erosion method. From [126].

### Extended finite element method–XFEM

With the standard FEM, cracks are viewed as internal boundary surfaces that are explicitly meshed. The modeling of such moving discontinuities with the FEM is cumbersome due to the need to update the mesh to match the geometry of the discontinuity [123]. On using a discontinuous (generalized Heaviside) enrichment function, a much simpler approach to model the crack interior was realized by [123], and this method was named the extended finite element method (XFEM) [48]. In the XFEM, crack discontinuities are incorporated via the kinematics: the displacement

field is enriched with discontinuous and crack-tip asymptotic functions. The XFEM permits simple meshes to be used that do not need to conform to the crack geometry, thereby avoiding the need to remesh for crack propagation simulations. Generally, the XFEM displacement approximation for any element comprising an arbitrary crack can be defined as [170]

$$\begin{aligned}
 u_e^h(x) = & \underbrace{\sum_{i \in I} N_i(x) u_i}_{\text{standard FE}} + \underbrace{\sum_{j \in J \subseteq I} N_j(x) \phi(x) a_j}_{\text{discontinuous contribution}} \\
 & + \underbrace{\sum_{t=1}^2 \sum_{k \in K_t \subseteq I} N_k(x) \sum_{\alpha=1}^4 F_{\alpha t}(x) b_{k\alpha t}}_{\text{crack-tip contribution}}
 \end{aligned} \tag{1.42}$$

with

$$F_{\alpha t}(x) = \sqrt{r} \left\{ \sin \frac{\theta}{2}, \cos \frac{\theta}{2}, \sin \frac{\theta}{2} \sin \theta, \cos \frac{\theta}{2} \sin \theta \right\} \tag{1.43}$$

where  $J$  is the index set of nodes whose basis function support is cut by the interior of the crack  $\Gamma_c$ , and  $K_1$  and  $K_2$  are the index sets of nodes whose basis function support contains the crack tips  $\Lambda_c^1$  and  $\Lambda_c^2$ , respectively. In addition,  $N_i(x)$  are the finite element shape functions,  $\phi(x)$  is a discontinuous (generalized Heaviside) function that is defined with respect to the crack, and  $F_{\alpha t}(x)$  in 1.43 are the crack-tip asymptotic functions defined with respect to a polar coordinate system  $(r, \theta)$  with origin at the crack-tip  $t$  (Figure 1.14).

The XFEM is arguably one of the most prevalent numerical methods for fracture and discontinuity analysis. This is due to many factors, not the least of which is the potential of the XFEM to circumvent long-standing issues in finite element mesh generation and adaptation for fracture problems. Moreover, even though there are many alternative numerical methods for fracture, none of them offer the combination of features that the XFEM affords: extension to nonlinear problems, relative ease of implementation, robustness, efficiency and accuracy. It has been successfully applied to solve crack problems in materials with different constitutive laws: isotropic media [123], bimetals [171], orthotropic materials [9], piezoelectric solids [14], magneto-electroelastic materials [151]. The XFEM has been extensively used for modeling anisotropic materials [78, 24, 84] as well as for hydraulic fracturing [178, 125, 194, 63]. Hattori et al. [78] used the XFEM to analyze fracture mechanics problems in elastic materials that exhibit general anisotropy, by introducing new anisotropic crack-tip enrichment functions for the XFEM. Bouhala [24] used XFEM to model crack propagation in thermo-anisotropic elastic materials. They modeled the discontinuity at the crack surface using the level set principle whereas the singularity at the crack tip is handled using special branch enrichment functions derived from the asymptotic analysis following Lekhnitskii's formalism in anisotropic media. Honggang [84] proposed a method for extracting fracture parameters in anisotropic thermoelastic materials cracking via interaction integral method. Mohammadnejad et al. [125] developed a fully hydromechanical coupled numerical model for the modeling of the hydraulic fracture propagation in porous media using the extended finite element method in conjunction with the cohesive crack model. By taking the advantage of the cohesive crack model, they simulated the nonlinear fracture processes developing along the fracture process zone. Faivre et al. [63] proposed a numerical model for the fully coupled hydro-mechanical analysis of groundwater flows through poroelastic saturated media. Paul et al. [141] extended the work of [63] from 2D to 3D and applied the hydromechanical coupled model to non-predefined paths and also investigated multiple hydraulic fractures interference.

### Other finite element-based methods

Several other methods have been developed based on FEM to simulate the failure process of brittle materials. [173] introduced a two-dimensional FEM code, namely realistic failure process analysis (RFPA) code, on the basis of continuum damage mechanics, and employed it to simulate

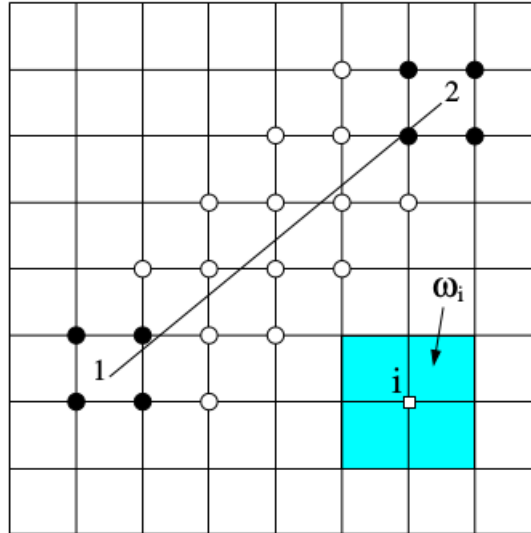


Figure 1.14: Enriched nodes for an embedded crack. The crack-tips are labeled as 1 and 2. The nodes that are enriched with the discontinuous function are shown by open-circles, whereas those that are enriched with the asymptotic near-tip crack functions are shown by filled-circles. The added region is the support  $\omega_i$  of the nodal finite element basis function for node  $i$ . From [170].

rock failure processes. RFPA has been also used to model hydraulic fracturing[114, 40]. RFPA has also been used to model the failure mechanisms in transversely isotropic rock masses [183]. FRANC 2D (FRacture ANalysis Code) is an interactive finite element code which was developed firstly based on the LEFM principles and then expanded into EPFM (elastic plastic fracture mechanics) and three-dimensional modelling [189]. Despite all the achievements of these codes, they suffer from basic difficulties of continuum-based methods such as mesh dependency and being untrustworthy in modelling of the transition from a continuum to a discontinuum domain [126]. It is also worth mentioning the use of enhanced finite element method (EFEM) by [81] for application to underground excavation where they introduced a 3D numerical model with strong discontinuities to address multi-cracking problems. Oliver et al. [135] used a continuum approach to model fracture propagation by considering (a) a continuum setting for representation of the fracture at both scales based on the Continuum Strong Discontinuity Approach (CSDA), and (b) the use, for the considered non-smooth (discontinuous) problem.

### 1.3.1.2 Finite Difference Method–FDM

FDM is a continuum-based method similar to FEM that differs in using a grid of nodes instead of elements for approximating the unknown fields such as displacement field. However, the conventional FDM suffers from the use of regular grid system for the description of material heterogeneity, complex boundary conditions and fractures [59, 95]. To overcome these shortcomings, the general FDM has been improved particularly thanks to the development of finite volume methods, which make it capable of using irregular quadrilateral, triangular and Voronoi grids (Figure 1.15b). [3] used FDM to model fracture in bimaterial (Figure 4.1a). He divided the nodal points into inner points and fictitious boundary points, and the location of the crack tip is assumed to be at the center of the mesh and never on a mesh point. The commercial FLAC code is the most common FDM tool for stress analysis in geomechanics problems. [105] developed and implemented an algorithm based on LEFM approach in FLAC 2D code. According to the algorithm, each element comprises a microcrack with a random length that propagates when the critical value is satisfied by SIFs. [179] developed a constitutive model based on FDM to simulate dynamic fracturing in coal. Despite all these improvements, FDM still suffers from inability to model fracture propagation appropriately due to its continuum nature where the entire domain is employed for calculation [126]. There is

no recorded evidence of extensive use of FDM in modeling crack propagation in anisotropic media nor hydrofracturing.

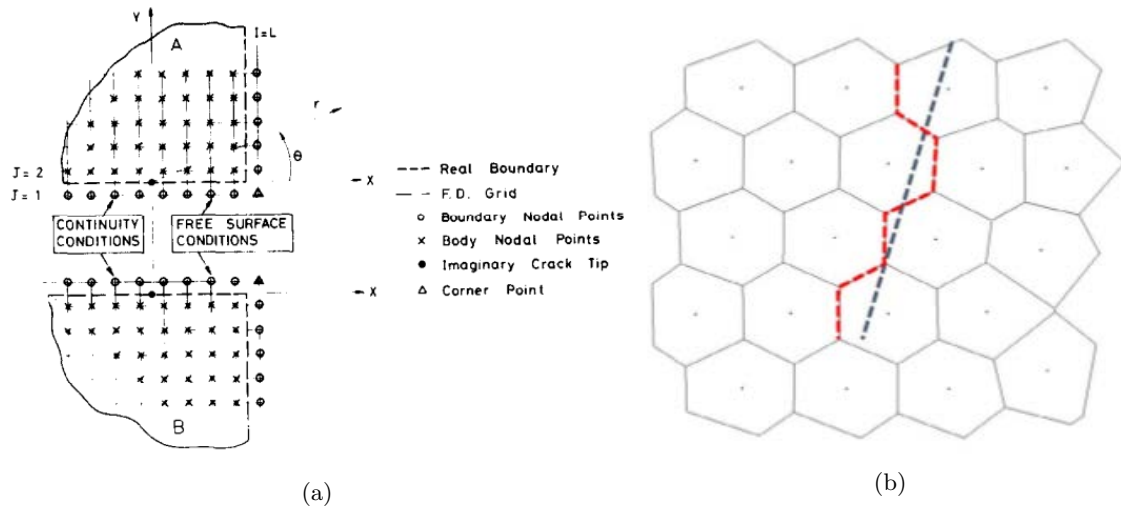


Figure 1.15: a) The finite difference grid for dissimilar materials and/or cracks. After [3] and b) Crack simulation via Voronoi grid. After [126].

### 1.3.1.3 Boundary Element Method–BEM

The Boundary Element Method (BEM) has emerged as a powerful alternative to FEM particularly in cases where better accuracy is required due to problems such as stress concentration. Also, if the medium extends to infinity, no artificial boundaries such as those needed in FDM or FEM are required because BEM automatically satisfies far-field conditions. The most important feature of BEM, however, is that the solution is approximated at the boundaries, while equilibrium and compatibility are exactly satisfied in the interior of the medium. In FDM and FEM, the approximations are made inside the medium [20]. The advantage of limiting the discretization to the boundaries is that the problem is reduced by one order: from three-dimensional (3D) to a 2D surface problem at the boundary and from 2D to a line problem. Hence, it only requires discretization of the surface rather than the volume (Figure 1.16).

This is in contrast to continuum methods (although we list BEM here amongst continuum methods), where the entire medium has to be discretized. The method is very attractive for those cases where the volume to boundary surface ratio is large. The technique used in BEM consists in essence of transforming the governing differential equations, which apply to the entire medium, to integral equations that only consider boundary values [180, 26]. In a boundary value problem, some parameters such as stresses and displacements are known, while others are not, which then are part of the solution. There are two approaches to solve for the unknown parameters. In the first approach (direct BEM), the unknowns are solved directly, and once they are found, stresses and displacements at any point in the continuum can be obtained directly from the solution. In the second approach (indirect BEM), the solution is given in terms of some ‘fictitious’ quantities, typically stresses or displacements. The fictitious quantities are found first, and the stresses and displacements at any point in the medium are expressed in terms of these fictitious quantities [20]. The difficulties of the standard direct BEM in dealing with fracture problems such as the coincidence of crack nodes, gave rise to new techniques such as sub-region boundary element method (SBEM), displacement discontinuity methods (DDM), dual-boundary element method (DBEM) and dual-reciprocity boundary element method. The SBEM and DBEM are direct BEMs, while the DDM is an indirect BEM (Figure 1.17).

There has been extensive use of BEM in anisotropic fracture modeling [137, 101, 102, 169]. Pan et al. [137] proposed a new formulation of the BEM to calculate SIFs for cracked 2D anisotropic materials. They presented a new approach to collocate the displacement and traction integral



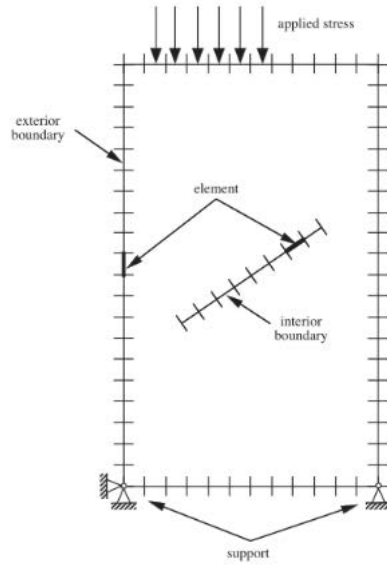


Figure 1.16: Discretization with BEM. After [20]

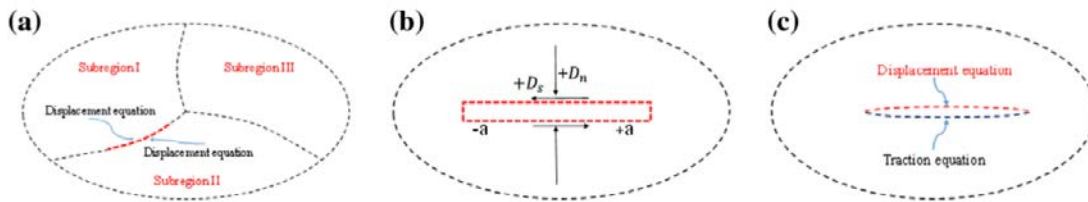


Figure 1.17: Three boundary element techniques in fracture analysis: a) Subregion method, b) DDM, c) DBEM. After [126].

equations on the outside boundary of the problem (no-crack boundary) only and on one side of the crack surfaces only, respectively. This new method was considered to provide an alternative and yet efficient numerical technique for the study of cracked 2-D anisotropic media, and for the simulation of quasi-static crack propagation. Ke et al. [101] presented a systematic procedure for determining fracture toughness of an anisotropic marble using the diametral compression test (Brazilian test) with a central crack on the discs. Their new fracture criterion is based on the examination of mode I, mode II and mixed mode (I-II) fracture toughness for different crack angles and anisotropic orientation. The method has also been utilized in modeling hydrofracture phenomenon [109, 29, 67]. Legan et al. [109] modeled the fracturing process taking into account the inhomogeneity of the stress state near the hole in a cylindrical bodies using the boundary elements method (in the variant of the fictitious load method) and the gradient fracture criterion. Cao et al. [29] proposed an improved Boundary Element Method for modeling fluid flow through fractured porous medium. In their proposed method they developed a theoretically sound, and practically robust numerical algorithm to accurately capture the flow behavior and dynamics in fractured reservoirs.

### 1.3.1.4 Meshfree methods

Different formulations in the concept of meshfree technique have been developed to remove limitations of continuum-based methods [196]. Meshless methods construct approximations in terms of nodes. The character of the nodes is provided by three functions: (i) approximation function, (ii) weight function and (iii) compact support of weight functions. The *approximation*

*function* is an essential feature of the method. A *weight function*, which plays an important role in the performance of the methods, is used in all varieties of meshless methods. The *compact support of weight functions*, also called the domain of influence of a node, gives a local character to the meshless methods, the most commonly used supports are discs and rectangles, as shown in Figure 1.18. The weight function is nonzero in the domain of support and zero outside of the domain of support. Based on this principle, pioneered by [72] for development of the smoothed particle hydrodynamics method (SPH), different formulations of the meshfree method have been established. These can be classified into two categories: the methods based on global weak form requiring background mesh for integration; and the methods based on local weak form requiring predefinition of particles for their mass.

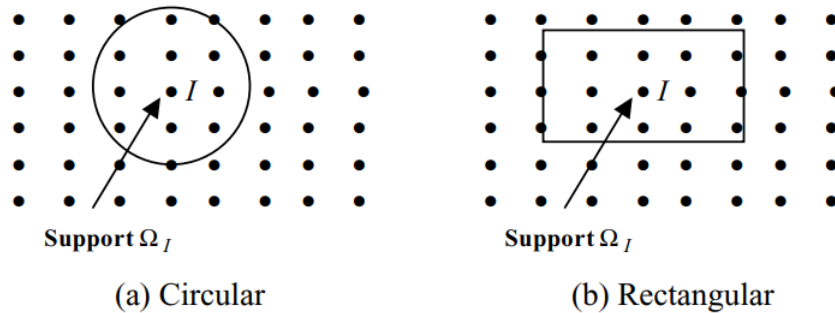


Figure 1.18: The commonly used supports of node I.

The flexibilities of meshless methods in dealing with fracturing problems make them suitable for rock mechanics application. They are also much advantageous when dealing with modelling of crack growth [196]. Meshfree methods have not been popular for anisotropic fracture modeling nor for hydraulic fracturing.

### 1.3.1.5 Peridynamics

The peridynamic (PD) theory is an extension of the standard mathematical theory of solid mechanics that is compatible with the discontinuous nature of cracks. The main advantage of the PD concept is the non-locality. In contrast to the PDEs (partial differential equations) of the standard theory, which cannot be applied directly on a growing crack, the PD theory uses integro-differential equations that do not involve the spatial derivatives of the deformation. This can solve the stress singularity problem at the crack tip. The field equations therefore apply on a crack [165]. The enhanced continuum mechanics theory of PD can be solved by either FEM or meshfree methods. The original PD method, i.e., bond-based PD, was introduced by [164].

In practice, the failure of one bond in a peridynamic body tends to increase the elongation of neighboring bonds, making it more likely that they too will break. This leads to progressive failure. The failures tend to organize themselves into two-dimensional surfaces that represent cracks. Bonds in many different directions contribute to crack growth, not just those bonds that are normal to the crack surface (Figure 1.19) [165].

PD has extensively been used for dynamic crack modeling in anisotropic materials [71, 79, 85]. PD seems to be a powerful technique for simulation of rock fracture as it can easily simulate the transition from continuum to discontinuum. However, it is a newly developed technique and mostly is used for dynamic fracture analysis and its capabilities in rock fracture analysis need to be explored much deeply in future.

### 1.3.1.6 Phase Field

The phase field (PF) is another recently developed phenomenological continuum algorithm, which has been successfully applied to simulate complex three-dimensional microstructural kinetics evolution of material at the meso-scale. This method is based on the thermo-dynamics equations

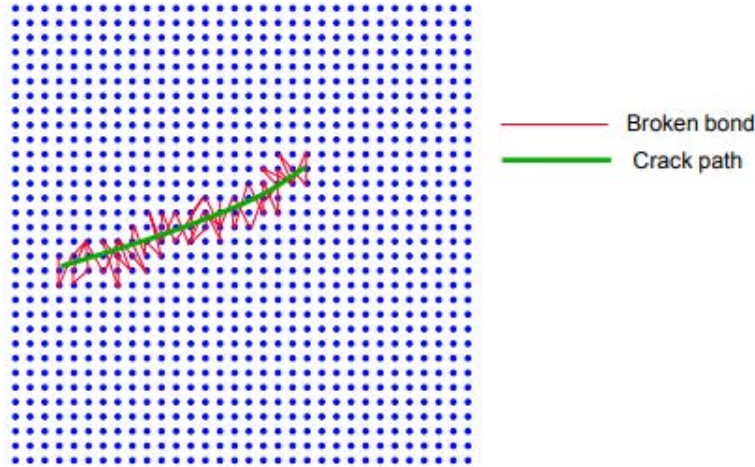


Figure 1.19: Crack growth in a peridynamic solid is determined by damage to bonds in many directions. After [165]

[113]. PF treats fracture problems based on energy minimisation principles and does not model a crack as a geometric feature with a physical discontinuity. Instead, PF differentiates fractured field using order parameter. The order parameter is a variable representing the state of the structure, and is coupled to elastic properties of the material using degradation function.

In order to circumvent the problems associated with numerically tracking the propagating discontinuity representing a crack, PF approximates the fracture surface. The PF approach takes a small piece of the crack boundary, smooths it, and then approximates the fracture surface (Figure 1.20). Two of the proposed benefits of this approach are that the crack no longer has to follow element edges and can propagate freely and that the solution will eventually converge, whereas in most FEM-based methods mesh refinement will only create higher and higher stress at the crack tip while not necessarily converging.

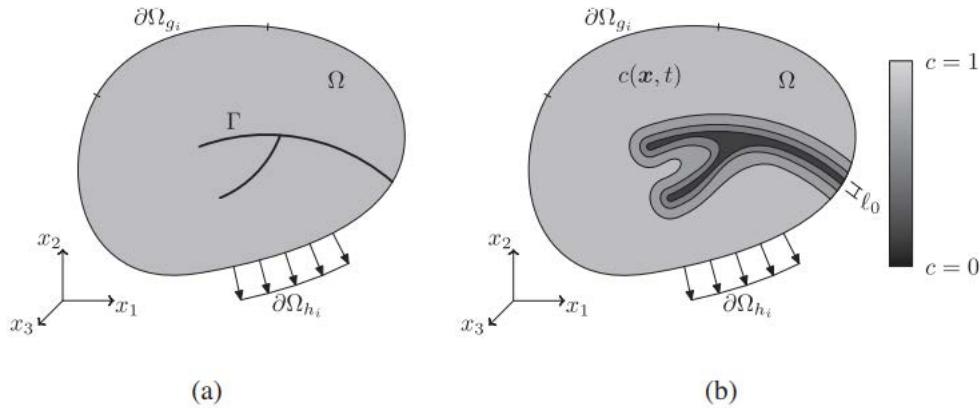


Figure 1.20: (a) Schematic representation of a solid body  $\Omega$  with internal discontinuity boundaries  $\Gamma$ . (b) Approximation of the internal discontinuity boundaries by the phase-field  $c(x, t)$ . The model parameter controls the width of the failure zone. The model parameter  $l_0$  controls the width of the failure zone. After [25]

Although, PF is becoming popular technique in fracture simulation, it suffers from inability to model detachment and separation. Its application in rock fracture analysis is currently limited to crack initiation and propagation problems [126]. In this context Xia et al. [192] proposed an extension of the phase field method for the modeling of hydraulic fracturing or cracking in heterogeneous saturated porous media. Their developed numerical framework is based on the phase

field method with a regularized description of both bulk and interface discontinuities, extended to a fully coupled hydro-mechanical framework. With regard to anisotropy, Nguyen et al. [133] proposed a phase field model to reproduce (energetically) non-free anisotropic crack bifurcation within a framework allowing for robust and fast numerical simulations.

### 1.3.2 Discontinuum-based methods

Discontinuum method can probably be considered as one of the mostly employed numerical techniques in the field of rock mechanics. Distinct Element Method–DEM (also known as Discrete Element Method), Discontinuous Deformation Analysis (DDA) and Bonded Particle Method (BPM) are the most common discontinuum methods in rock fracture analysis, and comprehensive explanations of these methods from theory to application can be found in many studies [77, 21, 97, 98].

#### 1.3.2.1 Distinct Element Method–DEM

The discrete (or distinct) element method (DEM) is a discontinuous analysis method proposed by [43] for studying two-dimensional slope stability problems in jointed rock masses. In DEM the objects are modelled as systems of bodies interacting with each other. The calculations performed in the DEM alternate between the application of Newton’s second law to the particles and a force–displacement law at the contacts. Newton’s second law is used to determine the translational and rotational motion of each particle arising from the contact forces, applied forces and body forces acting upon it, while the force–displacement law is used to update the contact forces arising from the relative motion at each contact. The DEM can take into account many kinds of discontinuities and material failure characterised with multiple fractures, making it a suitable tool to study rock fracturing [144]. The is based on a time-stepping algorithm in which the velocities and accelerations are assumed to be constant within each time step. The solution scheme is identical to that used by the explicit finite difference method for continuum analysis. The DEM is based on the idea that the time step chosen may be so small that, during a single time step, disturbances cannot propagate from any particle farther than its immediate neighbors. Then, at all times, the forces acting on any particle are determined exclusively by its interaction with the particles with which it is in contact. Because the speed at which a disturbance can propagate is a function of the physical properties of the discrete system (namely, the distribution of mass and stiffness), the time step can be chosen to satisfy the above constraint. The use of an explicit, as opposed to an implicit, numerical scheme provides the following advantages. Large populations of particles require only modest amounts of computer memory, because matrices are not stored. Also, physical instability may be modeled without numerical difficulty, because failure processes occur in a realistic manner—one need not invoke a non-physical algorithm, as is done in some implicit methods.

DEM is implemented in computer codes such as UDEC and 3DEC [92], PFC2D, PFC3D and ESYS Particles. It has been employed widely to investigate rock fracture and resultant fragmentation processes. In this method, cracks initiate and grow along the boundaries of blocks when the maximum stress exceeds tensile or shear strength thresholds defined at the blocks’ interfaces (Figure 1.21).

Generally, the distinct element method is a widely used technique in investigation of rock fracturing and failure process [157, 58, 51]. The DEM has become a popular method in modeling hydraulic fracturing. Damjanac et al. [47] used the DEM for simulating the hydraulic fracturing in naturally fractured reservoirs. [148] used the DEM in order to study the interaction between hydraulic fracture and discrete fracture network. There are also good instances of the DEM being used in fracture propagation in anisotropic rocks. [55] used the DEM to model an anisotropic rock fracturing behavior under Brazilian test conditions. [56] modeled inherently anisotropic rocks under uniaxial compression loading using the DEM.

#### 1.3.2.2 Bonded Particle Method–BPM

The BPM is one of the widely used particle-based methods used for study of fracturing process of rock. The BPM simulates the mechanical behavior of a collection of non-uniform-sized circular

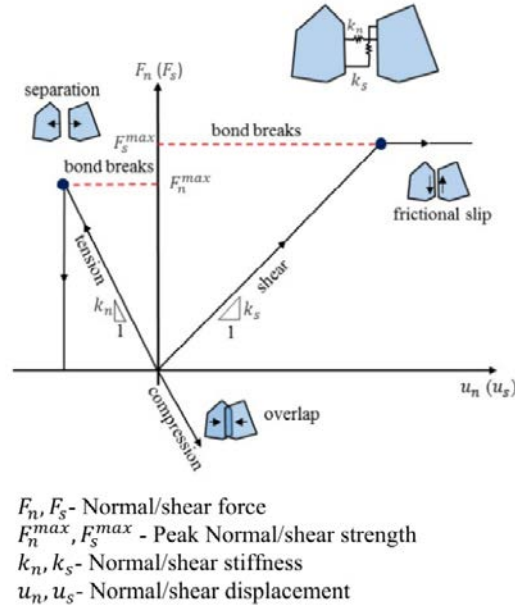


Figure 1.21: Intersurface behavior of DEM models. After [126]

or spherical rigid particles that are bonded together at their contact points. The term ‘particle’, as used here, differs from its more common definition in the field of mechanics, where it is taken as a body of negligible size that occupies only a single point in space. In the present context, the term ‘particle’ denotes a body that occupies a finite amount of space [144]. The rigid particles interact only at the soft contacts, which possess finite normal and shear stiffnesses. The mechanical behavior of this system is described by the movement of each particle and the force and moment acting at each contact. Newton’s laws of motion provide the fundamental relation between particle motion and the resultant forces and moments causing that motion. The assumptions inherent in BPM are listed in [144]. The BPM is confirmed to be an appropriate method to model fracture mechanism and be a good alternative to UDEC or 3DEC, but not without drawbacks. The main drawbacks include particle size dependency in both stages of simulation and calibration, overestimation of tensile strength, relying on linear failure envelope, considering low friction angle and difficulties in modelling of complex geometries.

BPM has been used in order to investigate the deformation and failure process in rocks by introducing the concept of weakness planes, giving an anisotropic characteristic of the medium [127] (Figure 1.22). BPM is also developed to study the damage and failure mechanism in transverse isotropic rocks such as Tournemire shale and Callovo Oxfordian rocks [51]. BPM has also been used quite significantly to deal with fracture and hydraulic fracture problems [144, 52].

### 1.3.2.3 Discontinuous Deformation Analysis–DDA

Firstly introduced by [160] as an implicit formulation of DEM, DDA has been developed rapidly in the field of rock mechanics and accordingly rock fracture analysis. This method shares some procedures with the FEM, but it is a discontinuum method satisfying the definition by [46]. Similar to FEM, in order to find a solution, the DDA minimises the total potential energy of model, while the domain comprises rigid blocks. The original DDA assumes stress and strain to be constant within the block which results in the limitation of block deformation. A wide range of DDA application and its validation in different fields of engineering is demonstrated by [120]. It has also been applied to model fluid flow and solid deformation for fractured rocks by [96]. Despite all of the efforts and validation reports of DDA application in rock engineering, it is relatively new and its performance, particularly for dynamic rock fracture and fragmentation analysis, is not fully developed and verified. Besides, it is still computationally expensive for highly dynamic and

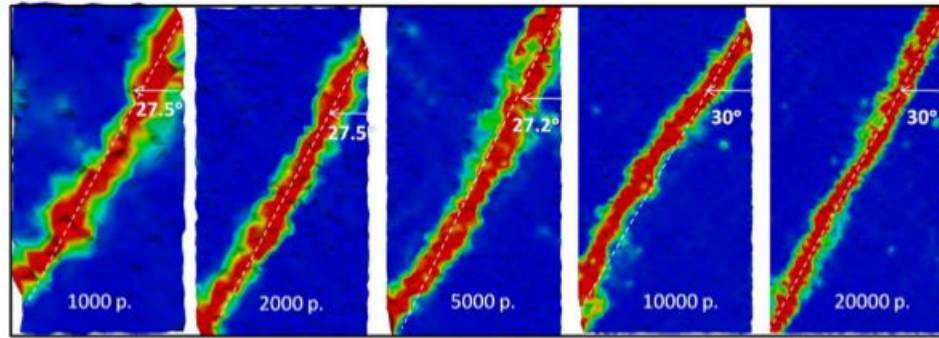


Figure 1.22: model's predictions in terms of shear banding obtained for biaxial compression tests performed on 5 packings presenting different numbers of particles (1000, 2000, 5000, 10,000, and 20,000, respectively) but same dimensions ( $1 \times 2 \times 0.1$  model units). After [51]

practical-scale simulations such as dynamic rock fragmentation. The DDA has not been among popular methods in modeling anisotropic rock fracture nor is it used as a popular method for hydraulic fracturing.

#### 1.3.2.4 Lattice model method

Lattice models, which are also known as dynamic lattice network models (DLNM), are relatively simpler, modern techniques among other discontinuum methods. The basic concept is similar to BPM, where material can be represented as a collection of interacting discrete masses. The medium comprises of a set of either regular or irregular distributed point masses, which interact through simple zero-size spring/beam with ability to transfer forces. Although the technique is not new, its application in fracture modelling is a recent development [190, 94]. Despite all merits of the lattice models, they suffer from difficulties in model calibration and practical-scale modelling [126]. Due to this difficulties lattice model method is not among popular methods for modeling anisotropic rock fracture. There is not any history of its use in hydraulic fracturing either.

#### 1.3.2.5 Molecular dynamics–MD

Because of the exponential growth of computing power, large-scale atomic simulations are being developed rapidly to study the failure mechanisms of materials [197]. Molecular Dynamics is a time-dependent numerical solution of Newton's equation of motion for all particles in atomic-scale [143]. The model in MD is composed of a collection of interacting spherical atoms under assumed interaction potential. The interaction are described using potential functions, i.e., Hooke's law, Lennard–Jones potential, embedded atom method potential and the reactive force field interatomic potential. Several studies have investigated the different aspects of crack initiation and propagation mechanism, such as the plastic deformation process at the crack, CZM parameters and dynamic crack processes using MD [198]. Generally, the MD simulation is a very useful tool for studying the change in the microstructure and therefore, it is a suitable technique for investigating crack nucleation and propagation at the micro-scale. However, the small computational system sizes and short time scales are two major limitations of this technique. Additionally, the nano/microstructures of rock materials are too complicated to model due to there being a multi-phase material. Molecular dynamics couldn't find its place among popular methods for fracture modeling in anisotropic rocks nor is it popular method among researchers for hydraulic fracturing modeling.

## 1.4 Conclusion

As discussed there are numerous numerical methods that can deal with fracture propagation. These methods ranging from continuum to discontinuum demonstrate strong points and also weak points in dealing with fracturing phenomenon. All numerical approaches are capable of properly

model the rock fracture process. This shortcoming arises mainly as a consequence of the complex nature of rock fracturing processes, which requires consideration of the effect of heterogeneity, softening behavior, transition mechanism from continuum to discontinuum, and the time and cost considerations. For instance the heterogeneity of the medium which plays a very important role in the fracturing process is not considered in most of the methods when discussing the failure mechanism in rocks. Hydraulic fracturing in particular exhibits very complex coupled processes which add to the difficulty of the modeling. Now adding the anisotropic characteristic of the rocks to the coupled processes introduced by hydraulic fracturing would add one more parameters to the phenomenon, making modeling of th fracturing process even more complicated. Since the nature of most of the rocks where hydraulic fracturing takes place is anisotropic, this should also be of interest for having a realistic description of the medium in question. Among all the continuum methods discussed in this chapter the XFEM is the most developed technic in the field of rock fracture analysis. the XFEM possesses the general advantages of the FEM namely, ability in dealing with complex geometries and boundary conditions, well-developed constitutive models for pre-failure behaviour of rock and ability to model explicit crack initiation and propagation. Among discontinuum methods the DEM is capable of modeling explicit crack initiation and propagation and proves to be a robust approach. Most of the DEMs are particle dependent in both simulation and calibration stages. One of the drawbacks of the DEM include relying on linear failure envelope. In this thesis we use two numerical methods of two different natures *i.e.* continuum (XFEM) and discontinuum (DEM). For what concerns the continuum approach we use an HM-XFEM model in this thesis. HM-XFEM model is capable of modeling hydraulic fracturing phenomenon. We improve the model making it capable of modeling hydraulic fracture opening in transverse isotropic rocks. We also build a BPM where we integrate the transverse isotropic characteristic for the medium by introducing the concept of weakness planes.

## Chapter 2

# A fully coupled 3D HM-XFEM model for transverse isotropic media

### 2.1 Introduction

The phenomena that govern the propagation of the hydraulic fracture in porous media include: the flow within the fracture, the flow through the surrounding porous medium, the deformation of the surrounding porous medium, the leak-off of the fluid from the fracture into the surrounding porous medium and the fracture propagation. Challenging difficulties in the numerical modeling of fluid-driven fractures in permeable porous media emanate from the hydromechanical couplings between the partial differential equations governing the fluid flow within the fracture, the pore fluid flow in the porous medium surrounding the fracture and the solid deformation [125].

Hydraulic fracture propagation results the progressive decay of the cohesive tractions within the fracture process zone and the imposition of the fluid pressure onto the fracture faces. The tractions acting on the fracture faces give rise to the mechanical coupling, and the fluid leak-off through the fracture faces leads to the mass transfer coupling between the fracture and the porous medium surrounding the fracture [125].

The combination of hydromechanical models with the XFEM seems effectively appropriate for the simulation of fluid-driven fractures propagation, in particular for complex fracture geometries. Indeed, when fractures are discretized with interface elements, it is necessary to generate a mesh that matches fractures geometries, which can be very difficult for 3D-non planar connected fractures. In addition, it requires to update the mesh at each propagation step, involving projection algorithms that are expensive. The XFEM circumvents these difficulties [141].

There has been numerous studies carried out with XFEM to investigate fracture propagation. [86] have modeled the reorientation of fractures depending on the regional stress state. [28] Developed a model to handle several fractures in the vicinity of a well in order to assess the competition that takes place between nearby fractures. [104, 161] Investigated interaction and junction between multiple fractures. [184, 185] Developed an XFEM-based cohesive zone model combined with Mohr–Coulomb theory of plasticity to investigate non-planar fracture propagation in both brittle and ductile formations. However, all the above mentioned models suffer different drawbacks. First, few of these models consider a fully coupled approach and fluid flow in the fractures is often described in a simplified way using a 1D leak-off model. Second, the vast majority of XFEM models are limited to short fractures propagation where plane strain assumptions are valid and very far to be able to describe a 3D realistic configuration with complex fracture geometries [141].

To overcome the above mentioned challenges, [141] developed a 3D numerical model of hydraulic fracture propagation. The model is based on the numerical model developed by [63] but with some distinguished features such as: (i) fully coupled hydromechanical coupling based on an improved XFEM enrichment technique, (ii) fracture propagation on non predefined paths, (iii) 3D formulation including the possibility to deal with complex non-planar fracture geometries and (iv) multiple-crack junction. Besides the extension of the model to fluid-filled cohesive crack junctions, most of these new features in [141] borrow on recently published advances on the XFEM [132, 140, 65].



## 2.2 HM-XFEM model representation

Considering  $\Omega \subset \mathbb{R}^3$  a domain entirely cut by a permeable fracture, with  $\mathbf{n}$  being the normal on the boundary  $\partial\Omega$  of the domain and  $\mathbf{n}_c$  the normal of the fracture surface  $\Gamma_c$ . The domain is divided in two sub-domains represented by  $\Omega_1$  and  $\Omega_2$  as superior and inferior respectively such that  $\Omega = \Omega_1 \cup \Omega_2$ . The domain's border  $\partial\Omega$  can thus be decomposed as  $\partial\Omega = \Gamma_u \cup \Gamma_t \cup \Gamma_p \cup \Gamma_F$  where the boundary conditions (i.e. Dirichlet, Neumann) are imposed (hydrodynamical— $\Gamma_p, \Gamma_F$  and mechanical— $\Gamma_u, \Gamma_t$ ). The fracture surface can also be decomposed as  $\Gamma_c = \Gamma_f \cup \Gamma_1 \cup \Gamma_2$  where  $\Gamma_1$  and  $\Gamma_2$  represent the walls of the fracture. The fluid flux conditions are imposed on  $\Gamma_f$  and the cohesive traction forces on  $\Gamma_1$  and  $\Gamma_2$ .

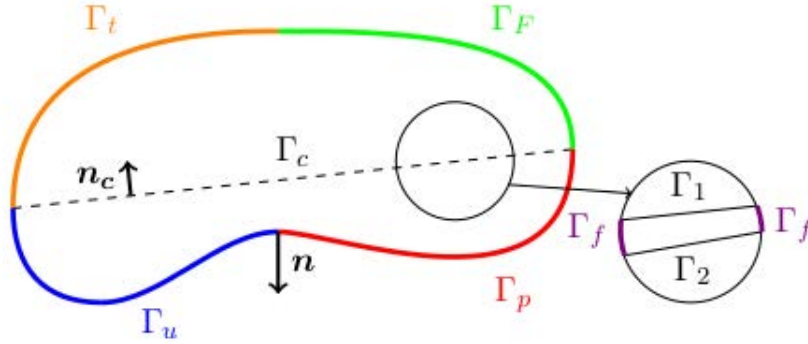


Figure 2.1: Domain  $\Omega$  decomposed into its subdomains.

### 2.2.1 Domain definition and hypotheses

#### Assumptions

The porous medium is supposed to be completely saturated and a fluid flow takes place between the fracture and the bulk. This exchange is considered by the help of two parameters  $q_1$  and  $q_2$  (representing fluid flux) having the unit of  $kg.m^{-2}.s^{-1}$ . The pore pressure field of the bulk is presented by  $p$  and that one of the fracture is denoted by  $p_f$ . The displacement field is  $\mathbf{u}$  and the displacement jump at the interface is  $[[\mathbf{u}]]$ . Considering  $P_1$  a point on  $\Gamma_1$  and  $P_2$  a point on  $\Gamma_2$  the normal to  $\Gamma_1$  is denoted as  $\mathbf{n}_c^1 = -\mathbf{n}_c$  and the normal to  $\Gamma_2$  is denoted as  $\mathbf{n}_c^2 = \mathbf{n}_c$  (Figure 2.2). The displacement normal is thus defined by the following equation:

$$[[\mathbf{u}]] \cdot \mathbf{n}_c = (\mathbf{u}(P_1) - \mathbf{u}(P_2)) \cdot \mathbf{n}_c \geq 0 \quad (2.1)$$

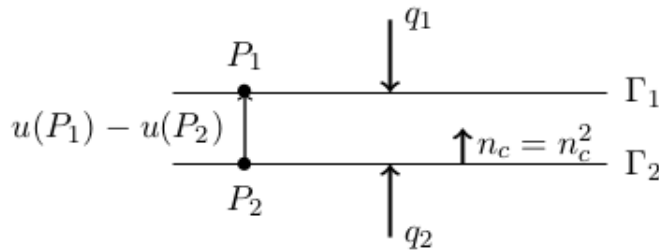


Figure 2.2: Adopted orientation convention at the interface level.

By considering Biot's effective stresses:

- In the bulk, the total stress is written as  $\boldsymbol{\sigma} = \boldsymbol{\sigma}' - \mathbf{B}p[\mathbf{Id}]$ , where  $\mathbf{B}$  is the Biot coefficient tensor,

- At the fracture level, the total stress is defined as  $t_c = t' - p_f \mathbf{n}_c$

In addition, the infinitesimal strain hypothesis is adopted.

### Boundary conditions

As shown in Figure 2.1, the boundary conditions on the border of the domain  $\Omega$  and at the fracture level are used to obtain the variational formulation of the conservation equations defining the HM-XFEM model.

On the exterior border of the  $\Omega$ , the following Dirichlet boundary conditions are imposed:

1.  $\mathbf{u} = \mathbf{u}_0$  on  $\Gamma_c$  (constant displacements),
2.  $p = p_0$  on  $\Gamma_p$  (constant pore pressure).

The Neumann's boundary condition's are:

3.  $\boldsymbol{\sigma} \cdot \mathbf{n} = \mathbf{t}$  on  $\Gamma_t$  (imposed surface forces),
4.  $\mathbf{M} \cdot \mathbf{n} = M_{ext}$  on  $\Gamma_F$  (constant mass flux).

Moreover the Dirichlet boundary conditions at the fracture level  $\Gamma_c$  are:

5.  $\mathbf{W} \cdot \mathbf{n}_c = W_{ext}$  on  $\Gamma_f$  (constant flux injection),
6.  $\mathbf{M} \cdot \mathbf{n}_c^1 = q_1$  on  $\Gamma_1$  and  $\mathbf{M} \cdot \mathbf{n}_c^2 = q_2$  on  $\Gamma_2$  (equality of flux at both fracture walls).
7.  $\sigma \cdot n_c^1 = -t_c$  on  $\Gamma_1$  (imposed cohesive traction forces),
8.  $\sigma \cdot n_c^2 = t_c$  on  $\Gamma_2$  (imposed cohesive traction forces).

Some supplementary boundary conditions are necessary to ensure the continuity of the pore pressure  $p$  with the fluid pressure on each fracture wall. This hypothesis is only valid when the thickness of the fracture is small. The additional conditions are:

9.  $p = p_f$  on  $\Gamma_1$ ,
10.  $p = p_f$  on  $\Gamma_2$ .

## 2.2.2 Governing equations

### Mass conservation for the fluid in the bulk

The interstitial fluid in the bulk, with the pore pressure is defined by the following mass balance equation:

$$\frac{\partial m_v}{\partial t} + Div(\mathbf{M}) = 0 \quad (2.2)$$

where  $\rho$  is the fluid density,  $\phi$  is the Eulerian porosity of the bulk,  $\epsilon_v = Tr(\nabla \mathbf{u}) = Tr(\boldsymbol{\epsilon})$  the volumetric strain and  $\mathbf{M}$  the fluid flux, and  $m_v = \rho \phi (1 + \epsilon_v)$  is the mass flow.

The variations of the fluid density and of the porosity are respectively of the form:

$$\frac{d\rho}{\rho} = \frac{dp}{K_w} \quad (2.3)$$

and

$$d\phi = \mathbf{B} : d\boldsymbol{\epsilon} - \phi d\epsilon_v + \frac{dp}{M_\phi} \quad (2.4)$$

where  $p$  is the pore pressure,  $k_w$  is the fluid compressibility modulus,  $\mathbf{B}$  is the Biot tensor,  $\frac{1}{M_\phi}$  is the Biot modulus for the bulk given as  $\frac{1}{M_\phi} = (\mathbf{B} - \phi \boldsymbol{\delta}) : \mathbf{S}_0^S : \boldsymbol{\delta}$ , and the mass flux for the fully saturated porous medium is given by Darcy's law (gravity is neglected):

$$\mathbf{M} = -\rho \frac{\mathbf{K}^{int}}{\mu} \nabla p \quad (2.5)$$

where  $\mathbf{K}^{int}$  represents the intrinsic permeability tensor for transverse isotropic medium, and  $\mu$  the dynamic viscosity.

### Mass conservation for the fluid in the fracture

In the cohesive fracture, the fluid pressure is denoted  $p_f$  and source terms  $q_+$  and  $q_-$  may occur from the fracture to the surrounding porous medium so that the mass balance equation is:

$$\frac{\partial(\rho[\mathbf{u}]\cdot\mathbf{n})}{\partial t} + \text{Div}(\mathbf{W}) = q_- + q_+ \quad (2.6)$$

where  $\mathbf{W}$  is the fluid flux inside the fracture. It is assumed that the fluid flux depends on the gradient of the fluid pressure, but that the conductivity depends on the aperture so that the flow  $\mathbf{W}$  is given by the cubic law (gravity is neglected):

$$\mathbf{W} = -\frac{\rho([\mathbf{u}]\cdot\mathbf{n})^3}{12\mu}\nabla p_f \quad (2.7)$$

The variation of the fluid density inside the fracture is given by:

$$\frac{d\rho}{\rho} = \frac{dp_f}{K_w} \quad (2.8)$$

### A stable ‘‘mortar’’ formulation for the cohesive zone model

In our study, the cohesive zone model is formulated by the new ‘‘mortar’’ formulation presented by [65]. In this new formulation, instead of inserting the CZM by collocation at each Gauss point based on the augmented Lagrangian formalism of Lorentz [118], one relies on the ‘‘mortar’’ formalism introduced by [65]. In this method, the whole internal variables set relative to the cohesive fracture is carried by the vertex nodes of the edges intersected by the discontinuity. In this way, one is able to implicitly locate the position of the cohesive crack front with a set of nodal values, compatible from one element to the other [141]. Additionally, a mixed linear cohesive law is used. This mixed linear cohesive law enhances the stability of our numerical model as it behaves elastically for unloading situations instead of traction free unloading for the Talon–Curnier cohesive law. The cohesive zone model along the fluid-driven fracture path is shown in Figure 2.3. The damage process takes place in zone 2 in which the effective cohesive stress is directly linked to the aperture via a linear softening relation (Figure 2.3 right). Considering the displacement jump  $\mathbf{w}$  across the cohesive crack, in the augmented Lagrangian formalism, a general expression of the surface density of energy for orthotropic potential laws, as given by [141] is:

$$\Pi(\mathbf{w}, \boldsymbol{\lambda}) = \phi(\lambda_n + r w_n, \boldsymbol{\lambda}_s + r_s \mathbf{w}_s) - \frac{\lambda_n^2}{2r} - \frac{\boldsymbol{\lambda}_s \cdot \boldsymbol{\lambda}_s}{2r_s} \quad (2.9)$$

with  $\phi$  a differentiable function depending on the shape of the cohesive law,  $r$  and  $r_s$  the normal and tangential augmentation parameters and  $\lambda$  a Lagrange multiplier. The traction-opening curve for a mixed linear non regularized cohesive law is depicted in Figure 2.3 right.

Cohesive traction is considered as  $\mathbf{t}'_c = \frac{\partial \Pi}{\partial \mathbf{w}}$ . Also the additional dual equation corresponding to the interfacial law reads  $\frac{\partial \Pi}{\partial \lambda} = 0$ .

The effective cohesive traction thus reads [141]:

$$\mathbf{t}'_{c,n}(\lambda_n + r w_n, \boldsymbol{\lambda}_s + r_s \mathbf{w}_s) = \frac{\partial \Pi}{\partial w_n} = r \frac{\partial \psi}{\partial (\lambda_n + r w_n)} \quad (2.10)$$

$$\mathbf{t}'_{c,s}(\lambda_n + r w_n, \boldsymbol{\lambda}_s + r_s \mathbf{w}_s) = \frac{\partial \Pi}{\partial \mathbf{w}_s} = r_s \frac{\partial \psi}{\partial (\boldsymbol{\lambda}_s + r_s \mathbf{w}_s)} \quad (2.11)$$

By omitting the dependence of  $\mathbf{t}'_c$  on  $\lambda_n + r w_n$  and  $\boldsymbol{\lambda}_s + r_s \mathbf{w}_s$ , the interfacial law reads  $\boldsymbol{\lambda} = \mathbf{t}'_c$ . An equivalent augmented traction can be introduced as [65]:

$$(\lambda + r w)_{eq} := \sqrt{(\lambda_n + r w_n)_+^2 + \frac{r}{r_s} (\boldsymbol{\lambda}_s + r_s \mathbf{w}_s)^2} \quad (2.12)$$

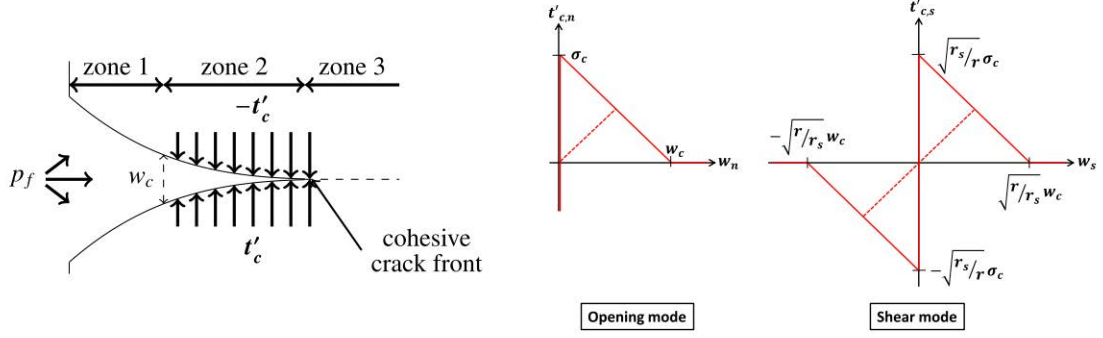


Figure 2.3: Representation of a cohesive zone model under fluid circulation (left) and the chart of a mixed linear cohesive law (right), from [141].

with  $\langle \lambda_n + r w_n \rangle_+^2$  the positive part of  $\lambda_n + r w_n$  and a threshold function  $\phi$  such that:

$$\phi\left((\lambda + r w)_{eq}\right) := \frac{(\lambda + r w)_{eq} - \sigma_c}{r w_c - \sigma_c} \quad (2.13)$$

with  $w_c$  the critical displacement jump for the cohesive law, corresponding to the vanishing of the cohesive traction.

A scalar dimensionless variable  $\alpha$  is then defined as:

$$\begin{aligned} \phi\left((\lambda + r w)_{eq}\right) - \alpha &\leq 0 \\ \dot{\alpha} &\geq 0 \\ \dot{\alpha} [\phi\left((\lambda + r w)_{eq}\right) - \alpha] &= 0 \end{aligned} \quad (2.14)$$

For an uncracked material,  $\alpha \leq 0$  and for a fully cracked material,  $\alpha \geq 1$ . For different loading conditions, we have [141]

$$\begin{cases} \dot{\alpha} > 0 \\ \alpha = \phi\left((\lambda + r w)_{eq}\right) \end{cases} \quad (2.15)$$

and the function  $\psi$  is defined by:

$$\psi(\lambda_n + r w_n, \lambda_s + r_s w_s) = 2G_c \left(1 - \frac{\sigma_c}{r w_c}\right) \alpha \left(1 - \frac{\alpha}{2}\right) + \frac{1}{2r} \langle \lambda_n + r w_n \rangle_-^2 \quad (2.16)$$

with  $\langle \lambda_n + r w_n \rangle_-^2$  the negative part of  $\lambda_n + r w_n$ .

For contact-free situations, the surface energy (Equation 2.9) depends only on  $\alpha$  and  $\lambda_{eq}$  :

$$\Pi(\alpha, \lambda_{eq}) = \psi(\alpha) - \frac{\lambda_{eq}^2}{2r}.$$

When the dissipation of energy starts:

$$\begin{cases} \alpha = 0 \\ \lambda_{eq} = \sigma \end{cases} \quad (2.17)$$

and when it ends (breaking point)

$$\begin{cases} \alpha = 1 \\ \lambda_{eq} = 0 \end{cases} \quad (2.18)$$

Then, we have:

$$\Pi(\alpha = 1, \lambda_{eq} = 0) - \Pi(\alpha = 0, \lambda_{eq} = \sigma_c) = G_c \quad (2.19)$$

which ensures that  $G_c$  corresponds to the energy that shall be provided to fully debond a unit surface of fracture. The resulting effective cohesive traction may be synthesized with an equivalent

effective cohesive traction:  $t'_{c,eq} = \sqrt{\langle t'_{c,n} \rangle_+^2 + \frac{r}{r_c} t'_{c,s}^2}$  linked to the augmented cohesive traction via:  $t'_{c,eq} = (1 - T_d)(\lambda + rw)_{eq}$  with  $T_d$  the damage tensor defined as:

$$T_d = \frac{\alpha}{\left(1 - \frac{\sigma_c}{rw_c}\right)\alpha + \frac{\sigma_c}{rw_c}} \quad (2.20)$$

It is considered,  $T_d = 0$  if  $\alpha = 0$  (perfect adherence) and  $T_d = 1$  if  $\alpha = 1$  (breaking point). The general expression for the effective cohesive traction is [141]:

$$t'_{c,n} = (1 - T_d)\langle \lambda_n + rw_n \rangle + \langle \lambda_n + rw_n \rangle_- \quad (2.21)$$

$$\mathbf{t}'_{c,s} = (1 - T_d)(\boldsymbol{\lambda}_s + r_s \mathbf{w}_s) \quad (2.22)$$

### 2.2.3 Variational formulations of conservation equations

#### Weak formulation for mechanical problem

The quantities related to the interface (the cohesive traction  $t_c$  and the energy density  $\Pi$ ) must be defined over a reduced space  $M_0$  adapted to the cohesive fracture compared to the definition space used for the displacement field  $U_0$ .  $w$  is introduced as a new unknown to the problem, defined over a different space from that of  $\llbracket u \rrbracket : M_0$ . The total energy of the domain  $\Omega$  cut by the cohesive interface  $\Gamma_c$  reads:

$$E(\mathbf{u}, \boldsymbol{\lambda}, \mathbf{w}) = \frac{1}{2} \int_{\Omega} \boldsymbol{\epsilon}(\mathbf{u}) : \mathbf{C} : \boldsymbol{\epsilon}(\mathbf{u}) d\Omega - \int_{\Gamma_t} \mathbf{t} \cdot \mathbf{u} d\Gamma_t + \int_{\Gamma_c} \Pi(\mathbf{w}, \boldsymbol{\lambda}) d\Gamma_c - \int_{\Gamma_c} p_f \mathbf{n} \cdot \mathbf{w} d\Gamma_c \quad (2.23)$$

The solution of the continuous problem implies to find  $(\mathbf{u}, \mathbf{w}, \boldsymbol{\lambda}) = \operatorname{argmin}_{\mathbf{w}^* = \llbracket u^* \rrbracket} E(\mathbf{u}^*, \mathbf{w}^*, \boldsymbol{\lambda}^*)$ . The Lagrangian of the problem is then:

$$\begin{aligned} \mathcal{L}(\mathbf{u}, \mathbf{w}, \boldsymbol{\lambda}, \boldsymbol{\mu}) = \frac{1}{2} \int_{\Omega} \boldsymbol{\epsilon}(\mathbf{u}) : \mathbf{C} : \boldsymbol{\epsilon}(\mathbf{u}) d\Omega - \int_{\Gamma_t} \mathbf{t} \cdot \mathbf{u} d\Gamma_t + \int_{\Gamma_c} \Pi(\mathbf{w}, \boldsymbol{\lambda}) d\Gamma_c + \int_{\Gamma_c} \boldsymbol{\mu} \cdot (\llbracket u \rrbracket - \mathbf{w}) d\Gamma_c \\ - \int_{\Gamma_c} p_f \mathbf{n} \cdot \mathbf{w} d\Gamma_c \end{aligned} \quad (2.24)$$

with  $\boldsymbol{\mu}$  a Lagrange multiplier introduced to enforce the condition  $\llbracket u \rrbracket = \mathbf{w}$  along the cohesive interface  $\Gamma_c$ .

The optimality conditions of this Lagrangian give the following discrete weak form regarding the mechanical problem:

$$\left\{ \begin{array}{l} \forall \mathbf{u}^* \in \mathbf{U}_0^*, \quad \int_{\Omega} \sigma(\mathbf{u}^*) d\Omega - \int_{\Gamma_t} \mathbf{t} \cdot \mathbf{u}^* d\Gamma_t + \int_{\Gamma_c} \boldsymbol{\mu} \cdot \llbracket u^* \rrbracket d\Gamma_c = 0 \\ \forall \boldsymbol{\mu}^* \in M_0, \quad \int_{\Gamma_c} \boldsymbol{\mu}^* \cdot (\llbracket u \rrbracket - \mathbf{w}) d\Gamma_c = 0 \\ \forall \mathbf{w}^* \in M_0, \quad - \int_{\Gamma_c} \mathbf{w}^* \cdot (\boldsymbol{\mu} + p_f \mathbf{n} - \mathbf{t}'_c) d\Gamma_c = 0 \\ \forall \boldsymbol{\lambda}_n^* \in M_0, \quad - \int_{\Gamma_c} \frac{\lambda_n - t'_{c,n}}{r} \lambda_n^* d\Gamma_c = 0, \quad \forall \boldsymbol{\lambda}_s^* \in M_0, \quad - \int_{\Gamma_c} \frac{\lambda_s - t'_{c,s}}{r_s} \lambda_s^* d\Gamma_c = 0 \end{array} \right. \quad (2.25)$$

with:  $\mathbf{U}_0 = \{\mathbf{u}^* \in H^1(\Omega) \text{ such that } \mathbf{u}^* \text{ is discontinuous across } \Gamma_c \text{ and } \mathbf{u}^* = 0 \text{ on } \Gamma_u\}$ .

The first optimality condition represents the global mechanical equilibrium of the system. In particular, the term  $\int_{\Gamma_c} \boldsymbol{\mu} \cdot \llbracket u^* \rrbracket d\Gamma_c$  accounts for the cohesive efforts at the interface. The second optimality condition is interpreted as the projection of the displacement jump  $\llbracket u \rrbracket$  on the reduced space  $M_0$ . The third optimality condition is interpreted as the projection of the total cohesive traction  $t_c$  on the reduced space  $M_0$ . Finally, the fourth optimality condition is the interfacial law [141].

### Weak formulation for hydromechanical problem

The weak form of the hydrodynamical problem is composed of 4 equations: the two mass balance equations and the two equations for the fluid pressure continuity along each fracture side. Both mass balance equations are discretized in time with a  $\theta$ -scheme that is unconditionally stable for  $\theta \geq \frac{1}{2}$  and of order 1 except when  $\theta = \frac{1}{2}$  for which it is of order 2. A value of  $\theta \neq \frac{1}{2}$  will be chosen in order to avoid spurious oscillations. The superscript + indicates that the variable is expressed at the current time-step whereas the superscript - refers to a variable expressed at the previous time-step, and  $\Delta t = t^+ - t^-$ .

According to the principle of Virtual Work, the weak formulation of the mass balance equation for the interstitial fluid is:

$$\begin{aligned} \forall p^* \in P_0 - \int_{\Omega} \frac{m_w^+ - m_w^-}{\Delta t} p^* d\Omega + \theta \int_{\Omega} \mathbf{M}^+ \cdot \nabla p^* d\Omega + (1 - \theta) \int_{\Omega} \mathbf{M}^- \cdot \nabla p^* d\Omega \\ = \theta \int_{\Gamma_F} \mathbf{M}_{ext}^+ p^* d\Gamma_F + (1 - \theta) \int_{\Gamma_F} \mathbf{M}_{ext}^- p^* d\Gamma_F - \theta \int_{\Gamma^-} q_-^+ p^* d\Gamma_- \\ - (1 - \theta) \int_{\Gamma^-} q_-^- p^* d\Gamma_- - \theta \int_{\Gamma^+} q_+^+ p^* d\Gamma_+ - (1 - \theta) \int_{\Gamma^+} q_+^- p^* d\Gamma_+ \end{aligned} \quad (2.26)$$

with:  $P_0 = \{p^* \in H^1(\Omega)$  such that  $p^*$  discontinuous across  $\Gamma_c$  and  $p^* = 0$  on  $\Gamma_p\}$  and  $m_w^+ - m_w^- = \rho^+ \phi^+ (1 + \epsilon_v^+) - \rho^- \phi^- (1 + \epsilon_v^-)$ .

In the same manner, the weak formulation of the mass balance equation for the fluid in the cohesive fracture is:

$$\begin{aligned} \forall p_f^* \in M_0 - \int_{\Gamma} \frac{w^+ - w^-}{\Delta t} p_f^* d\Gamma_c + \theta \int_{\Gamma_c} \mathbf{W}^+ \cdot \nabla p_f^* d\Gamma_c + (1 - \theta) \int_{\Gamma_c} \mathbf{W}^- \cdot \nabla p_f^* d\Gamma_c \\ = \theta \int_{\Gamma_f} \mathbf{W}_{ext}^+ p_f^* d\Gamma_f + (1 - \theta) \int_{\Gamma_f} \mathbf{W}_{ext}^- p_f^* d\Gamma_f - \theta \int_{\Gamma^-} q_-^+ p_f^* d\Gamma_- \\ - (1 - \theta) \int_{\Gamma^-} q_-^- p_f^* d\Gamma_- - \theta \int_{\Gamma^+} q_+^+ p_f^* d\Gamma_+ - (1 - \theta) \int_{\Gamma^+} q_+^- p_f^* d\Gamma_+ \end{aligned} \quad (2.27)$$

with:  $M_0 = \{\Lambda^* \in H^{-\frac{1}{2}}(\Gamma_c)\}$  and  $w^+ - w^- = \rho^+ [[\mathbf{u}]]^+ \cdot \mathbf{n}_c - \rho^- [[\mathbf{u}]]^- \cdot \mathbf{n}_c$ . Also the weak formulation of the pressure continuity along both fracture walls is given by:

$$\forall q_-^* \in M_0 \quad \int_{\Gamma^-} (p - p_f) q_-^* d\Gamma_- = 0 \quad (2.28)$$

$$\forall q_+^* \in M_0 \quad \int_{\Gamma^+} (p - p_f) q_+^* d\Gamma_+ = 0 \quad (2.29)$$

## 2.2.4 Discretization with XFEM

### Level set method

The level set method [136], [159] was introduced for fluid mechanics, in order to represent the evolution of interfaces between distinct phases (gas bubbles in a liquid phase for example). The idea consists in defining the interface as the iso-zero of a distance function.

We consider a crack  $\Gamma$  in a domain  $\Omega$ . We would like to implicitly define this discontinuity as the set of points  $\mathbf{x}$  satisfying  $\psi(\mathbf{x}, t) = 0$ . For this aim, we use two level-set functions. The first one is the normal level-set (lsn), it gives the signed distance to the interface in the direction normal to it regardless of the crack front. The second one is the tangential level-set, it gives the signed distance to the crack front in the direction tangential to the crack surface. The crack  $\Gamma$  is then defined as the intersection between the surface  $\{\mathbf{x} \in \Omega$  such that  $lsn(\mathbf{x}) = 0\}$  and the domain  $\{\mathbf{x} \in \Omega$  such that  $lsn(\mathbf{x}) < 0\}$  (see Figure 2.4). The crack front is the set of points:  $\{\mathbf{x} \in \Omega$  such that  $lst(\mathbf{x}) = lsn(\mathbf{x})\}$ . The level set functions allow to implicitly locate the discontinuity

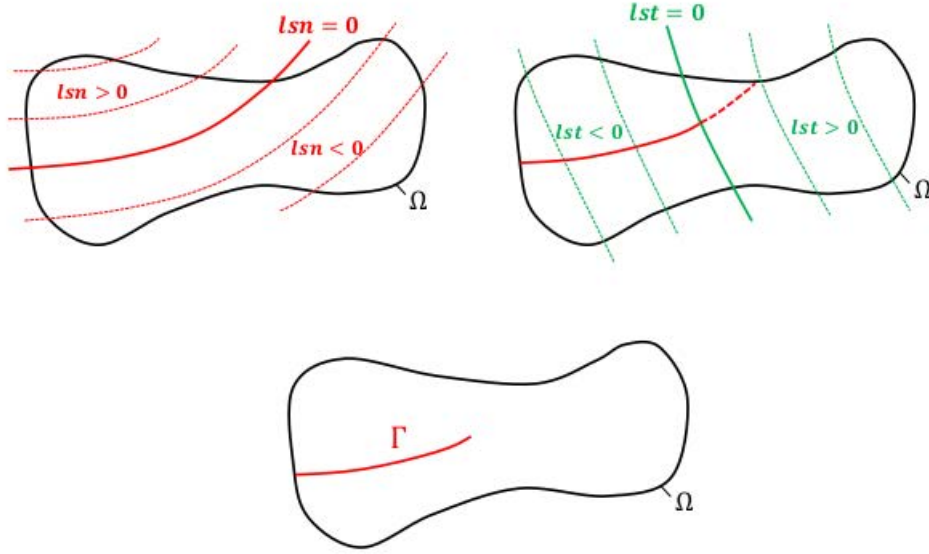


Figure 2.4: Normal level-set (left), tangential level-set (right) and the resulting crack  $\Gamma$  (bottom). After [141]

surface independently from the mesh. When the crack propagates, it is only necessary to update the level set functions.

In order to define an arbitrary crack  $\Gamma := \{\mathbf{x}, lsn(\mathbf{x}) = 0 \text{ and } lst(\mathbf{x}) \leq 0\}$ , it is not necessary for the level-set to satisfy the distance property. Nonetheless, that is the most common choice because it enables to define an orthonormal basis adapted to the crack front. Indeed, if the level-sets satisfy the distance property, we have by definition:

$$\begin{cases} \|\nabla(lsn)\| = 1 \\ \|\nabla(lst)\| = 1 \\ \nabla(lsn) \cdot \nabla(lst) = 0 \end{cases} \quad (2.30)$$

The vectors  $\mathbf{n} := \nabla(lsn)$  and  $\mathbf{t} := \nabla(lst)$  form an orthonormal basis adapted to the crack front (see Figure 2.5). And for a point  $\mathbf{x} \in \Omega$ , the polar coordinates are straightly given by:

$$\begin{cases} r(\mathbf{x}) = \sqrt{lsn^2 + lst^2} \\ \Theta(\mathbf{x}) = \arctan\left(\frac{lsn}{lst}\right) \end{cases} \quad (2.31)$$

### Discretization of the bulk's fields

In order to simulate a displacement jump across an interface  $\Gamma$  in a domain  $\Omega$ , XFEM introduces additional degrees of freedom  $\mathbf{b}_j$  at the nodes  $j$  whose support is intersected by the interface (see Figure 2.6). These degrees of freedom are associated to discontinuous shape functions defined with a Heaviside function. The interface is implicitly located in the mesh thanks to a normal level-set. The sign of this level-set enables the distinction between two subdomains  $\Omega_+$  and  $\Omega_-$  on both sides of the interface such that  $\Omega_+ \cup \Omega_- = \Omega$  (see Figure 2.6). Therefore, the Heaviside function is applied directly to the normal level-set. In this way, it is discontinuous precisely across the interface. In *Code\_Aster*, the Heaviside function is used to define the shape function associated to the degree of freedom  $\mathbf{b}_j$  of the node  $j$  whose position  $\mathbf{x}_j$  is:

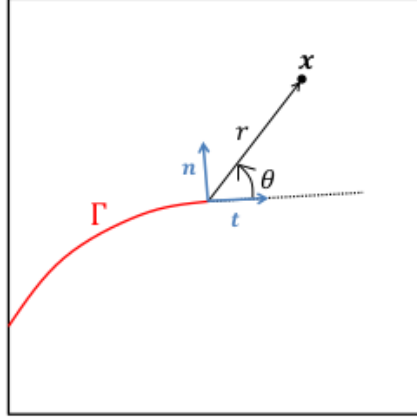


Figure 2.5: The polar basis associated to the crack front. After [139]

$$\begin{aligned} \text{If } \mathbf{x}_j \in \Omega_+, H_j(\text{lsn}(\mathbf{x})) &= \begin{cases} 0 & \text{if } \text{lsn}(\mathbf{x}) > 0 \\ -2 & \text{if } \text{lsn}(\mathbf{x}) \leq 0 \end{cases} \\ \text{If } \mathbf{x}_j \in \Omega_-, H_j(\text{lsn}(\mathbf{x})) &= \begin{cases} 0 & \text{if } \text{lsn}(\mathbf{x}) > 0 \\ +2 & \text{if } \text{lsn}(\mathbf{x}) \leq 0 \end{cases} \end{aligned} \quad (2.32)$$

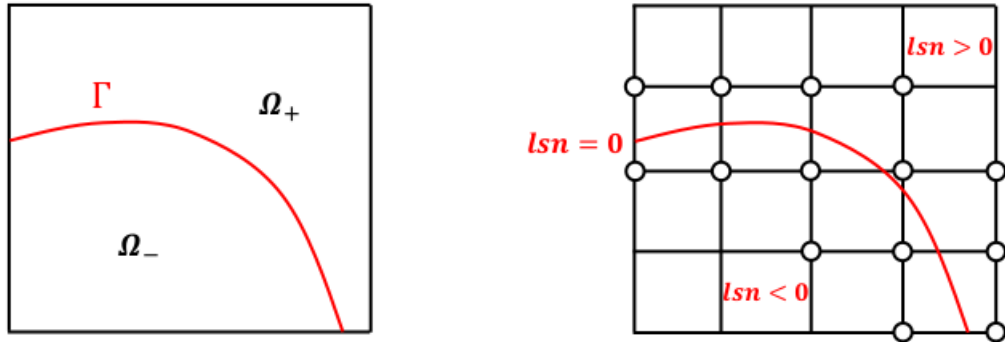


Figure 2.6: On the left, the two domains  $\Omega_+$  and  $\Omega_-$  formed by the arbitrary interface  $\Gamma$ . On the right, the associated mesh. The surrounded nodes carry the Heaviside enrichment. After [141]

This definition depends on the position of the node  $j$  compared to the interface  $\Gamma$ . The quantity  $H_j(\text{lsn}(\mathbf{x})) = 0$  if the point  $x$  and the node  $j$  are in the same subdomain and  $\pm 2$  otherwise. The coefficient 2 is introduced in order to facilitate the expression of the displacement jump along the interface [132]. This “complementary” formulation has been introduced by [132] and inspired by the work of [76].

### Discretization of the fracture’s fields

The HM-XFEM quadrangular element and its associated degrees of freedom are shown in Figure 2.7. For the fields related to the cohesive fracture  $\Gamma_c(p_f, q_+, q_-, \lambda, \boldsymbol{\mu}, \mathbf{w})$ , the set of admissible functions is:

$$M_0 = \{\Lambda^* \in H^{-\frac{1}{2}}(\Gamma_c)\} \quad (2.33)$$



The approximation space for the fields related to the cohesive fracture is then adapted to the fracture path. It relies on the vertex nodes of the edges intersected by the discontinuity  $\Gamma_c$ . The approximation space is reduced in order to satisfy the LBB (Ladyzenskaja-Babuška-Brezzi) stability condition [122] and avoid the appearance of spurious oscillations in the numerical resolution [63]. To achieve this latter objectives, the equality relationships are imposed across the discontinuity for fields related to the cohesive interface. Based on the work of [141] for a group of connected vital edges, a cohesive field  $\Lambda$  is approximated only by a single and common degree of freedom. An example of an interface that crosses a triangular mesh is depicted in Figure 2.8.

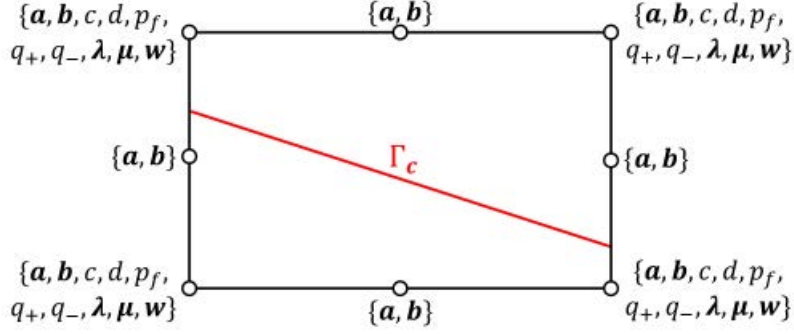


Figure 2.7: A quadrangle cohesive HM-XFEM element. After [141]

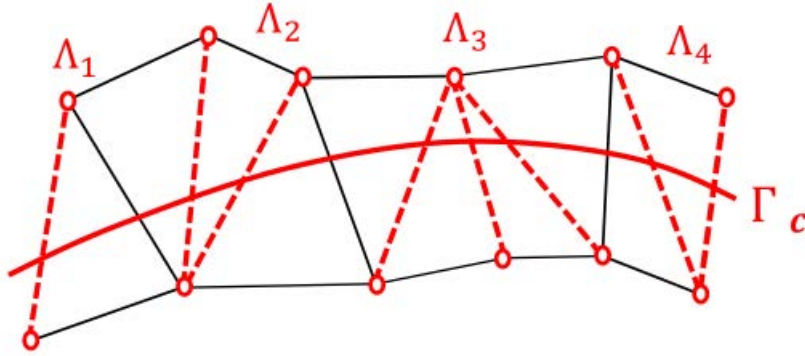


Figure 2.8: Approximation space for the fields related to the cohesive fracture. After [141]

### Asymptotic fields

The Heaviside enrichment function introduced previously 2.32 fails to approximate the displacement field at the crack tip. To circumvent this, the asymptotic representation of the displacement field is used. The displacement field at the crack tip for a plane crack embedded in an infinite isotropic domain is:

$$\begin{cases} u_1 = \frac{1}{2\mu} \sqrt{\frac{r}{2\pi}} [K_I \cos(\frac{\theta}{2})(\kappa - \cos \theta) + K_{II} \sin(\frac{\theta}{2})(\kappa + 2 + \cos \theta)] \\ u_2 = \frac{1}{2\mu} \sqrt{\frac{r}{2\pi}} [K_I \sin(\frac{\theta}{2})(\kappa - \cos \theta) + K_{II} \cos(\frac{\theta}{2})(\kappa - 2 + \cos \theta)] \\ u_3 = \frac{1}{2\mu} \sqrt{\frac{r}{2\pi}} K_{III} \sin(\frac{\theta}{2}) \end{cases} \quad (2.34)$$

with  $\mu = \frac{E}{2(1+\nu)}$  and  $\kappa = \begin{cases} 3 - 4\nu & \text{for plane strain} \\ \frac{3-\nu}{1+\nu} & \text{for plane stress} \end{cases}$ ,  $E$  the Young's modulus,  $\nu$  the Poisson ratio and  $(r, \theta)$  the polar basis adapted to the crack front (Figure 2.5). The displacements  $(u_1, u_2, u_3)$

correspond respectively to the kinematic modes I, II and III of the fracture and  $(K_I, K_{II}, K_{III})$  are the associated stress intensity factors. Equation 2.34 is solved by introducing the asymptotic solution to the finite element basis:

$$\{\sqrt{r} \sin \frac{\theta}{2}, \sqrt{r} \cos \frac{\theta}{2}, \sqrt{r} \sin \frac{\theta}{2} \sin \theta, \sqrt{r} \cos \frac{\theta}{2} \sin \theta\} \quad (2.35)$$

The enrichment functions given in Equation 2.35 are represented in the polar coordinates at the crack front  $(r, \theta)$ . The approximation of the displacement field is:

$$\mathbf{u}^h(\mathbf{x}) = \sum_{i \in N} \mathbf{a}_i \psi_i(\mathbf{x}) + \sum_{k \in N \cap N_A} \sum_{\alpha=1}^4 \mathbf{c}_k^\alpha \psi_k(\mathbf{x}) F^\alpha(\mathbf{x}) \quad (2.36)$$

with  $\{F^1, F^2, F^3, F^4\}$  the singular functions  $\{\sqrt{r} \sin \frac{\theta}{2}, \sqrt{r} \cos \frac{\theta}{2}, \sqrt{r} \sin \frac{\theta}{2} \sin \theta, \sqrt{r} \cos \frac{\theta}{2} \sin \theta\}$ ,  $\mathbf{c}_k^\alpha$  the associated degrees of freedom,  $N$  the set of nodes whose support contains the point  $x$  and  $N_A$  the set of nodes who carry the asymptotic enrichment.

To solve Equation 2.36 for a transverse isotropic medium we simply need to adapt Equation 2.34. The corresponding asymptotic equations for transverse isotropic are given by [100] as follows:

- For the symmetric problem (Mode I) we have:

$$\begin{aligned} u_n &= -\frac{K_I \sqrt{r}}{\beta_1} \left\{ \frac{n_1^{1/2}}{1+m_1} [\cos \theta + (\cos^2 \theta + n_1^{-1} \sin^2 \theta)^{1/2}]^{1/2} \right. \\ &\quad \left. - \frac{n_2^{1/2}}{1+m_2} [\cos \theta + (\cos^2 \theta + n_2^{-1} \sin^2 \theta)^{1/2}]^{1/2} \right\} + 0(r), \\ u_t &= 0(r), \\ u_z &= \frac{K_I \sin \theta \sqrt{r}}{\beta_1} \left\{ \frac{m_1}{n_1(1+m_1)} [\cos \theta + (\cos^2 \theta + n_1^{-1} \sin^2 \theta)^{1/2}]^{-1/2} \right. \\ &\quad \left. - \frac{m_2}{n_2(1+m_2)} [\cos \theta + (\cos^2 \theta + n_2^{-1} \sin^2 \theta)^{1/2}]^{-1/2} \right\} + 0(r), \end{aligned} \quad (2.37)$$

where  $\beta_1 = c_{44}(n_1^{1/2} - n_2^{1/2})$ .

- For the skew-symmetric cases we have:

$$\begin{aligned} u_n &= -\frac{K_{II}(n_1 n_2)^{1/2} \sin \theta \sqrt{r}}{c_{44}(n_1^{1/2} - n_2^{1/2})} \left\{ [(1+m_1)n_1]^{-1} [\cos \theta + (\cos^2 \theta + n_2^{-1} \sin^2 \theta)^{-1/2}]^{1/2} \right. \\ &\quad \left. - [(1+m_2)n_2]^{-1/2} [\cos \theta + (\cos^2 \theta + n_2^{-1} \sin^2 \theta)^{1/2}]^{-1/2} \right\} + 0(r), \\ u_t &= \frac{K_{III}(n_3)^{1/2} \sin \theta \sqrt{r}}{c_{44}(m_2 - m_1)} \left\{ \left[ \frac{(1+m_2)}{n_1} \right] [\cos \theta + (\cos^2 \theta + n_2^{-1} \sin^2 \theta)^{-1/2}]^{1/2} \right. \\ &\quad \left. - \frac{(1+m_2)}{n_1} [\cos \theta + (\cos^2 \theta + n_2^{-1} \sin^2 \theta)^{1/2}]^{-1/2} \right\} + 0(r), \\ u_z &= \frac{K_{II} \sqrt{r}}{\alpha_2 c_{44}(m_1 - m_2)} \left\{ \frac{m_1(1+m_1)}{n_1^{1/2}} [\cos \theta + (\cos^2 \theta + n_1^{-1} \sin^2 \theta)^{1/2}]^{1/2} \right. \\ &\quad \left. - \frac{m_2(1+m_1)}{n_2^{1/2}} [\cos \theta + (\cos^2 \theta + n_2^{-1} \sin^2 \theta)^{-1/2}]^{-1/2} \right\} + 0(r), \end{aligned} \quad (2.38)$$

where  $n_1, n_2$  are the roots of the following characteristic equation:

$$c_{11}c_{44}n^2 + [c_{13}(c_{13} + 2c_{44}) - c_{11}c_{33}]n + c_{33}c_{44} = 0 \quad (2.39)$$

with

$$m_j = \frac{c_{11}n_j - c_{44}}{c_{11} + c_{44}} = \frac{(c_{13} + c_{44})n_j}{c_{33} - c_{44}n_j}, \quad j = 1, 2 \quad (2.40)$$

and

$$\begin{aligned} n_3 &= \frac{2c_{44}}{(c_{11} - c_{12})} \\ \alpha_2 &= \frac{(1 + m_1)(1 + m_2)}{m_1 - m_2} \left[ \frac{1}{n_1^{1/2}} - \frac{1}{n_2^{1/2}} \right] \end{aligned} \quad (2.41)$$

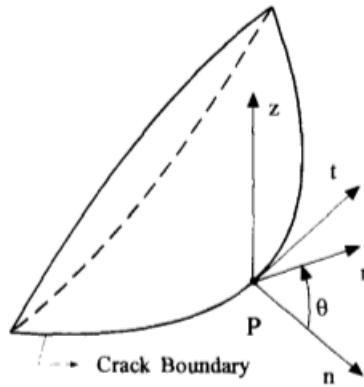


Figure 2.9: Normal stress ratio parameters. After [100]

## 2.2.5 Crack propagation along non-predefined paths in TI medium

In this section we discuss fracture propagation along non-predefined paths in transverse isotropic media. The proposed model is an extension of the model proposed by [141] where we integrate the transverse isotropic characteristic of the medium. The crack initiation is controlled by the CZM used by [141], where the turning (bifurcation) angle is determined a posteriori based on the post-processing of the cohesive state.

The procedure for the propagation on non-predefined paths has originally been suggested by [64] for crack propagation in concrete. It is based on the cohesive zone model depicted previously (Section 1.2). The originality of the procedure proposed by [64] lies in the *a posteriori* computation of the crack advance based on the computed cohesive state, instead of a most common determination beforehand from the stress state ahead of the front.

In previous studies the discontinuities in the HM-XFEM model have been represented by a normal level set field only. Along this immutable discontinuity surface, the CZM allows to distinguish the adherent zone from the debonding zones [141]. For the crack propagation on non-predefined paths, [64] suggested the crack front to be implicitly located with a tangential level-set field.

### The procedure of propagation along non-predefined paths

Here we give an extensive description of how the model handles crack propagation along non-predefined paths as [64] suggested. The discontinuity surface defined with the level-sets by:  $\{\mathbf{x} \in \Omega : lsn(\mathbf{x}) \leq 0 \cap lst(\mathbf{x}) < 0\}$  is interpreted as a potential crack surface. The actual fracture lies in the potential crack surface which is also called the traction-free zone. The traction free zone is

separated from its adjacent area called cohesive zone by cohesive or physical crack front, and the area beyond the cohesive zone which is separated from the cohesive zone by fictitious crack front. The procedure of crack propagation on non pre-defined path is depicted in Figure 2.10.

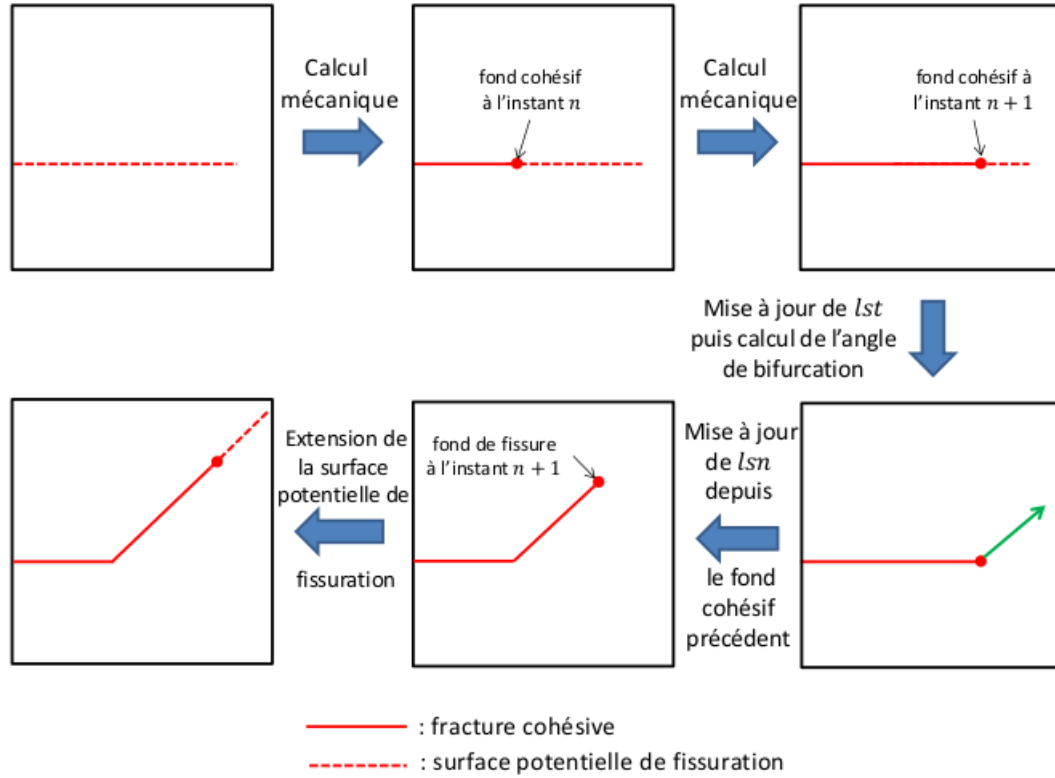


Figure 2.10: Procedure for the propagation on non predefined paths. After [141]

To interpret the procedure shown in Figure 2.10, one must consider an initial potential crack surface defined with a normal level-set field and a tangential level-set field (Figure 2.10 top left). Then the fluid will be injected in to the crack surface and at time  $n$  the cohesive crack front separating the debonding zones from the adherent zone is detected (Figure 2.10 top middle). The injection of the fluid continues up to time  $n + 1$ . When the equilibrium is determined, the cohesive crack front has advanced compared to the previous cohesive crack front (Figure 2.10 top right). The position of this new cohesive crack front is detected. At this point, the tangential level-set field is updated so as to merge the discontinuity front end and the cohesive crack front and to compute the bifurcation angle  $\beta$  (Figure 2.10 bottom right). At this iteration, the normal level set field from the cohesive crack front detected at the time  $n$  will be updated in accordance with the bifurcation angle  $\beta$  (Figure 2.10 bottom middle). Hence, the new crack front corresponds to the intersection between the iso-zeros of the updated level-set fields. From here the potential crack surface will be extended (Figure 2.10 bottom left).

### Bifurcation angle

The criterion adopted here to calculate the bifurcation angle is the Maximum Tangential Stress [60], given in terms of stress intensity factors as follows:

$$\beta = 2 \arctan \left[ \frac{1}{4} \left( K_I / K_{II} - \text{sign}(K_I) \sqrt{(K_I / K_{II})^2 + 8} \right) \right] \quad (2.42)$$

Equation 2.42 was defined for elastic isotropic materials and was used by [141] and [64]. In the case of transverse isotropic material, we adapt the bifurcation angle equation given by [155] based

on the concept given in [60]. The equivalent of Equation 2.42 for transverse isotropic materials is Equation 1.40. The detailed procedure on how to obtain the equation is presented in Section 1.2.

The calculation of the stress intensity factors appearing in the bifurcation angle equation are done according to the method proposed by [64]. According to [64] a J-integral may still be defined in the context of cohesive zone models. It is expressed in terms of a cohesive integral only:

$$J = - \int_{\Gamma_c} t_c \cdot \nabla[u] \cdot \theta \, d\Gamma_c \quad (2.43)$$

with  $[u]$  the displacement jump across the cohesive fracture,  $t_c$  the total cohesive traction applied on the fracture walls and  $\theta$  a virtual extension of the fracture (Figure 2.11)

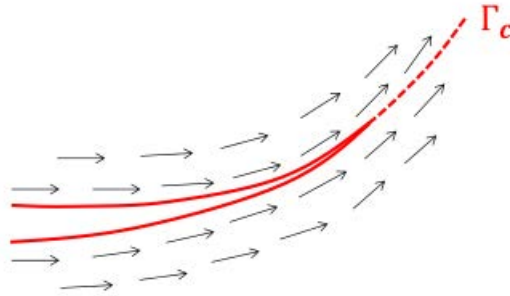


Figure 2.11: Virtual extension of the cohesive crack  $\Gamma_c$ . The arrows present the values of  $\theta$ , from [141].

The procedure on how we exploit this concept to calculate stress intensity factors in transverse isotropic medium is given in details in Section 1.2.

## 2.2.6 Numerical implementation

As transverse anisotropy essentially impacts the propagation of hydraulic crack along non-predefined paths, most of the numerical development and implementation in *Code\_Aster* were carried out in the *FORTRAN* and Python files related to the operators ruling this propagation. More specifically, the operators that are impacted by transverse isotropy are *CALC-G* and *PROPA\_FISS*, as well as *POST\_CHAM-XFEM* for the post-processing phase of the simulations. The operator *CALC-G* allows the calculation of the stress intensity factors, following Equation 1.26. This latter is implemented in the *FORTRAN* file *op0100.F90*, which thus had to be modified to integrate transverse isotropy. A number of *FORTRAN* files, called by *op0100.F90* had also to be modified. Amongst other, major modification had to be done in *FORTRAN* files such as *te0288.F90* and *te0297.F90*. We had to create new *FORTRAN* files corresponding to the transverse isotropic version of basic files of the code, for example *xsifel.F90*, *xsifle.F90*, *xsifl1.F90*, *xsifl2.F90*, *cahxi.F90*, *xcalfev.F90* and other files of the same family. All these files allow the calculation of the stress intensity factors. Particularly, we had to implement the enrichment functions for the asymptotic part linked to the crack tip. The aim was to introduce expressions 2.37 and 2.38 in the code.

The operator *PROPA\_FISS* allows the propagation of a crack in *Code\_Aster*. It is implemented in the Python file *propa\_fiss\_ops.py*, which we had to modify. This operator calls on the one hand the operator *POST-RUPTURE* which calculates the angle of bifurcation, and on the other hand the operator *DETEC\_FRONT*. *POST-RUPTURE* is implemented in a Python file *post-rupture\_ops.py*, which we had to modify since it calculates the bifurcation angle. In the basic standard file of *Code\_Aster* prior to the integration of transverse isotropy, only the isotropic criterion of Erdogan and Sih [60] was implemented, so that it was required to implement Equation 1.40 to account for transverse isotropy.

## 2.3 Validation of the HM-XFEM model

In this section, we verify the implementation of transverse isotropic characteristic in HM-XFEM model by running simulations. To fulfill this goal we use a standard test case defined in *Code\_Aster* to check the integrity of our model.

### 2.3.1 Properties and geometry of the medium and boundary conditions

The hydromechanical model used here is a 3D block with the height of  $LZ = 10\text{ m}$ , length of  $LX = 10\text{ m}$  and width of  $LY = 2\text{ m}$ . This block contains a cohesive interface type discontinuity. It is located by the normal level-set equation  $l_{sn} = Z - 5$  and crosses the entire block in the horizontal direction deviding it in two identical sub-blocks (Figure 2.12). The medium is crossed at mid-height by a planar cohesive interface represented by means of a normal level-set only. We do not use a tangential level-set as the medium is supposed to be entirely crossed by the potential crack surface. This test has been previously used for the validation of the hydromechanical elements implemented in *Code\_Aster*. Because of its hydromechanical properties and HM-XFEM configuration we decided to extend it to transverse isotropy in order to verify our own study.

In Figure 2.12, points  $A(0, 0, 5)$ ,  $A'(0, 2, 5)$ ,  $B(3, 0, 5)$  and  $B'(3, 2, 5)$  are used for the implementation of the boundary conditions and the evaluation of the magnitudes of displacement and stress field. The Dirichlet boundary conditions are imposed in the following manner:

- the displacement in the  $x$  direction is blocked on the left side of the domain
- the displacements in the  $y$  and  $z$  directions are blocked on the upper and lower boundaries of the domain.

A constant fluid flux  $Q_0 = 0.025\text{ kg.m}^{-1}.\text{s}^{-1}$  is injected punctually in a poro-elastic semi-infinite saturated medium, from the left side into the cohesive interface for a duration of 10s. The injected fluid is incompressible. Under the effects of the fluid injection in the center of the potential crack surface, fracture expands. The cohesive zone model naturally separates the opened zone from the adherent zone. The pore pressure is set to zero at the top and at the bottom of the model.

The material properties for the solid matrix, for the fluid and for the cohesive zone model are summarized in the Tables 2.1 and 2.2.

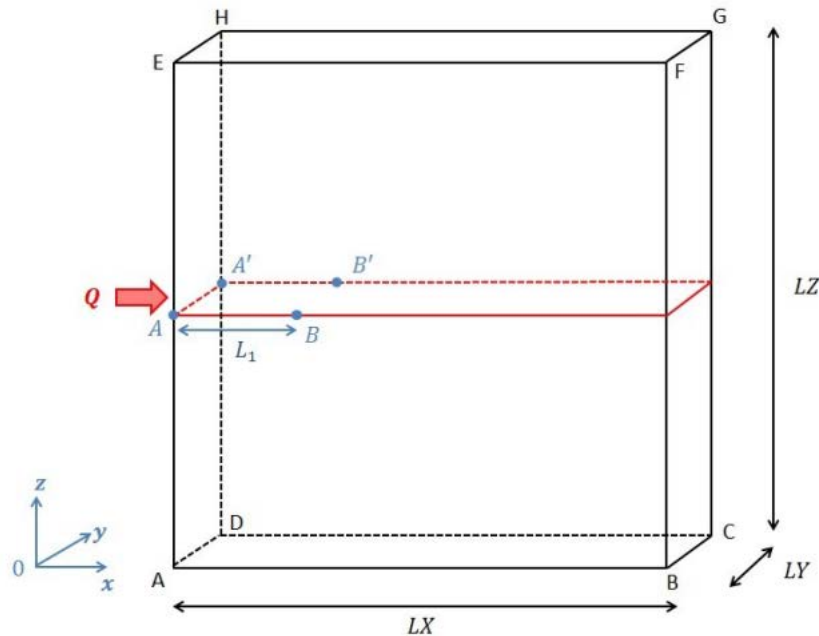


Figure 2.12: Configuration of the HM-XFEM model containing a cohesive interface discontinuity.

<b>Material parameters for the porous medium</b>	
Young's modulus ( $L$ )	$E_L = 5800 [MPa]$
Young's modulus ( $N$ )	$E_N = 3800 [MPa]$
Poisson ratio ( $LN$ )	$\nu_{LN} = 0.2 [-]$
Poisson ratio ( $LT$ )	$\nu_{LT} = 0.35 [-]$
Density of the fluid	$\rho = 2762 [kg.m^{-3}]$
Biot coefficient ( $L$ )	$b_L = 1 [-]$
Biot coefficient ( $N$ )	$b_N = 0.8 [-]$
Intrinsic permeability ( $L$ )	$k_L^{int} = 5 \times 10^{-18} [m^2]$
Intrinsic permeability ( $N$ )	$k_N^{int} = 10^{-18} [m^2]$
Viscosity of the fluid	$0.001 [Pa.s]$
Mobility of the fluid	$\lambda = 10^{-5} [m^2.Pa^{-1}.s^{-1}]$
Porosity	$\phi = 0.1 [-]$
Compressibility modulus for the fluid	$K_w [-]$
Compressibility modulus for the solid materix	$K_s [-]$
Compressibility modulus for the porous medium	$K_m [-]$

Table 2.1: Characteristics of the material and the fluid, L stand for longitudinal, N satnds for normal and T for transversal directions.

The material parameters for the cohesive zone are:

<b>Material parameters for the cohesive interface</b>	
Critical stress	$\sigma_c = 0.5 [MPa]$
Cohesive energy	$G_c = 0.9 \times 10^{-4} [Pa.m^{-1}]$

Table 2.2: Characteristics of the cohesive interface

### 2.3.2 Numerical results

The results presented in this section are based on the modified standard test-case of *Code\_Aster* presented in Section 2.3 with the transverse isotropic characteristics are integrated in the model. The displacement fields and pore pressure fields are investigated for different orientations of the material with respect to the interface plane. Bedding angles from  $0^\circ$  (parallel to the crack) to  $90^\circ$  (perpendicular to the crack) by a span of  $15^\circ$  difference are considered.

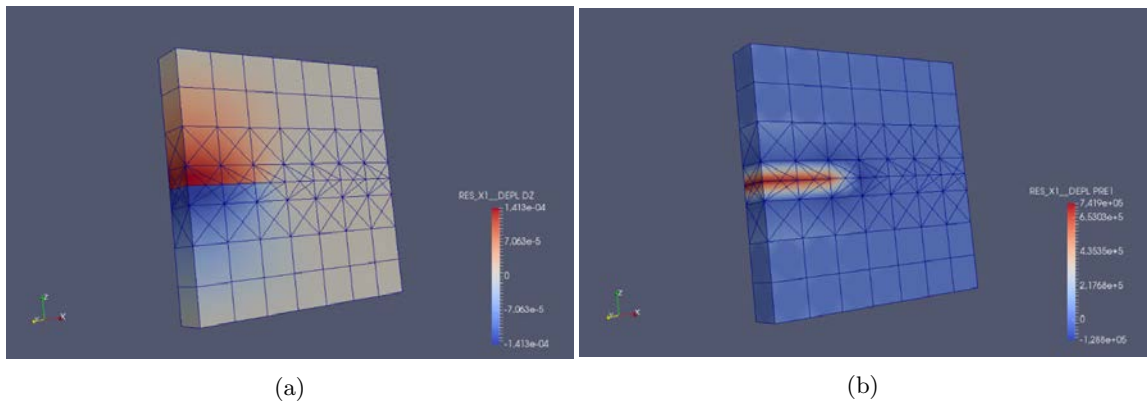


Figure 2.13: a) The resulting displacement field for bedding angle of  $\theta = 0^\circ$ . and b) The resulting pore pressure field for bedding angle of  $\theta = 0^\circ$ .

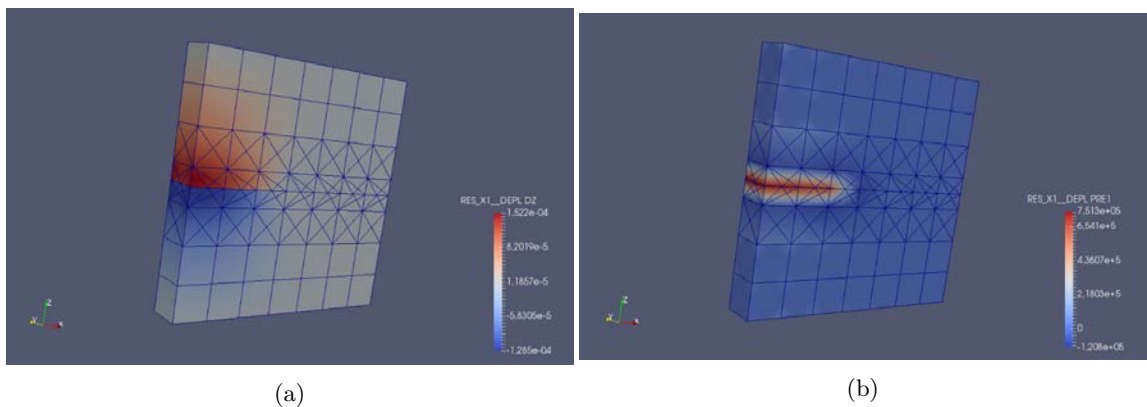


Figure 2.14: a) The resulting displacement field for bedding angle of  $\theta = 15^\circ$ . and b) The resulting pore pressure field for bedding angle of  $\theta = 15^\circ$ .



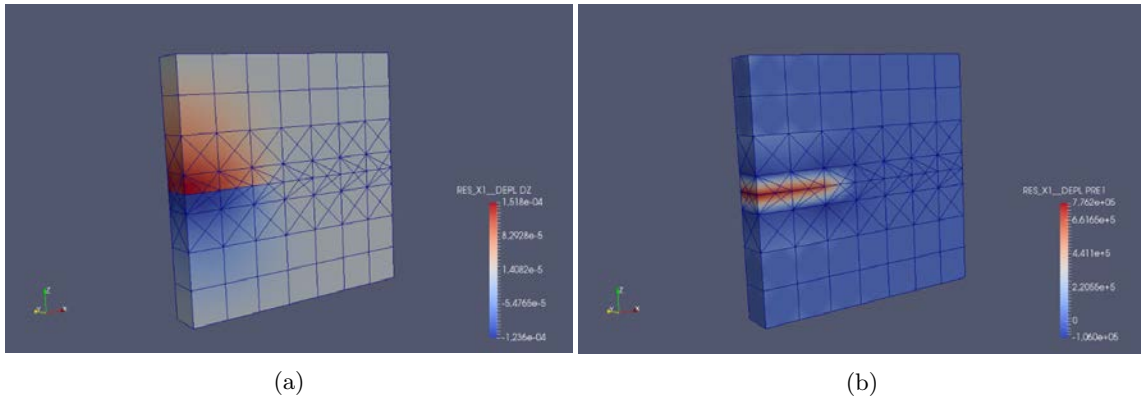


Figure 2.15: a) The resulting displacement field for bedding angle of  $\theta = 30^\circ$ . and b) The resulting pore pressure field in the discontinuity for bedding angle of  $\theta = 30^\circ$ .

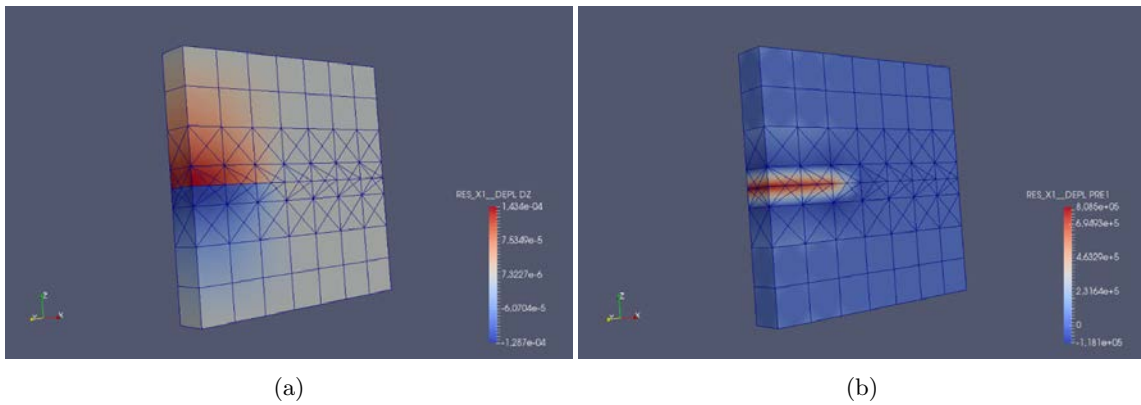


Figure 2.16: a) The resulting displacement field for bedding angle of  $\theta = 45^\circ$ . and b) The resulting pore pressure field for bedding angle of  $\theta = 45^\circ$ .

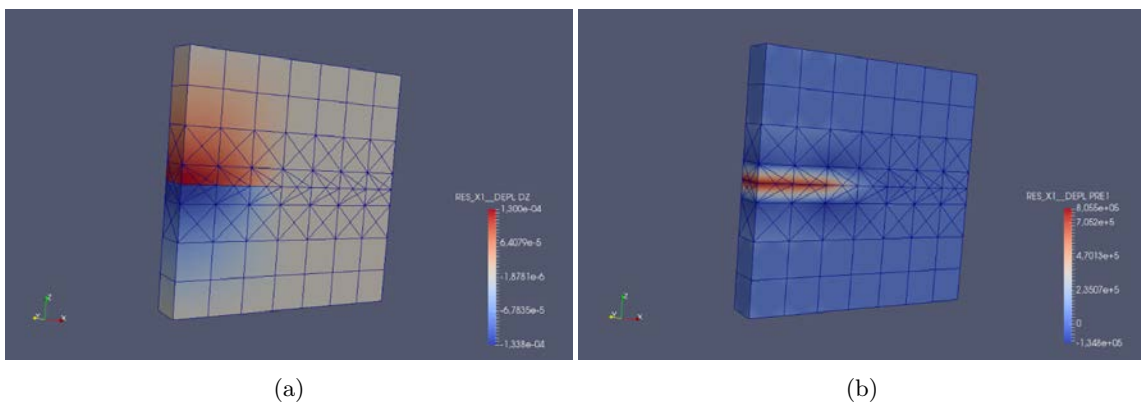


Figure 2.17: a) The resulting displacement field for bedding angle of  $\theta = 60^\circ$ . and b) The resulting pore pressure field for bedding angle of  $\theta = 60^\circ$ .

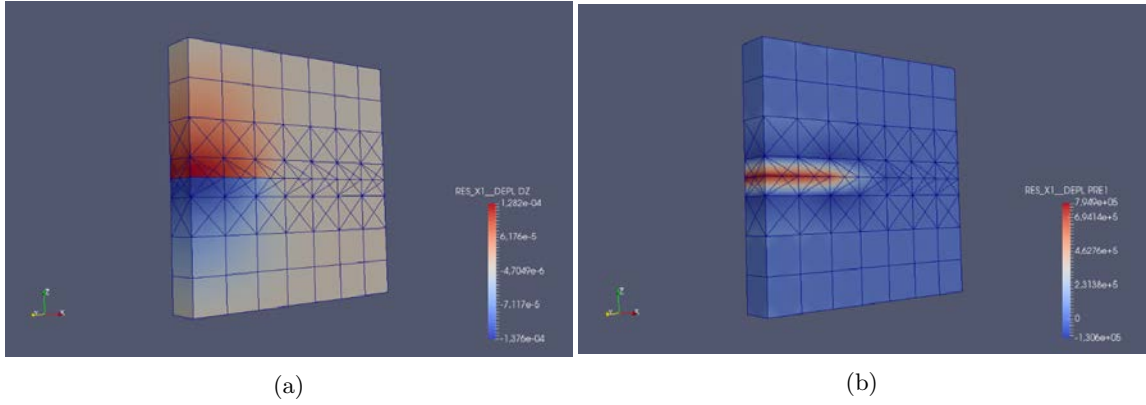


Figure 2.18: a) The resulting displacement field for bedding angle of  $\theta = 75^\circ$ . and b) The resulting pore pressure field for bedding angle of  $\theta = 75^\circ$ .

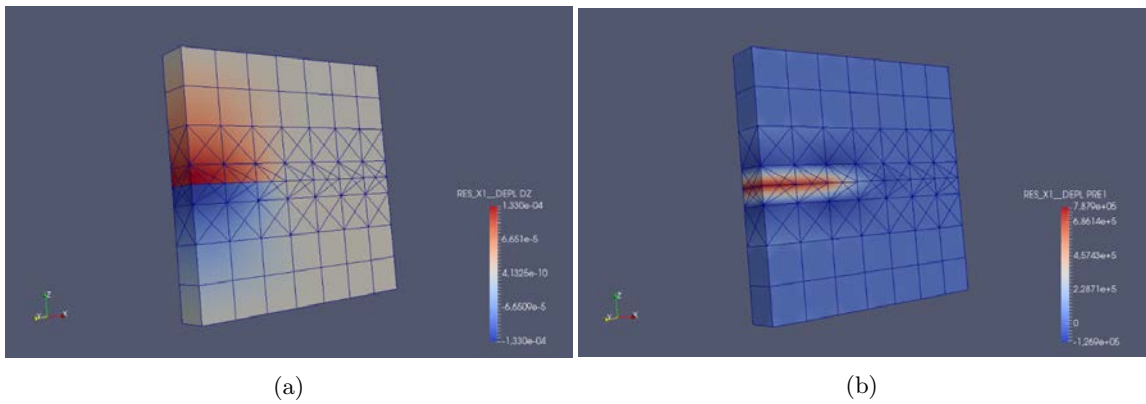


Figure 2.19: a) The resulting displacement field for bedding angle of  $\theta = 90^\circ$ . and b) The resulting pore pressure field for bedding angle of  $\theta = 90^\circ$ .

The impact of the anisotropy (transverse isotropy) can be seen on both pore pressure and displacement notably at the interface level. In the analysis of the both cases of pore pressure and displacement we can observe as the bedding angle increases from  $\theta = 0^\circ$  to  $\theta = 90^\circ$  the pore pressure and displacement also change. Although we can notice that displacement from  $\theta = 0^\circ$  to  $\theta = 45^\circ$  increases in a non monotonous fashion and  $\theta = 60^\circ$  to  $\theta = 90^\circ$  drops. The same pattern can be observed in the case of pore pressure although the drop from  $\theta = 60^\circ$  to  $\theta = 90^\circ$  is less drastic compared to that of observed in the case of displacement. The aforementioned results and features show the influence of transverse isotropy on the crack opening using an HM-XFEM developed using a previously existing model, the results shown here do not consider propagation along non predefined paths and it is currently an undergoing work.

## 2.4 Conclusion

In order to test the capabilities of the transverse isotropic version of the HM-XFEM model, we decided to run a test case requiring activation of the calculation of bifurcation angle and crack propagation. We selected the test case developed by Paul [141] dealing with the propagation of a 3D fluid-driven crack. In the isotropic version of this test, the crack path deviated towards the direction of the maximum confining stress. Let us consider a block of height  $H = 10 \text{ m}$ , length  $L = 16 \text{ m}$  and width  $B = 6 \text{ m}$ , with vertical displacements blocked on the lower and upper boundaries and normal displacements blocked on the front and back faces. The block is submitted to a normal stress  $\sigma = 0.6 \text{ MPa}$  on the left and right boundaries, as indicated in Figure 2.20.

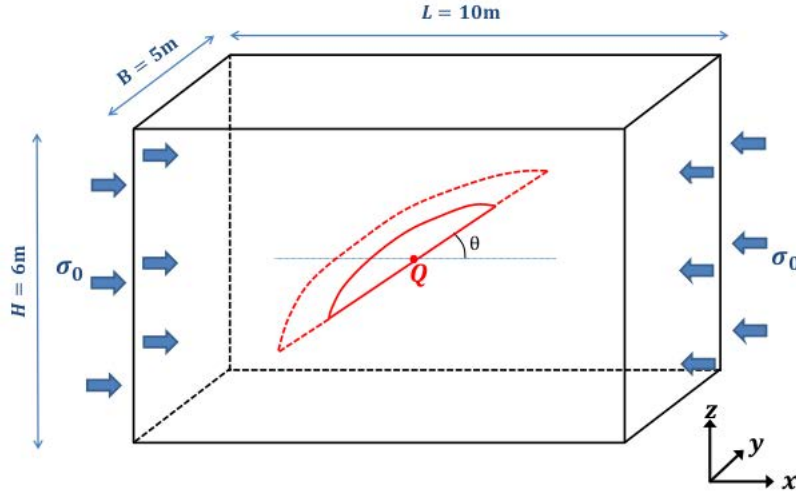


Figure 2.20: Geometry of the 3D hydraulic crack reorientation test, from [139]

A potential crack surface is introduced in the center of the front face of the model. This crack has the shape of half a disc and exhibits an angle of  $30^\circ$  (noted  $\theta$  in Figure 2.20) with the horizontal line. A fluid is injected with constant flow rate of  $Q = 6 \text{ kg.s}^{-1}$  at the center of the potential crack surface. In the basic version of the test, the fluid flow is maintained during 17 s. All the details on the basic version of the test, including time discretization and material parameters are given in [139]. Figure 2.21 from Paul [139] exhibits the reorientation of the crack surface from the beginning to the end of injection.

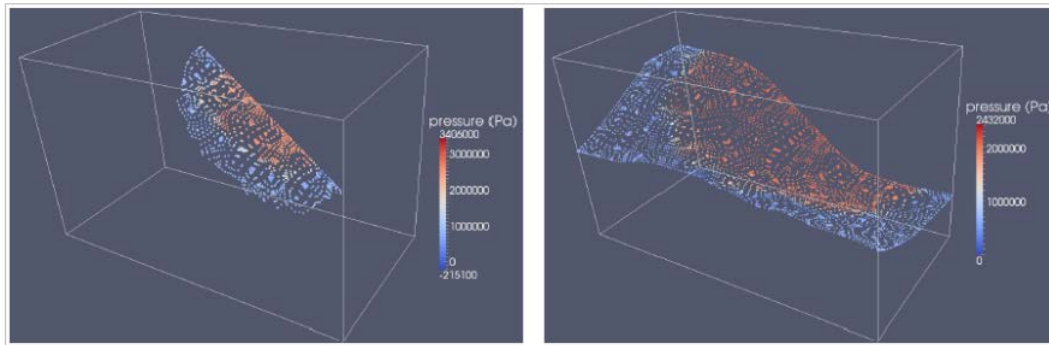


Figure 2.21: Initial and final crack surface and pore pressure for the 3D fluid-driven crack reorientation test, from [139]

This test case, as every test case of the HM-XFEM model involving crack propagation, is very sensitive to the time and space discretization.

We adapted this test case to the propagation of 3D fluid driven crack reorientation in a transverse isotropic medium. To this aim, the elastic and hydraulic properties of the rock matrix are defined as transverse isotropic. These properties are given in table 2.1.

We tested several orientations of the isotropy plane with respect to the horizontal plane: isotropy plane parallel to  $xy$ -plane,  $xz$ -plane and  $45^\circ$  between both previous orientations, referring to notations of Figure 2.20.

We did not manage to have these test cases run, neither for the transverse isotropic case, not for the isotropic case. This means that the current issue is not linked to transverse isotropy and our latest developments. Several reasons can be invocated. First, the propagation of cracks on non-predefined path was the last developments of Bertrand Paul thesis [139] and were implemented in

the current version of the code at that time. But due to a problem of time, they were not fully integrated in the official version of the code (restitution in the official language of *Code\_Aster* implementation). As a consequence, further versions of the code did not account for this development on crack propagation on no-predefined paths. This means that for every new version of the code, we have to re-integrate the development on crack propagation. We did this task with the version of the code from which we made our developments and implementation regarding transverse isotropy. Nevertheless, it is possible that another change in the code that we did not identified so far, has an implication on the developments on crack propagation on non-predefined path and finally blocks our latest modelling. Another explanation may lie in the mesh and time discretization. Indeed, we could not consider the same mesh as Paul, notably because of a matter of computational resources. Our mesh might be too coarse, not refined enough to allow a fair detection of cohesive crack front. Unfortunately, we were not able to refine our mesh for computational reasons.

## Chapter 3

# Modeling fracture propagation in TI media using the BPM

Unlike continuum methods, discontinuum-based methods use a bottom-up methodology and discretize the solid body with discrete elements [94] (Figure 3.1). Discontinuum methods do not require special treatment for the formulation of elements near the discontinuities and can simulate complete detachment of material, which is difficult to obtain in continuum-based methods. Crack propagation criteria in discontinuum methods are based on a stress or strain level threshold value between the discrete elements as opposed to energy method or SIF method in continuum methods.

The discrete element method (DEM), which is one of such discontinuum methods often referred to as a particle based method, was originally developed to simulate the micromechanical behavior of granular materials [44]. With this approach, the micro structure of the material is modeled as a statistically generated assembly of rigid particles of varying diameters. The overall behavior of the simulated medium emerges from the contact laws defined between particles which are typically assigned normal and shear stiffnesses as well as a friction coefficient. An evolved version of the DEM was eventually introduced [45] which applies cohesive bonds between particles to simulate the behaviors of rocks. The resultant model is commonly referred to as the bonded particle model (BPM).

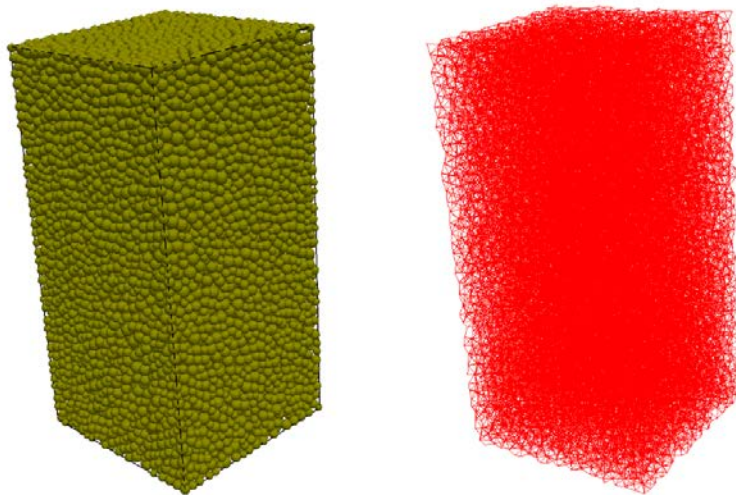


Figure 3.1: A BPM featured by its (left) randomly discretized particles and (right) inter-particle contact network.

In a BPM, crack nucleation is simulated through the breaking of inter-particle bonds while fracture propagation results from the coalescence of multiple bond breakages. Blocks of arbitrary shapes can form as a result of the simulated fracturing process and can subsequently interact with each other.

The computational cycle of BPM is based on an iterative procedure. In each computation cycle of duration  $\Delta t$ , Newton's  $2^{nd}$  law of motion is applied on each discrete element (DE) to obtain

its translational  $\ddot{\vec{x}}$  and angular  $\ddot{\vec{\omega}}$  accelerations whose  $k^{th}$  component ( $k = 1, 2, 3$  in 3D) are thus calculated as,

$$\begin{aligned}\ddot{x}_k &= \frac{F_k}{m} \\ \ddot{\omega}_k &= \frac{M_k}{J}\end{aligned}\quad (3.1)$$

with  $\vec{F}$  and  $\vec{M}$  the resultant force and torque applied on each DE and  $m$  and  $J$  their respective mass and moment of inertia.

The translational  $\dot{\vec{x}}$  and angular  $\dot{\vec{\omega}}$  velocities are then evaluated at time  $t + \Delta t/2$  using a second order centred difference scheme such that,

$$\begin{aligned}\dot{x}_k^{[t+\frac{\Delta t}{2}]} &= \dot{x}_k^{[t-\frac{\Delta t}{2}]} + \left(\ddot{x}_k^{[t]} + g_k\right)\Delta t \\ \dot{\omega}_k^{[t+\frac{\Delta t}{2}]} &= \dot{\omega}_k^{[t-\frac{\Delta t}{2}]} + \dot{\omega}^{[t]}\Delta t\end{aligned}\quad (3.2)$$

with  $\vec{g}$  the body force applied on the DE (*e.g.* gravity).

Finally, equations 3.2 is integrated over time and the final position of each particle at time  $t + \Delta t$  is calculated as,

$$x_k^{[t+\Delta t]} = x_k^{[t]} + \dot{x}_k^{[t+\frac{\Delta t}{2}]} \Delta t \quad (3.3)$$

BPM has proven to be an efficient modeling approach for crack propagation analysis in brittle materials [53, 99, 10] including rocks. For this reason, many recent works rely on BPM to study damage in rock and to reproduce experimental results such as acoustic emissions [80, 174] or constitutive behavior [181, 157]. DEM has also shown some promising results in reproducing the behavior of anisotropic rocks [55] as well as the failure mechanisms inherent to such media [51].

In the following, we have a look at the formulation of the BPM used for our study. Then we explain how we exploited this method in order to investigate fracture initiation and propagation in TI rocks.

## 3.1 A BPM for TI materials

### 3.1.1 Formulation

The behavior of the TI rock matrix is simulated using a BPM proposed by [157] implemented in the open source code YADE Open DEM [166]. The core of the model is to some extent similar to other BPMs [181, 144]. The rock material is represented by a dense polydisperse assembly of rigid and spherical particles bonded together and interacting following predefined contact laws. A major difference relies in the consideration, here, of near neighbor interactions through a controlled interaction range. This specific feature provides the possibility to adjust the degree of interlocking of the constitutive particles forming the numerical medium according to the relative microstructural complexity of the material to model.

Given the interaction range coefficient  $\gamma_{int}$  (Figure 3.2), bonds are created between particles of radius  $R_i$  if their respective interacting ranges defined by  $\gamma_{int}R_i$  overlap before the first time step of the simulation [54]. Interparticle bonds are created between pairs of particles for which the following condition is fulfilled:

$$D_{eq}^0 = \gamma_{int}(R_a + R_b) \quad (3.4)$$

with  $R_a$  and  $R_b$  the radii of the two particles  $a$  and  $b$ ,  $D_{eq}$  the initial distance between the two centroids of  $a$  and  $b$ , and  $\gamma_{int}$  a parameter of the model such that  $\gamma_{int} \geq 1$ . Following such concept, first proposed in [54], the average number of bonds per particle,  $N_b$ , can be increased by increasing  $\gamma_{int}$ . The approach provides a relatively simple yet effective alternative to the use of non spherical particles [38] or dedicated formulations proposed for instance by [145] or [52] to enhance particle interlocking and enables to simulate representative brittle rock behaviors characterized by high ratio of compressive to tensile strength and non linear failure envelopes.

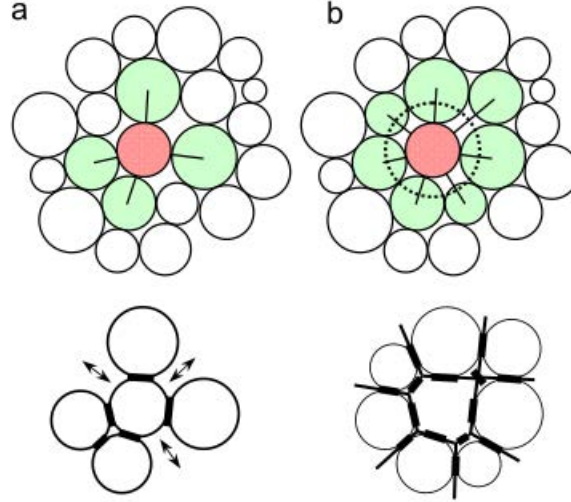


Figure 3.2: Illustration of the effect of the interaction range on the contact fabric and grain interlocking: (a)  $\gamma_{int} = 1$  and (b)  $\gamma_{int} > 1$ . After [157]

In addition to this microstructural feature, the behavior of the system is defined through the normal and shear forces developing between each pair of interacting particles.  $D_{ab}$  being the current value of the distance between the two centroids, the normal force  $F_n$  is computed from the normal relative displacement  $u_n = D_{eq}^0 - D_{ab}$  ( $u_n$  increases when spheres get closer to each other) such as:

$$F_n = k_n u_n \quad (3.5)$$

with  $k_n$  defined as:

$$k_n = 2Y \frac{R_a R_b}{R_a + R_b} \quad (3.6)$$

where  $R_a$  and  $R_b$  are the radii of the particles and  $Y$  is an equivalent elastic modulus (in Pa).

In compression,  $F_n$  is not restricted and can increase indefinitely. In tension,  $F_n$  can increase up to a threshold value  $F_n^{max}$  defined as (Figure 3.3a):

$$F_n^{max} = t A_{int} \quad (3.7)$$

with  $t$  the bond tensile strength (in Pa) and  $A_{int} = \pi \times \min(R_a, R_b)^2$  a surface related to the size of the particles. When the tensile strength of the bond is exceeded, a mode I (tensile) microcrack is generated, represented as a circular surface with an area equal to  $A_{int}$  and oriented perpendicularly to the branch vector joining a and b.

The shear force  $\vec{F}_s$  is computed in an incremental manner such as:

$$F_s^{(t)} = F_s^{(t-\Delta t)} + k_s \Delta u_s \quad (3.8)$$

with  $k_s$  the shear stiffness calculated from the second elastic parameter of the model,  $P$  (dimensionless) defined as:

$$k_s = P k_n \quad (3.9)$$

The shear force can increase up to a threshold value  $F_s^{max}$  defined by a Mohr-Coulomb type criterion (Figure 3.4):

$$F_s^{max} = c A_{int} + F_n \tan(\phi) \quad (3.10)$$

where  $\phi$  is the interparticle friction angle (in  $^\circ$ ) and  $c$  is the bond cohesion (in Pa). When the maximum shear force is exceeded, a mode II (shear) microcrack is generated, represented as a circular surface with an area equal to  $A_{int}$  and oriented perpendicularly to the branch vector joining a and b. If particles come into contact after a bond has broken, they interact in a purely frictional manner according to equations 3.5 and 3.8 (with  $t = c = 0$ ).

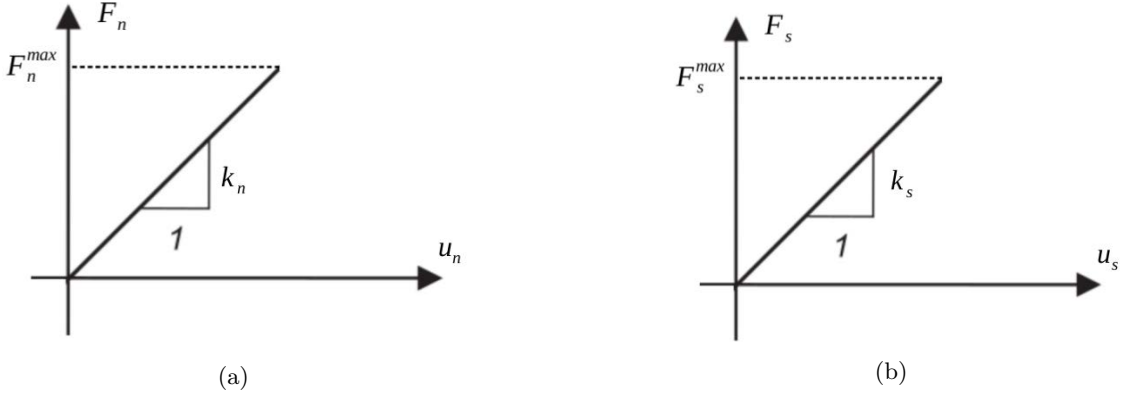


Figure 3.3: a) Interparticle law in tension, (redrawn after [157]) and b) Interparticle law in shear, (redrawn after [157]).

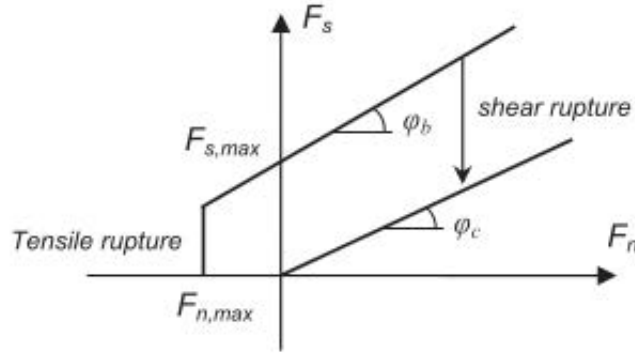


Figure 3.4: interparticle failure envelope, from [157].

In addition, a global non-viscous damping is used in the numerical scheme. The force  $F_d$  applied to each DE is computed from the resultant force  $F$  such as, such that:

$$\vec{F}^d = -\alpha \text{sign} \left( \sum \vec{F}^i(t) \cdot \left( \vec{v}^i(t) + \frac{dt}{2} \dot{\vec{a}}^i(t) \right) \right) \sum \vec{F}^i(t) \quad (3.11)$$

$\vec{F}^d$  depends on the damping parameter  $\alpha \in [0; 1]$ ,  $\alpha = 0$  corresponding to an undamped system and  $\alpha = 1$  to an static one. This damping method facilitates quasi-static simulations, by dissipating kinetic energy in the model. Note that energy dissipation also occurs in the model through sliding and brittle failure processes. Few authors present this global damping as an indirect modeling of other physical energy dissipation sources. Here, damping is considered only as a convenient numerical treatment that reduces computational costs, since it allows quasi-static conditions with higher loading rates [58]. Considering the damping coefficients used in literature such as  $\alpha = 0.7$  in [144] and  $\alpha = 0.4$  in [157] and  $\alpha = 0.2$  in [58], we fixed a damping of  $\alpha = 0.4$  in our work. This value was used for all the simulations performed in the present study and the loadings applied so as to ensure quasi-static responses of the models.

### 3.1.2 Introduction of TI

The BPM proposed by [157] has proven to be successful in reproducing the behavior of isotropic rocks. An enhanced version was proposed by [51] to model transversely isotropic rocks by introducing a dedicated textural component in the numerical medium. Following the approach developed by [55], a microstructural modification of the medium is operated by inserting weakness planes at the interparticle scale (Figure 4.2). These weakness planes are defined as contacts oriented



accordingly to the direction of the isotropy plane of the material (the bedding plane), and they are assigned mechanical properties that can be different from the ones making up the rock matrix. This modification of the microstructure is performed right after the creation of the bond network inside the numerical medium. The medium is generated using a classical growing technique applied to a cloud of particles randomly placed in the predefined volume. The particle assembly presents a uniform size distribution such that the maximum radius is equal to twice the minimum one so as to avoid any bias in the simulated behavior.

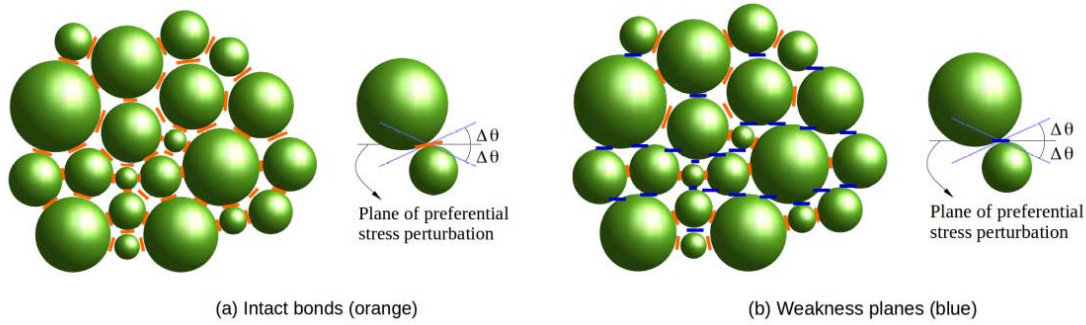


Figure 3.5: Introduction of transverse isotropy in the BPM: a) detection of the contacts dipping subparallel to the isotropy plane ( $\theta = 0^\circ$  here) according to the angle range  $\pm\Delta\theta$ , b) reorientation of the contacts along the direction of the isotropy plane.

Once the packing reaches the targeted density, bonds are created between each pair of interacting particles. At this stage, the numerical medium is isotropic. The procedure then consists in finding every interparticle contacts dipping subparallel to the isotropy plane and in replacing each one of them by a contact which orientation corresponds exactly to the direction of the isotropy plane. These reoriented contacts constitute the weakness planes. The weakness planes obey the joint contact logic introduced in [158], which was inspired by the smooth joint contact logic initially proposed by [121]. Essentially, the behavior of these weakness planes follows the contact laws defined for the bonds making up the rock matrix (Sect. 3.1.1). The only difference lies in the possibility to reorient these contacts following a predefined direction and to include local dilatancy when sliding occurs between the interacting particles such that the normal force is updated according to

$$F_n = k_n(D + \Delta u_n \tan(\psi)) \quad (3.12)$$

with  $\psi$  the interparticle dilatancy angle (in  $^\circ$ ). In addition, the properties ( $k_n$ ,  $k_s$ ,  $t$ ,  $c$ , and  $\phi$ ) of these weakness planes can be assigned different properties from the bonds making the medium.

The amount of weakness planes introduced inside the medium is controlled by the angle range  $\Delta\theta$  which defines the amount of bonds that are replaced by joint contacts. Polar representations of the contact normal ( $n$ ) orientation distribution are presented in Figure 3.6 for different values of  $\Delta\theta$ .  $\Delta\theta = 0^\circ$  corresponds to the case where no weakness planes are introduced in the medium and thus corresponds to an isotropic medium. When  $\Delta\theta > 0^\circ$ , a certain amount of bonds are replaced by weakness planes oriented accordingly to the isotropy plane ( $\theta = 0^\circ$  in this case). For instance, for  $\Delta\theta = 0^\circ$ , 6.4% of the contacts are identified as weakness planes and are thus reoriented accordingly to the isotropy plane. When  $\theta = 30^\circ$ , 13.75% of the contacts are weakness planes, whereas when  $\theta = 40^\circ$ , 23.9% of the contacts are weakness planes.  $\Delta\theta$  and the weakness planes properties are thus directly related to the degree of anisotropy of the medium [51].

## 3.2 Calibration of the model

For isotropic BPM, as discussed in [157], each interparticle parameter can be related to a given macroscopic property. For instance, for a given coordination number  $N_b$  (its value directly influences the UCS/UTS ratio and the shape of the failure envelope) [51]:

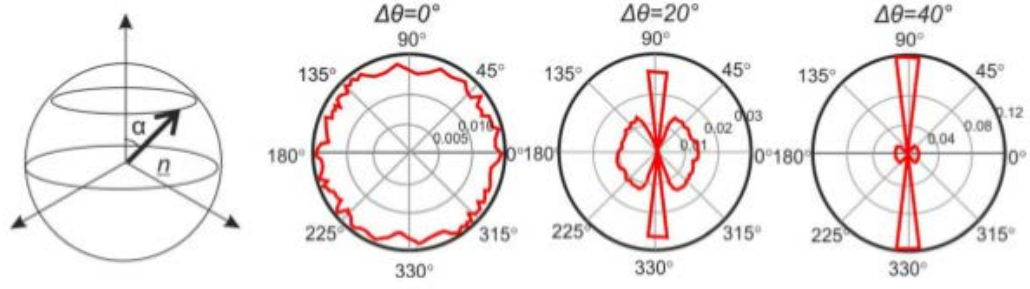


Figure 3.6: Polar representation of the contact orientation distribution of the numerical samples in the  $\alpha$  plane for different values of the angle range  $\Delta\theta$  (for the case where the bedding is horizontal, *i.e.*  $\theta = 0^\circ$ ).  $n$  is the branch vector linking the center of each pair of interacting particle.

- the elastic modulus  $Y$ , which defines the value of the contact normal stiffness  $k_n$ , has to be chosen in accordance with the Young's modulus  $E$ ;
- the constant  $P$ , which defines the value of the contact tangential stiffness  $k_s$ , has to be chosen in accordance with the Poisson's ratio  $\nu$ ;
- the local tensile strength  $t$  has to be chosen in accordance with the uniaxial tensile strength UTS and
- the local cohesion  $c$  and local friction angle  $\phi$  have to be chosen in order to match the failure envelope of the simulated material (including the UCS/UTS ratio). At this stage, if the failure envelope of the numerical model does not match the experimental one, the calibration procedure has to be performed again with a different value of  $N_b$ .

Obviously additional attention has to be paid for transversely isotropic BPM since they present different properties depending on their orientation with respect to the loading. First, a preliminary calibration should be performed without including the weakness planes into the model in order to obtain a behavior similar to the behavior of the transversely isotropic material loaded in the direction parallel to its bedding (configuration for which the behavior is the least affected by the bedding). Then, the weakness planes can be introduced. Because they directly modify the microstructure of the numerical medium, the amount of weakness planes controls the degree of its anisotropy. The determination of the angle range  $\Delta\theta$  defining the amount of weakness planes (see section 3.1.2) as well as the calibration of their local properties must thus be done considering the evolution of both elastic and strength properties with respect to the orientation of the material  $\theta$ . Since the weakness planes are considered as elastic-frictional interfaces here, the macroscopic behavior of the system is affected by their number *i.e.*  $\Delta\theta$ , stiffness *i.e.*  $Y^{wp}$  and frictional properties *i.e.*  $\phi^{wp}$ .

The influence of  $\Delta\theta$  on the evolution of elastic and strength properties as a function of  $\theta$  is noticeable. For instance, if a similar strength anisotropy can be obtained with different values of  $\Delta\theta$ , the corresponding elastic anisotropy is more or less pronounced depending on  $\Delta\theta$  (Figure 3.7a). In addition, for a given value of  $\Delta\theta$ , modifying  $Y^{wp}$  will affect both the elastic and the strength anisotropy (Figure 3.7b). Indeed, for a given value of  $\Delta\theta$ , the strength of the sample loaded perpendicular to its bedding ( $\theta = 0^\circ$ ) tends to decrease when  $Y^{wp}$  decreases. As a consequence, for a given amount of weakness planes, there is a minimum value of  $Y^{wp}$  below which the evolution of the strength as a function of  $\theta$  does not present the  $V$  shape usually reported in the literature for anisotropic rocks. To sum up, the pair  $\{\Delta\theta, Y^{wp}\}$  directly influences the evolution of both  $E$  and UCS as a function of  $\theta$ , and only the right combination of these two parameters can lead to the desired macroscopic behavior. The calibration procedure must thus encompass a systematic parametric study on these two parameters to make sure that both the evolutions of  $E$  and UCS as functions of  $\theta$  correspond to the targeted ones. Moreover, the frictional properties of the weakness

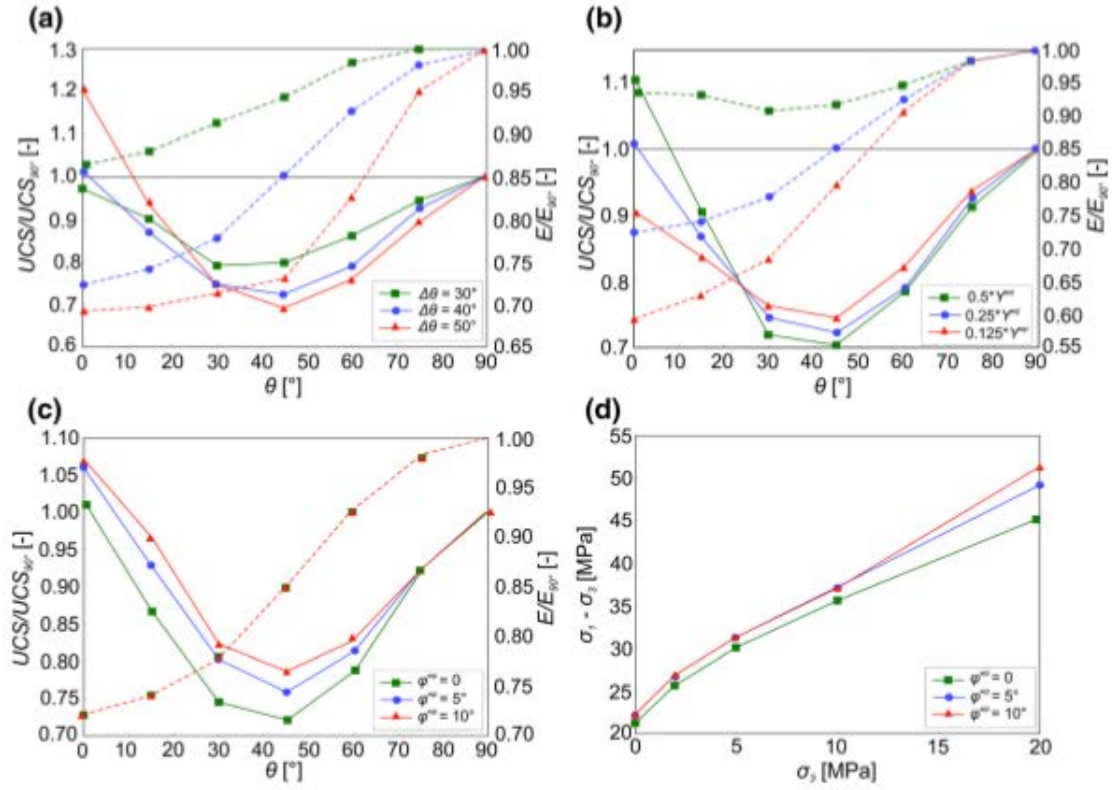


Figure 3.7: Influence of the amount and properties of the weakness planes on the macroscopic properties of the simulated medium. Effect of a) amount ( $\Delta\theta$ ), b) stiffness ( $Y^{wp}$ ), and c) friction angle ( $\psi^{wp}$ ) of the weakness planes on the evolution of the axial elastic modulus  $E$  (dashed lines) and UCS (solid lines) as a function of the material orientation with respect to the loading direction ( $\theta$ ). d) Effect of  $\psi^{wp}$  on the simulated failure envelope for the case where  $\theta = 0^\circ$  [51].

planes ( $\phi^{wp}$ ) have a slight influence on the evolution of the UCS as a function of  $\theta$  (Figure 3.7c) but needs to be chosen carefully as it may affect the failure envelope (Figure 3.7d).

### 3.2.1 Reference behaviors

In order to verify the capability of our BPM in simulating the mechanical behavior of transversely isotropic rocks, we confront its predictions with experimental results discussed in literature. For this purpose, the BPM was calibrated so that its properties are representative of the Callovo-Oxfordian (COx) claystone and of Tournemire shale respectively. Both rocks show transverse isotropic characteristic but Tournemire shale exhibits a more pronounced anisotropy than COx claystone.

#### Mechanical responses

To simulate triaxial compression tests, the loading is applied on the numerical samples ( $1 \times 2 \times 1$  model units) through six rigid frictionless walls (Figure 3.8). Once the relevant confining stress is reached, the top and bottom walls are moved vertically at a constant strain rate while the confining stress is controlled by adjusting the lateral walls positions during the simulation.

In this section we give a comparison between numerical and laboratory results. The elastic properties and failure envelopes of the calibrated BPM are compared with the experimental data.

– *Tournemire shale*

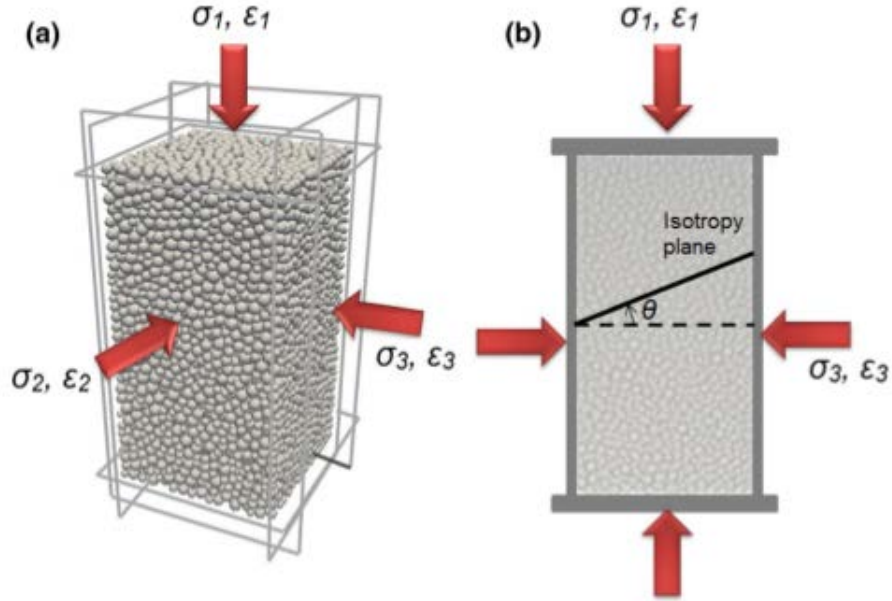


Figure 3.8: a) Triaxial compressive test configuration and b) definition of the isotropy plane orientation ( $\theta$ ) with respect to the loading [51].

We calibrated the BPM so as to reproduce a behavior representative of Tournemire shale which has been characterized in several studies [22, 134].

As illustrated in Figure 3.9a, the numerically predicted evolution of  $E$  as a function of  $\theta$  (the angle between the loading direction and the normal to the plane of isotropy) is in good qualitative agreement with experimental observations obtained by [22] on Tournemire shale rocks. [22] observed the value of 4 GPa as the apparent Young modulus for  $\theta = 0^\circ$  and the value of 10.4 GPa as the apparent Young modulus for  $\theta = 90^\circ$ . The maximum deviatoric stress is  $q_{max} = \sigma_{1Max} - \sigma_3$ , and the mean stress reads as  $p = \sigma_{1Max} + 2 \times \sigma_3$  for  $\sigma_3 = 0.1, 5, 10, 20, 40, 80$  [MPa]. The failure envelopes obtained for 3 different orientations of  $0^\circ, 45^\circ, 90^\circ$  are plotted in Figure 3.9b. There is a good agreement between numerical and experimental results. For  $\theta = 45^\circ$  the failure envelope obtained with the BPM does not match exactly the one obtained experimentally, although the trends are similar. The set of parameters resulting from the calibration are given in Table 3.1.

Parameters	Matrix	Weakness plane
Coordination number (-)	$N_b = 10$	-
Elastic modulus ([Pa])	$Y_m = 16e9$	$0.2Y_m$
Stiffness ratio ([-])	$P_m = 0.3$	$P_{wp} = 1$
Tensile strength ([Pa])	$t_m = 14e6$	$t_{wp} = 0$
Cohesion ([Pa])	$c_m = 32e6$	$c_{wp} = 0$
Friction angle ( $^\circ$ )	$\phi_{c,m} = 2$	$\phi_{c,wp} = 0$
Dilation angle ( $^\circ$ )	$\phi_{r,m} = 0$	$\phi_{r,wp} = 0$
Angle range ( $^\circ$ )	-	$\Delta\theta = 55^\circ$

Table 3.1: Microparameters of the calibrated BPM for Tournemire shale.

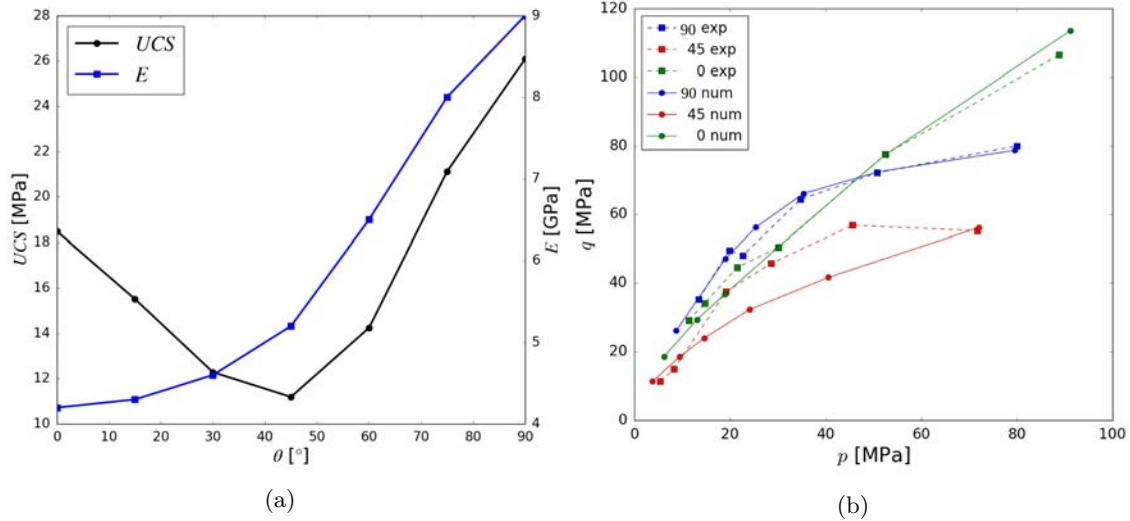


Figure 3.9: a) Influence of the direction of loading with respect to the material orientation on a the uniaxial compressive strength (UCS) and axial elastic modulus ( $E$ ) of the calibrated BPM for Tournemire shale and b) Comparison between numerical and experimental failure envelopes of Tournemire shale rock at different orientations.

– *Callovo-Oxfordian (COx) claystone*

In addition, we calibrated the BPM to the COx claystone which presents the particularity to be less anisotropic than Tournemire shale. Following the reference documents of Andra [5, 6], the ratio  $E_{90^\circ}/E_{0^\circ}$  of the axial elastic moduli, respectively, parallel ( $\theta = 0^\circ$ ) and perpendicular ( $\theta = 90^\circ$ ) to the bedding plane ranges from 1.05 to 1.4, with an average value  $E_{90^\circ}/E_{0^\circ} = 1.35$  [51]. As illustrated in Figure 3.10a, the numerically predicted evolution of  $E$  as a function of  $\theta$  is in good qualitative agreement with experimental observations obtained on argillaceous sedimentary rocks [134, 39]. Regarding the anisotropy of strength of the COx claystone, very few experimental data are available in the literature. In our study, the model is calibrated so that its minimum strength corresponds to the case where the loading is applied at  $45^\circ$  with respect to the bedding. The value obtained with the calibrated BPM matches the value of UCS observed by [8] in laboratory i.e.  $UCS = 21 \pm 6.8$  for  $\theta = 0^\circ$ . As shown in Figure 3.10b, the failure envelope predicted by the anisotropic BPM for the case where  $\theta = 0^\circ$  perfectly matches with the generalized Hoek-Brown failure criterion that was fitted to the experimental data by [8]. The set of parameters resulting from the calibration are given in Table 3.2.

Parameters	Matrix	Weakness plane
Coordination number (-)	$N_b = 8$	-
Elastic modulus ([Pa])	$Y_m = 18e9$	$4Y_m$
Stiffness ratio ([-])	$P_m = 0.3$	$P_{wp} = 1$
Tensile strength ([Pa])	$t_m = 16e6$	$t_{wp} = 0$
Cohesion ([Pa])	$c_m = 16e6$	$c_{wp} = 0$
Friction angle (°)	$\phi_{c,m} = 12$	$\phi_{c,wp} = 2$
Dilation angle (°)	$\phi_{r,m} = 0$	$\phi_{r,wp} = 0$
Angle range (°)	-	$\Delta\theta = 40^\circ$

Table 3.2: Microparameters of the calibrated BPM for COx claystone.

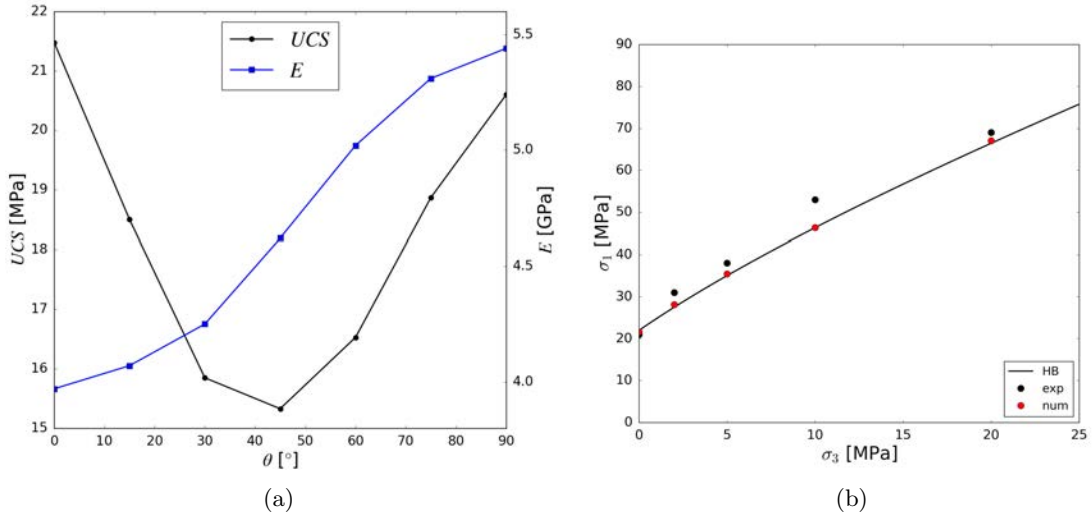


Figure 3.10: a) Influence of the direction of loading with respect to the material orientation on the uniaxial compressive strength (UCS) and axial elastic modulus (E) of the calibrated BPM for COx claystone. and b) Failure envelope of the COx claystone ( $\theta = 0^\circ$ ): comparison between the Hoek-Brown failure criterion provided in [8], the experimental data from [7] and the BPM predictions.

### Failure patterns

#### – *Tournemire shale*

Figure 3.11 (down row), shows strain field (deviatoric strain) at the end of the simulation for different confining pressures equal to: 20 MPa and three different orientation angles  $\theta = 0^\circ$ ,  $45^\circ$ ,  $90^\circ$ . For confining pressure of 20 MPa the predicted failure patterns by BPM are in good agreement with the experimental observations made by [22] on Tournemire shale as shown in Figure 3.11 (top row). For all the samples with different orientations it can be seen that the fracture occurs in a diagonal way and bisects the sample.

#### – *Callovo-Oxfordian (COx) claystone*

Because experimental evidences of failure processes taking place in the COx claystone were obtained from plane-strain biaxial compressive tests, we first performed simulations considering the exact same configuration. The difference of these tests from the triaxial tests presented in Sect. 3 is that the sample dimensions are  $1 \times 2 \times 0.1$  model units and that the strain component is fixed equal to zero through the z direction. Practically, the two walls located at the front and at the back of the sample (Z direction) are kept fixed during the simulation so that the out-of-plane deformation is avoided, hence ensuring the plane-strain conditions. The stress-strain response as well as the strain localization pattern obtained with the anisotropic BPM is compared in Figure 3.12 to the experimental observations done by [13] for a confining stress equal to 2 MPa and  $\theta = 0^\circ$ .

As one can see, the model's prediction is qualitatively in very good agreement with the experimental observations in terms of mechanical response and shear banding. The shear band emerges as a result of strain softening without any introduction of dedicated flaw within the numerical medium as opposed to what is commonly done with continuous approaches.

### Anisotropy of Tournemire shale and COx claystone

The anisotropy in Tournemire shale is more pronounced compared to COx claystone (Figure 3.13a). The ratio  $E_{90}/E_0$  is equal to 2.14 and 1.37 for Tournemire shale and COx respectively, while their pertaining ratio of  $UCS_{max}/UCS_{min}$  is 2.33 and 1.40 consecutively.

Overall for both rock types, the Young's modulus  $E$ , increases when  $\theta$  increases from  $0^\circ$  to  $90^\circ$  (Figure 3.13). This results from the fact that, for  $\theta = 90^\circ$ , the weakness planes representing the

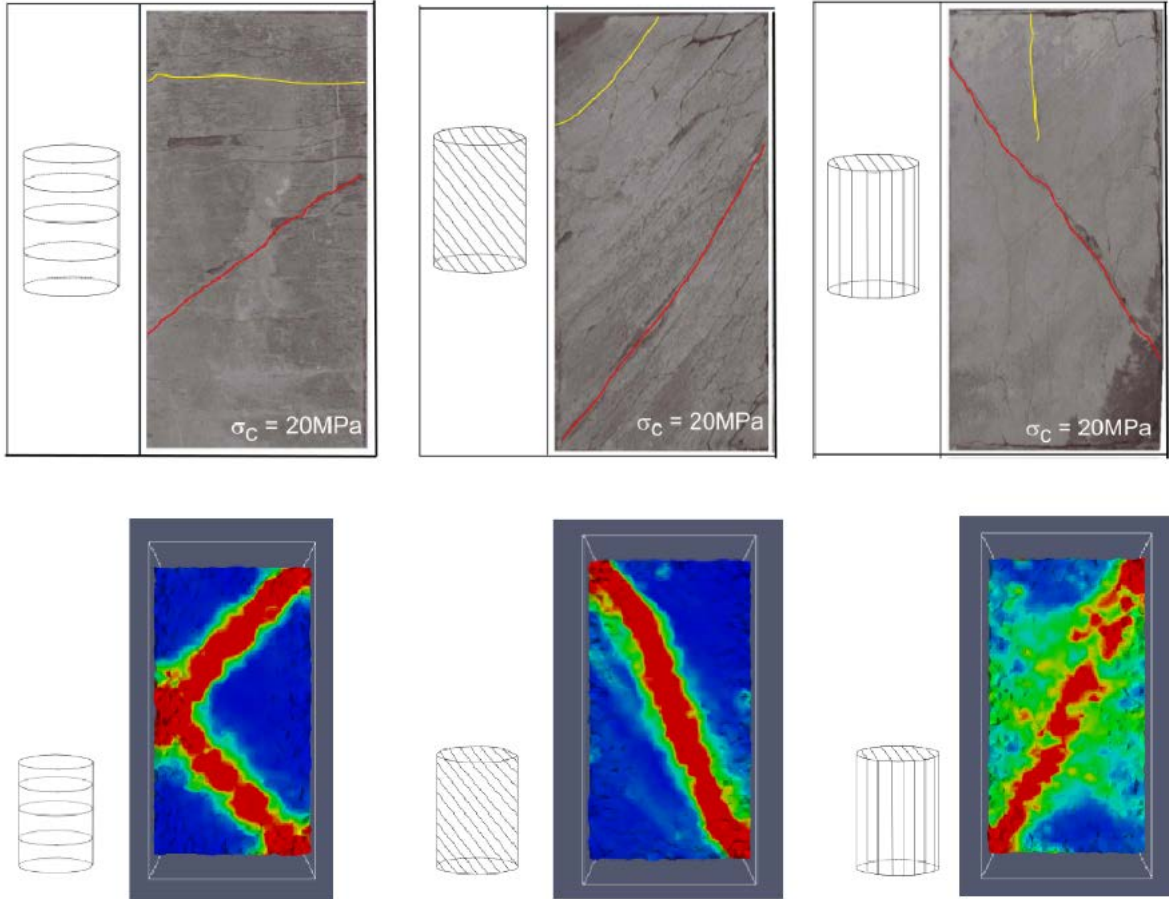


Figure 3.11: top row) Failure patterns observed by [22] on Tournemire shale samples subjected to triaxial compressive tests performed under 20 MPa with different orientations. down row) Failure patterns obtained from BPM on Tournemire shale samples subjected to triaxial compressive tests performed under 20 MPa with different orientations.

beddings are parallel to the loading direction and thus have a limited effect on the distribution of the maximum principal stress inside the medium. The increase of  $E$  as a function of  $\theta$  tends to be monotonic for both Tournemire shale and COx claystone. An experimental observation has been made by [22] and [8] showing the importance of bedding orientation on the brittle strength. Concerning the strength of Tournemire shale and COx claystone we can observe a minimum strength for both rock at  $\theta = 45^\circ$  (Figure 3.13b) as it is commonly observed in non laminated transversely isotropic rocks. In the case of COx claystone the strength at  $\theta = 0^\circ$  and  $\theta = 90^\circ$  are similar. This is slightly different for Tournemire shale.

### 3.3 Fracture propagation

The proposed BPM has been successfully utilized to simulate the initiation and propagation of fractures in isotropic rocks at different scales and under different loading conditions [158, 75, 58]. We focus here on the propagation of mode I fracture in order to investigate the influence of TI on such a critical process. The discontinuity representing a pre-existing fracture in the sample is introduced in the medium in the form of a closed flaw. Closed flaws can be simulated in BPM by removing the cohesive feature of all interactions located along the flaw surface as proposed by [144, 182, 107]. This is different compared to the open flaw approach where the fracture is simulated by removing the particles (see Figure 3.14).

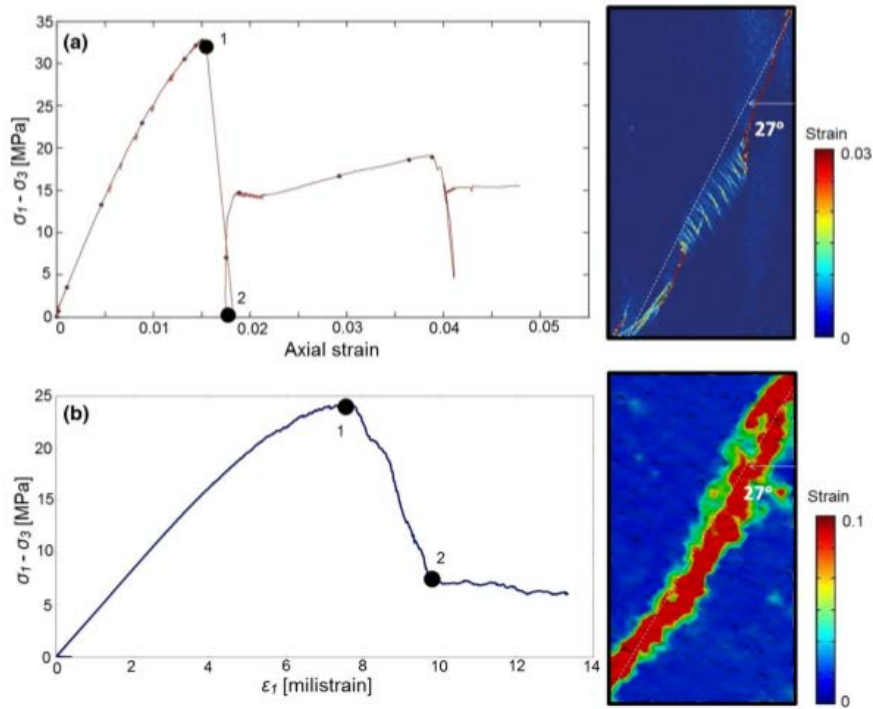


Figure 3.12: Shear banding observed during a biaxial compression test performed under a confining stress of 2 MPa and for  $\theta = 0^\circ$ : a) incremental deviatoric (shear) strain field measured experimentally (between 1 and 2) through digital image correlation ([13] modified from [49]), b) incremental deviatoric (shear) strain field computed (between 1 and 2) in the BPM simulations.

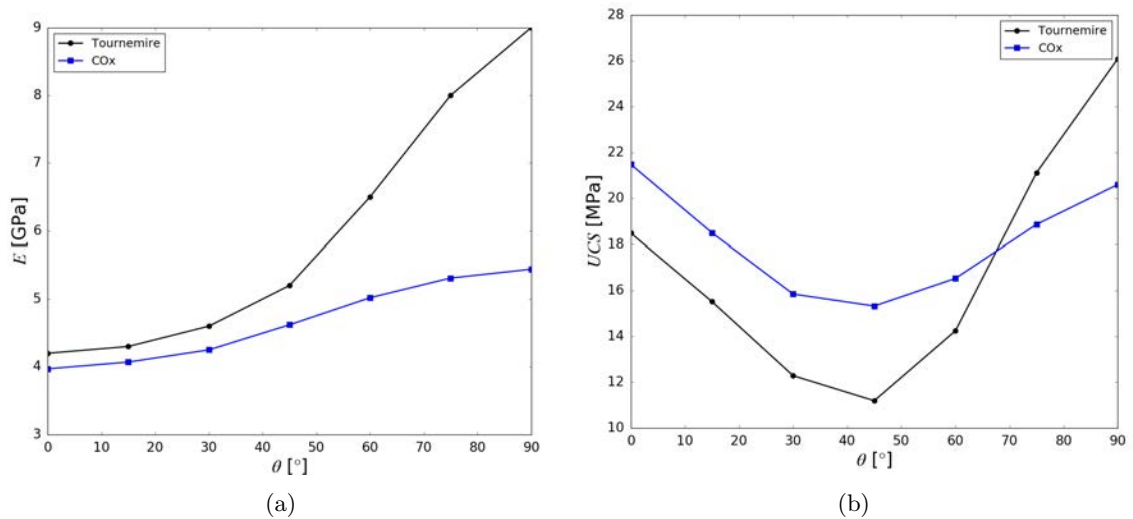


Figure 3.13: Variations of a) Young's modulus ( $E$ ) and b) uniaxial compressive strength (UCS) as functions of bedding orientation with respect to the loading direction  $\theta$ , for both COx and Tournemire shale.

The study is performed on samples of  $1 \times 2 \times 0.5 \text{ m}^3$  containing an edge through thickness crack of length 0.3 m (see Figure 3.15a). This pre-existing crack has no initial aperture and can thus be considered as a closed purely frictional fracture. Zones of high strength are defined at both ends of the sample to avoid boundary effects during the loading. In addition, in order to ensure plane strain condition, the translation of the particles in the out of plane direction (Z), as well as their rotations around the X and Y axes are blocked to force the model to behave as a pseudo 2D model.



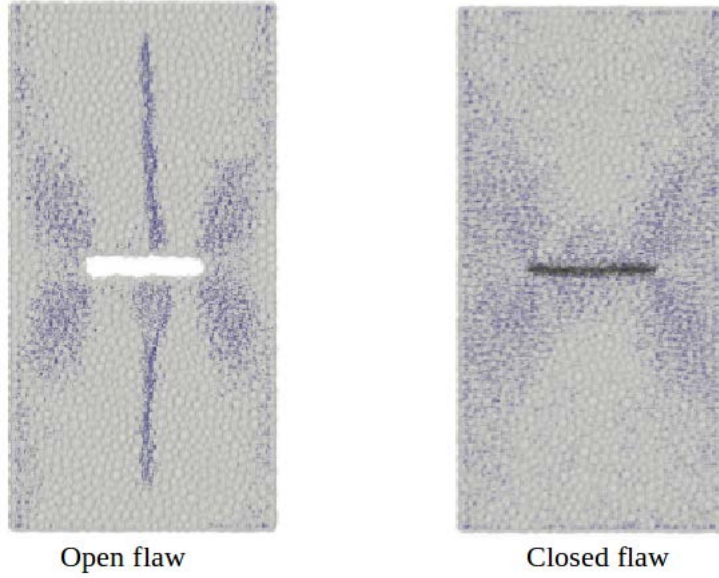


Figure 3.14: Crack propagation patterns by BPM from Open (left) and closed (right) flaws, in open flaw the discontinuity is created by removing the particles located at the vicinity of crack and in closed flaw the discontinuity is created by removing the interparticle cohesive bonds along the crack surface. blue dots correspond to broken interparticle bonds locations. from [58].

We chose to use such a configuration rather than a 3D sample with a finite thickness to eliminate the influence of the third dimension on the emergent properties of the simulated medium as well as to optimize the computational effort.

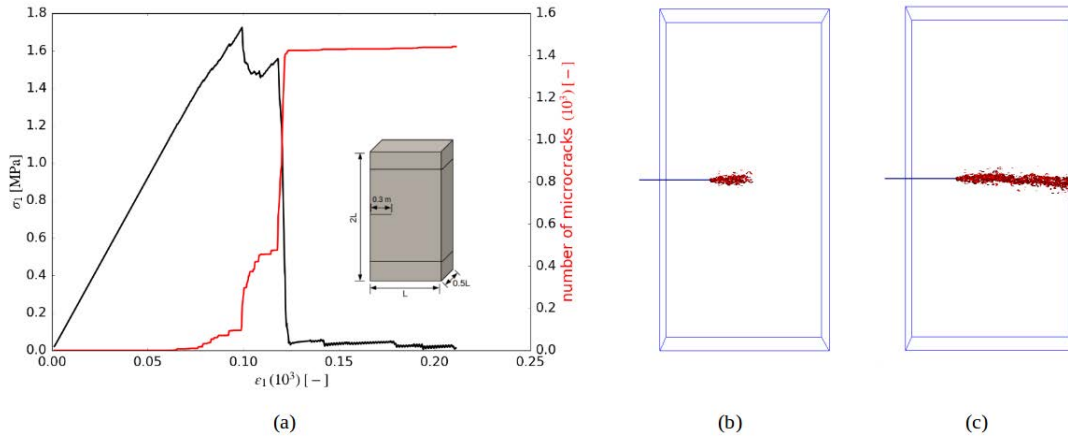


Figure 3.15: Uniaxial tensile test simulation on an edge cracked isotropic sample: a) stress-strain response and spatio-temporal distribution of induced microcracks b) before the stress peak and c) after the stress peak.

### 3.3.1 Homogeneous/isotropic material

In this section, we first present several numerical results intended to emphasize the capability of BPM to simulate representative isotropic rock behaviors focusing more particularly on uniaxial tensile loading conditions, causing mode I fracture propagation.

As shown in Figure 3.15, the simulated behavior corresponds to the behavior expected for a quasi-brittle material with, first, an elastic response and, second, the appearance of microcracks

at the crack tips before the complete rupture of the sample. Material failure corresponds to the propagation of a fracture aligned with the initial flaw. The fracture initiates from stress concentration in the vicinity of the crack tips associated to the generation of a process zone, and propagates along the direction of the minimum principal stress, as expected from classic fracture mechanics.

### Assessment of the BPM with respect to LEFM

As mentioned in section 1.2.2 stress intensity factors (SIFs) are the means by which LEFM evaluates the stress state of a cracked material. One of the most prominent methods to calculate SIFs numerically relies on the J-integral introduced by [149]. An alternative consists in using the displacement extrapolation method proposed by [108] which evaluates the apparent SIFs from the relative displacements of the crack lips. For instance, in the case of mode I loading, the apparent mode I SIF ( $K_I^*$ ) at the crack tip can be extrapolated from the local  $K_{I,i}^*$  calculated from the local normal displacements  $u_{n,i}$  along the crack lips through the following equation given by [32]:

$$K_{I,i}^* = \frac{E}{4(1-\nu^2)} \sqrt{\frac{2\pi}{r}} u_{n,i} \quad (3.13)$$

where  $r$  corresponds to the distance from the crack tip,  $E$  is the Young's modulus of the material and  $\nu$  its Poisson's ratio.

We applied the displacement extrapolation method to our case (Figure 3.15) and there is a good match between the value obtained from the displacement method and the value obtained from the theoretical expression given by:

$$K_I = \sigma \sqrt{\pi a} \left[ 1.122 - 0.231 \left(\frac{a}{b}\right) + 10.55 \left(\frac{a}{b}\right)^2 - 21.71 \left(\frac{a}{b}\right)^3 + 30.382 \left(\frac{a}{b}\right)^4 \right] \quad (3.14)$$

where a sample with dimensions of  $2h \times b$  with an edge crack of length  $a$  is concerned.  $2h$  being the height,  $b$  being the width of the sample.

The same approach was also adopted and verified by [127] for a centered through thickness cracked model (see Appendix A).

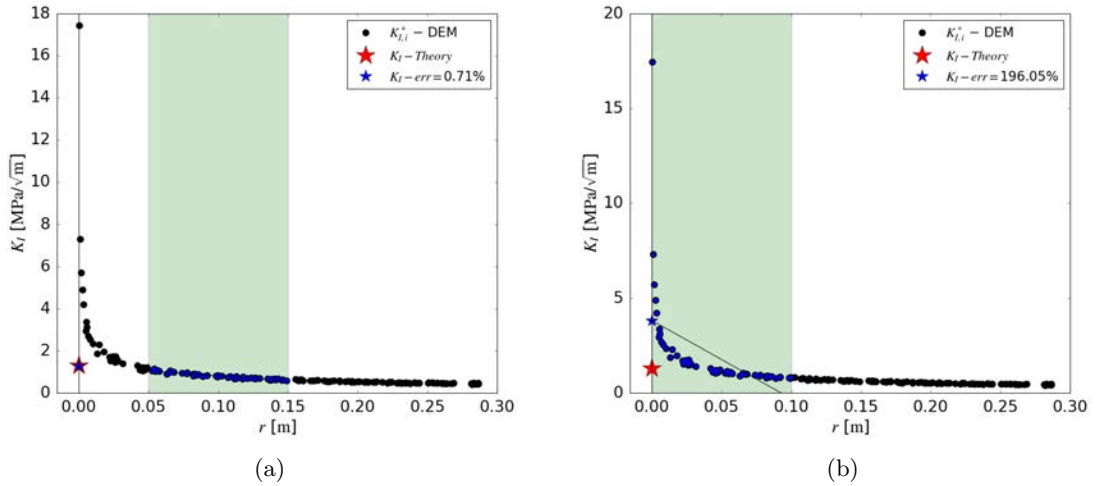


Figure 3.16: Assessment of the BPM predictions with respect to LEFM: (tensile loading of a edge through thickness cracked plate at  $\sigma = 1 \text{ MPa}$ , stress intensity factor computed from the particles displacement (the shaded area illustrates the mean diameter of the particle) a) neglecting the particles to close to the crack tip, b) considering particles close to the crack tip. The theoretical value from equation 3.14 is plotted on the graph for comparison purpose.

The value of the SIF calculated using the displacement extrapolation method (Figure 3.16) is in very good agreement with the value computed from the boundary stress, confirming therefore the

relevance of the BPM with respect to LEFM concepts. One has to mention that the extrapolation of  $K_I^*$  from the local  $K_{I,i}^*$  must follow certain rules to be efficient. For instance, the set of particles used for the extrapolation must be chosen carefully as discussed in a recent study where the displacement extrapolation method was applied to compute SIFs in a lattice model [34]. In particular, these particles must be located sufficiently far from the tip of the crack to avoid the effect of stress singularity in the evaluation of  $K_{I,i}^*$  and, at the same time, they must be located far enough from the middle of the crack so as to limit the influence of the change in curvature of the crack lips. As it is illustrated in Figure 3.16a, by considering the particles with coordinate  $r \in \{\frac{a}{6}, \frac{3a}{6}\}$  indicated by the shaded area, the resulting  $K_I^*$  is in a good agreement with the theoretical SIF, showing an error of 0.71%, while by considering the particles too close to the crack tip with coordinate  $r \in \{0, \frac{a}{3}\}$  the SIF shows an error of 196.05% with respect to the theoretical value.

### 3.3.2 TI medium

In this section, we investigate the influence of TI on mode I fracture propagation by performing tests on BPM calibrated to Tournemire shale and COx claystone. In transversely isotropic media, three principal crack orientations with respect to the isotropy (bedding) plane, are known as Divider, Short Transverse, and Arrester, respectively, as illustrated in Figure 3.17. In the Divider orientation, the crack plane is normal to the isotropy (bedding) plane. In the Short Transverse orientation both the crack plane and the crack propagation direction are parallel to the isotropy plane. Finally, in the Arrester orientation, the crack plane normal to the isotropy plane. For a horizontally bedded material, the Divider, Short Transverse, and Arrester orientations correspond respectively to a vertically oriented fracture propagating horizontally, a horizontal fracture propagating horizontally, and a vertically propagating fracture [33].

In this section, we present simulations intended to gain some insights into the propagation of mode I fractures in TI rocks by considering the aforementioned 3 configurations. In an attempt to ensure the representativity of our results, we considered models calibrated to both COx claystone and Tournemire shale which present different degrees of anisotropy (see section 3.2).

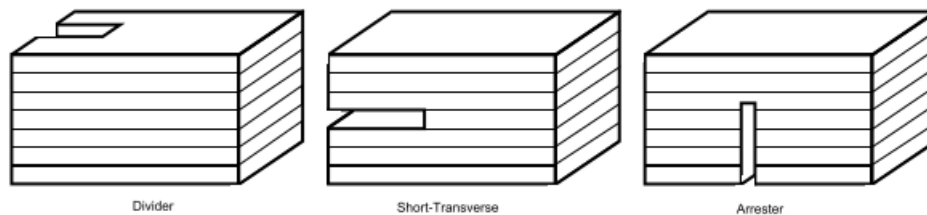


Figure 3.17: The three principal crack-plane orientations relative to bedding in transversely isotropic materials: Divider, Short Transverse, and Arrester. After [33].

The stress-strain responses corresponding to each configuration are illustrated in Figure 3.18. It is clear from the figure that the short transverse configuration provide a lower strength while the two others show similar strengths. Interestingly, the stress-strain responses present slightly different characteristics, the divider configuration showing a more brittle behavior than the arrester.

The fracture propagation in both COx claystone and Tournemire shale are shown in Figures 3.19 and 3.20. For both rocks, the fracturing process initiates at the crack tip and propagates along the initial crack direction until the ultimate failure of the model. Despite the more anisotropic characteristic of Tournemire shale compared to COx claystone, the failure patterns for both rocks are quite similar. It seems that failure takes more time in the Tournemire shale as if it exhibits less brittleness, suggesting more branching than in the COx claystone. This would make sense given the denser network of weakness planes in the shale. For the Arrester configuration, the failure pattern seems to be different from the other two configuration as it deviates from the initial crack direction. The fracture path is more straight and localized for the divider configuration. We observe cracks far from the fracture for the short transverse configuration.

We carried out BPM simulations on both COx claystone and Tournemire shale, considering different orientations of the bedding with respect to the loading ranging from  $\theta = 15^\circ$  to  $\theta = 75^\circ$

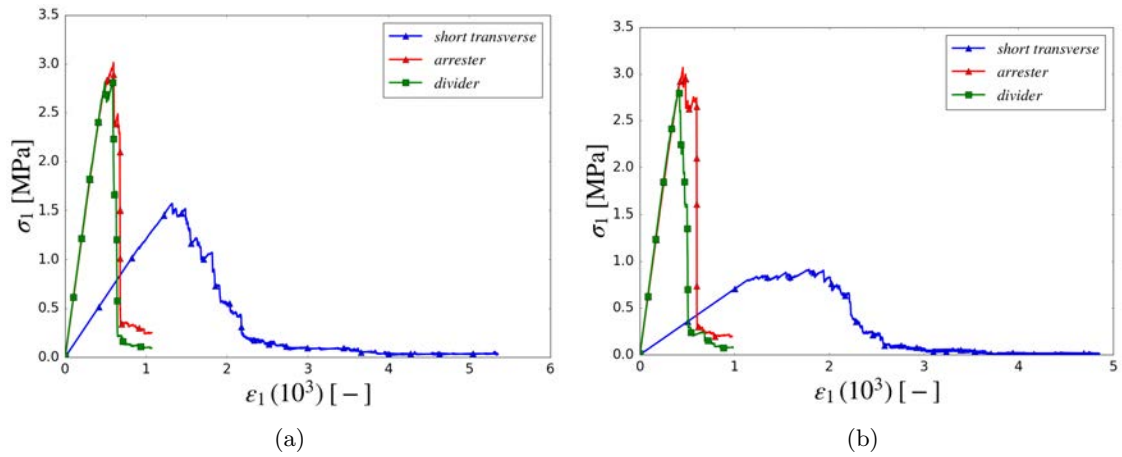


Figure 3.18: Stress-strain responses (uniaxial tension) of 3 edge cracked samples subjected to tensile loading considering, Divider, short transverse and arrester configurations for a) *COx* claystone. and b) Tournemire shale.

(Figures 3.21 to 3.24). It can be observed that bedding angles higher than  $\theta = 15^\circ$  causes the deflection of propagating fracture for both materials. For  $\theta = 15^\circ$ , the fracture path is horizontal and aligned with the pre-existing crack. For  $\theta > 15^\circ$  the failure doesn't seem to be necessarily affected by the change in bedding orientation. The same observation can be made for Tournemire shale (Figure 3.24).

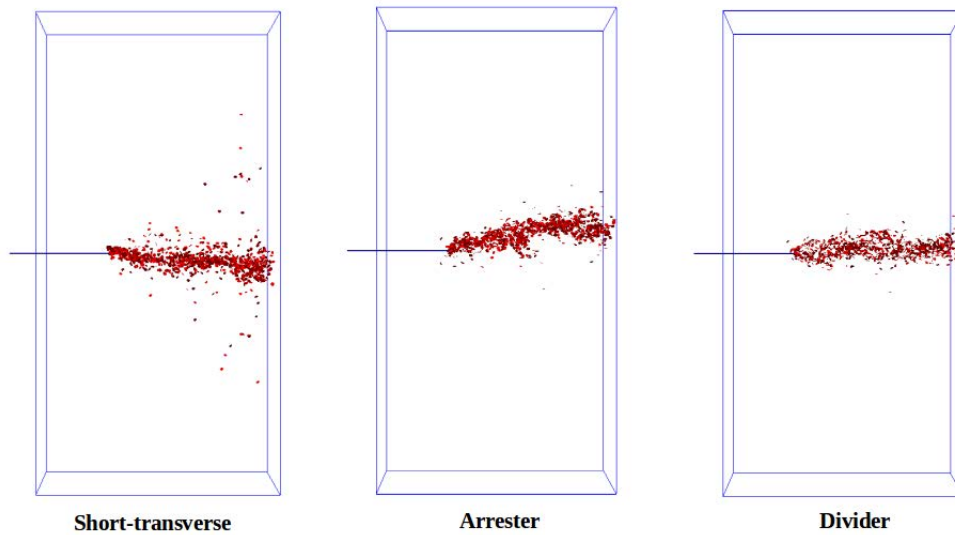


Figure 3.19: Fracture propagation in *COx* claystone samples (Divider, Short Transverse, and Arrester) containing an edge notch.

The associated stress-strain responses are presented in Figures 3.22 and 3.23. As expected, the strength (toughness) of the material increases when the beddings tend toward a parallel direction with respect to the loading. For the COx claystone, the toughness as a function of bedding orientation shows a monotonous evolution in general. Although from the bedding angle of  $\theta = 75^\circ$  to  $\theta = 90^\circ$  (Figure 3.22b) a drop can be seen. For Tournemire shale, the nonlinearity of the evolution of toughness as a function of bedding angle is more pronounced (Figure 3.23b). Concerning the fracture toughness  $K_{Ic}$  for both materials the same qualitative trend can be seen, this trend is very similar to the trends observed experimentally for the uniaxial tensile strength.  $K_{Ic}$  is minimum for  $\theta = 15^\circ$  and increases quasi-monotonously with  $\theta$  to reach its maximum value for  $\theta = 75^\circ$ . Considering that both COx claystone and Tournemire shale are anisotropic rocks we can have a comparison between their degrees of anisotropy by having a look at the ratio of  $K_{Ic90^\circ}/K_{Ic0^\circ}$ . This ratio is 1.92 and 3.37 for COx and Tournemire respectively.

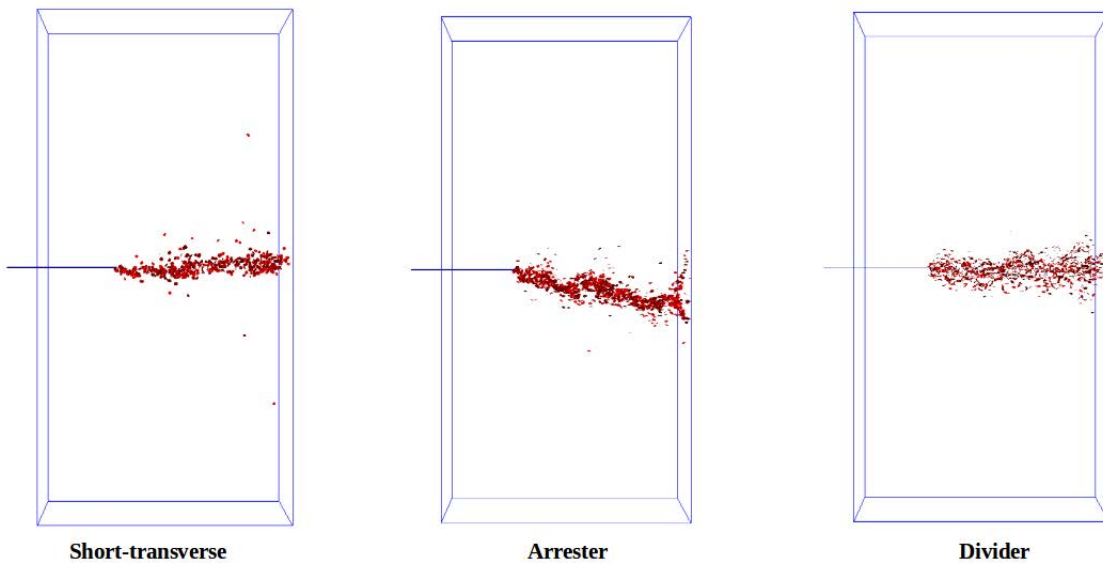


Figure 3.20: Fracture propagation for three configurations of Tournemire shale (Divider, Short Transverse, and Arrester) containing an edge notch.

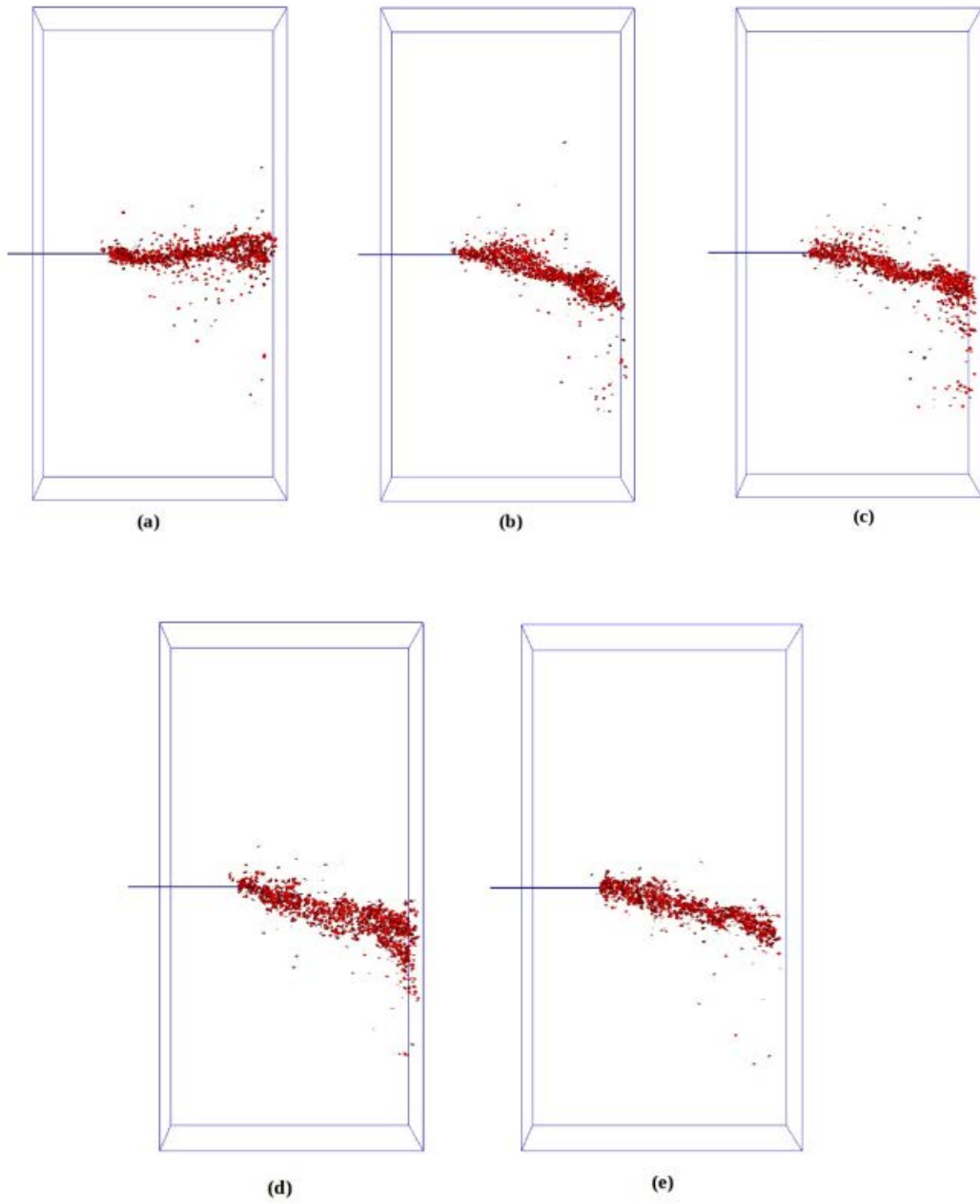


Figure 3.21: Fracture patterns for COx with Short-Transverse configuration, for beddings with different degrees a)  $\theta = 15^\circ$ , b)  $\theta = 30^\circ$ , c)  $\theta = 45^\circ$ , d)  $\theta = 60^\circ$ , e)  $\theta = 75^\circ$ .

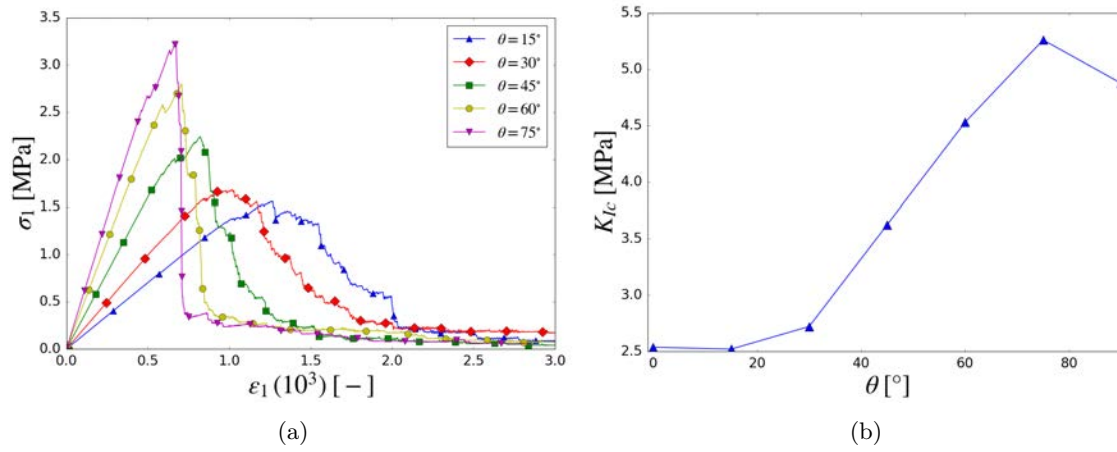


Figure 3.22: a) Stress-strain response (uniaxial tension) of edge cracked samples of Short-Transverse COx for different beddings,  $\theta = 15^\circ, 30^\circ, 45^\circ, 60^\circ, 75^\circ$ , b) Evolution of  $K_{Ic}$  as a function of bedding angle  $\theta$ .

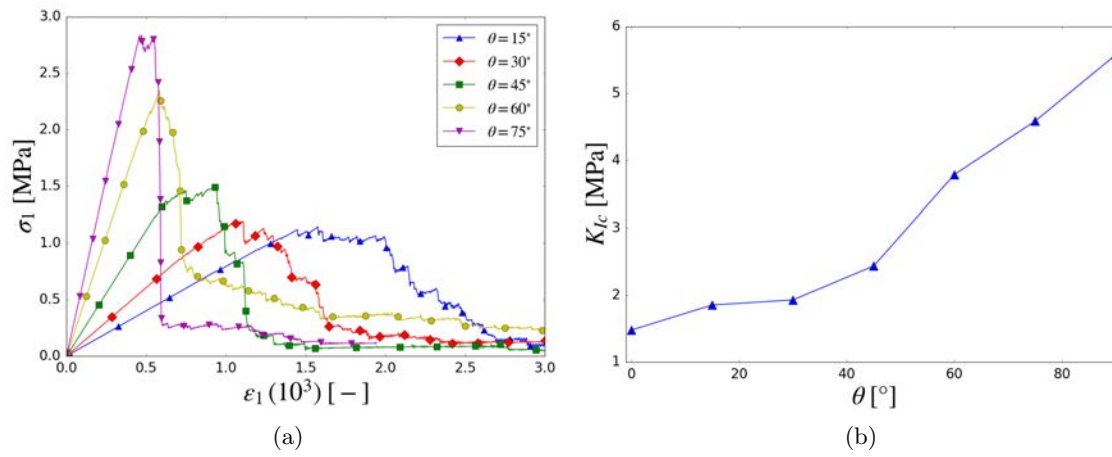


Figure 3.23: a) Stress-strain response (uniaxial tension) of edge cracked samples of Short-Transverse Tournemire shale for different beddings,  $\theta = 15^\circ, 30^\circ, 45^\circ, 60^\circ, 75^\circ$ , b) Evolution of  $K_{Ic}$  as a function of bedding angle  $\theta$ .

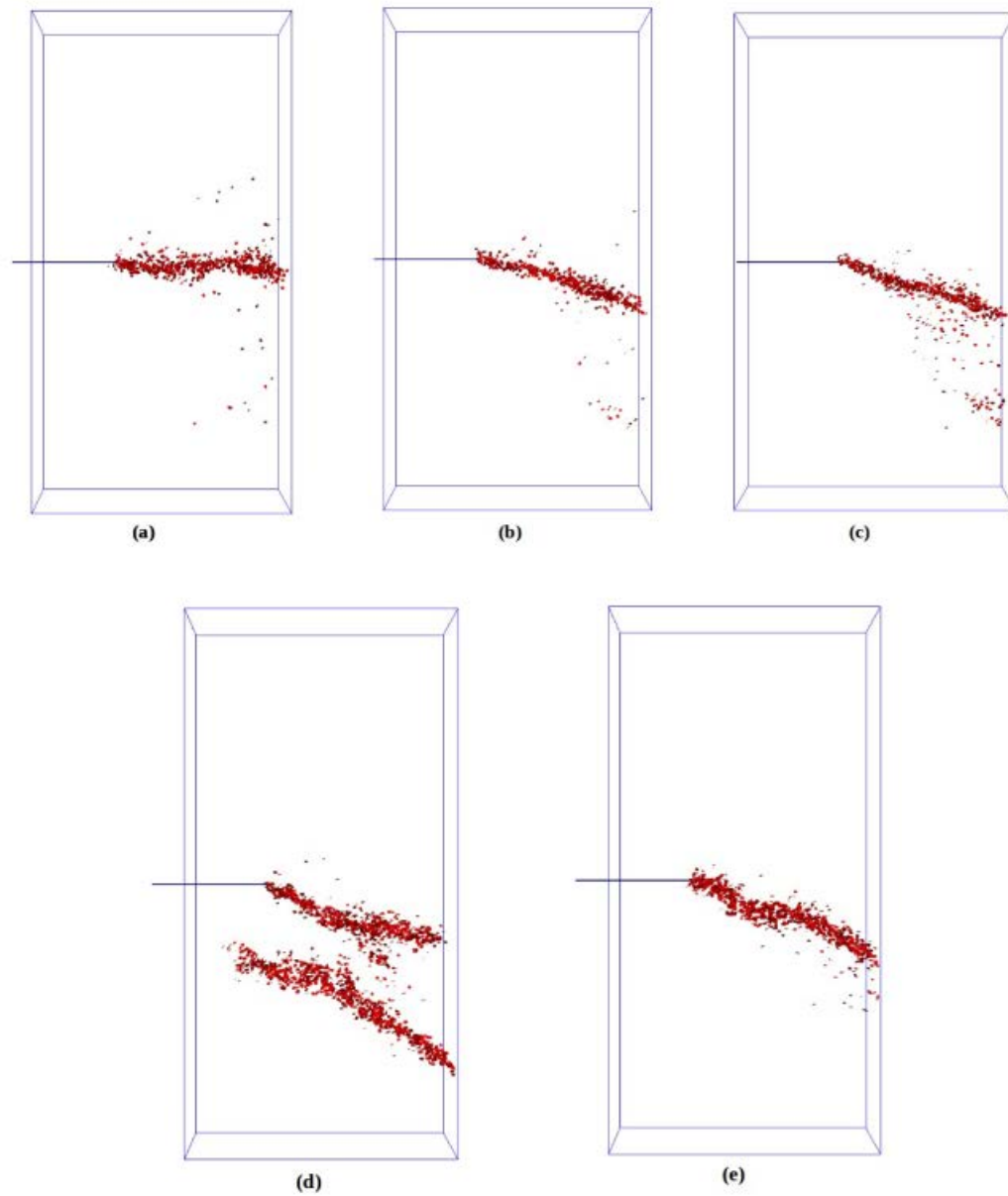


Figure 3.24: Fracture patterns for Tournemire shale with Short-Transverse configuration, for beddings with different degrees a)  $\theta = 15^\circ$ , b)  $\theta = 30^\circ$ , c)  $\theta = 45^\circ$ , d)  $\theta = 60^\circ$ , e)  $\theta = 75^\circ$



### 3.4 Conclusion

An effort was made to have a more profound understanding of fracturing process in transverse isotropic media. For this purpose a BPM was developed to investigate the influence of transverse isotropy on initiation and propagation of fractures. Two models were calibrated to represent the behavior of two transverse isotropic rocks namely, COx claystone and Tournemire shale. Tournemire shale shows a stronger anisotropy compared to COx claystone and this aspect was shown by comparing the elastic moduli and fracture toughness of both rocks. The formulation of the BPM and the introduction of weakness planes were extensively described. The calibration process is explained and justified for both rocks. The mechanical behavior of both intact rocks were modeled using the BPM to show the ability of the BPM in simulating rock materials. For this purpose the mechanical properties of both rocks such as Young's modulus and UCS were studied in compression. The failure patterns of both rocks were simulated and compared with experimental observations which showed a good agreement.

After justifying and describing the calibrated models the BPMs were then employed in simulating propagation of mode I fractures. For this purpose and in an attempt to study the fracture initiation and propagation in crack contained media, a single pre-existing edge notch was introduced into the models. Three different configurations *i.e.* Divider, Short-Transverse and Arrester were considered. The impact of different bedding orientations were studied and the results for both calibrated models were interpreted. Mode I SIFs were calculated using a displacement extrapolation approach and then compared to theoretical values showing a good agreement between two types of results. Fracture propagation paths and the impact of different bedding orientations were then studied considering the anisotropic BPM calibrated to Tournemire shale and COx claystone. The simulations performed using the BPM were merely mechanical and no hydromechanical aspect was considered, however, the BPM has the ability to deal with hydromechanical couplings. Ongoing efforts are currently done in order to characterize the propagation of hydraulically driven fractures using the BPM.

# Chapter 4

## Conclusion

We developed two different approaches based on two numerical methods namely the BPM and the HM-XFEM in order to study the fracture propagation in transverse isotropic materials. Our HM-XFEM is based on a numerical tool previously introduced by [65] and [139] for the simulation of fluid-driven fracture propagation in transverse isotropic media. We managed to integrate the transverse isotropic property into the existing HM-XFEM model where the impact of transverse isotropy on the propagation of hydraulic fracture is studied. For this purpose we used a test-case developed for the hydraulic fracture propagation in isotropic material and we adapted this test case to the propagation of 3D fluid driven crack reorientation in a transverse isotropic medium (Figure 4.1). We tested several orientations of the isotropy plane. In the developed model the XFEM, is used in order to handle the discontinuities, which is an appropriate method in order to avoid the difficulties encountered in the FEM, such as remeshing and the discontinuity conforming to the mesh element edges. Our model is capable of simulating a total hydromechanical coupling between the discontinuities (cracks) and the porous media; the transvers isotropic behavior of the medium is taken into account. Our model relies on the recent developments carried out by [139] where a cohesive approach is considered approach for the propagation of cracks on non-predefined paths developed by Ferté [65]. The stability of the current model is ensured by the use of three distinct approximation spaces developed in the precedent model [139]. The displacements field is interpolated in a quadratic way, the pore pressure field is interpolated in a linear way and finally, the fields associated to the cohesive cracks are discretized over an appropriate reduced approximation space based on the vertex nodes of the edges intersected by the fracture.

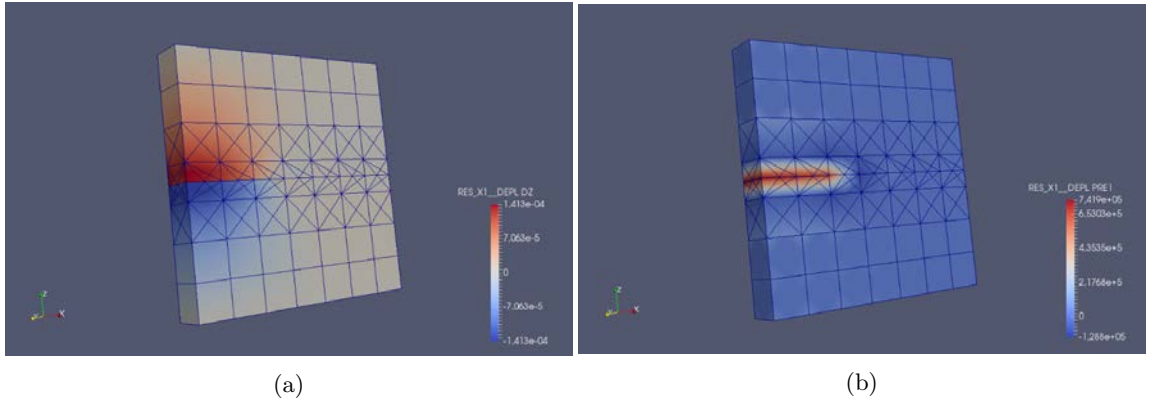


Figure 4.1: a) The resulting displacement field for bedding angle of  $\theta = 0^\circ$ . and b) The resulting pore pressure field for bedding angle of  $\theta = 0^\circ$ .

A discrete modeling approach is also proposed to investigate fracture propagation in transverse isotropic medium without the hydraulic coupling. Transverse isotropic characteristics are given to the medium by introduction of the concept of weakness palens (Figure 4.2). For that purpose, a bonded particle model is utilized to simulate uniaxial tensile tests on synthetic rock samples containing a pre-existing crack. The approach reproduces all the typical characteristics of brittle materials including, linear elastic behavior at small deformation, nucleation of stress induced microcracks before failure and development of macroscopic failure surfaces through the coalescence of

these microcracks. Furthermore, the relevance of the modeling approach for studying mode I fracture propagation is confirmed by assessing its capabilities with respect to classic fracture mechanics concepts such as the consistency of the stress intensity factors at the fracture tip with respect to the far field stress, the description of a process zone resulting from stress induced microcracks at the fracture tip and the prediction of adequate fracture paths.

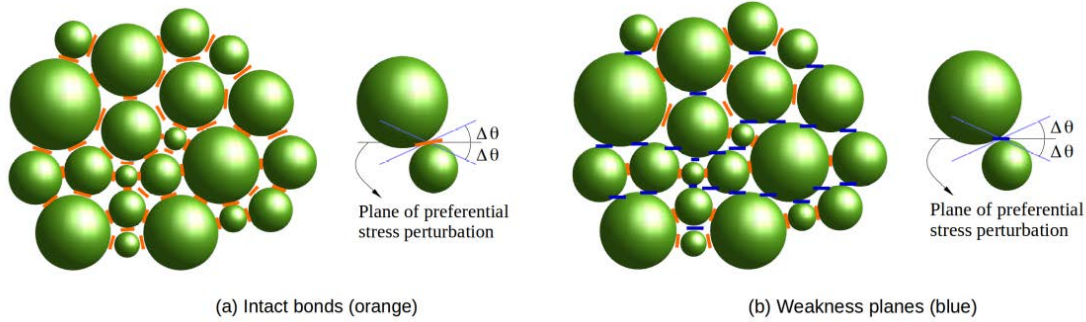


Figure 4.2: Introduction of transverse isotropy in the BPM: a) detection of the contacts dipping subparallel to the isotropy plane ( $\theta = 0^\circ$  here) according to the angle range  $\pm\Delta\theta$ , b) reorientation of the contacts along the direction of the isotropy plane.

Furthermore Using the proposed anisotropic BPM, a very good description of two transversely isotropic rock's behavior is achieved both in terms of deformation and failure processes. The model is able to describe both damage evolution and strain localization prior to failure. A comparison between the stress intensity factor obtained from BPM predictions and LEFM is done, showing a great agreement between two. Different configurations for both rocks were considered where we studied the effect of different bedding orientations on the failure patterns of the medium. The influence of bedding orientation on the fracture toughness ( $K_{Ic}$ ) is investigated. There are further steps currently being taken in order to extend and develop the current models for more complicated phenomena. There are ongoing efforts to develop the current BPM for the simulation of hydraulicfracturing in transverse isotropic media which is a challenging problem in geomechanical engineering. The HM-XFEM model that we developed currently is only able to simulate the propagation of hydralic fractures along pre-defined paths. Further efforts need to be done in order to extend the current model to fracture propagation on non-predefined paths.

# Bibliography

- [1] Abdi H., Labrie D., Nguyen T. S., Barnichon J. D., Su G., Evgin E., Simon R., Fall M. “*Laboratory investigation on the mechanical behaviour of Tournemire argillite*”, Canadian Geotechnical Journal, Vol. 52, Issue 3, pp. 268-282, 2014.
- [2] Adachi J. I., “*Plane Strain Propagation of a Hydraulic Fracture in a Permeable Rock*”, Engineering Fracture Mechanics, Vol. 75, pp. 4666-4694, 2008.
- [3] Altus E., “*The Finite Difference Technique For Solving Crack Problems*”, Engineering Fracture Mechanics, Vol. 19, Issue 5, pp. 947-957, 1984.
- [4] Anderson T.L., “*Fracture Mechanics: Fundamentals and Applications*”, Boca Raton, FL: CRC Press; 1991.
- [5] Andra D., “*Dossier Argile: Synthesis—evaluation of the feasibility of a geological repository in an Argillaceous formation, Meuse/Haute Marne Site*”, Technical Report Paris, France, 2005.
- [6] Andra D., “*Dossier: Référentiel du site Meuse/Haute-Marne Tome 2: Caractérisation comportementale du milieu géologique sous perturbation*”, 2nd edn. Paris, France, 2005.
- [7] Armand G., Noiret A., Zghondi J., Seyedi D. M. “*Short- and long-term behaviors of drifts in the Callovo-Oxfordian claystone at the Meuse/Haute-Marne Underground Research Laboratory*” Journal of Rock Mechanics and Geotechnical Engineering, Vol. 5, pp. 221-230, 2011.
- [8] Armand G., Leveau F., Nussbaum C., de La Vaissiere R., Noiret A., Jaeggi D., Landrien P., Righini C. “*Geometry and Properties of the Excavation-Induced Fractures at the Meuse/Haute-Marne URL Drifts*” Rock Mechanics and Rock Engineering, Vol. 47, Issue 1, pp. 21-41, 2014.
- [9] Asadpour A., Mohammadi S. “*Developing new enrichment functions for crack simulation in orthotropic media by the extended finite element method*”, International Journal for numerical methods in engineering, 69:2150-2172, 2007.
- [10] Azevedo N. M., Lemos J. de Almeida J. R. “*Influence of aggregate deformation and contact behaviour on discrete particle modelling of fracture of concrete*”, Engineering Fracture Mechanics, Vol. 75, Issue 6, pp. 1569-1586, 2008.
- [11] Barenblatt G. I. “*Development and applications of rock fracture mechanics modelling with FRACOD: a general review*”, Geosystem Engineering, 17:4, pp. 235-252. 2014.
- [12] Barenblatt G. I. “*The mathematical theory of equilibrium cracks formed in brittle fracture*”, Zhurnal Prikladnoy Mekhaniki i Tekhnicheskoy Fiziki, No. 4, pp. 3-56. 1961.
- [13] Bézuelle P., Hall S. A., “*Characterization of the strain localization in a porous rock in plane strain condition using a new true triaxial apparatus. In: Bonelli S, Dasalu C, Nicot F (eds) Advances in bifurcation and degradation in geomaterials.*”, Springer series in geomechanics and geoengineering. Springer, Berlin.
- [14] Bechet E., Scherzer M., Kuna M. “*Application of the XFEM to the fracture of piezoelectric materials*”, International Journal for Numerical Methods in Engineering, Vol. 77, pp. 1535-1565, 2009.

- [15] Beissel S. R., Johnson G. R., Popelar C. H. “*An element-failure algorithm for dynamic crack propagation in general directions*”, Engineering Fracture Mechanics, Vol. 61, Issue 3-4, pp. 407-425, 1998.
- [16] Paul B. “*Modeling fluid-driven cracks with the eXtended Finite Element Method*”, PhD dissertation, Université de Lorraine, 2016.
- [17] Blanton T. L. “*An experimental study of interaction between hydraulically induced and pre-existing fractures*”, in Proceedings of the SPE Unconventional Gas Recovery Symposium, Pittsburgh, Penn, USA, May 1982.
- [18] Blanton T. L. “*Propagation of hydraulically and dynamically induced fractures in naturally fractured reservoirs*”, in Proceedings of the SPE Unconventional Gas Recovery Symposium, May 1986.
- [19] Blue A. J. “*Experimental evaluations of selected sealants to remediate CO<sub>2</sub> leakage*”, Master thesis, Missouri University of Science and Technology, 2016.
- [20] Bobet A., Marin G. V. “*A stress and displacement discontinuity element method for elastic transversely anisotropic rock*”, International Journal for Numerical and Analytical Methods in Geomechanics, Vol. 38, pp. 1898-1922, 2014.
- [21] Bobet A., Fakhimi A., Johnson S., Morris J., Tonon F., Yeung M. “*Numerical models in discontinuous media: Review of advances for rock mechanics applications*”, Journal of Geotechnical and Geoenvironmental Engineering, Vol. 135, Issue: 11, pp. 1547-1561, 2009.
- [22] Bonnelye A., Schubnel A., Christian D., Henry P., Guglielmi Y., Gout C., Fauchille A. L., Dick P. “*Strength anisotropy of shales deformed under uppermost crustal conditions*”, Journal of Geophysical Research: Solid Earth, Vol. 122, Issue: 1, pp. 110-129, 2017.
- [23] Boone T. J., Wawrzynek P. A., Ingraffea A. R. “*Finite element modelling of fracture propagation in orthotropic materials*”, Engineering Fracture Mechanics, Vol. 26, Issue: 2, pp. 185-201, 1987.
- [24] Bouhala L., Makradi A., Belouettar S, “*Thermo-anisotropic crack propagation by XFEM*”, International Journal of Mechanical Sciences, Vol. 103, pp. 235-246, 2015.
- [25] Borden M. J., Verhoosel C. V., Scott M. A., Hughes T. J. R., Landis C. M. “*A phase-field description of dynamic brittle fracture*”, Computer Methods in Applied Mechanics and Engineering, Vol. 217-220, pp. 77-95, 2012.
- [26] Brebbia C. A., Telles J. C. F., Wrobel L. C. “*Boundary Element Techniques*”, Springer-Verlag: Berlin, 1984.
- [27] Bungler A., Detournay E., Garagash D., “*Toughness-dominated Hydraulic Fracture with Leak-off*”, International Journal of Fracture, Vol. 134, No. 2, pp. 175-190, 2005.
- [28] Bungler A., Pierce A. “*Numerical simulation of simultaneous growth of multiple interacting hydraulic fractures from horizontal wells*”, in: ASCE Shale Energy Engineering Conference, 2014.
- [29] Cao Y., Killough J. E., “*An Improved Boundary Element Method for Modeling Fluid Flow through Fractured Porous Medium*”, SPE Reservoir Simulation Conference, 20-22 February, Montgomery, Texas, USA, 2017.
- [30] Catwright D. J., Rooke D. P. “*Approximate stress intensity factors compounded from known solutions*”, Engineering Fracture Mechanics, Vol. 6, Issue 3, 563-571, 1974.
- [31] Carrier B., Granet S. “*Numerical modeling of hydraulic fracture problem in permeable medium using cohesive zone model*”, Engineering Fracture Mechanics, Vol. 79, pp. 312-328, 2012.

- [32] Chan S. K., Tuba I. S., Wilson W. K., “*On the finite element method in linear fracture mechanics*”, Engineering Fracture Mechanics, Vol. 2, pp. 1-17, 1970.
- [33] Chandler M.R., Meredith P.G., Brantut N., Crawford B.R. “*Fracture toughness anisotropy in shale*”, Journal of Geophysical Research Solid Earth, Vol. 121, pp. 1706-1729, 2016.
- [34] Chao J., Gao-Feng Z., Khalili N. “*On crack propagation in brittle material using the distinct lattice spring model*”, International Journal of Solids and Structures, Vol. 118-119, pp. 41-57, 2017.
- [35] Cherepanov G.P. “*Crack Propagation In Continuous Media*”, Journal of applied mathematics and mechanics, Vol. 31, No. 3, pp. 476-488, 1967.
- [36] Chen M., Pang F., Jin Y. “*Experiments and analysis on hydraulic fracturing by a large-size triaxial simulator*”, Chinese Journal of Rock Mechanics and Engineering, Vol. 19, pp. 868-872, 2000.
- [37] Chen M., Zhou J., Jin Y., Zhang G. “*Experimental study on fracturing features in naturally fractured reservoir*”, Acta Petrolei Sinica, Vol. 29, Issue 3, pp. 431-434, 2008.
- [38] Cho N., Martin C. D., Sego D. C. “*A clumped particle model for rock*”, International Journal of Rock Mechanics and Mining Sciences, Vol. 44, pp. 997-1010, 2007.
- [39] Cho J. W., Kim H., Jeon S., Min K. B. “*Deformation and strength anisotropy of Asan gneiss, Boryeong shale, and Yeoncheon schist*”, International Journal of Rock Mechanics and Mining Sciences, Vol. 50, pp. 158-169, 2012.
- [40] Chun’an T., Shibin T. “*Applications of rock failure process analysis (RFPA) method*”, Journal of Rock Mechanics and Geotechnical Engineering, Vol. 3, Issue 4, pp. 352-372, 2011.
- [41] Clifton R. J. “*Three-Dimensional Fracture-Propagation Model*”, In: Recent Advances in Hydraulic Fracturing - SPE Monograph, 1989, 95-108.
- [42] Cruse T. A., Wilson R. B. “*Advanced applications of the boundary-integral equation method*”, Nuclear Engineering and Design, Vol. 6, pp. 223-234, 1978.
- [43] Cundall P. A., “*Computer model for simulating progressive large scale movements in blocky systems*”, in: Proceedings of the Symposium of the International Society for Rock Mechanics, Nancy, France, paper No. II-8, Vol. 1, 1971.
- [44] Cundall P. A., Strack O. D. L. “*A discrete numerical model for granular assemblies*”, Geotechnique, Vol. 29, Issue 1, 1979.
- [45] Cundall P. A., Strack O. D. L. “*The distinct element method as a tool for research in granular media*”, Report to NSF Concerning Grant ENG 76-20711, Part II, 1979.
- [46] Cundall P. A., Hart R. D. “*Numerical modelling of discontinua*”, Engineering Computations, Vol. 9, Issue 2, pp. 101-113, 1992.
- [47] Damjanac B., Cundall P. “*Application of distinct element methods to simulation of hydraulic fracturing in naturally fractured reservoirs*”, Computers and Geotechnics, Vol. 71, pp. 283-294, 2016.
- [48] Daux C., Moës N., Dolbow J. “*Arbitrary branched and intersecting cracks with the eXtended Finite Element Method*”, International Journal for Numerical Methods in Engineering, Vol. 48, Issue. 12, pp. 1741-1760, 2000.
- [49] Desbois G. “*Deformation in cemented mudrock (Callovo-Oxfordian Clay) by microcracking, granular flow and phyllosilicate plasticity: insights from triaxial deformation, broad ion beam polishing and scanning electron microscopy*”, Solid Earth, Vol. 8, pp. 291-305, 2017.

- [50] Detournay E. “*Propagation Regimes of Fluid-Driven Fractures in Impermeable Rocks*”, International Journal of Geomechanics, Vol. 4, Issue. 1, pp. 35-45, 2004.
- [51] Ding O., Scholtès L. “*Discrete Analysis of Damage and Shear Banding in Argillaceous Rocks*”, Rock Mechanics and Rock Engineering, Vol. 51, Issue 5, pp. 1521-1538, 2018.
- [52] Ding X., Zhang L. “*A new contact model to improve the simulated ratio of unconfined compressive strength to tensile strength in bonded particle*”, International Journal of Rock Mechanics and Mining Sciences, Vol. 69, pp. 111-119, 2000.
- [53] Donzé F. V., Magnier S. A. “*Formulation of a three-dimensional numerical model of brittle behavior*”, Geophysical Journal International, Vol. 122, Issue 3, pp. 790–802, 1995.
- [54] Donzé F. V., Bouchez J., Magnier S. A. “*Modeling fractures in rock blasting*”, International Journal of Rock Mechanics and Mining Sciences, Vol. 34, Issue 8, pp. 1153-1163, 1997.
- [55] Duan K., Kwok C., Pierce M. “*Discrete element method modeling of inherently anisotropic rocks under uniaxial compression loading*”, International Journal for Numerical and Analytical Methods in Geomechanics, Vol. 40, Issue 8, pp. 1150-1183, 2015.
- [56] Duan K., Kwok C. Y. “*Discrete element modeling of anisotropic rock under Brazilian test conditions*”, International Journal of Rock Mechanics and Mining Sciences, Vol. 78, pp. 46-56, 2015.
- [57] Dugdale D. S. “*Yielding of steel sheets containing slits*”, Journal of mechanics and physics of solids, Vol. 8, pp. 100-104, 1960.
- [58] Duriez J., Scholtès L., Donzé F. V. “*Micromechanics of wing crack propagation for different flaw properties*”, Engineering Fracture Mechanics, Vol. 153, pp. 378-398, 2016.
- [59] Elmo D. “*Evaluation of a hybrid FEM/DEM approach for determination of rock mass strength using a combination of discontinuity mapping and fracture mechanics modelling, with particular emphasis on modelling of jointed pillars*”, Doctoral dissertation, University of Exeter, Exeter, UK, 2006.
- [60] Erdogan F., Sih G. C. “*On the crack extension in plates under plane loading and transverse shear*”, Journal of basic engineering, pp. 519-525, 1963.
- [61] Exadaktylos G. E. “*On the constraints and relations of elastic constants of transversely isotropic geomaterials*”, International Journal of Rock Mechanics and Mining Sciences, Vol. 38, pp. 941-956, 2001.
- [62] Faivre M. “*Code\_Aster Manual, Élément Hydromécanique couplé avec XFEM*”, Clé : R7.02.18, Date: 06.03.2014
- [63] Faivre M., Paul B., Golfier F., Giot R., Massin P., Colombo D. “*2D coupled HM-XFEM modeling with cohesive zone model and applications to fluid driven fracture network*”, Engineering Fracture Mechanics, Vol. 159, pp. 115-143, 2016.
- [64] Ferté G. “*Développement de l’approche X-FEM cohésive pour la modélisation de fissures et d’interfaces avec le logiciel libre EDF R&D Code\_Aster.*”, Ph.D. Thesis, Ecole Centrale de Nantes, 2014.
- [65] Ferté G., Massin P., Moës N. “*3D crack propagation with cohesive elements in the extended finite element method*”, Computer Methods in Applied Mechanics and Engineering, Vol. 300, pp. 347-374, 2016.
- [66] Frank U., Barkley N. “*Remediation of low permeability subsurface formations by fracturing enhancements of soil vapor extraction*”, Journal of Hazardous Materials, Vol. 40, Issue. 2, pp. 191-201, 2005.

- [67] Ganis B., Mear M. E., Sakhaee-Pour A., Wheeler M. F., Wick T. “*Modeling Hydraulic Fractures with a Reservoir Simulator Coupled to a Boundary Element Method*”, ICES REPORT 13-17, The Institute for Computational Engineering and Sciences, The University of Texas at Austin, June 2013.
- [68] Garagash D., Detournay E. “*The Tip Region of a Fluid-Driven Fracture in an Elastic Medium*”, Journal of Applied Mechanics, Vol. 67, Issue. 1, pp. 183-192, 1999.
- [69] Geertsma J., de Klerk F. “*A rapid method of predicting width and extent of hydraulically induced fractures*”, Journal of Petroleum Technology, Vol. 21, Issue. 12, pp. 1571-1581, 1969.
- [70] Gdoutos E. E., Democritus University of Thrace, Xanthi, Greece “*Fracture mechanics, an introduction*”, Springer, Dordrecht, The Netherlands, 2005.
- [71] Ghajari M., Lannucci L., Curtis P. “*A Peridynamic Material Model for the Analysis of Dynamic Crack Propagation in Orthotropic Media*”, Computer Methods in Applied Mechanics and Engineering, Vol. 276, pp. 431-452, 2014.
- [72] Gingold R. A., Monaghan J. J. “*Smoothed particle hydrodynamics: Theory and application to non-spherical stars.*”, Monthly Notices of the Royal Astronomical Society, Vol. 181, Issue 3, pp. 375–389, 1977.
- [73] Gonzalez M., Teixeira P., Wrobel L.C., Martinez M. “*A new Displacement-based Approach to Calculate Stress Intensity Factors With the Boundary Element Method*”, Latin American Journal of Solids and Structures, Vol. 12, No. 9, 2015.
- [74] Griffith, A.A. “*The phenomena of rupture and flow in solids*”, Philosophical Transaction of the Royal Society of London, A221:163-198, 1920.
- [75] Hamdi J., Scholtès L., Souley M., Al Heib M. “*Effect of discretization at laboratory and large scales during discrete element modelling of brittle failure*”, International Journal of Rock Mechanics and Mining Sciences, Vol. 100, pp.48-61, 2017.
- [76] Hansbo A., Hansbo P., “*A finite element method for the simulation of strong and weak discontinuities in solid mechanics*”, Computer Methods in Applied Mechanics and Engineering, Vol. 193, Issue 33-35, pp. 3523-3540, 2004.
- [77] Hart R. D. “*An overview of methods for discontinuum analysis*”, Itasca Consulting Group, 1988.
- [78] Hattori G. et al., “*New anisotropic crack-tip enrichment functions for extended finite element method*”, Comput Mech 50:591-601, 2012.
- [79] Hattori G., Trevelyan J., Coombs C. W. “*A non-ordinary peridynamics implementation for anisotropic materials*”, Preprint submitted to Computer Methods in Applied Mechanics and Engineering, 19 October. 2017.
- [80] Hazzard J. F., Young R. P., Maxwell S. C. “*Micromechanical modeling of cracking and failure in brittle rocks*”, Journal of Geophysical Research: Solid Earth, Vol. 105, Issue B7, pp. 16683-16697, 2000.
- [81] Hauseux P., Roubin E., Seyedi D. M., Colliat J. B. “*FE modelling with strong discontinuities for 3D tensile and shear fractures: Application to underground excavation*”, Computer Methods in Applied Mechanics and Engineering, Vol. 309, pp. 269-287, 2016.
- [82] He J., Afolagboye O. L., Lin C., Wan X. “*An Experimental Investigation of Hydraulic Fracturing in Shale Considering Anisotropy and Using Freshwater and Supercritical CO<sub>2</sub>*”, Energies 2018, 11, 557.



- [83] Hillerborg A., Modéer M., Petersson P.E. “*Analysis of crack formation and crack growth in concrete by means of fracture mechanics and finite elements*”, Analysis of crack formation and crack growth in concrete by means of fracture mechanics and finite elements, Vol. 6, Issue 6, pp. 773-781, 1976.
- [84] Honggang J., Yufeng N., Junlin L., “*XFEM for Fracture Analysis in 2D Anisotropic Elasticity*”, Advances in Applied Mathematics and Mechanics, Vol. 9, Issue 1, pp. 125-143, 2017.
- [85] Hue W. “*Peridynamic Models for Dynamic Brittle Fracture*”, PhD Dissertation, University of Nebraska, 2012 .
- [86] Huygue J., Remij E., Remmers J., Smeulders D. “*The enhanced local pressure model for the accurate analysis of fluid pressure driven fractures in porous materials*”, Computer Methods in Applied Mechanics and Engineering, Vol. 286, pp. 293-312, 2015.
- [87] Hussain M.A., Pu S.L., Underwood J. “*Strain energy release rate for a crack under combined mode I and mode II*”, Fract Anal ASTM STP, Vol. 560, pp. 2-28, 1974.
- [88] Irwin G. R. “*Analysis of Stresses and Strains Near the End of a Crack Traversing a Plate*”, Journal of Applied Mechanics, Vol. 24, pp. 361-364, 1957.
- [89] Irwin G. R. “*Fracture*”, Handbuch der Physik, Vol. 6, Springer pp. 551-590.
- [90] Irwin G. R. “*Relation of Crack-Toughness Measurements to Practical Applications*”, AWS-ASME meeting, Cleveland, Ohio, 1962.
- [91] Irwin G. R. “*Fracture Mechanics*”, Structural Mechanics, Pergamon Press, New York, N. Y., pp.557-592, 1960.
- [92] “*UDEC (Universal Distinct Element Code). Theory and background volume*”, Minneapolis, MN: Author. Itasca. (2017). Bonded block model in 3DEC. Retrieved from <http://www.itascacg.com>.
- [93] Jeffrey R. G., Settari A., Mills K. W., Zhang X., Detournay E. “*Hydraulic fracturing to induce caving: fracture model development and comparison to field data*”, In: Elsworth D, Tinucci JP, Heasley KA, editors. Rock mechanics in the national interest - proceedings of the 38th US rock mechanics symposium, vol. 1. Lisse: Balkema; pp. 251-259, 2001.
- [94] Jiang C., Zhao G. F., Khalili N. “*On crack propagation in brittle material using the distinct lattice spring model*”, International Journal of Solids and Structures, Vol. 118-119, pp. 41-57, 2017.
- [95] Jing L., Hudson J. A. “*Numerical methods in rock mechanics*”, International Journal of Rock Mechanics and Mining Sciences, Vol. 39, Issue 4, pp. 409-427, 2002.
- [96] Jing L., Ma Y., Fang Z. “*Modeling of fluid flow and solid deformation for fractured rocks with discontinuous deformation analysis (DDA) method*”, International Journal of Rock Mechanics and Mining Sciences, Vol. 38, Issue 3, pp. 343-355, 2001.
- [97] Jing L., “*A review of techniques, advances and outstanding issues in numerical modelling for rock mechanics and rock engineering*”, International Journal of Rock Mechanics and Mining Sciences, Vol. 40, Issue 3, pp. 283-353, 2003.
- [98] Jing L., Stephansson O. “*Fundamentals of discrete element methods for rock engineering: Theory and applications*”, Amsterdam: Elsevier, 2007.
- [99] Jirásek M., Bazant Z. “*Particle model for quasibrittle fracture and application to sea ice*”, Journal of Engineering Mechanics, Vol. 121, Issue 9, pp. 1016-1025, 1995.
- [100] Kassir M.K., Sih G.C. “*Three-Dimensional Stress Around Elliptical Cracks In Transversely Isotropic Solids*”, Engineering Fracture Mechanics. Vol. 1, pp. 327-345, 1968.

- [101] Ke C. C., Chen C. S., Tu C. H, “*Determination of Fracture Toughness of Anisotropic Rocks by Boundary Element Method*”, Rock Mechanics and Rock Engineering. Vol. 41, Issue 4, pp. 509-538, 2008.
- [102] Ke C. C., Chen C. S., Ku C. Y, Chen C. H. “*Modeling crack propagation path of anisotropic rocks using boundary element method*”, International Journal for Numerical and Analytical Methods in Geomechanics. Vol. 33, Issue 9, pp. 1227-1253, 2009.
- [103] Khan S.M.A., Khraisheh M.K. “*Analysis of mixed mode crack initiation angles under various loading conditions*”, Engineering Fracture Mechanics. Vol. 67, pp. 397-419, 2000.
- [104] Khoei A. R., Barani O. R., Mofid M. “*Modeling the interaction between fluid-driven fracture and natural fault using an enriched-FEM technique*”, International Journal of Fracture, Vol. 197, Issue 1, pp. 1-24, 2016.
- [105] Konietzky H., Heftenberger A., Feige M. “*Life-time prediction for rocks under static compressive and tensile loads: A new simulation approach*”, Acta Geotechnica. Vol. 4, Issue 1, pp. 73-78, 2009.
- [106] Krajcinovic D. “*Damage mechanics*”, Mechanics of Materials. Vol. 8, pp. 117-197, 1989.
- [107] Kulatilake P., Malama B., Wang J. “*Physical and particle flow modeling of jointed rock block behavior under uniaxial loading*”, International Journal of Rock Mechanics and Mining Sciences. Vol. 38, Issue 5, pp. 641-657, 2001.
- [108] Kuang J. H., Chen L. S., “*A displacement extrapolation method for two-dimensional mixed-mode crack problems*”, Engineering Fracture Mechanics, Vol. 46, pp. 735-741, 1993.
- [109] Legan M. A., Blinov V. A., Larichkin A. Y., Novoselov A. N. “*Application of the boundary elements method for modeling of the fracture of cylindrical bodies by hydraulic fracturing*”, Journal of Physics: Conference Series, Vol. 894, Issue 1, 2017.
- [110] Lee H.P., Olson J.E., Holder J., Gale J.F.W., Myers R.D. “*The interaction of propagating opening mode fractures with preexisting discontinuities in shale*”, Journal of Geophysical Research Solid Earth, Vol. 120, pp. 169-181, 2015.
- [111] Lekhnitskii, S.G. “*Theory of Elasticity of an Anisotropic Body*”, Mir Publisher, Moscow (English Translation), 1981.
- [112] Levasseur S., Charlier R., Freig B., Collin, F. “*Hydro-mechanical modeling of the excavation damaged zone around an underground excavation at Mont Terri Rock Laboratory.*”, International Journal of Rock Mechanics and Mining Sciences, 47:414-425, 2010.
- [113] Li Y., Hu S., Sun X., Stan M. “*A review: Applications of the phase field method in predicting microstructure and property evolution of irradiated nuclear materials*”, npj Computational Materilas, Vol. 3, Issue 1, 11 p.
- [114] Lianchong L., Yingjie X., Bo H., Liaoyuan Z., Ming L., Aishan L. “*The Behaviour of Fracture Growth in Sedimentary Rocks: A Numerical Study Based on Hydraulic Fracturing Processes*”, Energies, Vol. 9, Issue 3, pp. 1-28. 2016.
- [115] Liebowitz H., Sandhu J. S., Lee J. D., Menandro F. C. M. “*Computational Fracture Mechanics: Research and Application*”, Engineering Fracture Mechanics, Vol. 50, Issue 5-6, pp. 653-670, 1995.
- [116] Lin G., Hen X. G., Cornec A., Schwalbe K.H. “*The effect of strength mis-match on mechanical performance of weld joints*”, International Journal of Fracture, Vol. 96, Issue 1, pp. 37-54, 1999.
- [117] Liu A., “*Summary of stress intensity factor*”, Rockwell international.

- [118] Lorentz E., “*A mixed interface finite element for cohesive zone model*”, Computer Methods in Applied Mechanics and Engineering, Vol. 198, Issue 2, pp. 302-317, 2008.
- [119] Luo Y., Xie H.P., Ren L., Zhang R., Li C.B., Gao C. “*Linear Elastic Fracture Mechanics Characterization of an Anisotropic Shale*”, Scientific Reports 8, Article number: 8505 (2018).
- [120] MacLaughlin M. M., Doolin D. M. “*Review of validation of the discontinuous deformation analysis (DDA) method*”, International Journal for Numerical and Analytical Methods in Geomechanics, Vol. 30, Issue 4, pp. 271-305, 2006.
- [121] Mars I. D., Pierce M. E., Darcel C., Reyes-Montes J., Potyondy D. O., Young R. P., Cundall P. A. “*The synthetic rock mass approach for jointed rock mass modelling*”, International Journal of Rock Mechanics and Mining Sciences, Vol. 48, Issue 2, pp. 219-244, 2011.
- [122] Melenk J. M., Babuska I., “*The partition of unity finite element method: Basic theory and applications*”, Computer Methods in Applied Mechanics and Engineering, Vol. 139, Issue 1-4, pp. 289-314, 1996.
- [123] Moës N., Dolbow J., Belytschko T., “*A finite element method for crack growth without remeshing*”, International journal for numerical methods in engineering, Vol. 46, pp. 131-150, 1999.
- [124] Mohammadi S., “*Extended finite element method*”, Wiley, 2008.
- [125] Mohammadnejad M., Khoei A. R. “*An extended finite element method for hydraulic fracture propagation in deformable porous media with the cohesive crack model*”, Finite Elements in Analysis and Design, Vol. 73, pp. 77-95, 2013.
- [126] Mohammadnejad M., Liu H., Chan A., Dehkhoda S., Fukuda D., “*An overview on advances in computational fracture mechanics of rock*”, Geosystem Engineering, pp. 1-25, 2018.
- [127] Moosavi S., Scholtès L. Giot R. “*Influence of stress induced microcracks on the tensile fracture behavior of rocks*”, Computers and Geotechnics, Vol. 104, pp. 81-95, 2018.
- [128] Moreira P. M. G. P., “*A contribution to the study of fatigue of riveted lap joints*”, MSc thesis, FEUP - Faculdade de Engenharia da Universidade do Porto, Porto, Portugal, 2004.
- [129] Moschovidis Z. et al. “*The Mounds drill-cuttings injection experiment: final results and conclusions*”, In: Proceedings of the IADC/SPE drilling conference. Richardson: Society of Petroleum Engineers; 2000 [SPE 59115].
- [130] Murdoch L. C., “*Mechanical analysis of idealized shallow hydraulic fracture*”, Journal of Geotechnical and Geoenvironmental Engineering. Vol. 128, No. 6, pp. 488-495 2002.
- [131] Murdoch L. C., Slack W. W. “*Forms of hydraulic fractures in shallow fine-grained formations*”, Journal of Geotechnical and Geoenvironmental Engineering. Vol. 128, No. 6, pp. 479-487 2002.
- [132] Ndeffo M., Massin P., Moës N., Martin A., Gopalakrishnan S. “*On the construction of approximation space to model discontinuities and cracks with linear and quadratic extended finite elements*”, Advanced Modeling and Simulation in Engineering Sciences, Vol. 4-6, pp. 1-52, 2017.
- [133] Nguyen T. T., Réthoré J., Baietto M. C. “*Phase field modelling of anisotropic crack propagation*”, European Journal of Mechanics - A/Solids, Vol. 65, pp. 279-288, 2017.
- [134] Niandou H., Shao J. F., Henry J. P., Fourmaintraux D. “*Laboratory investigation of the mechanical behaviour of Tournemire shale*”, International Journal of Rock Mechanics and Mining Sciences, Vol. 34, Issue 1, pp. 3-16, 1997.

- [135] Oliver J., Caicedo M., Roubin E., Heuspe A. E., Hernandez J. A. “*Continuum approach to computational multiscale modeling of propagating fracture*”, Computer Methods in Applied Mechanics and Engineering, Vol. 294, pp. 384-427, 2015.
- [136] Osher S., Sethian J. A., “*Fronts propagating with curvature-dependent speed: algorithm based on hamilton-jacobi formulations*”, Journal of Computational Physics, Vol. 79, pp. 12-49, 1988.
- [137] Pan E., Amadei B. “*Fracture mechanics analysis of cracked 2-D anisotropic media with a new formulation of the boundary element method*”, International Journal of Fracture, Vol. 77, Issue 2, pp. 161-174, 1996.
- [138] Paris P. C., Sih G. C. “*Stress analysis of cracks*”, In Fracture Toughness Testing and its Applications, ASTM STP 381, pp. 30-83, Philadelphia, 1965. ASTM (American Society for Testing and Materials).
- [139] Paul B., “*Modeling fluid-driven cracks with XFEM*”, PhD dissertation, Université de Lorraine, 2016.
- [140] Paul B., Ndeffo M., Massin P., Moës N. “*An integration technique for 3D curved cracks and branched discontinuities within the extended Finite Element Method*”, Finite Elements in Analysis and Design, Vol. 123, pp. 19-50, 2017.
- [141] Paul B., Faivre M., Massin P., Giot R., Colombo D., Golfier F., Martin A. “*3D coupled HM-XFEM modeling with cohesive zone model and applications to non planar hydraulic fracture propagation and multiple hydraulic fractures interference*”, Computer Methods in Applied Mechanics and Engineering, Vol. 342, pp. 321-353, 2016.
- [142] Pelfrene J., Van Dam V., Sevenois R., Gilibert F., Paepegem V. W. “*Fracture Simulation of Structural Glass by Element Deletion i Explicit FEM*”, Conference on Architectural and Structural Application of Glass, Gent University, June 2016.
- [143] Poschel T., Schwager T., “*Computational granular dynamics: Models and algorithms*”, (1st ed.). Berlin Heidelberg: Springer-Verlag, 2005.
- [144] Potyondy D. O., Cundall P. A., “*A bonded-particle model for rock*”, International Journal of Rock Mechanics & Mining Sciences, Vol. 41, pp. 1329-1364, 2004.
- [145] Potyondy D. O. “*A flat-jointed bonded-particle material for hard rock*”, 46th US Rock Mechanics/Geomechanics Symposium, ARMA (2012).
- [146] Raju S., Newman Jr J. C. “*Three dimensional finite-element analysis of finite-thickness fracture specimens*”, Technical report, Langley Research Center, NASA TN D-8414, May 1977.
- [147] Rabczuk T. “*Computational methods for fracture in brittle and quasi-brittle solids: State of the art review and future perspectives*”, Applied Mathematics, 2013, 38 pages.
- [148] Riahi A., Damjanac B. “*Numerical Study of Interaction Between Hydraulic Fracture and Discrete Fracture Network*”, INTECH open source books, Chapter13, pp. 271-286, 2013.
- [149] Rice J.R. “*A path independent integral and the approximate analysis of strain concentration by notches and cracks*”, Journal of applied mechanics, Vol. 38, pp. 379-386, 1968.
- [150] Rice J.R. “*Mathematical analysis in the mechanics of fracture*”, In Fracture - An advanced treatise, Vol. II, pp. 191-308, 1968.
- [151] Rojas-Diaz R., Sukumar N., Saez A., Garcia-Sanchez F. “*Fracture in magnetoelastoelectric materials using the extended finite element method*”, International Journal in Numerical Methods in Engineering, Vol. 88, Issue 12, pp. 1238-1259, 2011.

- [152] Rossmannith H.P. Technical university of Vienna, “*Rock fracture mechanics*”, Springer-Verlag Wien, 1983.
- [153] Rybicki E. F., Kanninen M. F. “*Finite-element calculation of stress intensity factors by a modified crack closure integral*”, Engineering Fracture Mechanics, Vol. 9, Issue 4, pp. 931-938, 1977.
- [154] Santos J. E., Carcione J. M. “*Finite-element harmonic experiments to model fractured induced anisotropy in poroelastic media*”, Computer Methods in Applied Mechanics and Engineering, Vol. 283, pp. 1189-1213, 2015.
- [155] Saouma V.E., Ayari M.L., Leavell D.A. “*Mixed modes crack propagation in homogeneous anisotropic solids*”, Engineering fracture mechanics, Vol. 27, No. 2, pp. 171-184, 1987.
- [156] Schmidt R.A., Huddle C.W. “*Fracture mechanics of oil shale:some preliminary results*”, Report No. SAND-76-0727 United States 10.2172/7119762 Dep. NTIS SNL English, Medium: ED; Size: Pages: 29 (Sandia Labs., Albuquerque, NM (USA)) (1977).
- [157] Scholtès L., Donzé F. V. “*A dem model for soft and hard rocks: Role of grain interlocking on strength*”, Journal of the Mechanics and Physics of Solids, Vol. 61, Issue 2, pp. 352-369, 2013.
- [158] Scholtès L., Donzé F. V. “*Modelling progressive failure in fractured rock masses using a 3D discrete element method*”, International Journal of Rock Mechanics and Mining Science, Vol. 52, pp. 18-30, 2010.
- [159] Sethian A. J. “*Level set methods and fast marching methods*”, (2nd edition), 1999.
- [160] Shi G. H., Goodman R. E. “*Two dimensional discontinuous deformation analysis*”, International Journal for Numerical and Analytical Methods in Geomechanics, Volume: 9, Issue: 6, pp. 541-556, 1985.
- [161] Shi F., Wang X., Liu C., Liu H., Wu H. “*An XFEM-based method with reduction technique for modeling hydraulic fracture propagation in formations containing frictional natural fractures*”, Engineering Fracture Mechanics, Vol. 173, pp. 64-90, 2017.
- [162] Sih G.C., Paris P.C., Irwin G.R. , “*On cracks in rectilinearly anisotropic bodies*”, International Journal Of Fracture Volume: 1 Issue: 3 (1965-01-01) p. 189-203. ISSN: 0376-9429.
- [163] Sih G.C., “*Strain-energy-density factor applied to mixed mode crack problems*”, International Journal Of Fracture Volume: 10 Issue: 3, p. 305-321.
- [164] Silling S. A. “*Reformulation of elasticity theory for discontinuities and long-range forces*”, Journal of the Mechanics and Physics of Solids, Vol. 48, Issue: 1, pp. 175-209, 2000.
- [165] Silling S. A., Askari A. “*Peridynamic Model for Fatigue Cracking*”, Sandia Report, Sandia National Laboratories, SAND2014-18590, Unlimited Release, Printed September 2014.
- [166] Šmilauer V. et al. “*Yade Documentation 2nd ed. The Yade Project*”, 2015.
- [167] Smith S. A., Raju I. S. “*Evaluation of stress-intensity factors using general finite-element models*”, Fatigue and Fracture Mechanics, American Society for Testing and Materials, ASTM STP 1321, pp. 176-200, 1998.
- [168] Song J. H., “*Computations of the dynamic fracture of quasi-brittle plane and shell structures by the extended finite element method*”, Evanston, II: Northwestern University. 2012.
- [169] Sollero P., Aliabadi M. H. “*Anisotropic analysis of cracks in composite laminates using the dual boundary element method*”, Composite Structures, Vol. 31, Issue 3, pp. 229-233, 1995.
- [170] Sukumar N., Dolbow J. E., Mões N. “*Extended finite element method in computational fracture mechanics: a retrospective examination*”, International Journal of Fracture. Vol. 196, Issue 1-2, pp. 189-206, 2015.

- [171] Sukumar N., Huang Z. Y., Prévost J. H., Suo Z. “*Partition of unity enrichment for bimaterial interface cracks*”, International Journal for Numerical Methods in Engineering. Vol. 59, pp. 1057-1102, 2004.
- [172] Sulem J., Li X., “*Thermo-hydro-mechanical effects in clay host rocks for radioactive waste repositories.*”, Rock Mechanics and Rock Engineering, 47:1-1, 2014.
- [173] Tang C. A., Yang W. T., Fu Y. F., Xu X. H., “*A new approach to numerical method of modelling geological processes and rock engineering problems – Continuum to discontinuum and linearity to nonlinearity.*”, Engineering Geology, Vol. 49, Issue 3-4, pp. 207-214, 1998.
- [174] Tang C., Tham L., Wang S., Liu H., Li W. “*A numerical study of the influence of heterogeneity on the strength characterization of rock under uniaxial tension*”, Mechanics of Materials, Vol. 39, Issue 4, pp. 326-339, 2007.
- [175] Tavares S.M.O., Moreira P.M.G.P., Pastrama S.D., Castro P.M.S.T., “*Stress intensity factors by numerical evaluation in cracked structures*”,
- [176] Tijssen M. G. A., van der Giessen E., Sluys L.J., “*Modeling of crazing using cohesive surface methodology*”, Mechanics of Materials, Vol. 32, Issue 1, pp. 19-35, 2000.
- [177] Tsai V., Rice J.R. “*A model for turbulent hydraulic fracture and application to crack propagation at glacier beds*”, Journal of Geophysical Research, Vol. 115, Issue: F3, 2010.
- [178] Venticinque V., Remmers J. J., Barnhoorn A., Smeulders D. M. “*A Numerical Study on the Effect of Anisotropy on Hydraulic Fractures*”, Journal of Rock Mechanics and Rock Engineering, pp. 1-19, 2017.
- [179] Venticinque G. A., Nemeik J. “*New fracture models for the progressive failure of rock slopes*”, Paper presented at the 14th Coal Operators’ Conference University of Wollongong, 2014.
- [180] Venturini W. S. “*Boundary Element Method in Geomechanics*”, In Lecture Notes in Engineering, Brebbia CA, Orszag SA (eds.). Springer-Verlag: Berlin, 1983.
- [181] Wang Y., Tonon F. “*Calibration of a discrete element model for intact rock up to its peak strength*”, International Journal for Numerical and Analytical Methods in Geomechanics, Vol. 34, Issue 5, pp. 447-469, 2010.
- [182] Wang Y., Mora P. “*Modeling wing crack extension: implications for the ingredients of discrete element model*”, Pure and Applied Geophysics, Vol. 165, Issue 3-4, pp. 609-620, 2008.
- [183] Wang S., Sloan S. W., Tang C. A., Zhu W. “*Numerical simulation of the failure mechanism of circular tunnels in transversely isotropic rock masses*”, Tunnelling and Underground Space Technology, Vol. 32, pp. 231-244, 2012.
- [184] Wang H. “*Numerical modeling of non-planar hydraulic fracture propagation in brittle and ductile rocks using XFEM with cohesive zone method*”, Journal of Petroleum Science and Engineering, Vol. 135, pp. 127-140, 2015.
- [185] Wang H. “*Numerical investigation of fracture spacing and sequencing effects on multiple hydraulic fracture interference and coalescence in brittle and ductile reservoir rocks*”, Engineering Fracture Mechanics, Vol. 157, pp. 107-124, 2016.
- [186] Warpinski N. R., Teufel L. W. “*Influence of geologic discontinuities on hydraulic fracture propagation*”, Journal of Petroleum Technology, Vol. 39, Issue 2, pp. 209-220, 1987.
- [187] Warpinski N. R. “*Hydraulic fracturing in tight, fissured media*”, Journal of Petroleum Technology, Vol. 43, Issue 2, pp. 146-151, 1991.
- [188] Warpinski N. R., Mayerhofer M. J., Vincent M. C., Cipolla C. L., Lolon E. P. “*Stimulating unconventional reservoirs: maximizing network growth while optimizing fracture conductivity*”, in Proceedings of the SPE Unconventional Reservoirs Conference, pp. 237–255, February 2008.

- [189] Wawrzynek P., Ingraffea A. R. “*FRANC2D: A two-dimensional crack propagation simulator*”, Version 2.7, User’s guide, 1994.
- [190] Wong J. K. W. “*Three-dimensional multi-scale hydraulic fracturing simulation in heterogeneous material using Dual Lattice Model*”, Doctoral thesis, Cambridge, Massachusetts, 2018.
- [191] Wu E.M. “*Fracture Mechanics of Anisotropic Plates*”, Composite Materials Workshop (Edited by Tsai, Halpin and Pagano), pp. 20-43. Technomic Press, Stamford, CT 1968.
- [192] Xia L., Yvonnet J., Ghabezloo S. “*Phase field modeling of hydraulic fracturing with interfacial damage in highly heterogeneous fluid-saturated porous media*”, Engineering Fracture Mechanics, Vol. 186, pp. 158-180, 2017.
- [193] Zamani A., Eslami R. M., “*Implementation of the extended finite element method for dynamic thermoelastic fracture initiation*”, International journal of Solids and Structures, Vol. 47, pp. 1392-1404, 2010.
- [194] Zeng Q. D., Jun Y., Jianfu S. “*Numerical study of hydraulic fracture propagation accounting for rock anisotropy*”, Journal of Petroleum Science and Engineering, Vol. 160, pp. 422-432, 2018.
- [195] Zhang X., Detournay E., Jeffrey R. G., “*Propagation of a penny-shaped hydraulic fracture parallel to the free-surface on an elastic half-space*”, International journal of fracture, Vol. 58, Issue: 2, pp. 115-125, 2002.
- [196] Zhang X., Lu M., Wegner J. L., “*A 2-D meshless model for jointed rock structures*”, International journal of Numerical Methods in Engineering, Vol. 47, Issue: 10, pp. 1649-1661, 2000.
- [197] Zhang J., Ghosh S. “*Molecular dynamics based study and characterization of deformation mechanisms near a crack in a crystalline material*”, Journal of the Mechanics and Physics of Solids, Vol. 61, Issue: 8, pp. 1670-1690, 2013.
- [198] Zhou S. J., Lomdahl P. S., Thomson R., Holian B. L. “*Dynamic crack processes via molecular dynamics*”, Physical Review Letters, Vol. 76, Issue: 13, pp. 2318-2321, 1996.

## Appendix A

# Influence of stress induced microcracks on the tensile fracture behavior of rocks

The following paper is the result of a more comprehensive study on the fracture propagation using BPM, complementary to Chapter 3 of this thesis.





## Research Paper

## Influence of stress induced microcracks on the tensile fracture behavior of rocks

Sourena Moosavi<sup>a,\*</sup>, Luc Scholtès<sup>a</sup>, Richard Giot<sup>b</sup><sup>a</sup> Université de Lorraine, CNRS, GeoRessources, F-54000 Nancy, France<sup>b</sup> Université de Poitiers, CNRS, Institut de Chimie des Milieux et des Matériaux de Poitiers (IC2MP), 86000 Poitiers, France

## ARTICLE INFO

## Keywords:

Rock  
Microcracks  
Tensile strength  
Fracture toughness  
DEM

## ABSTRACT

The study characterizes the influence of preferentially oriented microcracks on the tensile fracture behavior of rocks by means of a discrete modeling approach. A series of numerical experiments is performed so as to systematically evaluate the emergent properties of media containing microcracks swarms with predefined intensities and orientations. Emphasis is put on the apparent Young's modulus, tensile strength and fracture toughness. Microcracks swarms reduce the strength of materials, affect their overall brittleness and induce anisotropic behavior. They also directly influence the initiation and propagation of mode I fractures which can deviate from their expected path as a result of branching.

## 1. Introduction

Knowledge of the strength and deformability of fractured rocks is important for design, construction and stability evaluation of slopes, foundations and underground excavations in either civil, mining or petroleum engineering. At large scales, fractures control the strength and deformation properties of natural and engineering rock structures [1–3]. At a smaller scale, it is well known that microcracks affect both the hydraulic and mechanical properties of rocks [4–8] and thus have direct consequences on the stability of structures [9]. Due to their formation conditions and to the stress states they were submitted to, rocks generally exhibit microcracks. These microcracks are often preferentially oriented because they are related to the rock fabric itself as, for example, in sedimentary or metamorphic rocks, but also because they form as a result of stress perturbations related to either natural or anthropogenic processes as detailed exhaustively in [10–12] (Fig. 1).

Microcracks (also referred to as microfractures in the literature) generally form as mode I (opening) fractures in locations where the minimum principal stress exceeds the local tensile strength of the material and are thus preferentially oriented along the maximum principal stress direction. Microcracks hence provide critical information on the growth and development of fault zones, the evolution of regional stress fields as well as on the earthquake cycle [11]. Obviously, depending on their intensity, these microcracks may affect the propagation of fractures and might thus have non-negligible impacts on the fracturing processes developing in rock masses. Indeed, growth and propagation

of tension and shear fractures in rocks result from the nucleation and coalescence of microcracks within the fracture process zone [14–16]. Fracture propagation occurs through branching mechanisms or “step-path” failure mechanisms taking place at the grain scale which, in the case of pre-cracked material, is most likely influenced by the amount as well as by the orientation of natural or mechanically induced microcracks.

Nonetheless, although the importance of microstructures on macroscopic behaviors has been recognized for decades now [17], relatively few experiments have systematically evaluated the influence of pre-existing preferentially oriented microcracks on the fracture behavior of rocks. For instance, Nasseri et al. [18] or Griffiths et al. [19] did characterize the role of thermally induced microcracking on both the strength and deformation properties of rock but only Nasseri et al. [20] actually highlighted the consequences of preferentially oriented microcracks on the propagation of fractures. Of course, numerous analytical works proposed to estimate effective properties of cracked or damaged materials [21,22,6,23]. However, despite the obvious elegance of analytical methods for calculating macroscopic properties, difficulties arise when it comes to the description of discrete mechanisms at stake, e.g., in fracture propagation problems. In this context, numerical methods provide more flexibility as they can take into account more refined mechanical behaviors as well as rather complex geometric characteristics for the discontinuities. Numerous computational methods have been proposed to study the mechanical behavior of fractured media. On one side of the spectrum, continuum numerical

\* Corresponding author.

E-mail address: [sourena.moosavi@univ-lorraine.fr](mailto:sourena.moosavi@univ-lorraine.fr) (S. Moosavi).

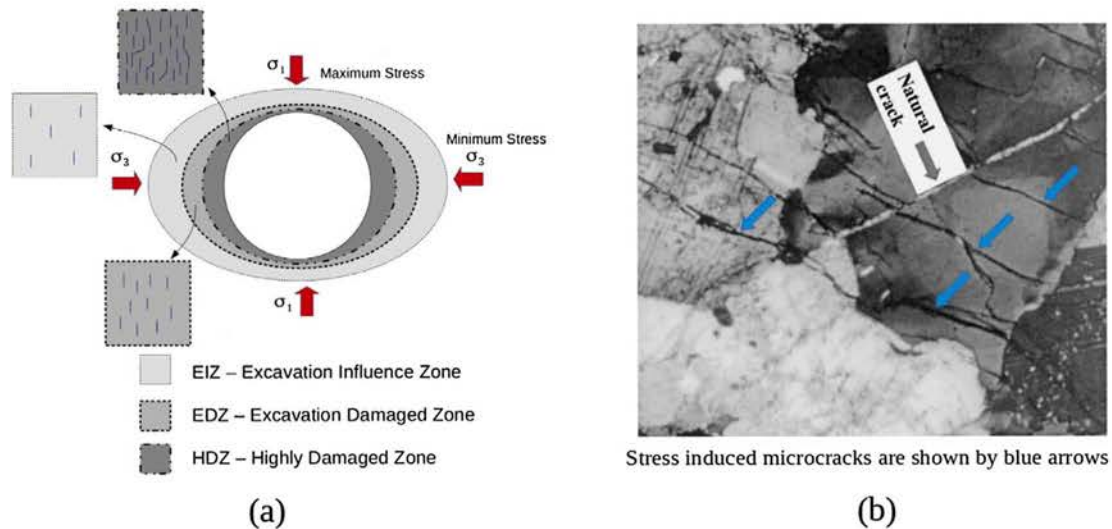


Fig. 1. Preferentially oriented microcracks in rocks: (a) at the engineering scale in an excavation damaged zone (EDZ), (b) at the grain scale in a granite (from [13]).

methods such as the finite element method (FEM), the extended finite element method (XFEM) or the boundary element method (BEM) use criterion generally based on the stress intensity factors (SIF) to simulate fracture initiation and propagation. On the other side of the spectrum, discontinuum methods like bonded particle models (BPMs) or lattice based methods (LMs) propagate cracks as a result of interparticle or element breakages according to the definition of their strength (e.g., their tensile strength). In such models, the propagation of fracture results from the nucleation, interaction and coalescence of microcracks and does not require specific numerical treatments contrary to most continuum approaches. Furthermore, discrete models such as BPMs are appealing since they constitute pertinent analogs to rock materials which present inherent discrete microstructures and provide an explicit framework to test hypotheses about how the microstructure affects the macroscopic behavior of material as proposed, for instance, by Schöpfer et al. [24] or Hamdi et al. [25].

The focus of this work being toward understanding how stress induced microcracks affect the mechanical properties of rocks, a comprehensive study is proposed based on a series of simulations performed on synthetic rock samples containing pre-existing microcracks. In Section 2, we provide a brief description of the BPM utilized for the study and describe the strategy used to include microcracks swarms of different intensities and orientations in the numerical specimens. In Section 3, the uniaxial tensile behavior of both intact and microcracked media is assessed and discussed. In Section 4, the initiation and propagation of mode I fracture is investigated considering, here again, both intact and microcracked media. Finally, conclusions are given in Section 5.

## 2. Methodology

To investigate the influence of microcracks on the tensile fracture behavior of rocks we utilized the BPM implemented in the open source software YADE Open DEM [26]. As for any classical DEM, the numerical algorithm consists of two steps. In the first step, the interaction forces taking place between the particles constituting the medium are calculated following pre-defined force-displacement laws. In the second step, the acceleration of each particle is computed by applying Newton's second law of motion and their position updated by an explicit time domain integration scheme. This process is repeated iteratively until the end of the simulation.

The formulation of the BPM used in the present study is introduced in Section 2.1. In Section 2.2, we describe the strategy proposed to introduce pre-existing microcracks swarms into the numerical medium.

### 2.1. Model formulation

The rock material is simulated as an assembly of bonded spherical particles. Even though the model is substantially similar to other BPM (e.g. [27] or [28]), a major difference lies in the consideration of near neighbor interactions through a controlled interaction range. This specific feature provides the possibility to adjust the degree of interlocking of the constitutive particles forming the numerical medium and to reproduce characteristic features of rock like materials [29]. In particular, by increasing the number of bonds per particle, high values of the compressive to tensile strength ratio as well as non linear failure envelopes can be simulated. Practically, the definition of an interaction range coefficient enables to define bonds between particles that are not in strict geometric contact with one another but still in the neighboring zone. Given a previously generated particle assembly, interparticle bonds are formed between pairs of particles for which the following equation is fulfilled:

$$D_{AB}^0 \leq \gamma_{int}(R_A + R_B) \quad (1)$$

with  $R_A$  and  $R_B$  the radii of the two particles A and B,  $D_{AB}^0$  the initial distance between the two centroids of A and B, and  $\gamma_{int} \geq 1$  the interaction range coefficient. Following such concept, first proposed in [30], the average number of bonds per particle,  $N_b$ , can be increased by increasing  $\gamma_{int}$ . The approach provides a relatively simple yet effective alternative to the use of non spherical particles [31] or dedicated formulations proposed for instance by [32] or [33] to enhance particle interlocking.

In addition to this microstructural feature, the behavior of the system is defined through the normal and shear forces developing between each pair of interacting particles.  $D_{AB}$  being the current value of the distance between the two centroids, the normal force  $F_n$  is computed from the normal relative displacement  $u_n = D_{AB}^0 - D_{AB}$  ( $u_n$  increases when spheres get closer to each other) such as:

$$F_n = k_n u_n \quad (2)$$

with  $k_n$  computed as:

$$k_n = 2Y \frac{R_A R_B}{R_A + R_B} \quad (3)$$

where  $R_A$  and  $R_B$  are the radii of the particles and  $Y$  is an equivalent elastic modulus (in Pa).

In compression,  $F_n$  is not restricted and can increase indefinitely. In tension,  $F_n$  can increase up to a threshold value  $F_n^{max}$  defined as:

$$F_n^{max} = tA_{int} \quad (4)$$

with  $t$  the bond tensile strength (in Pa) and  $A_{int} = \pi \times \min(R_A, R_B)^2$  a surface related to the size of the particles. When the tensile strength of the bond is exceeded, a mode I (tensile) microcrack is generated, represented as a circular surface with an area equal to  $A_{int}$  and oriented perpendicularly to the branch vector joining A and B.

The shear force  $\vec{F}_s$  is computed in an incremental manner such as:

$$F_s^{(t)} = F_s^{(t-\Delta t)} + k_s \Delta u_t \quad (5)$$

with  $k_s$  the shear stiffness calculated from the second elastic parameter of the model,  $P$  (dimensionless) defined as:

$$k_s = Pk_n \quad (6)$$

The shear force can increase up to a threshold value  $F_s^{max}$  defined by a Mohr-Coulomb type criterion:

$$F_s^{max} = cA_{int} + F_n \tan(\phi) \quad (7)$$

where  $\phi$  is the friction angle (in  $^\circ$ ) and  $c$  is the cohesion (in Pa). When the maximum shear force is exceeded, a mode II (shear) microcrack is generated, represented as a circular surface with an area equal to  $A_{int}$  and oriented perpendicularly to the branch vector joining A and B.

In addition, a global non-viscous damping is used in the numerical scheme in order to dissipate kinetic energy and to facilitate convergence toward quasi-staticity (see for example [28] for details). This numerical damping was arbitrarily fixed equal to 0.4 for all the simulations performed in the present study and the loadings applied so as to ensure quasi-static responses of the models.

## 2.2. Introduction of microcracks swarms

BPMs are classically built considering initially intact media within which microcracks can nucleate as a result of the loading (the so-called “stress-induced microcrack”). The purpose of the study being to grasp the influence of pre-existing microcracks on the behavior of rocks, a strategy was developed to replace a certain amount of the interparticle bonds by microcracks prior to loading (Fig. 2). These debonded contacts can be reoriented irrespective of their initial orientation thanks to the joint contact logic introduced in [34]. Here, in order to represent microcracks swarms resulting from a mechanical perturbation of the rock material like, for example, a tunnel excavation, the drilling of a borehole or even a certain tectonic history, we chose to define a unique orientation for all the pre-existing microcracks (Fig. 2). Doing so, these microcracks can be interpreted as resulting from local mode I rupture due to either direct or indirect tensile loadings as commonly observed in zones of high deviatoric stresses, e.g., in the vicinity of an excavation. Obviously, the number of pre-existing microcracks introduced in the medium can be adjusted depending on the degree of the stress perturbation or of the damage under consideration. The amount of pre-existing microcracks is controlled by the angle range  $\Delta\theta$ , which identifies every interparticle bonds dipping subparallel to the plane of preferential stress perturbation so as to replace them by non cohesive contacts exactly parallel to the plane of perturbation. This approach is

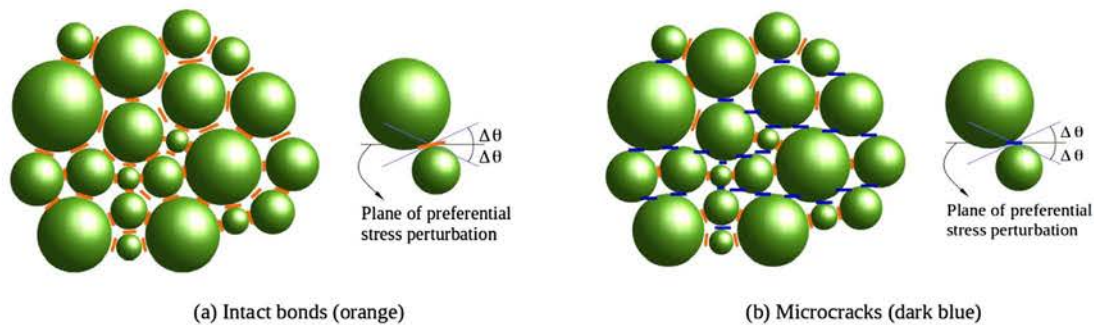


Fig. 2. Introduction of microcracks in the numerical medium: (a) identification of the interparticle bonds dipping subparallel to the plane of preferential stress perturbation thanks to the angle range  $\pm \Delta\theta$ , (b) debonding and reorientation of the identified contacts along the plane of preferential stress perturbation.

an adaptation of the technique used by Dinç and Scholtès to model anisotropic argillaceous rocks [35].

Two parameters are defined to characterize the microcracks swarms introduced within the medium:

- the microcracks intensity  $P_{32}$  (in  $m^{-1}$ ) defined as the total surface of microcracks over the total volume of the medium (as proposed in [36]), calculated in our BPMs such as:

$$P_{32} = \frac{\sum_{i=1}^{N_{mc}} A_{mc,i}}{V} \quad (8)$$

with  $A_{mc}$  the surface of each microcrack such that  $A_{mc} = A_{int}$  with  $A_{int}$  defined in Section 2.1,  $N_{mc}$  the total number of microcracks and  $V$  the volume of the sample under consideration.

- the microcracks orientation  $\theta$  (in  $^\circ$ ) defined, in the following, with respect to the direction of the loading applied to the medium ( $\theta = 0^\circ$  means that the microcracks are oriented perpendicular to the loading direction).

## 3. Tensile behavior

The capability of the BPM to model brittle rocks has been demonstrated in many studies during the last decades [28,37,29]. In this section, we first present several numerical results intended to emphasize the relevance of such an approach to simulate representative rock behaviors, focusing more particularly on uniaxial tensile loading conditions. Then, we illustrate how microcracks affect the tensile properties of rocks depending on their intensity and orientation.

### 3.1. Intact material

#### 3.1.1. Reference behavior

The model was calibrated so that its properties are representative of a sedimentary rock (Tournemire argillite characterized in [38]) presenting a Young's modulus  $E$  equal to 21 GPa, a Poisson's ratio  $\nu$  of 0.15, a uniaxial tensile strength  $UTS$  of 5 MPa and a uniaxial compressive strength  $UCS$  of 30 MPa. The calibration procedure of the BPM was presented in [29] and will not be detailed here. The parameters resulting from the calibration are given in Table 1.

In order to illustrate the model's predictions, a direct tensile test simulation was performed on a 3D sample of  $0.1 \times 0.2 \times 0.1 m^3$  (Fig. 3). A loading rate of  $0.2 m.s^{-1}$  was selected based on a preliminary study so as to ensure the quasi-staticity of the simulated response. In addition, because the loading consists in forcing the displacement of the particles making up the boundaries of the sample, interparticle bonds were strengthened in the vicinity of the sample ends in order to avoid stress concentration and to ensure the rupture to result from material failure only. These zones of high strength present a length equal to  $0.2 \times 2L$ , with  $2L$  being the total length of the sample.

Overall, the simulated stress-strain response shows characteristics of

**Table 1**  
Microproperties of the calibrated BPM model (see Section 2.1 for definitions).

Interparticle parameters	Value
Coordination number $N_{b0}$ [-]	10
Elastic modulus $Y_0$ [GPa]	27
Stiffness ratio $P_0$ [-]	0.4
Tensile strength $t_0$ [MPa]	6
Cohesion $c_0$ [MPa]	15
Friction angle $\phi_0$ [°]	0

brittle rocks behavior with, firstly, a linearly elastic behavior, secondly, the nucleation of microcracks at about 75% of the peak stress and, thirdly, the brittle rupture of the sample. Pre and post failure spatial distributions of stress induced microcracks are presented in Fig. 3b and c respectively. As expected for brittle rock materials, all these microcracks result from mode I interparticle rupture and present a preferential orientation subperpendicular to the loading direction. One can note that, before the appearance of a localized surface associated to the rupture of the sample, the microcracks are homogeneously distributed inside the medium at nucleation (Fig. 3b). In agreement with rock damage mechanics, these stress induced microcracks tend to decrease progressively the overall stiffness of the material before failure. These homogeneously distributed and preferentially oriented microcracks are also commonly observed in rock samples subjected to compressive loading and constitute a key feature of stress induced damage that we aim to study in the following.

### 3.1.2. Sensitivity analysis

Before proceeding further into the analysis, it is essential to identify potential bias emerging from the model formulation and its implementation. Based on the set up presented in the previous section, a series of simulations was performed on the exact same specimen to determine the influence of the numerical parameters on the emergent macroscopic properties. Because we focus specifically here on the tensile fracture behavior, we only consider the effect of the model’s parameters on its Young’s modulus  $E$  and on its uniaxial tensile strength  $UTS$ .

In accordance with the calibration procedure presented in [29], the uniaxial tensile response of the model is directly affected by  $Y$  and  $t$  (see definitions in Section 2.1). More precisely,  $E$  is proportional to  $Y$  while the  $UTS$  is proportional to  $t$  as illustrated in Figs. 4 and 5 respectively. One can note also that these two parameters have independent effect on the simulated macroscopic properties with no influence of  $Y$  on the  $UTS$

and no influence of  $t$  on  $E$ .

To sum up, the Young’s modulus  $E$  of the numerical medium is a direct function of the elastic modulus  $Y$ , while its uniaxial tensile strength  $UTS$  is a direct function of the interparticle tensile strength  $t$ .

In addition to the constitutive parameters of the model, it is also important to determine whether or not the simulated behavior is affected by the resolution of the model (i.e. the size of its constitutive particles). For instance, the particles making up a BPM do not necessarily correspond to the grains of the material under consideration and may rather be considered as mesh elements whose size might be chosen arbitrarily as in classical continuum approaches. For that matter, another series of simulations was run on samples presenting the same dimensions but containing different numbers of particles. As depicted in Fig. 6, the model is mesh objective in the sense that the overall behavior is not affected by its resolution.

Going further, in an attempt to grasp the variability inherent to the packing method (compaction of a cloud of particles randomly distributed within the predefined volume), each simulation was run on 5 different samples presenting similar overall properties. As depicted in Fig. 6, the influence of the discretization on the emergent properties is negligible even though one can notice a slight decrease of the tensile strength with the decrease of the particle size.

This capability of the proposed BPM to ensure constant emergent properties results from the possibility to adjust the interaction range coefficient  $\gamma_{int}$  for each sample in order to ensure the same coordination number  $N_b$  whatever the particle assembly ( $N_b = 10$ , for this study). Of course, the assemblies must have similar structural properties (density, particle size distribution and overall homogeneity) for this feature to be effective.

With such result in mind, the discretization of the model can be considered as a measure to control some aspects of the simulation such as, e.g., the size distribution of the induced microcracks. Running models with given particle size distributions can also be considered depending on the objectives of the study. In such a case, the size of the simulated domain would have to be adjusted so as to comply with the computational effort since the latter is directly proportional to the number of particles making up the medium.

### 3.2. Material containing microcracks

In this section we discuss the impact of pre-existing microcracks on the Young’s modulus  $E$  and uniaxial tensile strength  $UTS$  of rock materials. To fulfill this objective, a series of simulations was performed on samples containing microcracks swarms of different intensities ( $P_{32}$ ) and orientations ( $\theta$ ).

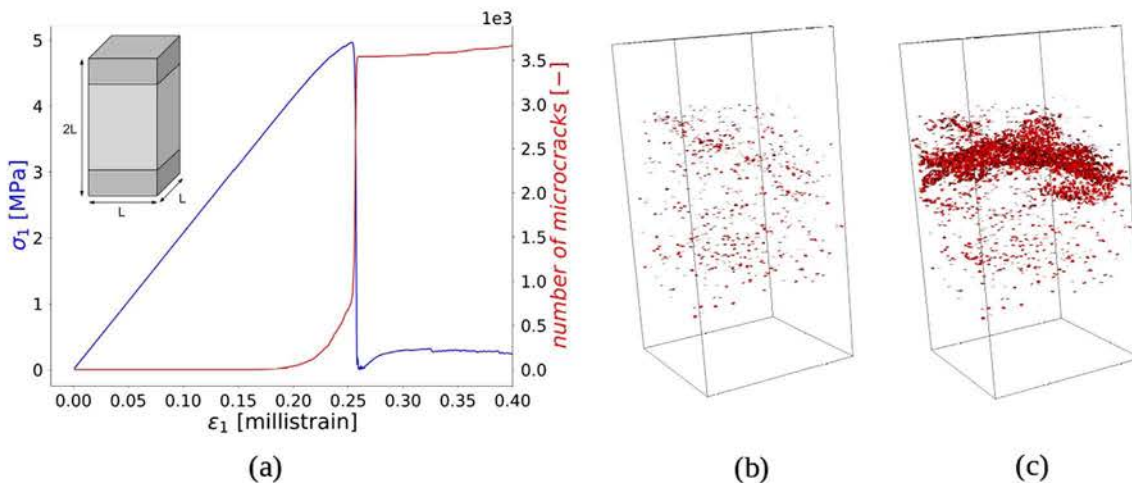


Fig. 3. Uniaxial tensile test simulation on an intact sample: (a) stress-strain response and spatio-temporal distribution of induced microcracks, (b) before the stress peak and (c) after the stress peak.

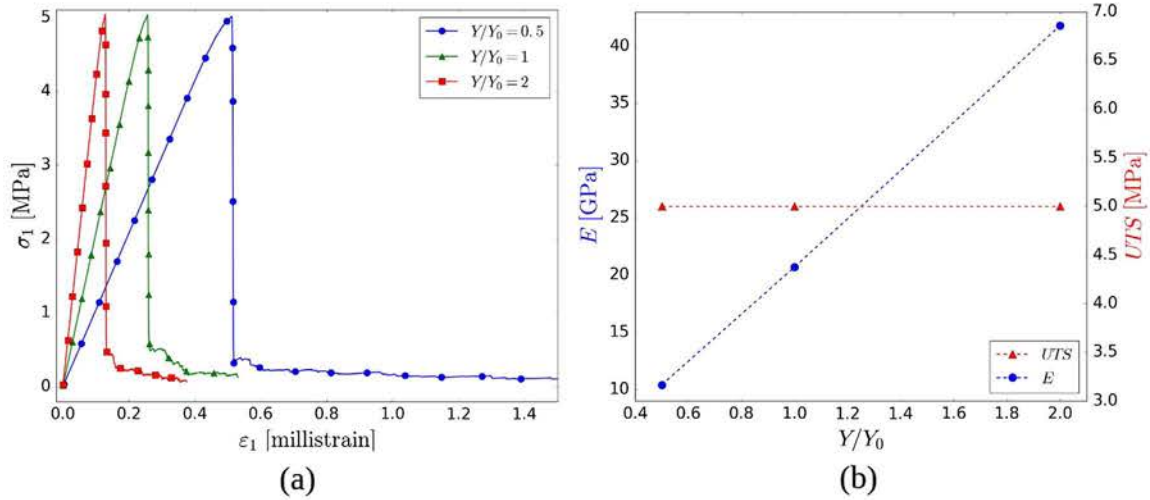


Fig. 4. Influence of  $Y$  on the tensile behavior of the BPM: (a) stress-strain responses and (b) variation of  $E$  and  $UTS$  as functions of  $Y/Y_0$ , with  $Y_0$  the elastic modulus of the reference material (see Table 1).

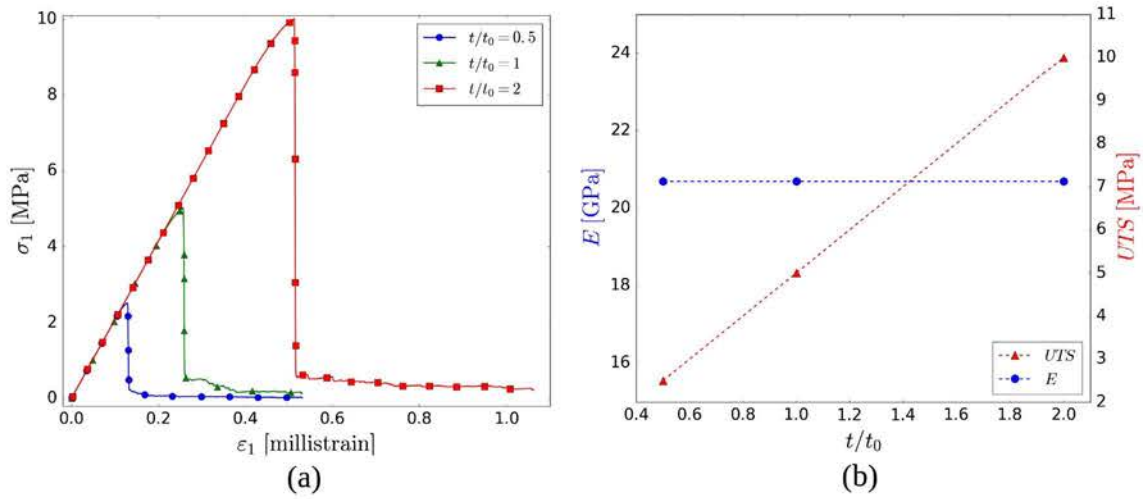


Fig. 5. Influence of  $t$  on the tensile behavior of the BPM: (a) stress-strain responses and (b) variation of  $E$  and  $UTS$  as functions of  $t/t_0$ , with  $t_0$  the interparticle tensile strength of the reference material (see Table 1).

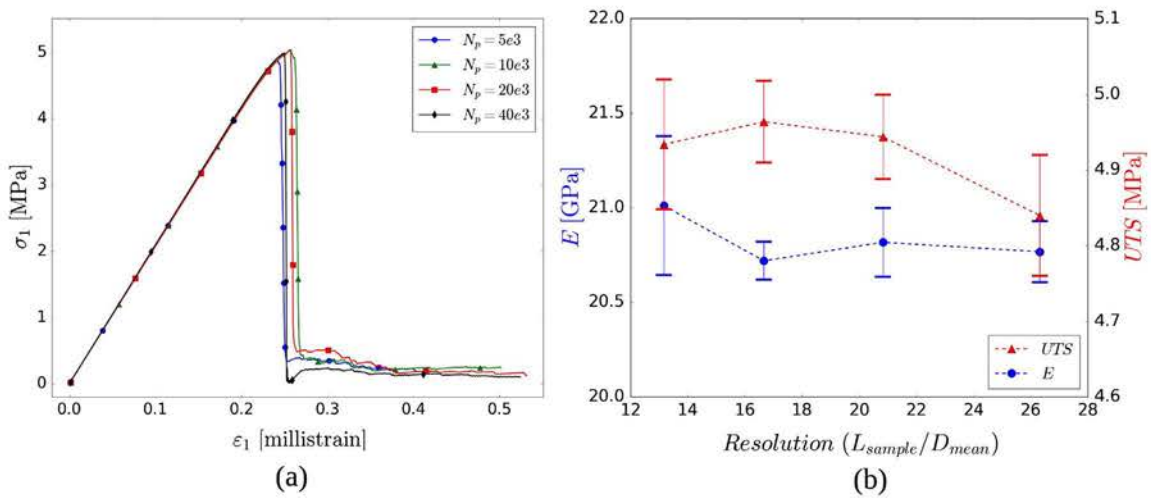


Fig. 6. Influence of the resolution of the BPM on its tensile behavior: (a) stress-strain responses of samples with same dimensions ( $0.1 \times 0.2 \times 0.1$  m) containing different numbers of particles  $N_p$ , (b) variation of  $E$  and  $UTS$  as functions of the resolution defined as the ratio between the sample smallest size  $L_{sample} = 0.1$  m and the mean particle size  $D_{mean}$ .

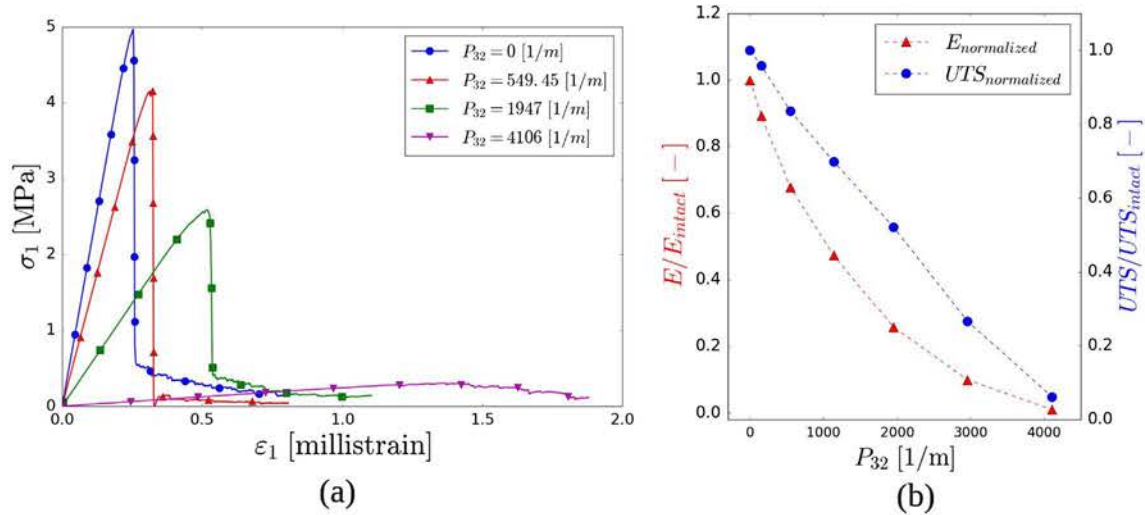


Fig. 7. (a) Stress-strain responses (uniaxial tension) of 3 samples containing different amounts ( $P_{32}$ ) of horizontal ( $\theta = 0^\circ$ ) microcracks. (b) Evolution of Young's modulus ( $E$ ) and uniaxial tensile strength ( $UTS$ ) as functions of the microcracks intensity ( $P_{32}$ ).

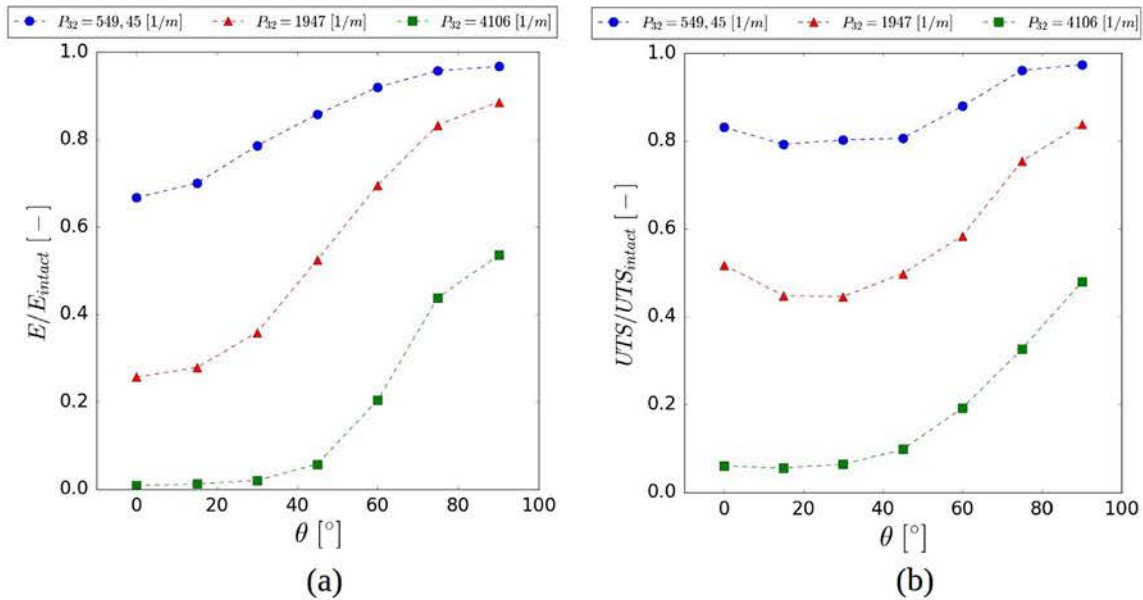


Fig. 8. Variations of (a) Young's modulus ( $E$ ) and (b) uniaxial tensile strength ( $UTS$ ) as functions of the microcracks orientation with respect to the loading direction ( $\theta$ ), considering different microcracks intensities ( $P_{32}$ ).

The numerical model used here is the same that was used in Section 3.1 (Fig. 3). Pre-existing microcracks are simply inserted within the medium following the methodology presented in Section 2.2.

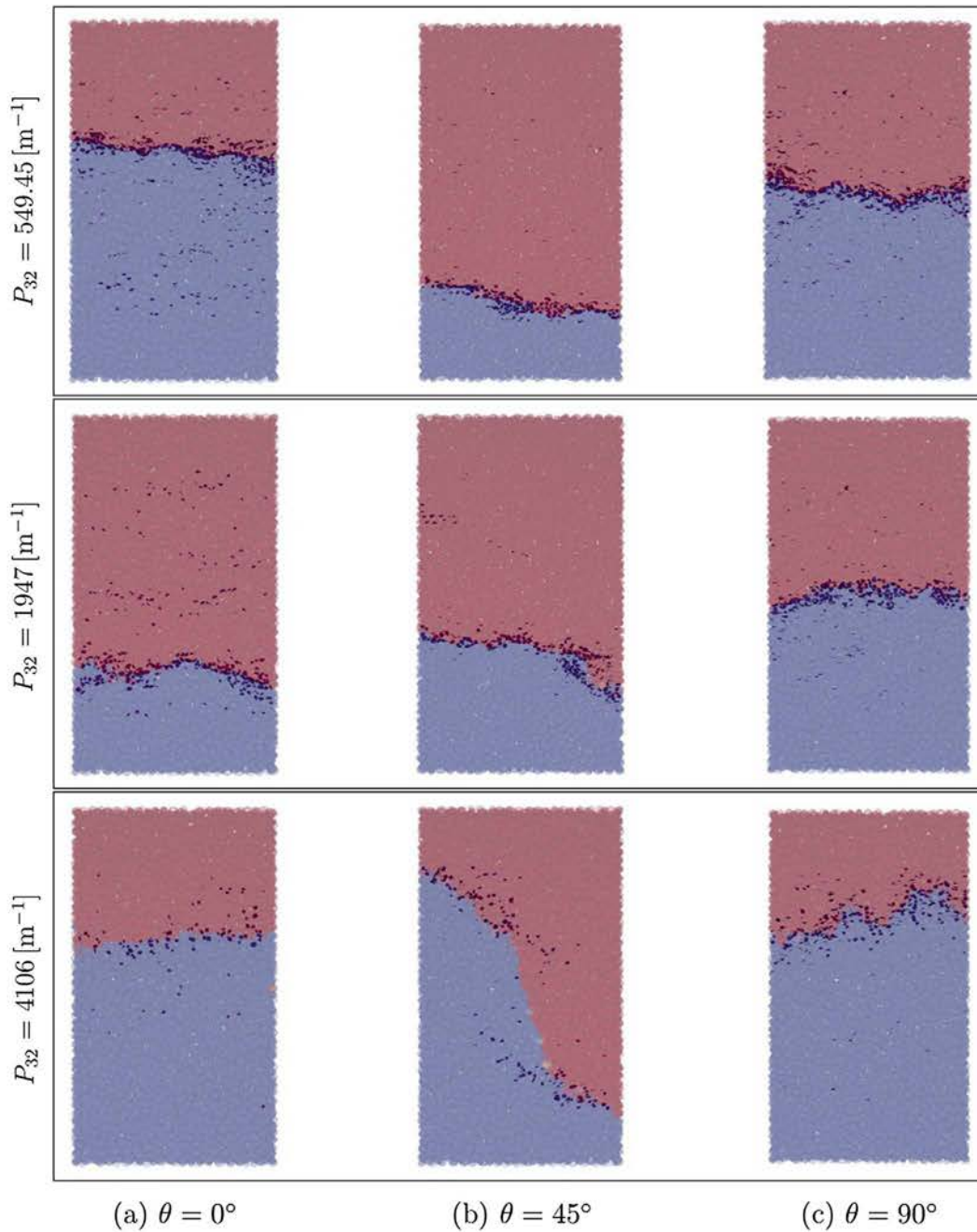
First, we considered microcracks swarms oriented perpendicular to the loading direction ( $\theta = 0^\circ$ ) and focused on the influence of their number on the simulated behavior. The stress-strain responses obtained for specimens with microcrack intensity  $P_{32}$  equal respectively to  $0 \text{ m}^{-1}$  (intact material),  $549.45 \text{ m}^{-1}$ ,  $1947.0 \text{ m}^{-1}$  and  $4106.0 \text{ m}^{-1}$  are presented in Fig. 7a. Clearly, both the elastic modulus and material strength decrease with the increase in microcrack intensity. In addition, one can note that the samples with  $P_{32} = 0 \text{ m}^{-1}$ ,  $P_{32} = 549.45 \text{ m}^{-1}$  and  $P_{32} = 1947 \text{ m}^{-1}$  exhibit brittle behaviors with a sharp decrease of the stress after the peak while the model with  $P_{32} = 4106.0 \text{ m}^{-1}$  doesn't show the same characteristic. The evolution of  $E$  and  $UTS$  as functions of  $P_{32}$  (Fig. 7b) reveals the detrimental impact of microcracks on the tensile behavior of the medium. Using least squares approximations, the relationships between  $E$  and  $P_{32}$  and  $UTS$  and  $P_{32}$  can be formulated as follows:

$$\frac{E}{E_{intact}} \approx (6.4e-8) \times P_{32}^2 - (5e-4) \times P_{32} + 0.967 \quad (9)$$

$$\frac{UTS}{UTS_{intact}} \approx (-2.3e-4) \times P_{32} + 0.978 \quad (10)$$

To go further, we investigated the influence of the microcracks orientation on the response of our synthetic rock material. For that purpose, we considered different values of  $\theta$  ranging from  $0^\circ$  (cracks perpendicular to the loading direction) to  $90^\circ$  (cracks parallel to the loading direction). The results are summarized Fig. 8.

Overall, it appears that  $E$  and  $UTS$  increase when  $\theta$  increases from  $0^\circ$  to  $90^\circ$  whatever the amount of microcracks present in the medium. This results from the fact that, for  $\theta = 90^\circ$ , the microcracks are parallel to the loading direction and thus have a limited effect on the distribution of the maximum principal stress inside the medium while, for  $\theta = 0^\circ$ , the microcracks projected fractured surface is maximum with respect to the maximum principal stress direction. The increase of  $E$  and  $UTS$  as a function of  $\theta$  tends to be monotonic, except for the case of the sample with  $P_{32} = 1947 \text{ m}^{-1}$  for which the  $UTS$  reaches its minimum value for



**Fig. 9.** Failure patterns resulting from uniaxial tension tests simulations performed on samples containing different intensities ( $P_{32}$ ) of microcracks presenting different orientations ( $\theta$ ) with respect to the loading direction. The colors represent the displacement of the particles: blue for displacements oriented toward the bottom of the sample and red for displacement oriented toward the top. The dark disks represent the induced microcracks. (For interpretation of the references to color in this figure legend, the reader is referred to the web version of this article.)

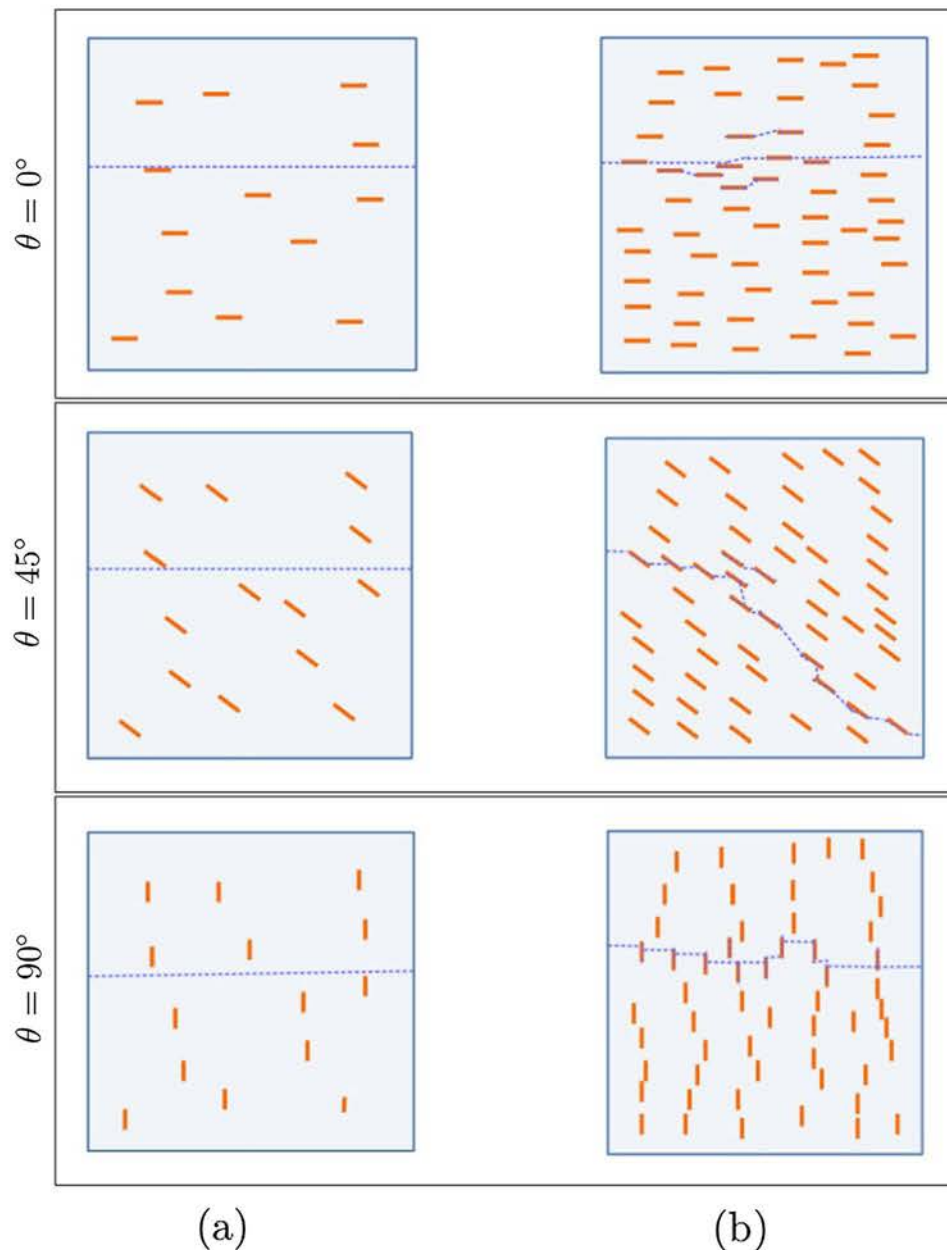
$15^\circ \leq \theta \leq 30^\circ$ .

Remarkably, the induced anisotropy is more pronounced when more microcracks are present within the medium. For instance, the ratio  $E_{90}/E_0$  is equal to 1.45, 3.45 and 59.16 for  $P_{32}$  respectively equal to  $549.45 \text{ m}^{-1}$ ,  $1947 \text{ m}^{-1}$  and  $4106 \text{ m}^{-1}$ . Similarly, the ratio  $UTS_{90}/UTS_0$  is equal to 1.17, 1.62 and 8 for  $P_{32}$  respectively equal to  $549.45 \text{ m}^{-1}$ ,  $1947 \text{ m}^{-1}$  and  $4106 \text{ m}^{-1}$ . It is also interesting to notice that for the highest value of  $P_{32}$  ( $4106 \text{ m}^{-1}$ ),  $E$  and  $UTS$  are almost null when  $\theta < 45^\circ$ . This characteristic emphasizes the role of the microcracks orientation with respect to the loading direction and, hence, the resulting anisotropy which, in this case, suggest that the medium could not support any load oriented such that  $\theta < 45^\circ$ .

### 3.3. Discussion

As previously demonstrated in [24,39,19] for randomly distributed sets of microcracks (*i.e.*, for thermally induced microcracks), the strength of rocks is dependent upon the amount of microcracks contained inside the medium. An increase in the number of microcracks results in a decrease of both  $UTS$  and  $E$  which can be related to the microcrack intensity  $P_{32}$  (Fig. 7b and Eqs. (9) and (10)). The relationships between  $E$  and  $P_{32}$  and between  $UTS$  and  $P_{32}$  are certainly influenced by the microcracks orientation distribution (Fig. 8) but, overall, seems logical since microcracks tend to weaken the structural integrity of the material.

Preferentially oriented microcracks induce an anisotropy to the



**Fig. 10.** Conceptual representation of tensile failure (dashed blue lines) developing in samples containing respectively small (a) and large (b) amounts of pre-existing microcracks (orange dashes), considering different orientations with respect to the loading direction (oriented in the vertical direction here). (For interpretation of the references to color in this figure legend, the reader is referred to the web version of this article.)

medium whose degree is directly related to their intensity (Fig. 8). The higher  $P_{32}$  is, the more pronounced the degree of induced anisotropy is. Moreover, because of the preferential orientation of the microcracks, the induced anisotropy show directional dependencies similar to what has been observed in transversely isotropic rocks [40,41]. This microcracks induced transverse isotropy has already been described in numerous studies focusing on the effect of stress induced cracks on elastic properties and wave propagation in rocks [42–45] or on damage induced permeability [46–48]. We show here how they directly affect both the elastic and strength properties of rocks.

Focusing now on the influence of pre-existing microcracks on the failure patterns of the different specimens (Fig. 9), one can see that, on the one hand, low microcrack intensities (e.g.,  $P_{32} = 200.3 \text{ m}^{-1}$ ) do not affect the development of the failure surface which tends to remain sub-perpendicular to the loading direction for all orientations. On the other hand, for the highest microcrack intensity ( $P_{32} = 4106 \text{ m}^{-1}$ ), the failure

surface is greatly deviated when  $\theta = 45^\circ$  (see Fig. 9). A conceptual representation of the mechanisms involved is proposed in Fig. 10. For low  $P_{32}$ , failure develops without seeing the pre-existing defects. The microcracks are scarcely distributed within the medium, thus limiting the chance for the failure surface to be deviated from its intrinsic path. The final failure surface remains sub-perpendicular to the loading regardless of the orientation of the microcracks and the response of the specimen remains brittle (Fig. 11a)). For high  $P_{32}$ , failure develops as a result of branching across the pre-existing microcracks (in a step-path manner) and might thus be strongly deviated from its intrinsic path if these microcracks are inclined with respect to the direction of the maximum principal stress. This branching mechanism produces different responses at the material scale depending on  $\theta$  as shown in Fig. 11b. For  $\theta = 90^\circ$ , the sample fails in a very brittle manner, resulting from the simultaneous ruptures of all the intact rock bridges located in between the microcracks. On the contrary, these rock bridges break in a



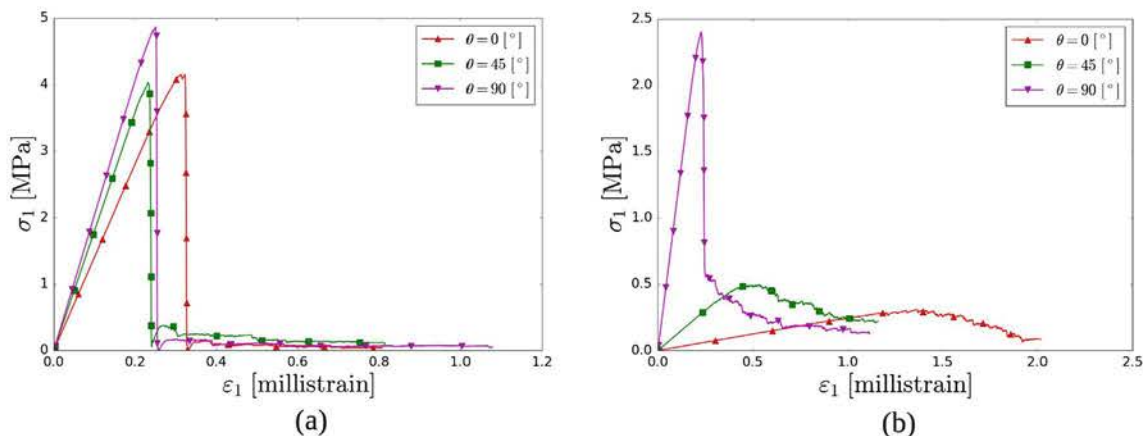


Fig. 11. Stress-strain responses (uniaxial tension) of samples containing microcracks swarms presenting different orientations ( $\theta$ ) with respect to the loading direction: (a) low microcracks intensity ( $P_{32} = 549.45 \text{ m}^{-1}$ ) and (b) high microcracks intensity ( $P_{32} = 4106.0 \text{ m}^{-1}$ ).

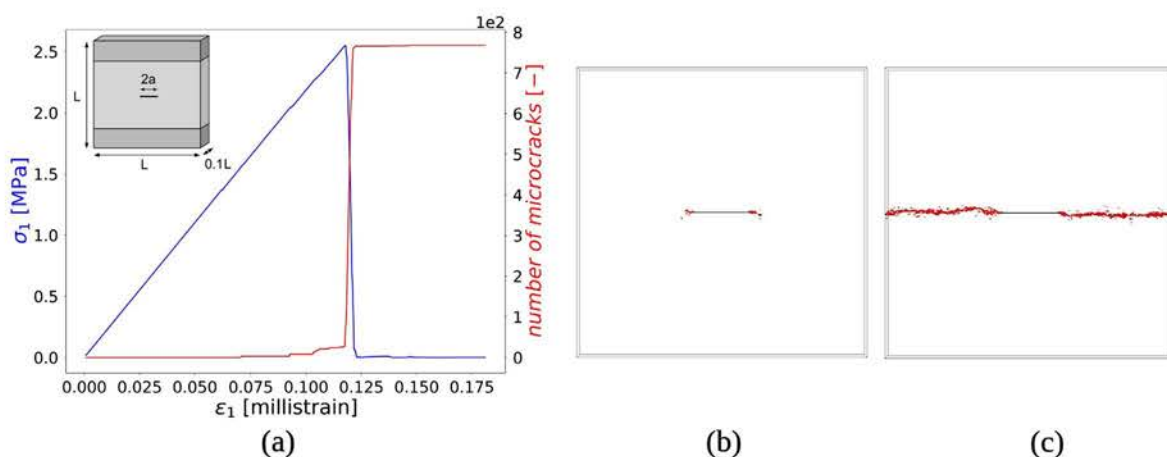


Fig. 12. Uniaxial tensile test simulation on a centre cracked sample: (a) stress-strain response and spatio-temporal distribution of induced microcracks, (b) before the stress peak and (c) after the stress peak.

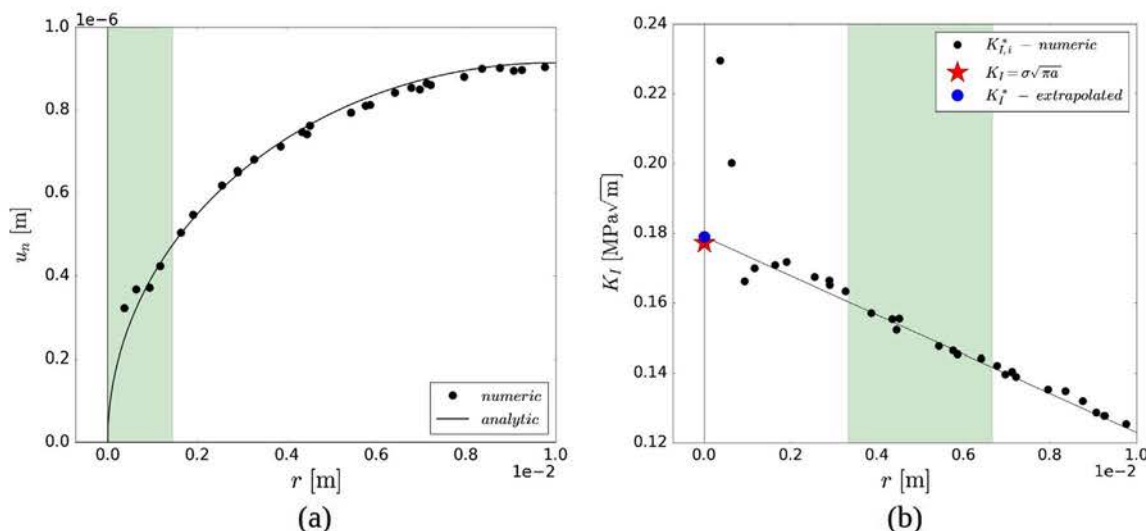


Fig. 13. Comparison of the BPM predictions with respect to LEFM (tensile loading of a centre cracked plate at  $\sigma = 1 \text{ MPa}$ ): (a) crack opening computed respectively from the particles displacement and from Eq. (12) (the shaded area illustrates the mean diameter of the particle) and (b) apparent stress intensity factor  $K_I^*$  computed with the displacement extrapolation method proposed by Kuang [51] (the shaded area indicates the portion of the crack lips used for the extrapolation). The theoretical value  $K_I = \sigma\sqrt{\pi a}$  is plotted on the graph for comparison purpose.

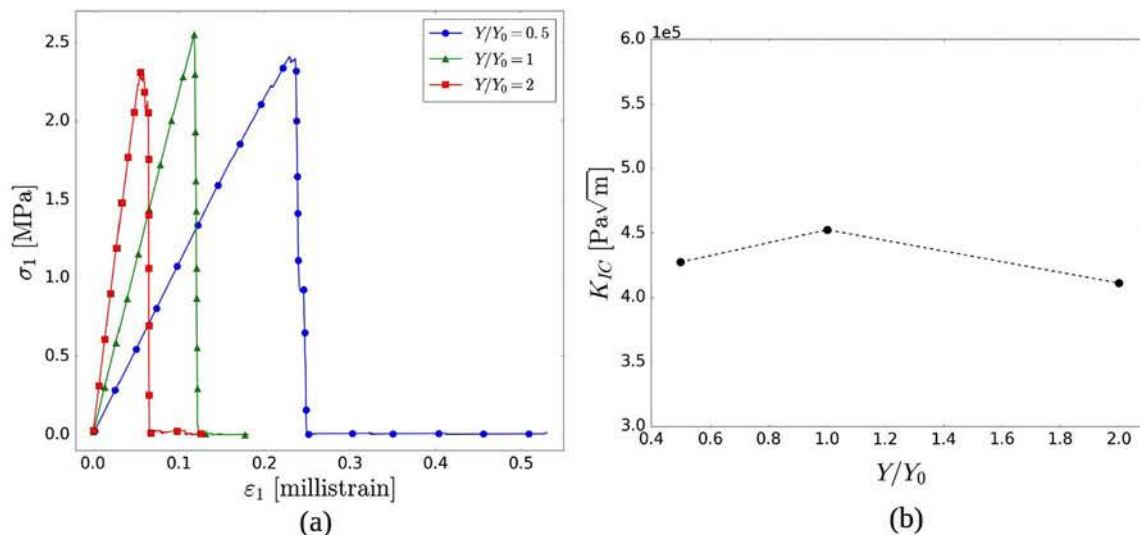


Fig. 14. Influence of  $Y$  on the mode I fracture behavior of the BPM: (a) stress-strain responses and (b) variation of  $K_{IC}$  as a function of  $Y/Y_0$ , with  $Y_0$  the elastic modulus of the reference material (see Table 1).

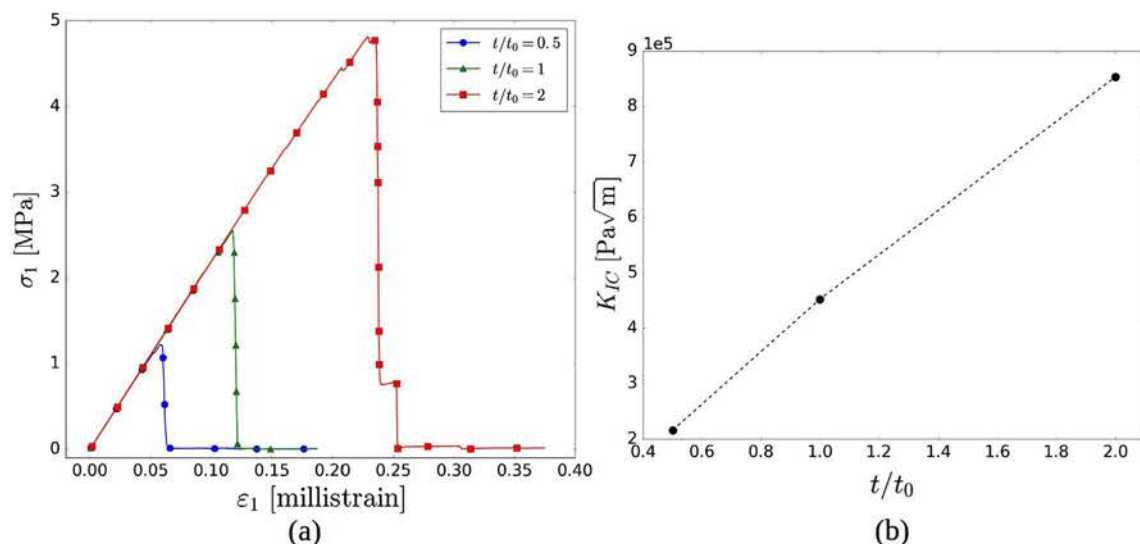


Fig. 15. Influence of  $t$  on the mode I fracture behavior of the BPM: (a) stress-strain responses and (b) variation of  $K_{IC}$  as a function of  $t/t_0$ , with  $t_0$  the interparticle tensile strength of the reference material (see Table 1).

progressive manner when the microcracks are inclined with respect to the loading direction, producing a less brittle behavior at the macroscopic scale. The failure surface develops by finding its path along the weakest regions of the medium which tends to delay the occurrence of failure at the material scale in both pre and post peak regimes. This delay in the failure process and the associated reduced brittleness can actually be observed for  $\theta < 45^\circ$  when a large amount of microcracks are present in the medium.

#### 4. Mode I fracture propagation

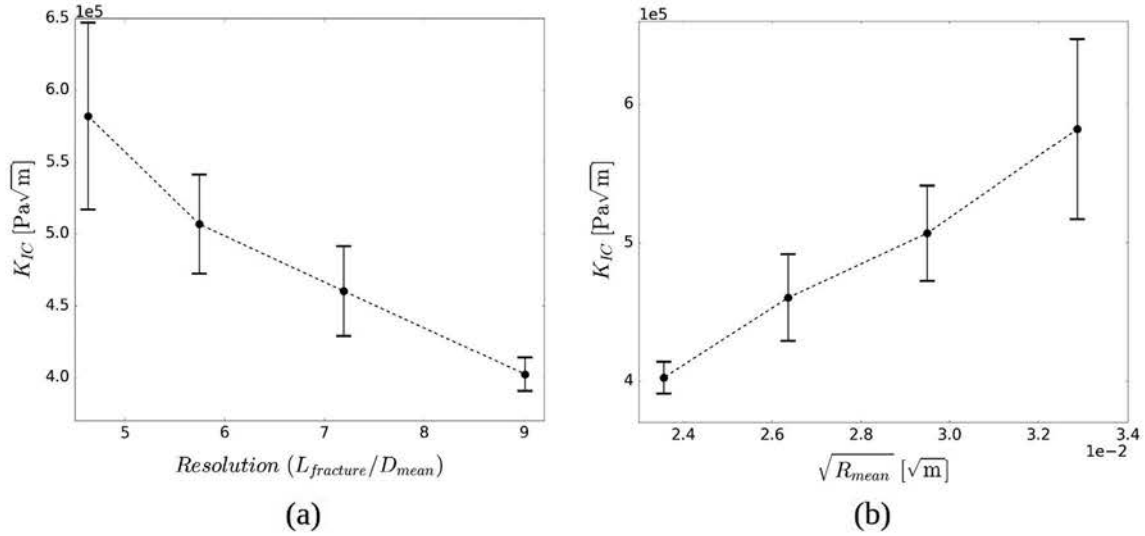
The proposed BPM has been successfully utilized to simulate the initiation and propagation of fractures in rocks at different scales and under different loading conditions [34,49,39]. We focus here on the propagation of mode I fractures in order to investigate the influence of microcracks on such a critical process. Firstly, we confront the BPM predictions to elementary Linear Elastic Fracture Mechanics (LEFM) concepts by simulating a cracked specimen under tension so as to assess its relevance for such purpose. Secondly, we illustrate how fracture propagation is affected by the presence of pre-existing microcracks

depending on their intensity and orientation.

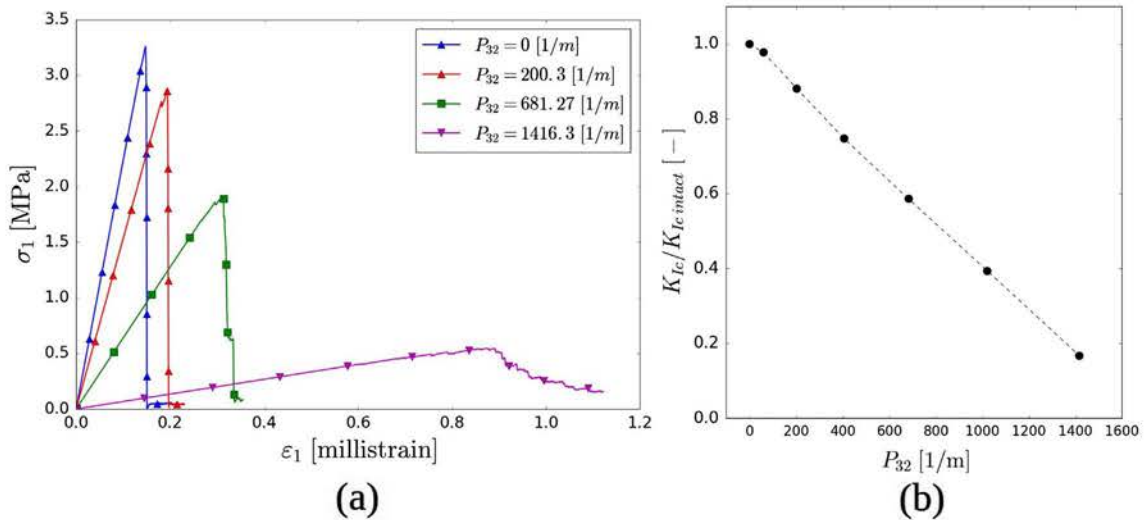
##### 4.1. Intact material

###### 4.1.1. Reference behavior

The study is performed on samples of  $0.1 \times 0.1 \times 0.01 \text{ m}^3$  containing a centre through thickness crack of length 0.02 m (Fig. 12). The crack is modelled as an interface along which the particles are initially unbonded. This pre-existing crack has no initial aperture and can thus be considered as a closed purely frictional fracture. As for the tests performed in Section 3, zones of high strength are defined at both ends of the sample to avoid boundary effects during the loading. In addition, in order to ensure plane strain condition, the translation of the particles in the out of plane direction (Z), as well as their rotations around the X and Y axes are blocked to force the model to behave as a pseudo 2D model. We chose to use such a configuration rather than a 3D sample with a finite thickness to eliminate the influence of the third dimension on the emergent properties of the simulated medium as well as to optimize the computational effort with respect to the objective of the study (propagation of mode I planar fractures).



**Fig. 16.** Influence of the resolution of the BPM model on its mode I fracture toughness. (a) Variation of  $K_{IC}$  as a function of the resolution defined as the ratio between the crack half length  $a = 0.001$  m and the mean particle diameter  $D_{mean}$ . (b) Variation of  $K_{IC}$  as a function of the square root of the mean particle radius  $R_{mean}$ .



**Fig. 17.** (a) Stress-strain responses (uniaxial tension) of 4 centre cracked samples containing different amounts ( $P_{32}$ ) of horizontal ( $\theta = 0^\circ$ ) microcracks. (b) Evolution of the fracture toughness ( $K_{IC}$ ) as a function of the microcracks intensity ( $P_{32}$ ).

As shown in Fig. 12, the simulated behavior corresponds to the behavior expected for a quasi-brittle material with, first, an elastic response and, second, the appearance of microcracks at the crack tips before the complete rupture of the sample. Material failure corresponds to the propagation of a fracture aligned with the initial flaw. One can note that, contrary to the case of the non-cracked specimen (Section 3.1.1), pre-failure damage is only concentrated in the vicinity of the crack tips due to the concentration of stress in these areas (the so-called “process zone”) and that all the microcracks nucleate along the final failure surface without any damage induced in the bulk of the simulated medium. The fracture initiates from stress concentration in the vicinity of the crack tips and propagates along the direction of the minimum principal stress, as expected from classic fracture mechanics.

#### 4.1.2. Comparison with LEFM

Stress intensity factors (SIFs) are the means by which LEFM evaluates the stress state of a cracked material. One of the most prominent methods to calculate SIF numerically relies on the J-integral introduced by Rice [50]. An alternative consists in using the displacement extrapolation method proposed by Kuang [51] which evaluates the apparent

SIFs from the relative displacements of the crack lips. For instance, in the case of mode I loading, the apparent mode I SIF  $K_I^*$  at the crack tip can be extrapolated from the local  $K_{I,i}^*$ , calculated from the local normal displacements  $u_{n,i}$  along the crack lips through the following equation [52]:

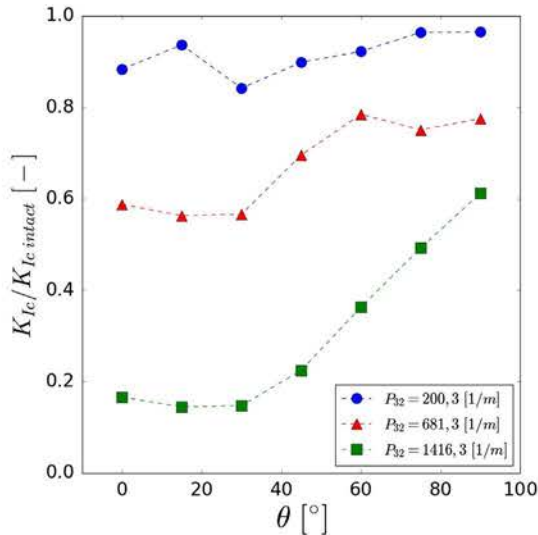
$$K_{I,i}^* = \frac{E}{4(1-\nu^2)} \sqrt{\frac{2\pi}{r}} u_{n,i} \quad (11)$$

where  $r$  corresponds to the distance from the crack tip,  $E$  is the Young’s modulus of the material and  $\nu$  its Poisson’s ratio.

In order to assess the capability of the BPM to describe the problem at stake (loading of a cracked homogeneous isotropic medium in this specific case), we first verified that the crack opening predicted by the model corresponds to the theoretical opening given by the following equation [53]:

$$u_n(r) = \frac{2(1-\nu^2)}{E} \sigma \sqrt{r(2a-r)} \quad (12)$$

where  $u_n$  is the normal displacement along the crack lips,  $\sigma$  the far field stress and  $a$  the half crack length.



**Fig. 18.** Variation of fracture toughness ( $K_{IC}$ ) as a function of the microcracks orientation with respect to the loading direction ( $\theta$ ), considering different microcracks intensities ( $P_{32}$ ).

The comparison between the displacement of the particles located along the crack lips and the analytical solution given by Eq. (12) confirms the accuracy of the BPM for describing the elastic deformation of a cracked medium (Fig. 13a). One can note that the displacement of the particles located close to the crack tip are slightly offset compared to the analytic solution due to the fact that the particle assembly was not built to be exactly conformed to the crack (the crack tips are not necessarily located at the exact location of an interparticle bond location). Nonetheless, the values of the SIF calculated using the displacement extrapolation method (Fig. 13b) is in very good agreement with the value computed from the boundary stress (relative error of 1% for this specific case), confirming therefore the relevance of the BPM with respect to LEFM concepts. One has to mention that the extrapolation of  $K_I^*$  from the local  $K_{I,i}^*$  must follow certain rules to be efficient. For instance, the set of particles used for the extrapolation must be chosen carefully as discussed in a recent study where the displacement extrapolation method was applied to compute SIFs in a distinct lattice model [54]. In particular, these particles must be located sufficiently far from the tip of the crack to avoid the effect of stress singularity in the evaluation of  $K_{I,i}^*$  and, at the same time, they must be located far enough from the middle of the crack so as to limit the influence of the change in curvature of the crack lips. In our case, we considered the particles with coordinate  $r \in \left[\frac{a}{3}, \frac{2a}{3}\right]$  for the extrapolation of  $K_I^*$  as indicated by the shaded area in Fig. 13b.

#### 4.1.3. Sensitivity analysis

As for the non-cracked material studied in Section 3, it is essential to determine how the predictions of the BPM can be affected by its constitutive parameters when applied to fracture propagation problems. More precisely, because the propagation of fractures in quasi-brittle materials is uniquely characterized by the value of their fracture toughness  $K_{IC}$ , we focus here on identifying which numerical parameters control the toughness of the BPM model by performing a series of simulations based on the set up presented in Section 4.1.1.

As expected from Section 3.1.2,  $K_{IC}$  is independent of  $Y$  (Fig. 14) while it is directly proportional to  $t$  (Fig. 15). The toughness  $K_{IC}$  of the numerical medium is thus a direct function of the interparticle tensile strength  $t$ .

In order to assess the influence of the model resolution on its fracture behavior, we performed another series of simulations on samples having the same dimensions but containing different numbers of particles. As shown in Fig. 16, the  $K_{IC}$  of the BPM model depends on the

size of its constitutive particles. More precisely,  $K_{IC}$  is proportional to the square root of mean radius ( $R_{mean}$ ) as suggested in previous studies by Potyondy and Cundall [28] and Duriez [49].

In views of these results, it appears that the size of the particles of BPM models dedicated to study fracture propagation cannot be chosen arbitrarily in order to match the fracture toughness of a given material if the model is calibrated based on the tensile strength of the same material. Obviously, this limitation does not exist if the model is calibrated based on the fracture toughness of the material or, if its formulation is modified so as to be non-local as proposed, in e.g. [55] or [56].

In the following, we get rid of this limitation by always considering the same particle size distribution for all simulations and by discussing the results in terms of relative variation of  $K_{IC}$  instead of absolute values.

#### 4.2. Material containing microcracks

In this section, we investigate the influence of pre-existing microcracks on mode I fracture propagation by incorporating microcracks swarms of different intensities and orientations in the numerical set up presented in Section 4.1.1.

We first studied the influence of the microcracks intensity  $P_{32}$  on the simulated behavior by considering microcracks oriented perpendicular to the loading direction such as  $\theta = 0^\circ$  (the microcracks are thus parallel to the initial crack). The associated stress-strain responses are presented in Fig. 17a. As expected, the strength (toughness) of the material decreases with the increase in microcracks intensity. As for the  $UTS$ , this diminution of  $K_{IC}$  is actually a linear function of  $P_{32}$  as shown in Fig. 17b and can be estimated from a least squares approximation as:

$$\frac{K_{IC}}{K_{IC, intact}} \approx (-6e-4) \times P_{32} + 0.99 \quad (13)$$

Regarding now the influence of the microcracks orientation on the material toughness, one can notice that the evolution of  $K_{IC}$  vs.  $\theta$  (Fig. 18) is qualitatively similar to the evolution of  $UTS$  vs.  $\theta$  (Fig. 8b).  $K_{IC}$  is minimum for  $\theta = 0^\circ$  and increases quasi-monotonously with  $\theta$  to reach its maximum value for  $\theta = 90^\circ$ . The toughness of the material is thus minimum when the microcracks are oriented sub-parallel to the initial fracture while it is maximum when the microcracks are oriented sub-perpendicular to it. Moreover, as for the  $UTS$ , the degree of anisotropy induced by microcracks increases with the increase in microcracks' intensity with  $K_{IC,90}/K_{IC,0}$  being equal respectively to 1.09 for  $P_{32} = 200.3 \text{ m}^{-1}$ , 1.32 for  $P_{32} = 681.3 \text{ m}^{-1}$  and 3.68 for  $P_{32} = 1416.3 \text{ m}^{-1}$ .

#### 4.3. Discussion

The decrease of the material toughness observed when more and more microcracks are present in the medium is, overall, logical and confirms the trends observed in experiments dedicated to assess the impact of thermal damage on fracture propagation [57,18]. It also corresponds to the trend observed for the evolution of  $UTS$  as a function of  $P_{32}$  in Section 3.2 which is consistent with experimental observations showing that  $UTS$  and  $K_{IC}$  are linearly related one with another [58]. The toughness anisotropy induced by the presence of preferentially oriented microcracks has already been observed in granitic rocks [20] and is, of course, more or less pronounced depending on the number of microcracks present in the material. As for the Young's modulus and the uniaxial tensile strength of microcracked samples (see Section 3.2), the evolution of the toughness as a function of the microcracks orientation shows a trend similar to what has been observed in transversely isotropic rocks (e.g., in shales [58]) with minimum toughness corresponding to the case where the fracture propagates parallel to the microcracks plane ( $\theta = 0^\circ$ ) and maximum toughness when the fracture propagates perpendicular to the microcracks plane.

Obviously, the dependence of the material toughness on the

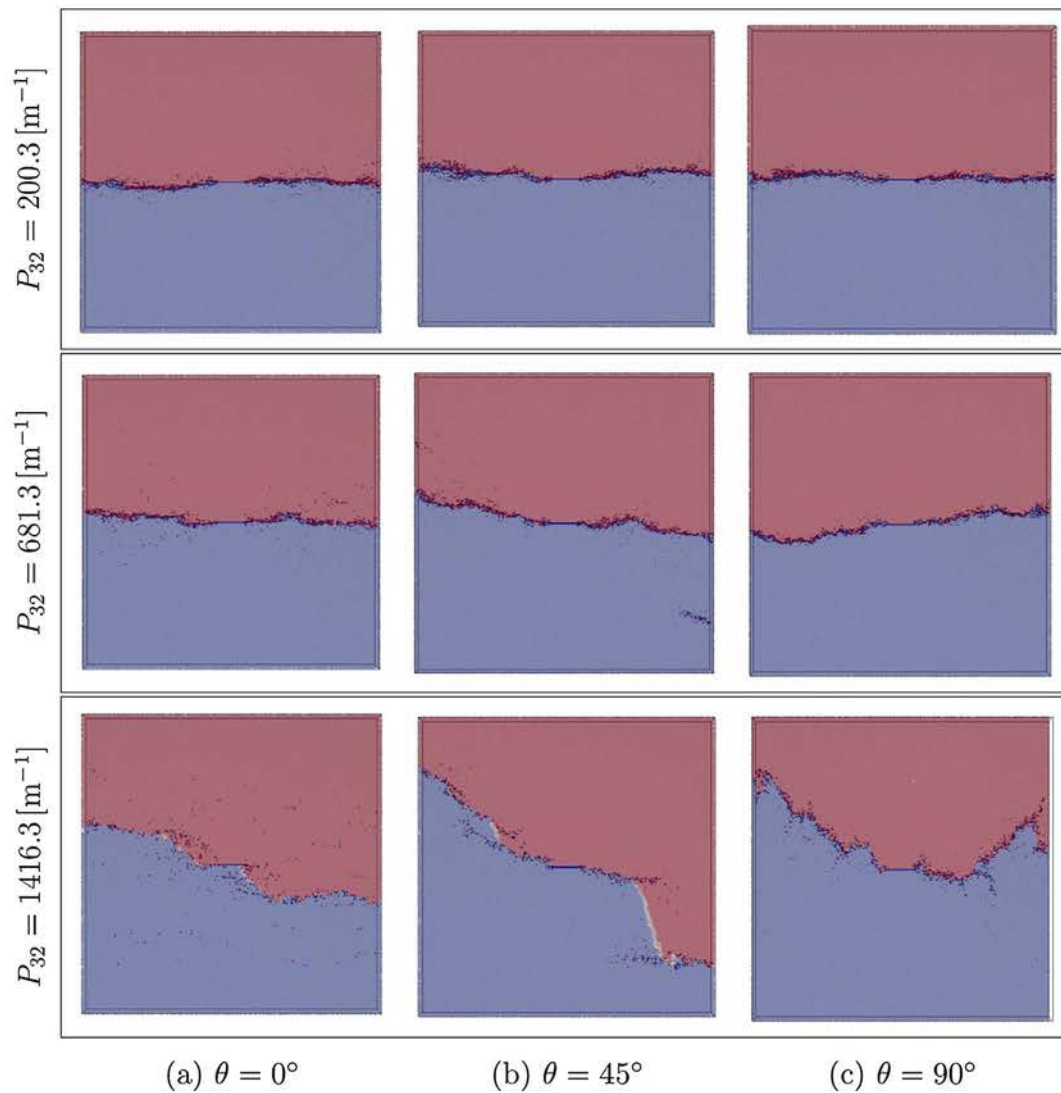


Fig. 19. Fracture patterns corresponding to centre cracked samples containing different amounts ( $P_{32}$ ) of microcracks presenting different orientations ( $\theta$ ) with respect to the loading direction subjected to uniaxial tension (vertical direction). The colors represent the displacement of the particles: blue for displacements oriented toward the bottom of the sample and red for displacement oriented toward the top. The dark disks represent the induced microcracks. (For interpretation of the references to color in this figure legend, the reader is referred to the web version of this article.)

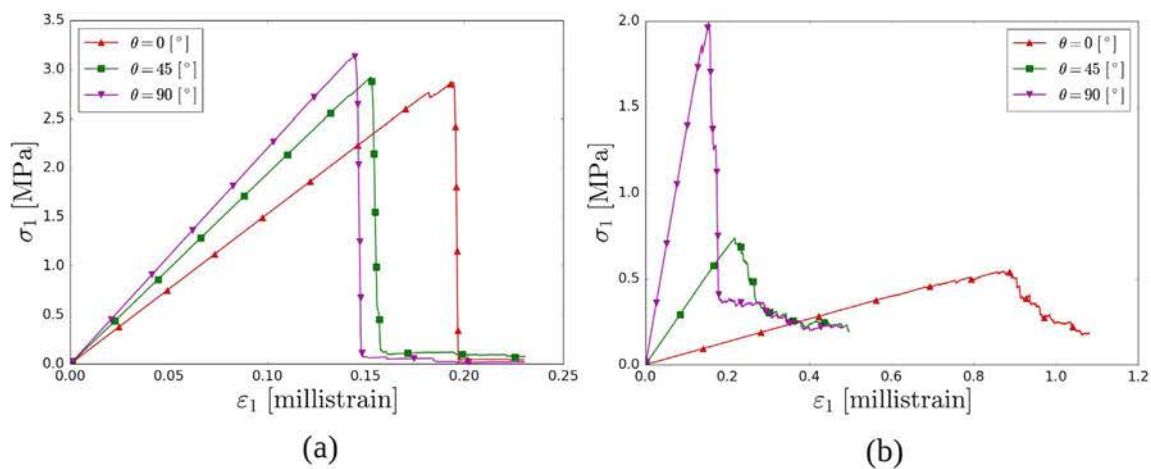


Fig. 20. Stress-strain responses (uniaxial tension) of centre cracked samples containing microcracks swarms presenting different orientations ( $\theta$ ) with respect to the loading direction: (a) low microcracks intensity ( $P_{32} = 549.45 \text{ m}^{-1}$ ) and (b) high microcracks intensity ( $P_{32} = 4106.0 \text{ m}^{-1}$ ).

orientation distribution of microcracks is directly related to the mechanisms taking place at the microscale. Microcracks act as weakness planes which can cause the deflection of propagating fractures depending on their amount as shown in Fig. 19. In general, the failure mechanisms correspond to the ones observed in the intact material (Fig. 10). On the one hand, scarcely distributed microcracks (e.g.,  $P_{32} = 200.3 \text{ m}^{-1}$ ) do not affect the failure process and the fracture propagates along the expected path whatever the microcracks orientation. On the other hand, densely distributed microcracks significantly interfere with the propagating fracture as illustrated for  $P_{32} = 1416.3 \text{ m}^{-1}$  where the fracture significantly deviates from its initial direction. The fracture kinks repeatedly during its propagation and presents thus a much greater final surface area than a straight crack. This is even more remarkable for the case where  $\theta = 0^\circ$  for which the fracture propagates in a non horizontal manner despite the fact that both pre-existing fracture and microcracks are oriented perpendicular to the loading. One can note however that, contrary to what has been observed experimentally in shale [58], the propagating fracture does not evidently tend to reorient itself along the microcracks plane, except maybe for intermediate orientations (e.g.,  $\theta = 45^\circ$ ). This characteristic might be due to the centre crack configuration used here which produces a symmetric distribution of stress within the medium and would thus deserve further investigation.

In terms of stress-strain responses (Fig. 20), it appears that the microcracks orientation modify the overall material behaviors only if they are densely distributed within the medium (hence when they affect the fracture process).

## 5. Conclusion

A discrete modeling approach is proposed to investigate the tensile fracture behavior of rock like materials containing pre-existing microcracks having a mechanical origin. For that purpose, a bonded particle model is utilized to simulate uniaxial tensile tests on synthetic rock samples containing microcracks swarms with pre-defined intensities and orientations.

The approach reproduces all the typical characteristics of brittle materials including, linear elastic behavior at small deformation, nucleation of stress induced microcracks before failure and development of macroscopic failure surfaces through the coalescence of these microcracks. Furthermore, the relevance of the modeling approach for studying mode I fracture propagation is confirmed by assessing its capabilities with respect to classic fracture mechanics concepts such as the consistency of the stress intensity factors at the fracture tip with respect to the far field stress, the description of a process zone resulting from stress induced microcracks at the fracture tip and the prediction of adequate fracture paths.

Overall, pre-existing microcracks tend to weaken both the elastic and strength properties of the materials in which they exist. More precisely, it is observed that the Young's modulus  $E$  decreases quadratically as a function of the microcrack intensity  $P_{32}$  while both the uniaxial tensile strength  $UTS$  and mode I fracture toughness  $K_{IC}$  decrease linearly with  $P_{32}$ . In addition, because stress induced microcracks usually present preferential orientations related to the loading history of the material, they induce anisotropy of material properties of otherwise apparently isotropic media. More specifically, the resulting anisotropy, whose degree is directly related to the microcracks intensity, show great similarities with transverse isotropy as confirmed by the evolutions of  $E$  and  $UTS$  as functions of the microcracks orientation with respect to the loading direction. Finally, if scarcely distributed microcracks do not affect the way rupture occurs in brittle materials, large amount of microcracks critically modify the mechanisms as well as the kinematics toward the overall material failure by enhancing branching or "step-path" failure mechanisms during fracture propagation. As a result of these incremental events occurring during the fracturing process, fractures can greatly deviate from their expected

path, producing tortuous failure surfaces within the medium.

The outcomes of this study might find applications in civil and petroleum engineering where damage zones containing tension induced cracks can influence either the overall deformation of the rock structure or the propagation of fractures from the excavation toward the rock mass. Although the uniaxial conditions considered in this paper are rather simplistic compared to most in-situ stress conditions, the possibility to relate crack intensities to properties such as the tensile strength or the fracture toughness, for instance, could be considered to explicitly adjust constitutive parameters when modeling rock structures. Ongoing efforts are currently done to pursue this study so as to characterize the influence of microcracks on permeability changes in damaged zones and on the propagation of hydraulically driven fractures.

## Acknowledgments

The authors thank the Région Grand-Est as well as the Fondation NIT for financially supporting this project.

## References

- [1] Hoek E, Brown ET. Practical estimates of rock mass strength. *Int J Rock Mech Min Sci* 1997;34:1165–86.
- [2] Cai M, Kaiser P, Uno H, Tasaka Y, Minami M. Estimation of rock mass deformation modulus and strength of jointed hard rock masses using the GSI system. *Int J Rock Mech Min Sci* 2004;41:3–19.
- [3] Pouya A, Ghoreychi M. Determination of rock mass strength properties by homogenization. *Int J Numer Anal Meth Geomech* 2001;25:1285–303.
- [4] Kachanov M. Elastic solids with many cracks and related problems. Hutchinson JW, Wu TY, editors. *Advances in applied mechanics*, vol. 30. Elsevier; 1993. [https://doi.org/10.1016/S0065-2156\(08\)70176-5](https://doi.org/10.1016/S0065-2156(08)70176-5) <<http://www.sciencedirect.com/science/article/pii/S0065215608701765>> .
- [5] Homand-Etienne F, Hoxha D, Shao J. A continuum damage constitutive law for brittle rocks. *Comput Geotech* 1998;22:135–51.
- [6] Guéguen Y, Kachanov M. Effective elastic properties of cracked and porous rocks - an overview. In: Leroy YM, Lehner FK, editors. *Mechanics of crustal rocks* Springer; 2011. p. 73–125. [https://doi.org/10.1007/978-3-7091-0939-7\\_3](https://doi.org/10.1007/978-3-7091-0939-7_3) <[https://link.springer.com/chapter/10.1007/978-3-7091-0939-7\\_3](https://link.springer.com/chapter/10.1007/978-3-7091-0939-7_3)> .
- [7] Levasseur S, Collin F, Charlier R, Kondo D. A micro macro approach of permeability evolution in rocks excavation damaged zones. *Comput Geotech* 2013;49:245–52.
- [8] Lu Y, Elsworth D, Wang L. Microcrack-based coupled damage and flow modeling of fracturing evolution in permeable brittle rocks. *Comput Geotech* 2013;49:226–44.
- [9] Cai M, Kaiser P, Tasaka Y, Maejima T, Morioka H, Minami M. Generalized crack initiation and crack damage stress thresholds of brittle rock masses near underground excavations. *Int J Rock Mech Min Sci* 2004;41:833–47.
- [10] Kranz RL. Microcracks in rocks: a review. *Tectonophysics* 1983;100:449–80.
- [11] Anders MH, Laubach SE, Scholz CH. Microfractures: a review. *J Struct Geol* 2014;69:377–94.
- [12] Ougier-Simonin A, Renard F, Boehm C, Vidal-Gilbert S. Microfracturing and microporosity in shales. *Earth Sci Rev* 2016;162:198–226.
- [13] Homand F, Hoxha D, Belem T, Pons M, Hoteit N. Geometric analysis of damaged microcracking in granites. *Mech Mater* 2000;32:361–76.
- [14] Moore D, Lockner D. The role of microcracking in shear-fracture propagation in granite. *J Struct Geol* 1995;17:95–114.
- [15] Vermilye JM, Scholz CH. The process zone: a microstructural view of fault growth. *J Geophys Res: Solid Earth* 1998;103:12223–37.
- [16] Fossen D. *Structural geology*. 1st ed. Cambridge University Press; 2010.
- [17] Paterson MS. *Experimental rock deformation - the brittle field*. Springer; 1978.
- [18] Nasser MHB, Schubnel A, Young RP. Coupled evolutions of fracture toughness and elastic wave velocities at high crack density in thermally treated westerly granite. *Int J Rock Mech Min Sci* 2007;44:601–16.
- [19] Griffiths L, Heap MJ, Baud J, Schmittbuhl J. Quantification of microcrack characteristics and implications for stiffness and strength of granite. *Int J Rock Mech Min Sci* 2017;100:138–50.
- [20] Nasser MHB, Mohanty B. Fracture toughness anisotropy in granitic rocks. *Int J Rock Mech Min Sci* 2008;45:167–93.
- [21] Kachanov M. Effective elastic properties of cracked solid: critical review of some basic concepts. *Appl Mech RevASME* 1992;45:304–35.
- [22] Hudson J, Pointer T, Liu E. Effective-medium theories for fluid-saturated materials with aligned cracks. *Geophys Prospect* 2001;49:509–22.
- [23] Zhu QZ. A new rock strength criterion from microcracking mechanisms which provides theoretical evidence of hybrid failure. *Rock Mech Rock Eng* 2017;50:341–52.
- [24] Schöpfer MPJ, Abe S, Childs C, Walsh JJ. The impact of porosity and crack density on the elasticity, strength and friction of cohesive granular materials: Insights from dem modelling. *Int J Rock Mech Min Sci* 2009;46:250–61.
- [25] Hamdi P, Doug S, Elmo D. Characterizing the influence of stress-induced microcracks on the laboratory strength and fracture development in brittle rocks using a finite-discrete element method-micro discrete fracture network FDEM- $\mu$ DFN

- approach. *J Rock Mech Geotech Eng* 2015;7:609–25.
- [26] Smilauer V, et al. *Yade* documentation. 2nd ed. The Yade Project; 2015.
- [27] Place D, Mora P. A lattice solid model to simulate the physics of rocks and earthquakes: incorporation of friction. *J Comput Phys* 1999;150:332–72.
- [28] Potyondy D, Cundall PA. Bonded-particle model for rock. *Int J Rock Mech Min Sci* 2004;41:1329–64.
- [29] Scholtès L, Donzé FV. A DEM model for soft and hard rocks: role of grain interlocking on strength. *J Mech Phys Solids* 2013;61:352–69.
- [30] Donzé FV, Bouchez J, Magnier S. Modeling fractures in rock blasting. *Int J Rock Mech Min Sci* 1997;34:1153–63.
- [31] Cho N, Martin CD, Segol DC. A clumped particle model for rock. *Int J Rock Mech Min Sci* 2007;44:997–1010.
- [32] Potyondy D. A flat-jointed bonded-particle material for hard rock. In: *46th US rock mechanics/geomechanics symposium, ARMA*; 2012.
- [33] Ding X, Zhang L. A new contact model to improve the simulated ratio of unconfined compressive strength to tensile strength in bonded particle. *Int J Rock Mech Min Sci* 2000;69:111–9.
- [34] Scholtès L, Donzé FV. Modelling progressive failure in fractured rock masses using a 3d discrete element method. *Int J Rock Mech Min Sci* 2012;52:18–30.
- [35] Dinç O, Scholtès L. Discrete analysis of damage and shear banding in argillaceous rocks. *Rock Mech Rock Eng* 2018;51:1521–38.
- [36] Dershowitz WS, Herda H. Interpretation of fracture spacing and intensity. In: *Proceedings of the 33rd US symposium on rock mechanics*; 1992. p. 757–66.
- [37] Asadi MS, Rasouli V, Barla G. A bonded particle model simulation of shear strength and asperity degradation for rough rock fractures. *Rock Mech Rock Eng* 2012;45:649–75.
- [38] Abdi H, Labrie D, Nguyen TS, Barnichon JD, Su G, Evgin E, et al. Laboratory investigation on the mechanical behaviour of tournemire argillite. *Can Geotech J* 2015;52:268–82.
- [39] Hamdi J, Scholtès L, Souley M, Al Heib M. Effect of discretization at laboratory and large scales during discrete element modelling of brittle failure. *Int J Rock Mech Min Sci* 2017;100:48–61.
- [40] Liao JJ, Yang MT, Hsieh HY. Direct tensile behavior of a transversely isotropic rock. *Int J Rock Mech Min Sci* 1997;34:837–49.
- [41] Nova R, Zaninetti A. An investigation into the tensile behavior of a schistose rock. *Int J Rock Mech Min Sci* 1990;27:231–42.
- [42] Douglass PM, Voight B. Anisotropy of granites: a reflection of microscopic fabric. *Géotechnique* 1969;19:376–98.
- [43] Nur A, Simmons G. Stress induced velocity anisotropy in rock: an experimental study. *J Geophys Res: Solid Earth* 1969;74:6667–74.
- [44] Sayers CM, Kachanov M. Microcrack induced elastic wave anisotropy of brittle rocks. *J Geophys Res: Solid Earth* 1995;100:4149–56.
- [45] Johnson PA, Rasolofosaon PNJ. Nonlinear elasticity and stress-induced anisotropy in rock. *J Geophys Res: Solid Earth* 1996;101:3113–24.
- [46] Bruno MS. Micromechanics of stress-induced permeability anisotropy and damage in sedimentary rock. *Mech Mater* 1994;18:31–48.
- [47] Souley M, Homand F, Pepa S, Hoxha D. Damage-induced permeability changes in granite: a case example at the URL in Canada. *Int J Rock Mech Min Sci* 2001;38:297–310.
- [48] Shao JF, Zhou H, Chau KT. Coupling between anisotropic damage and permeability variation in brittle rocks. *Int J Numer Anal Meth Geomech* 2005;29:1231–47.
- [49] Duriez J, Scholtès L, Donzé FV. Micromechanics of wing crack propagation for different flaw properties. *Eng Fract Mech* 2016;153:378–98.
- [50] Rice J. A path independent integral and the approximate analysis of strain concentration by notches and cracks. *J Appl Mech* 1968;35:379–86.
- [51] Kuang JH, Chen LS. A displacement extrapolation method for two-dimensional mixed-mode crack problems. *Eng Fract Mech* 1993;46:735–41.
- [52] Chan SK, Tuba IS, Wilson WK. On the finite element method in linear fracture mechanics. *Eng Fract Mech* 1970;2:1–17.
- [53] Clayton JQ, Knott JF. Observations of fibrous fracture modes in a prestrained low-alloy steel. *Met Sci* 1976;10:63–71.
- [54] Chao J, Gao-Feng Z, Khalili N. On crack propagation in brittle material using the distinct lattice spring model. *Int J Solids Struct* 2017;118–119:41–57.
- [55] Grassl P, Jirásek M. Meso-scale approach to modelling the fracture process zone of concrete subjected to uniaxial tension. *Int J Solids Struct* 2010;47:957–68.
- [56] Chen H, Liu Y. A non-local 3d lattice particle framework for elastic solids. *Int J Solids Struct* 2016;81:411–20.
- [57] Labuz JF, Chen CN, Berger DJ. Microcrack-dependent fracture of damaged rock. *Int J Fract* 1990;51:231–40.
- [58] Chandler MR, Meredith PG, Brantut N, Crawford BR. Fracture toughness anisotropy in shale. *J Geophys Res: Solid Earth* 2016;121:1706–29.